Contents

List of Figures

List of Tables

1 Model overview

Tethys-Chloris (T&C) simulates energy, water and elements budgets at the land-surface, and the physiological cycle of plants, representing different carbon and nutrient compartments. Simulated plant life-cycle processes include photosynthesis, phenology, carbon allocation and tissues turnover. Vegetated and non-vegetated surfaces represent the land-cover and in specific conditions the land surface can be covered by snow and/or ice. In a domain of study, the dynamics of each computational element are resolved using local meteorological forcing (eventually affected by distant topography) and boundary conditions, in terms of soil and vegetation properties. Spatial interactions are introduced by considering the surface and subsurface water transfers among elements that affect the soil moisture states. Soil moisture, in turn, impacts local dynamics via the coupled energy-water-carbon-nutrient interactions. Shading cast by remote terrain is also considered. A quasi-three-dimensional representation of land-surface dynamics in a given domain is thus achieved, where incoming energy and water lateral transfers can influence the spatio-temporal variability of the simulated fluxes and states.

Multiple processes are represented in the model that interact with each other in a dynamic fashion, mimicking the inter-coupled vegetation-hydrology-soil biogeochemistry system. An outline of the simulated hydrological processes is sketched in Figure 1. The coupling among various plant life regulatory mechanisms is illustrated in Figure 2 and an overview of the soil biogeochemistry component is presented in Figure 3. The simulated components are also listed in the following.

◇ **Hydrological components**

- absorption, reflection, and transmittance of solar shortwave radiation and atmospheric longwave radiation (Section 4);
- sensible and latent heat fluxes, ground heat flux and other energy processes, including the partition of latent heat into transpiration and various evaporation components (Section 5);
- resistance schemes for water and energy fluxes, including aerodynamic resistance, leaf boundary layer resistance, within canopy turbulence profile, soil and litter resistances, and stomatal resistance (Section 6);
- snow hydrology component, including snowpack energy balance, snowmelt, and snow interception by canopy (Section 7) and avalanches (Section 16);
- ice hydrology component, including ice energy balance, and ice melt (Section 8);
- interception, throughfall, water logging and water influx to soil (Section 9);
- hydrology of surface water bodies and fractured rocks (Section 10);
- rainfall induced erosion (Section 11);
- interaction between plants and water availability (Section 13);

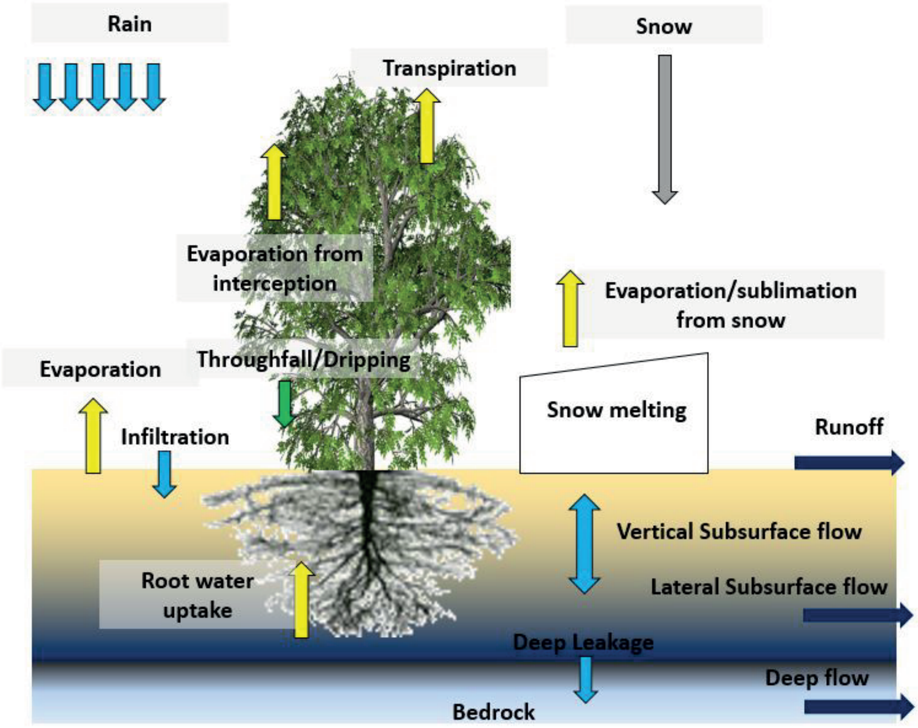

Figure 1: A diagram of the included hydrological components.

- infiltration and unsaturated and saturated zone water dynamics in a multi-layer soil, including runoff formation (Section 12);
- subsurface (Section 14) and surface flow routing (Section 15).

◇ **Vegetation components**

- photosynthesis and plant respiration, carbon balance including allocation and translocation and tissue turnover (Section 17);
- plant biophysical relations (Section 18);
- plant nutrient budget (Section 19);
- vegetation phenology (Section 20);
- vegetation management (Section 22).

◇ **Soil biogeochemistry components**

- carbon and nutrient budgets of litter (Section 21.2 and 21.3);
- soil organic carbon budget (Section 21.4);
- soil nitrogen, phosphorus, and potassium budgets (Section 21.6, 21.7 and 21.8);
- nutrient leakage, deposition, biological nitrogen fixation, and supply of primary minerals (Section 21).

The hydrological budget is formulated at an *hourly* time scale to preserve sub-daily meteorological variability and the diurnal cycle. Most vegetation dynamics are simulated at the daily time scale, however biochemical processes of photosynthesis and stomatal physiology are computed at the hourly time scale, as a necessary component affecting the hydrological budget. Soil biogeochemistry dynamics are resolved at the daily scale. Other modules operate at the sub-hourly resolution, e.g., the subsurface water dynamics are formulated to have an adaptive time step (minutes). The infiltration component can be forced disaggregating rainfall at the 5 minute time scale. The surface flow routing uses internal time steps in the order of seconds (Section 15). Mass and energy budgets are conserved at their respective computational steps.

1.1 Short model history

The idea to develop Tethys-Chloris model originates back in 2007 from the emerging interest that the previous decade reversed toward ecohydrological studies and related scientific questions. The original idea was to build a physical-based mechanistic tool that could account for the coupled interactions of energy-water-vegetation in distributed and topographically complex domains where water was the dominant

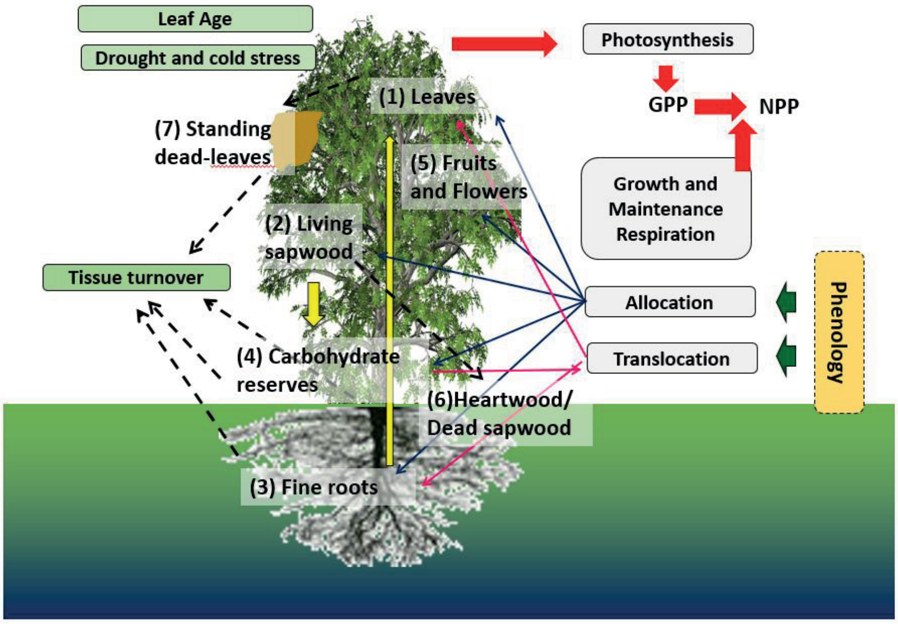

Figure 2: A conceptual diagram of carbon fluxes and processes simulated by the model. The seven carbon pools represent leaves, fine roots, living sapwood, carbohydrate reserves, fruit and flowers, heartwood/dead sapwood and standing dead leaves. The red arrows indicate the general fluxes related to photosynthetic products. The blue solid-line arrows show allocation fluxes, while the magenta lines show translocation fluxes. The black dashed-line arrows indicates turnover from carbon pools. The yellow arrows indicate allometric constraint controls.

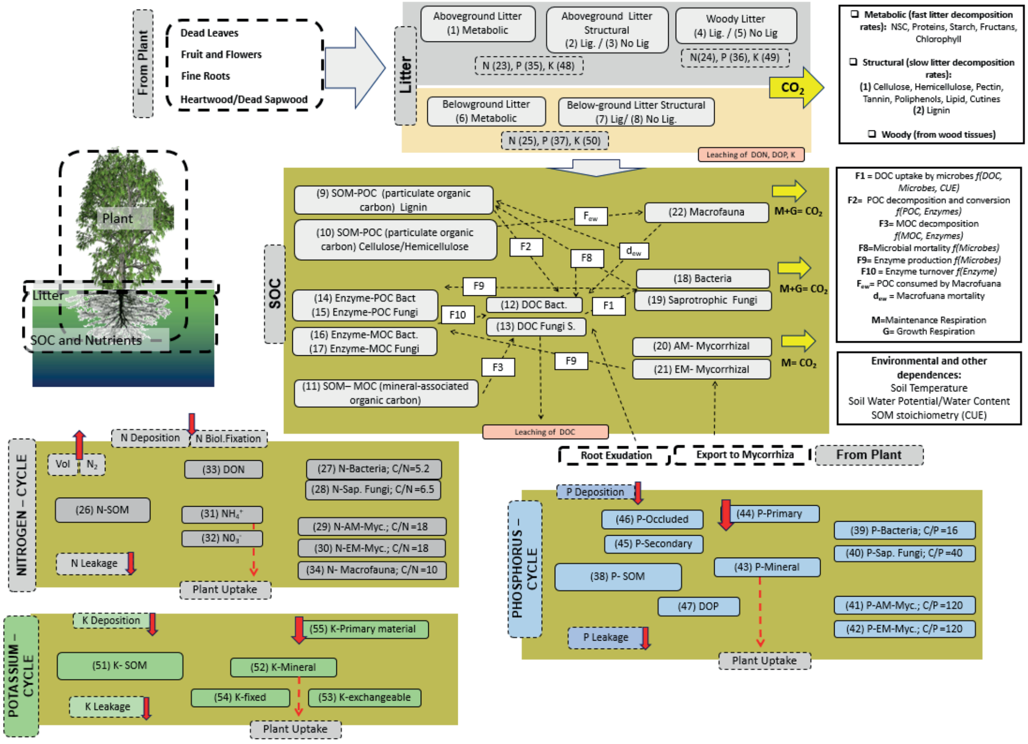

Figure 3: A conceptual scheme of the 55 carbon and nutrient pools simulated by the model. Aboveground and belowground litter pools are presented in the top panel. Soil Organic Carbon (SOC) pools and corresponding fluxes are presented in the central panel. The nitrogen, phosphorus and potassium cycles are presented in the bottom panels. The CO_2 respiration fluxes are indicated with yellow arrows, nutrient inputs and outputs with red arrows.

component affecting vegetation functioning. This is reflected in the earliest publications (*Fatichi*, 2010; *Fatichi et al.*, 2012a,b) introducing the model. Since then, the scope of the model has been continuously expanded to deal with a large variety of ecosystems and climates and address new problems. This has led to the revision of original model solutions, the improvement of parameterizations, and, for instance, the inclusion of management components (*Fatichi et al.*, 2014b). Recently a major effort has been dedicated to add an entire module dealing with plant mineral nutrition and soil biogeochemical dynamics (*Fatichi et al.*, 2019). In this evolution, T&C moved from its original ecohydrological design to become a mechanistic ecosystem model, or Terrestrial Biosphere Model (TBM) to use a more recent terminology. Since 2012, it has been used to tackle scientific questions about global change and the future of water and carbon resources where complex non-linear interactions between hydrological, soil and vegetation dynamics are at play. Being a research tool, T&C is evolving continuously, there are periods when small changes or additions are occurring on a daily or weekly basis, which makes difficult to document precisely the details of all the latest implementations. The pages you will be reading in this technical reference are the best effort to summarize T&C structure at October 2019, but surely by the time you read, some change would have occurred. Regardless, we deem extremely important for any model to have such a technical reference, this does not only represent the main source of model documentation, but it can be seen as the platform for guiding further model developments.

As a final note, the model names may seem unfamiliar, however Tethys (Greek: $T\eta\theta\nu\varsigma$) in Greek mythology, was an archaic Titaness and aquatic sea goddess and she was considered as an embodiment of the waters of the world. Chloris (Greek: $X\lambda\omega\rho\ iota\varsigma$) was a Nymph associated with spring, flowers, and new growth, thus, now this name is way less surprising for such a model.

2 Basic computational element geometry and surface composition

In a distributed model, the domain is typically represented using a number of elementary computational units (*Kampf and Burges*, 2007). These are referred to here as *basic computational elements*, implying smallest elements for which the model computes all the state variables and the energy, water, carbon, and nutrient fluxes. In the case of hydrological basin, or a region, the basic computational element is characterized by a topographic representation, and interacts with the neighbors elements (Section 3). The basic element is further characterized by a land cover composition that summarizes one or more of the possible land use.

Basic computational elements can be represented in different ways, with unstructured grids as triangulated irregular networks (TIN) or hexagons, or with regular grid domains (*Tucker et al.*, 2001; *Ivanov et al.*, 2004; *Vivoni et al.*, 2005; *Kampf and Burges*, 2007; *Khanna and Medvigy*, 2014). T&C uses a regular square grid (Figure 4a), which corresponds to the grid of a Digital Elevation Model (DEM), or Digital Terrain Model (DTM). Such a geometrical description has been widely used in hydrology (*O'Callaghan and Mark*, 1984; *Abbott et al.*, 1986; *Quinn et al.*, 1991; *Wigmosta et al.*, 1994; *Bertoldi et al.*, 2006b). While this is not a parsimonious computational choice, the pros and cons of the approach are well known and algorithms retrieving topographic features (e.g., slope, aspect, and curvature) from DTMs are advanced. The same holds true with regards to terrain parameters affecting incoming solar radiation (*Kumar et al.*, 1997; *Dubayah and Loechel*, 1997; *Rigon et al.*, 2006; *Fatichi et al.*, 2011), or important hydrologic characteristics such as flow direction (*O'Callaghan and Mark*, 1984; *Tarboton*, 1997; *Orlandini et al.*, 2003; *Nardi et al.*, 2008).

2.1 Land cover composition

Basic computational elements of T&C can account for up to four different land cover types: vegetated areas, bare soil areas, rocks, and water surfaces. The model also computes ice and snow cover that can modify the representation of the surface, even though ice and snow are not independent land covers. Fractions of land cover

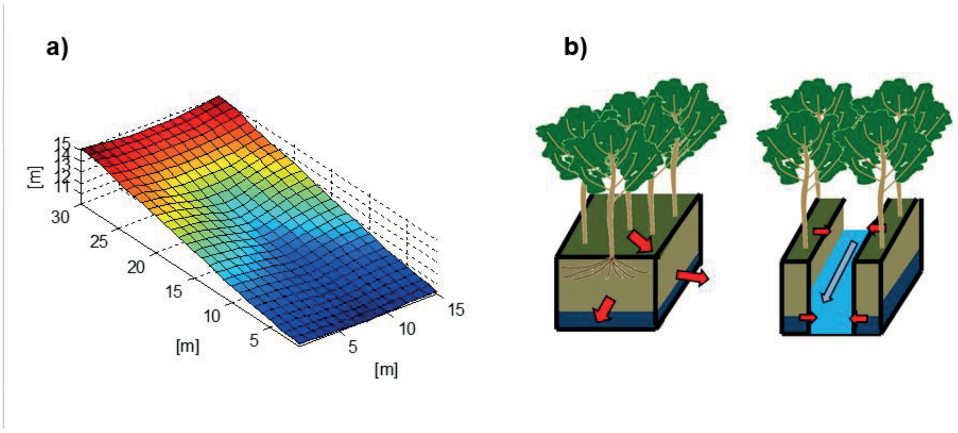

Figure 4: A representation of topographic features and connections among basic computational elements. (a) A fragment of a Digital Elevation Model. (b) A conceptual scheme of a basic computational element with and without a subgrid channel element.

are indicated with the following symbols: C_{veg}, C_{bare}, C_{rock}, and C_{wat} $[-]$, which respectively represent the fraction occupied by vegetation, bare soil, rocks, and water in a given computational element (Figure 5). It follows that the equation $C_{veg} + C_{bare} + C_{rock} + C_{wat} = 1$ must be always true. Even though, the model is theoretically designed for any type of land-cover composition, i.e., the C_{veg}, C_{bare}, C_{rock}, and C_{wat} fractions can assume any feasible combination of values, model assumptions are more appropriate for small computational elements as much homogenous as possible. This suggests that land-cover representations should have elements small enough to belong to a single land-use category or maximum two for sparse canopies in semi-arid environments where $C_{veg} < 1$ and $C_{bare} > 0$.

The presence or absence of snow and ice is indicated with binary variables C_{sno} and C_{ice} $[-]$ that assumes the value of *1* in presence of snow, ice and *0* otherwise. This means that ice can be present or form over other land-uses (e.g., bare soil or rocks), as well as snow can cover the various land uses. If the original land-use is water, under the right conditions it may freeze and subsequently snow can accumulate over the frozen water (Section 10). These situations are indicated with two additional binary variables $C_{ice,w}$ and $C_{sno,w}$ $[-]$ that assume the value of *1* when there is ice and snow above a water surface and *0* otherwise. The other assumptions are that when snow is present on the ground it entirely covers bare soil areas and rocks, while snow can be intercepted by the vegetation canopy. More specifically, intercepted snow modifies the radiative and roughness properties of a vegetated element and snow can eventually bury completely vegetation (Section 7.3). Properties are modified using the relative height of snow and vegetation as further detailed later on. Additionally, water can be present on top of other land-uses as a result of ponding (Section 9.6) and modifies the radiative and roughness properties of the computational element.

An important input that needs to be assigned to each computational element is the reference height of measurements z_{atm} $[m]$. This is a unique value regardless

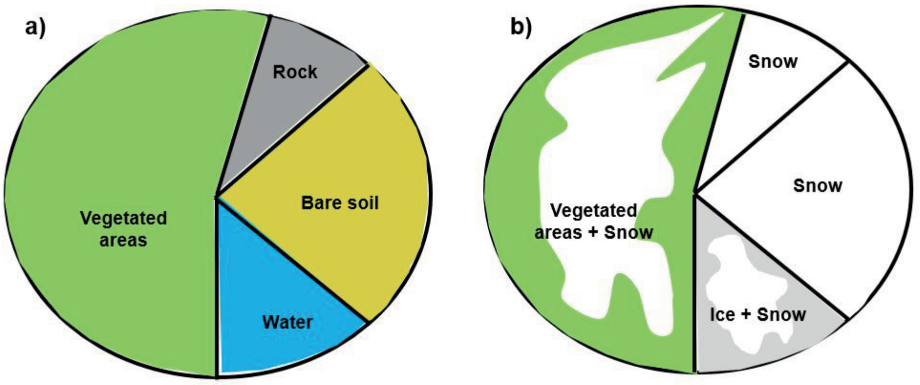

Figure 5: An illustration of the potential land cover composition of a *basic computational element*. (a) The element in the most general case is subdivided into vegetated areas, bare soil areas, rocks, and water surfaces. (b) The presence of snow $C_{sno} = 1$ and frozen water $C_{sno,w} = C_{ice,w} = 1$ alters the surface composition.

of the land cover composition and represents the height at which meteorological measurements used to force the model have been collected, e.g., the flux-tower height in case of a model application using flux-tower data (*Baldocchi et al.*, 2001) or about 2 m above ground for meteorological data collected with standard meteorological stations. In any case, z_{atm} should be higher than the maximum canopy height in the computational domain to allow a meaningful computation of roughness and aerodynamic properties.

2.2 Vegetation composition

The vegetated fraction of a basic computational element, C_{veg}, can include one or many vegetation types. In many applications vegetation species that share the same life form (tree, shrub, or grass), broad bioclimatic limits (e.g., temperate, tropical, boreal), leaf morphology (broadleaves, needleleaves) and phenology (e.g., evergreen, deciduous) are considered to belong to the same Plant Functional Type (PFT), as described by *Bonan et al.* (2002). The Plant Functional Type representation is convenient because it lumps various plant strategies in a handful of categories, but has also several weaknesses and limitations (*Pappas et al.*, 2016). Plant response is, in fact, mediated by functional traits, defined as plant morphological, phenological or physiological characteristics that control plant functioning and thus its fitness, and they can be linked to model parameters (*Pappas et al.*, 2016). For this reason, rather than a classic plant-functional-type parametrization with a few dozens of pre-defined (PFT), T&C is flexible in accounting for a generic number of vegetation units and can theoretically use a different parametrization of vegetation for each case study. The total vegetation cover C_{veg}, is partitioned in T&C in subunits which are called *Crown Areas*. The model can consider both horizontal and vertical composition of vegetation with one or two vertically "stacked" vegetation type corresponding to a single *Crown Area*. The spatial fractions of *Crown Areas* are represented with the symbol C_{crown} $[-]$. The total number n_c of *Crown Areas* depends on the given element, and their sum always corresponds to the entire vegetated area $\sum_{i=1}^{n_c} C_{crown} = C_{veg}$. Therefore, the maximum number of different vegetation types in a element is given by $2\,n_c$ if in any C_{crown}, there is a overstory canopy henceforth named the *High-vegetation* (H_v) layer, and understory canopy named the *Low-vegetation* (L_v) layer. The horizontal land cover composition of T&C is presented in Figure 6. A bare soil fraction and different vegetation patches (the *Crown Areas*) are included. The term *Crown Area* is used because spatial vegetation classification follows the surface projected area of tree crowns for tree species, while it is assumed to represent the area effectively occupied by grass and shrub for these plant forms. A *Crown Area* can be occupied by a single vegetation type in the *High-vegetation* and another single one in the *Low-vegetation.* While theoretically possible such a vertical composition of vegetation is rarely used in model applications. This is because of the strong light limitations, as simulated by the simple radiative transfer scheme, it is almost impossible to have two co-existing different vegetation layers which are exactly overlapping in the vertical. Therefore, in basically all applications the number of *Crown Areas* also correspond to the the number of vegetation types and the choice of defining a vegetation belonging to the *High-vegetation* or *Low-vegetation* category is simply dictated by its interaction with snow.

The vegetation unit which occupies a *Crown Area* may correspond to a single species (*Fatichi and Leuzinger*, 2013), aggregation of species, or even to the classic *PFT* definition in certain conditions. This flexibility allows one to consider variability of plant-traits also for species sharing the same environmental conditions (e.g., *Reich et al.*, 1997; *Wright et al.*, 2004; *Kattge et al.*, 2009). The model does not have an upper limit for the number of *Crown Areas*, therefore when computational time is not limiting, a complete representation of multiple species can be obtained.

The definition of *Crown Area* is important in T&C since refers to the smallest spatial unit of vegetation that has a unique parametrization. To obtain the element-scale flux values, each *Crown Area* and eventually the bare soil fraction are used as weights to the relative flux contributions. This partition strongly affects the estimation of the surface water and energy fluxes (Section 5). Note that since the energy fluxes and soil water budget are computed at the element scale, their values affect quantities as photosynthesis or stomatal conductance, which are instead computed at the *Crown Area* scale, which is indicated with $m^{-2}\,VEG\,area$.

Vegetation attributes such as leaf area index, LAI $[m^2\ leaf\ area\, m^{-2}\ ground\,area]$, or the Gross Primary Production GPP $[gC\ day^{-1}\ m^{-2}\ \ ground\,area]$, can represent: (i) the result of perpendicular projections to the terrain over the total element area, e.g., for unit of ground or (ii) the quantities at the *Crown Area* level, i.e., LAI $[m^2\ leaf\ area\ m^{-2}\ \ VEG\,area]$ and GPP $[gC\ day^{-1}\ m^{-2}\ \ VEG\,area]$, where the *Crown Area* is only the area effectively occupied by the vegetation. In T&C all the vegetation quantities (e.g., LAI, GPP) are computed for unit of *Crown Area*, the corresponding quantities at the element scale are obtained by multiplying their

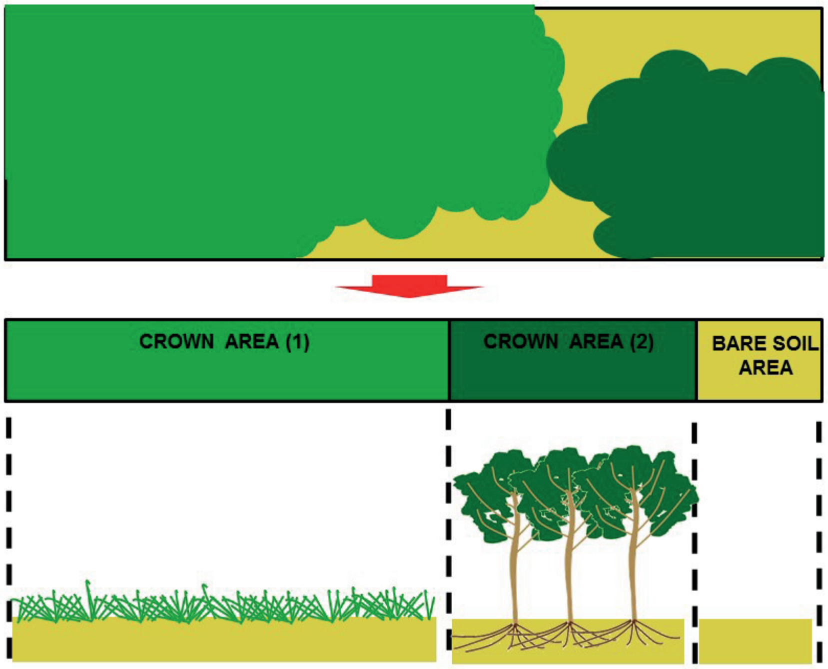

Figure 6: An illustration of vegetation representation at the element scale. The area is subdivided into patches of bare soil and patches of vegetation (*Crown Areas*). In each *Crown Area*, vegetation may include up to two types: the upper canopy (High-vegetation H_v) and the lower canopy (Low-vegetation L_v). All vegetation types tap on the same soil moisture and nutrient pools at the element scale.

Crown Area-scale magnitudes by the relative *Crown Area* fractions, C_{crown}. In the following, whenever the m^{-2} units of LAI or other vegetation variables are not specified, they are considered to be at the *Crown Area* level ($m^{-2}\,VEG\,area$).

In a fully dynamic vegetation model, the fractions, C_{crown}, can be subject to change due to crown expansions (e.g., in a plantation), species competition, and mortality. In T&C, direct species competition is neglected and thus *Crown Area* fractions are inputs, which remain constant during the entire simulation with the exception of young plantations or other young expanding ecosystems, where a temporal dynamics of C_{crown} can be prescribed (Section 22). Nonetheless, competition for resources, such as water and light is indirectly accounted for in the model, as a consequence of vegetation characteristics, e.g., plant traits as photosynthetic or water uptake properties, rooting profiles. This still creates a dynamic and interacting simulation framework.

An additional important categorization of vegetation in T&C is made through the variable Ξ, which identifies the broad vegetation category. Currently, T&C distinguishes between four vegetation categories: normal evergreen plants ($\Xi = 0$), seasonally deciduous plants ($\Xi = 1$), grass ($\Xi = 2$) and evergreen tropical plants ($\Xi = 3$). This separation is necessary because different broad vegetation categories have substantially different phenology and carbon allocation and translocation dynamics and must use different model structures and not only model parameters (Section 17).

2.3 Soil biogeochemically active zone

In each basic computational element if soil and organic matter are present, there are biogeochemical transformations affecting soil organic carbon and soil nitrogen, phosphorus, and potassium budgets (Section 21). For the sake of simplicity, T&C does not solve the vertical soil profile of carbon content and other nutrients and consider a single lumped compartment where all the biogeochemical reactions co-occur. This is identified as the biogeochemically active zone and correspond to the first Z_{bio} $[mm]$ of soil, where $Z_{bio} = 250$ mm is a reference value currently used in the model applications, and implies that most of the carbon and nutrient cycling is assumed to occur in the first 25 cm of soil. Concurrently, soil temperature and soil moisture (simulated over the one-dimensional vertical profile) are averaged over this depth to characterize the environmental conditions for the soil biogeochemical reactions (Section 21). This is a restrictive assumption since having an explicit vertical resolution in a soil biogeochemistry model has been shown to improve considerably simulations (*Koven et al.*, 2013). However, representing the vertically resolved carbon and nutrient cycles responsible for soil organic carbon and litter turnover and plant-soil nutrient interactions would imply to compute all the soil biogeochemistry fluxes and track all the states variables for each soil-layer. Given the large number of state variables and fluxes in the soil biogeochemistry module (Figure 3 and Section 21) and the n_s layers used in the model (Section 12.1), such a solution is particulary burdensome.

3 Spatial connections among basic computational elements

The basic computational elements can be characterized by topographic features, once grid elements have been identified in a domain representation. As introduced in Section 2, each element is represented by a square with typical dimensions of 25-10,000 m^2. The slope and aspect are calculated on the basis of the DTM, along with less conventional topographic attributes, such as the sky-view factor, the shadow effect (also time dependent), and the terrain configuration factor (*Bertoldi et al.*, 2006a; *Fatichi et al.*, 2011) (Section 3.3). These attributes are used to directly account for local and remote effects on incoming radiation. The vertical reference system of each element is represented by the normal to the surface, n, that is used to define all dimensions in the normal direction (e.g., the soil layer mesh). The state variables and fluxes of the one-dimensional equations are function of the normal direction, n. For simplicity the dependence by n is omitted later in the text, where we refer to a flat element where normal and vertical reference systems coincide. The basic computational element may represent a part of a hillslope and it exchanges water in the subsurface and over the surface with neighboring elements (Figure 4b). Energy fluxes are computed normally to the surface and no lateral energy advection is considered.

3.1 Flow directions

The approach used to route water over the surface and the subsurface domains in T&C follows the well developed concept of topographic flow directions (*O'Callaghan and Mark*, 1984; *Quinn et al.*, 1991; *Tarboton and Rodriguez-Iturbe*, 1991; *Costa-Cabral and Burges*, 1994; *Tarboton*, 1997; *Orlandini et al.*, 2003; *Nardi et al.*, 2008; *Orlandini and Moretti*, 2009; *Schwanghart and Kuhn*, 2010). T&C has various options of approximating flow directions. For instance, a multiple direction method (*Quinn et al.*, 1991) can be used to compute directions for the subsurface, and the D-∞ method (*Tarboton*, 1997) or more advanced methods (*Orlandini et al.*, 2003; *Orlandini and Moretti*, 2009) for the surface domain (Figure 4a). When water moves into a neighboring cell, the flow window width that is assumed in the flux computation always corresponds to the length of the square in the cardinal direction. This is an approximation for diagonal transfers, where the window width is not defined, as compared to other methodologies (*Quinn et al.*, 1991). The same cell length is also used to compute the actual distance covered by the flow, regardless whether the movement occurs in the diagonal or cardinal direction.

Note that in order to obtain surface flow paths from DTMs a pre-processing exercise is typically required, since all DTMs present some spurious errors or real topographic features that act as sinks, commonly indicated as depressions or pits (*Grimaldi et al.*, 2007). Natural or artificial depressions and flat areas within a DTM are critical in the computation of the flow directions (*Nardi et al.*, 2008). The absence of slope, indeed, does not allow to directly identify the direction of flow and generates problem to all the flow routing algorithms that are topographically based (e.g. kinematic routing) as the one adopted in T&C (Section 15). Therefore, some form of DTM pre-processing to eliminate pits and univocally define the flow directions is required (*Orlandini et al.*, 2003). The flow direction matrix is used to route subsurface and surface water flows (see Sections 14 and 15). Flow directions are also computed to route snow when an avalanche occurs (Section 16). Maps of flow accumulation, i.e. upslope area according to the calculated flow directions, are shown in Figure 7. The difference among various methods is evident, with the multiple flow algorithm producing a much larger dispersion of the flow.

3.2 Channels

A further topographic characteristic required for flow routing is the distinction between cells that belong or do not to the channel network. This distinction leads to the delineation of the channel network and can be easily made when geographical information about the stream position is available. Methodologies to identify

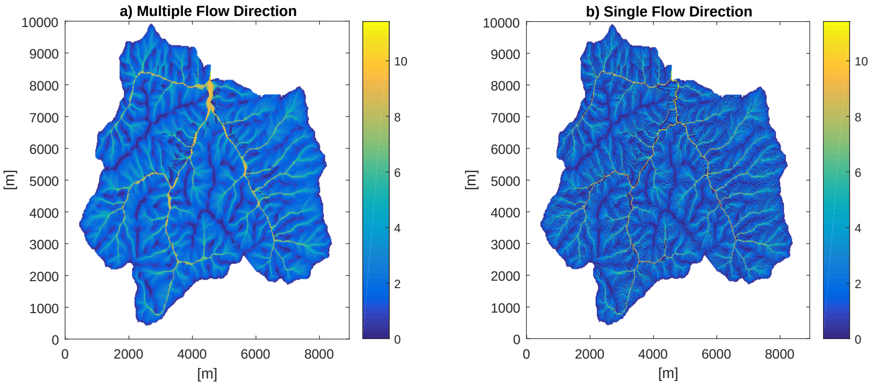

Figure 7: Maps of flow accumulation (logarithm of the number of upstream cells), i.e. upslope area according to the calculated flow directions. a.) D-infinity method (*Tarboton*, 1997). b.) Single flow method of *Orlandini et al.* (2003) using lateral transversal deviation with $\lambda = 1$. The domain is the Cerfone creek watershed in Tuscany (Italy).

the channel network directly from DTM have been also provided (*Montgomery and Dietrich*, 1988, 1989; *Orlandini et al.*, 2011). The simplest method is to set a threshold on the contributing area, i.e, identify a channel cell when the flow accumulation is larger than a given value (Figure 7). When no information on the position of the channels is available, such a method is used in T&C. Alternatively, the channel locations can be imposed on the basis of available geographical information.

Once identified channels are considered as *subgrid* elements. Specifically, channels are a particular type of grid cells that contain a channel reach along with a hillslope fragment (Figure 4b). In these cells overland and channel flows may occur simultaneously. Both the overland flow and the subsurface flow are assumed to flow toward the channel. Irregular channel geometries cannot be accounted for and a rectangular cross section is used based on a prescribed channel width, potentially different for each channel cell, which is part of the model inputs. Further details concerning the treatment of channels are described in Section 14 and 15.

3.3 Terrain effects

Solar radiation originating from the sun travels through the atmosphere and is modified by topography and other surface features. Solar radiation at the ground surface can be intercepted as direct beam, $R^T_{B,\Lambda}$, diffuse, $R^T_{D,\Lambda}$, and reflected radiation, $R^T_{R,\Lambda}$, where the subscript Λ indicates the wavelength band. Incoming solar radiation is function of the local topography through site aspect and slope, and of the surrounding terrain through sky view factor, $S_{vf}(\vec{x})$, and shadow effect, $S_h(\vec{x},t)$, where $\vec{x}$ is the position and t is the local time. A brief description of incoming solar radiation components and topographic effects is provided in Figure 8.

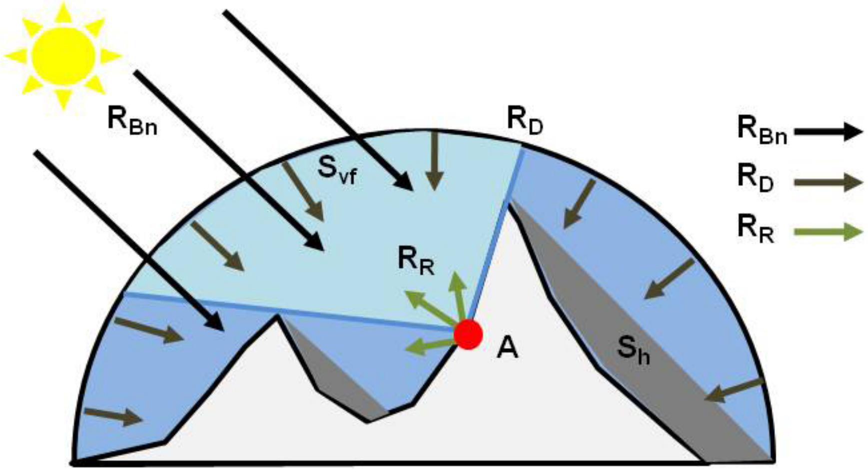

Figure 8: Components of incoming solar radiation on a slope: direct beam radiation at normal incidence, R_{Bn}, diffuse radiation, R_D, and diffuse and direct radiations reflected off by nearby terrain, R_R. The reflected contribution from a generic A location is shown as example. Sky view factor, S_{vf}, from A and shadow effects, S_h, in the represented landscape are also shown. The figure is adapted from *Dubayah and Loechel* (1997).

The importance of topographic variability in hydrological and biophysical processes is well known (*Bertoldi et al.*, 2006a; *Ivanov et al.*, 2008c). For such a reason the quantities used to take into account topographic influences on solar radiation are described in the following.

The principal variable controlling incident radiation on a slope, in mountainous terrain, is the local solar illumination angle, $\varphi_{S,T}$ $[rad]$, that is defined as the angle between the sun beam and the normal to the slope surface (*Dozier and Frew*, 1990), given by :

$$\cos\varphi_{S,T} = \cos\beta_T \sin h_S + \sin\beta_T cosh_S \cos(\zeta_S - \zeta_T)\,, \tag{1}$$

where β_T $[rad]$ is the slope of the site, ζ_T $[rad]$ is the local aspect (clockwise direction from north), and h_S $[rad]$, ζ_S $[rad]$ are the solar altitude and azimuth angles respectively.

Another important parameter is the sky view factor, S_{vf} (*Chen et al.*, 2006). The sky dome viewed by the slope surface in mountainous terrain can be obstructed by neighboring surfaces. *Dozier and Frew* (1990) provide a method to take this effect into account, defining the sky-view factor, S_{vf}, as:

$$\begin{aligned} S_{vf} \;\approx\; & \frac{1}{2\pi}\int_0^{2\pi}\Big[\cos\beta_T \sin^2 H_\zeta + \\ & \sin\beta_T\cos(\zeta-\zeta_T)(H_\zeta - \sin H_\zeta\cos H_\zeta)\Big]d\zeta\,, \end{aligned} \tag{2}$$

where H_ζ is the horizon angle (Figure 9), measured from the zenith downward to the local horizon, for direction ζ. Further details on the calculation of Eq. (2) are provided in *Dozier and Frew* (1990). Equation (2) includes the possibility to account for a variable horizon angle surrounding the point of interest, and not only for a constant horizon as assumed in other sky-view factor formulations.

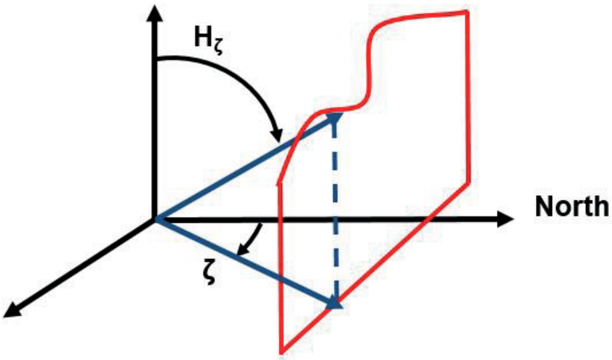

Figure 9: Horizon angle, H_ζ, for a direction ζ, adapted from *Dozier and Frew* (1990).

Dozier and Frew (1990) derived also a terrain configuration factor, C_t [$-$], which approximates the total area between the point and the surrounding terrain for which the points are mutually visible:

$$C_t \quad \approx \quad \frac{1+\cos\beta_T}{2} - S_{vf}\,. \tag{3}$$

As counterpart of sky view factor, the terrain configuration factor, C_t, estimates the fraction of the surrounding terrain visible to the point and varies from 0 (only sky visible) to 1 (only terrain visible). Further details on the calculation of Eq. (3) are provided in *Dozier and Frew* (1990). The shadow effect S_h [0/1] is finally calculated as a binary coefficient, which value is zero when the sloping surface is shadowed by neighboring terrain, while equal to one otherwise (*Dubayah and Loechel*, 1997; *Chen et al.*, 2006).

The direct beam, $R_{dir,\Lambda} = R^T_{B,\Lambda}$, flux on a generic slope is thus given by:

$$R^T_{B,\Lambda} \quad = \quad S_h\,\cos\varphi_{S,T}\,R_{Bn,\Lambda}\,, \tag{4}$$

where $R_{Bn,\Lambda}$ is the direct beam radiation at normal incidence. Wherever $\cos\varphi_{S,T}$ is negative, the point is "self-shadowed", i.e. the sun is below the local horizon caused by the slope itself. When instead $S_h = 0$ is cast shadowed, i.e. the shadow is caused by nearby terrain blocking the sun (*Dubayah and Loechel*, 1997). Note that when there is no shadow and the surface is flat $\beta_T = 0$, Eq. (4) reduces to $R^T_{B,\Lambda} = \sin h_S\;R_{Bn,\Lambda}$, which is the conventional equation for a flat surface (*Fatichi et al.*, 2011).

The diffuse sky irradiance, $R^T_{D,\Lambda}$, on a surface oriented in space is composed of three components: the circumsolar, the circumzenith, and isotropic irradiation (*Olseth* *et al.*, 1995; *Olseth and Skartveit*, 1997), and for each of these components a specific topographic correction should be applied, see for example *Olseth and Skartveit* (1997). For simplicity the entire incident diffuse radiation $R_{D,\Lambda}$ is considered as isotropic (*Dozier and Frew*, 1990; *Dubayah and Loechel*, 1997; *Chen et al.*, 2006) and is given by:

$$R^T_{D,\Lambda} \quad = \quad S_{vf}\, R_{D,\Lambda}\,. \tag{5}$$

Another contribution to diffuse irradiance is given by reflected radiation, $R^T_{R,\Lambda}$, on surrounding topography. Incoming radiation, in fact, may be reflected from nearby terrain toward the point of interest and can rarely be expected to be isotropic. In order to account for this effect, an approximate terrain configuration factor, C_t, is usually employed (Eq. 3) (*Dozier and Frew*, 1990; *Dubayah and Loechel*, 1997). This is motivated by the complexity in determining the geometric relationships between a particular location and all the surrounding terrain elements. Therefore, the reflected radiation, $R^T_{R,\Lambda}$, from surrounding terrain is simply estimated as:

$$C_t\, R^T_{R,\Lambda} = C_t\, \rho_g \big(R_{Bn,\Lambda} \cos(\varphi_{S,T}) + (1 - S_{vf}) R_{D,\Lambda}\big)\,, \tag{6}$$

where ρ_g is the average ground albedo refereing to a large area of 5-50 $[km]$ radius around the point (*Gueymard*, 2008). Note that when an unobscured flat surface is considered $C_t = 0$, since $\beta_T = 0$ and $S_{vf} = 1$, i.e. all the sky dome is visible. Consequently the reflected radiation component is $R^T_{R,\Lambda} = 0$.

The diffuse shortwave radiation on a slope is the sum of two components: $R_{dif,\Lambda} = R^T_{D,\Lambda} + C_t\, R^T_{R,\Lambda}$. Finally, the global shortwave radiation, $R_{sw,\Lambda}$, is:

$$R_{sw,\Lambda} = R_{dir,\Lambda} + R_{dif,\Lambda} = R^T_{B,\Lambda} + R^T_{D,\Lambda} + C_t\, R^T_{T,\Lambda}\,. \tag{7}$$

The information required to evaluate the previous equations, such as local site slope, $\beta_T(\vec{x})$ $[rad]$, local site aspect, $\zeta_T(\vec{x})$ $[rad]$, and horizon angle, $H_\zeta(\vec{x}, \zeta)$ $[rad]$, can be obtained from the analysis of the DTM. Specifically, in order to calculate the horizon angle, $H_\zeta(\vec{x}, \zeta)$, the viewsheds for each cell $\vec{x}$ of an input DTM should be calculated. A viewshed is the angular distribution of sky visibility versus obstruction. This is similar to the view provided by upward-looking hemispherical (fisheye) photographs. A viewshed is calculated by searching in a specified set of directions around a location of interest. The resolution of the viewshed array must be sufficient to adequately represent all sky directions but small enough to enable rapid calculations, for the following examples an eight directions algorithm is used. Horizon angles for other directions are interpolated from the principal ones.

An example of the values assumed by the above mentioned variables is provided in Figure 10 and in Figure 11 for the *Versilia* watershed in Tuscany (Italy). Sky-view factor, S_{vf}, terrain configuration factor, C_t, and shadow effect, S_h, in each cell and for a particular date and hour are calculated using the DTM.

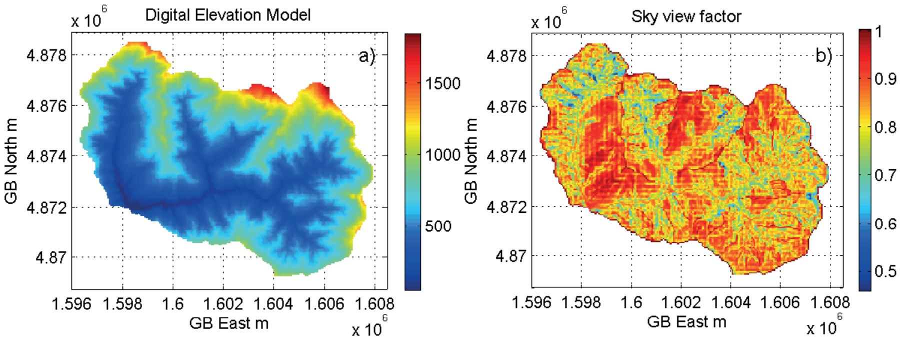

Figure 10: Digital Elevation Model (a), and sky-view factor, S_{vf}, (b) for the the *Versilia* watershed in Tuscany (Italy).

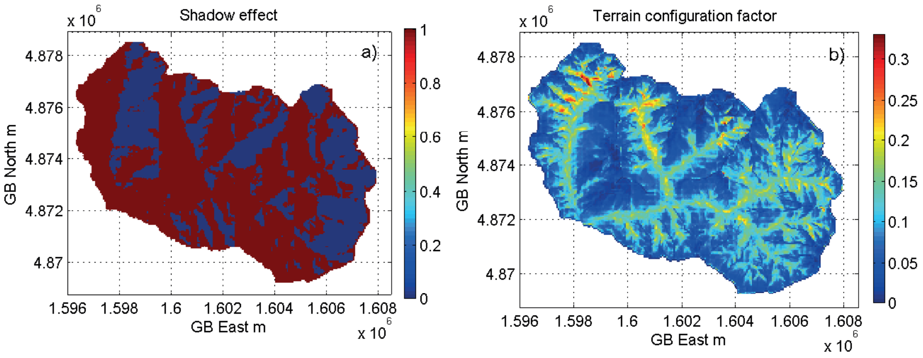

Figure 11: Shadow effect, S_h, (a) and terrain configuration factor, C_t, (b) for the *Versilia* watershed in Tuscany (Italy). The shadow effect is calculated with sun height in the barycenter of the watershed, the 26 April 1982 at 8 am, local time.

4 Radiative fluxes

The net radiation, R_n $[W\ m^{-2}]$, is given by the sum of the absorbed shortwave, R_{abs} $[W\ m^{-2}]$, and absorbed longwave fluxes L_{abs} $[W\ m^{-2}]$ in a given computational element. Net radiation, R_n, and the incoming heat with precipitation, Q_v, are successively partitioned into sensible heat, H, latent heat, λE, ground heat, G, and energy consumed in the photosynthetic process $\lambda_P A_C$, since heat storage in the air column and vegetation biomass is current neglected (Section 5).

A distinction between vegetated and non-vegetated surfaces is made in the description of model components. The presence of canopy structure and the spatial distribution of leaf area affects the radiation regime and the computation of mass and energy exchange between the ground and the atmosphere.

4.1 Shortwave fluxes

At the element scale, the incoming solar radiation input is already partitioned into direct beam, R_{dir} $[W\ m^{-2}]$, and diffuse radiation, R_{dif} $[W\ m^{-2}]$. The direct beam and diffuse radiation are further partitioned into the ultraviolet/visible (UV/VIS), $\Lambda 1$ $[0.29 \div 0.70\ \mu m]$, and the near-infrared (NIR), $\Lambda 2$ $[0.70 \div 4.0\ \mu m]$, wavebands. When these fluxes are not directed toward an horizontal plane, the remote and local topographic effects are accounted for and the values of R_{dir} and R_{dif} are modified using topographic and illumination metrics such as sky-view factor and shadow effect (Section 3.3).

The incoming shortwave energy is either absorbed or reflected by the elements composing the land-surface such as vegetation, soil, or other land cover components. The conservation of global shortwave radiation could be described formally through Eq. (8):

$$\sum_{\Lambda} [R_{dir,\Lambda} + R_{dif,\Lambda}] \quad = \quad R_{abs,H_v} + R_{abs,L_v} + R_{abs,g} + \sum_{s=1}^{n} R_{abs,s} + R_{ref}\ , \qquad (8)$$

where R_{abs,H_v}, R_{abs,L_v}, $R_{abs,g}$, and $R_{abs,s}$ $[W\ m^{-2}]$ are the shortwave radiation fluxes absorbed by *high-vegetation*(H_v), *low-vegetation* (L_v) layers, bare ground under the vegetation layer and other possible n surfaces (e.g., bare soil, water, snow, ice, rocks). The variable R_{ref} $[W\ m^{-2}]$ represents the total reflected shortwave energy, its value depends on the land cover composition and more specifically on the albedos of the surfaces facing the sky.

4.1.1 Vegetated surface

For a vegetated surface, in the most general case, the shortwave radiation is considered to impact the *high-vegetation* canopy (H_v) and to transfer first through the *high-vegetation* and than through the *low-vegetation* (L_v) layer, ultimately reaching the ground as shown in Figure 12.

The radiative transfer through and absorption by the two vegetation canopies

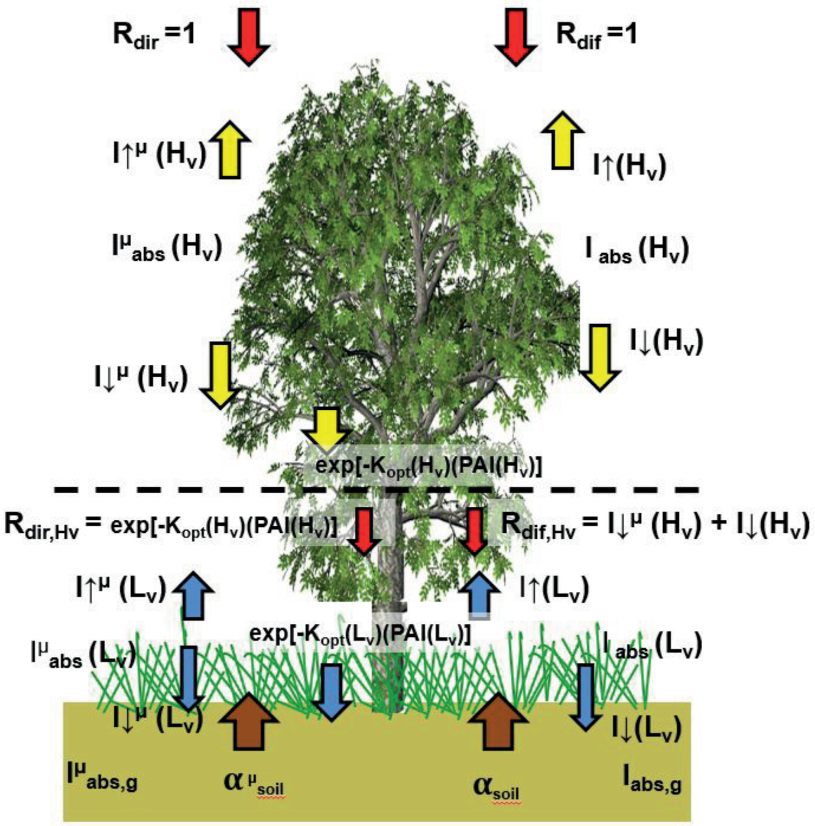

Figure 12: A schematic diagram of the beam and diffuse solar radiation absorbed, transmitted, and reflected by high-vegetation, low-vegetation, and under-canopy ground. In this case the underneath surface is bare ground $s = g$, with albedos $\alpha^{\mu}_{soil,\Lambda}$-$\alpha_{soil,\Lambda}$. The scheme is valid for both the wavebands $\Lambda 1$ and $\Lambda 2$.

is calculated by applying twice the two-stream approximation method (*Dickinson*, 1983; *Sellers*, 1985; *Dai et al.*, 2004). This violates the assumption of a homogenously scattering (Lambertian) surface below the canopy but given the overall simplified scheme it is not expected to worsen significantly the computation of shortwave radiation transmission. Additionally, as discussed in Section 2.2, the presence of two vertically stacked vegetation unit represents a rare exception rather than the rule.

The absorbed direct beam, $I^{\mu}_{\Lambda,abs}$ $[-]$, and diffuse, $I_{\Lambda,abs}$ $[-]$, radiation fluxes in the two wavebands in a general situation with two vegetation layers (H_v and L_v) are described by the equations (9)-(12) and in Figure 13 for a single vegetation layer. Equations (9)-(12) are formulated per unit incident flux and the superscript μ indicates the direct beam component.

$$\begin{aligned}
I^{\mu}_{\Lambda,abs}(H_v) &= 1 - S_{vf} I \uparrow^{\mu}_{\Lambda} (H_v) - [1 - I \uparrow_{\Lambda} (L_v)] I \downarrow^{\mu}_{\Lambda} (H_v) - \\
&\quad [1 - I \uparrow^{\mu}_{\Lambda} (L_v)] e^{-K_{opt}(H_v)[PAI(H_v)]} \,, && (9) \\
I_{\Lambda,abs}(H_v) &= 1 - S_{vf} I \uparrow_{\Lambda} (H_v) - [1 - I \uparrow_{\Lambda} (L_v)] I \downarrow_{\Lambda} (H_v) \,, && (10) \\
I^{\mu}_{\Lambda,abs}(L_v) &= e^{-K_{opt}(H_v)[PAI(H_v)]} - I \uparrow^{\mu}_{\Lambda} (L_v) - \\
&\quad (1 - \alpha^{\mu}_{s\Lambda}) e^{-K_{opt}(L_v)[PAI(L_v)]} \,, && (11) \\
I_{\Lambda,abs}(L_v) &= I \downarrow_{\Lambda} (H_v) + I \downarrow^{\mu}_{\Lambda} (H_v) - I \uparrow_{\Lambda} (L_v) - \\
&\quad (1 - \alpha_{s\Lambda}) [I \downarrow^{\mu}_{\Lambda} (L_v) + I \downarrow_{\Lambda} (L_v)] \;. && (12)
\end{aligned}$$

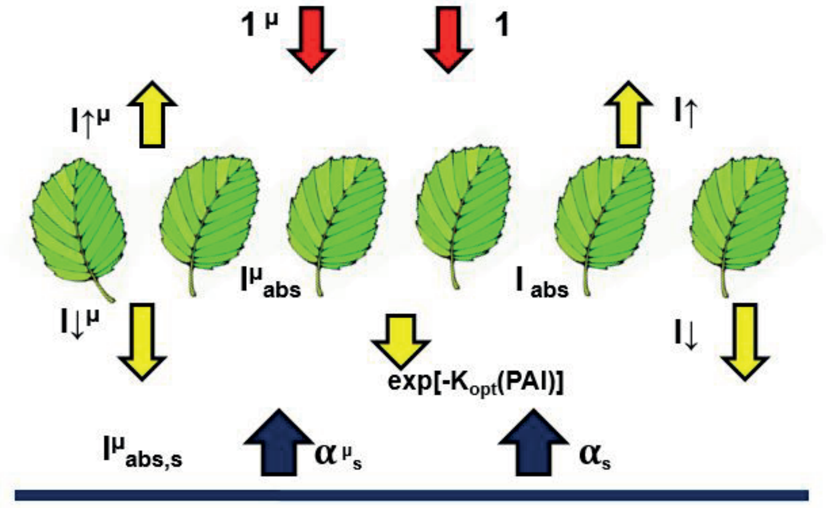

Figure 13: A schematic diagram of the beam and diffuse solar radiation absorbed, transmitted, and reflected by a general layer of vegetation with and underneath surface s. The scheme is valid for both the wavebands $\Lambda1$ and $\Lambda2$.

For both vegetation layers (H_v and L_v), the terms $I \uparrow^{\mu}_{\Lambda}$ and $I \uparrow_{\Lambda}$ $[-]$ are the upward diffuse fluxes per unit incident direct beam and diffuse flux. $I \downarrow^{\mu}_{\Lambda}$ and $I \downarrow_{\Lambda}$ $[-]$ are the downward diffuse fluxes per unit incident direct beam and diffuse radiation. $e^{-K_{opt}(PAI)}$ $[-]$ is the direct beam flux transmitted through a generic canopy per unit incident flux that is approximated through the Beer's law (*Monsi and Saeki*, 2005), where $PAI = LAI + SAI + LAI_{dead}$ is the plant area index $[m^2\ leaf\ area\ m^{-2}\ VEG\,area]$. The term LAI $[m^2\ leaf\ area\ m^{-2}\ VEG\,area]$ is the leaf area index, SAI $[m^2\ stem\ area\ m^{-2}\ \ VEG\,area]$ is the stem area index, and LAI_{dead} $[m^2\ leaf\ area\ m^{-2}\ VEG\,area]$ is the leaf area index of standing dead leaves. K_{opt} $[-]$ is the optical depth of direct beam per unit plant area. Upward fluxes $I\uparrow^{\mu}_{\Lambda}$, $I\uparrow_{\Lambda}$ $[-]$, downward fluxes $I\downarrow^{\mu}_{\Lambda}$ and $I\downarrow_{\Lambda}$ and, K_{opt} are calculated through a canopy radiative transfer scheme (Section 4.2.1). All these quantities are function of the two canopy layers H_v and L_v (Section 2.2), since they depends on canopy type and structure. The terms $\alpha^{\mu}_{s\Lambda}$ and $\alpha_{s\Lambda}$ $[-]$ are the direct beam and diffuse albedos of the generic surface underneath the canopy that can be represented by bare soil, snow, or ponding water (Section 4.2). The terms $I\uparrow^{\mu}_{\Lambda}$ and $I\uparrow_{\Lambda}$ in the Eq. (9)-(12) are multiplied by the sky view factor S_{vf} to take into account the eventual smaller portion of sky available to receive the diffuse radiation

A "two big leaves" approximation is used to partition the canopy in a sunlit and shaded fractions (*Dai et al.*, 2004; *Ivanov*, 2006; *Ivanov et al.*, 2008b). The sunlit fraction of the canopy F_{sun} $[-]$ is estimated assuming that the sunfleck penetration in the canopy is given by $f_{sun}(x) = e^{-K_{opt}{}'x}$ (*Dai et al.*, 2004; *Ivanov et al.*, 2008b). The variable $f_{sun}(x)$ decays exponentially and is controlled by the light extinction parameter K'_{opt}, according to the Beer's law (*Monsi and Saeki*, 2005):

$$F_{sun} = \frac{1}{(PAI)} \int_0^{PAI} f_{sun}(x)dx = \frac{1}{PAI}\frac{1 - e^{-K'_{opt}(PAI)}}{K'_{opt}}\ , \tag{13}$$

where $e^{-K'_{opt}(PAI)}$ is the fractional area of the direct beam radiation (sunflecks) on a horizontal plane below the plant area index $PAI = LAI + SAI + LAI_{dead}$. The shaded fraction is the complementary fraction $F_{shd} = 1 - F_{sun}$ and the sunlit and shaded leaf area indexes are: $LAI_{sun} = F_{sun}LAI$ and $LAI_{shd} = F_{shd}LAI$ $[m^2\ m^{-2}]$. In calculating F_{sun}, T&C uses the expression of *Sellers* (1985), $K'_{opt} = K_{opt}\sqrt{1-\omega^{veg}_{vis}}$, where $\sqrt{1-\omega^{veg}_{vis}}$ accounts for scattering within the canopy (Section 4.2.1), while other authors assumed $K'_{opt} = K_{opt}$ (*Dai et al.*, 2004). Following *Ivanov* (2006), in order to prevent numerical instabilities $F_{sun} = 0$ when the sunlit fraction is less than 1% (e.g., early morning and late evening hours). Note that the fractions change during the day with the solar position since K'_{opt} depends on the solar altitude h_S. Therefore also the radiation absorption and the photosynthetic rates of sunlit and shaded leaf fractions are modified because the subdivision between the sunlit and shaded portions of the canopy varies during the day.

The total solar radiation absorbed by *high-vegetation* R_{abs,H_v} $[W\ m^{-2}]$ is the sum of the fraction absorbed by sunlit canopy R_{abs,sun,H_v} $[W\ m^{-2}]$ and shaded canopy

R_{abs,shd,H_v} $[W\ m^{-2}]$:

$$\begin{aligned} R_{abs,H_v} &= R_{abs,sun,H_v} + R_{abs,shd,H_v} \, , \qquad (14) \\ R_{abs,sun,H_v} &= \sum_{\Lambda} \left[R_{dir,\Lambda} I^{\mu}_{\Lambda,abs}(H_v) + R_{dif,\Lambda} F_{sun}(H_v) I_{\Lambda,abs}(H_v) \right] \\ R_{abs,shd,H_v} &= \sum_{\Lambda} \left[R_{dif,\Lambda} F_{shd}(H_v) I_{\Lambda,abs}(H_v) \right] \, . \end{aligned}$$

The equation for shortwave solar radiation absorbed by *low-vegetation* R_{abs,L_v} $[W\ m^{-2}]$ is similar to the previous one, with a different downward incoming flux and different albedos used to computed the absorbing coefficient Eq. (9)-(12).

$$\begin{aligned} R_{abs,L_v} &= R_{abs,sun,L_v} + R_{abs,shd,L_v} \qquad (15) \\ R_{abs,sun,L_v} &= \sum_{\Lambda} \left[R_{dir,\Lambda,H_v} I^{\mu}_{\Lambda,abs}(L_v) + R_{dif,\Lambda,H_v} F_{sun}(L_v) I_{\Lambda,abs}(L_v) \right] \\ R_{abs,shd,L_v} &= \sum_{\Lambda} \left[R_{dif,\Lambda,H_v} F_{shd}(L_v) I_{\Lambda,abs}(L_v) \right] \, . \end{aligned}$$

where R_{dir,Λ,H_v} and R_{dif,Λ,H_v} are the direct beam and diffuse radiation transmitted by the upper vegetation layer (H_v) and $I^{\mu}_{\Lambda,abs}(L_v)$, $I_{\Lambda,abs}(L_v)$ are estimated from Eq. (9)-(12) with the albedos referring to the appropriate underneath surface (Section 4.2).

$$\begin{aligned} R_{dir,\Lambda,H_v} &= R_{dir,\Lambda} \left[e^{-K_{opt}(H_v)[PAI(H_v)]} \right] \qquad (16) \\ R_{dif,\Lambda,H_v} &= R_{dir,\Lambda} I \downarrow^{\mu}_{\Lambda} (H_v) + R_{dif,\Lambda} I \downarrow_{\Lambda} (H_v) \, . \qquad (17) \end{aligned}$$

The solar radiation flux absorbed by the under-canopy layer $R_{abs,s}$ $[W\ m^{-2}]$ that, depending on the current condition, could be bare ground, water, or snow is:

$$\begin{aligned} R_{abs,s} = \sum_{\Lambda} \Big[& R_{dir,\Lambda,H_v} e^{-K_{opt}(L_v)[PAI(L_v)]} (1 - \alpha^{\mu}_{s\Lambda}) + \\ & [R_{dir,\Lambda,H_v} I \downarrow^{\mu}_{\Lambda} (L_v) + R_{dif,\Lambda,H_v} I \downarrow_{\Lambda} (L_v)](1 - \alpha_{s\Lambda}) \Big] . \qquad (18) \end{aligned}$$

The scheme provided in Figure 12 summarizes the complete case with two vegetation layers, although in most occasions only one of the two layers is present. In this case, the shortwave transfer scheme reduces to the one described in *Oleson et al.* (2004); *Ivanov et al.* (2008b).

The presence of snow on the canopy modifies the optical parameters of the canopy radiative transfer scheme (Section 4.2.1). Besides, the presence of snow or ponding water at the ground also alters the underneath albedo. For this reason, Eq. (9)-(12) are dynamically updated to take into account the current underneath albedo. Bare ground, $\alpha^{\mu}_{soil,\Lambda}$, $\alpha_{soil,\Lambda}$, or low-vegetation, $I \uparrow^{\mu}_{\Lambda} (L_v)$, $I \uparrow_{\Lambda} (L_v)$, albedos are eventually substituted with water albedos $\alpha^{\mu}_{wat,\Lambda}$, $\alpha_{wat,\Lambda}$ or snow albedos, $\alpha^{\mu}_{snow,\Lambda}$,

$\alpha_{snow,\Lambda}$. Such modifications are a function of the relative difference between the height of ponding water or the height of the snowpack and the canopy height, as illustrated for snow in Figure 14.

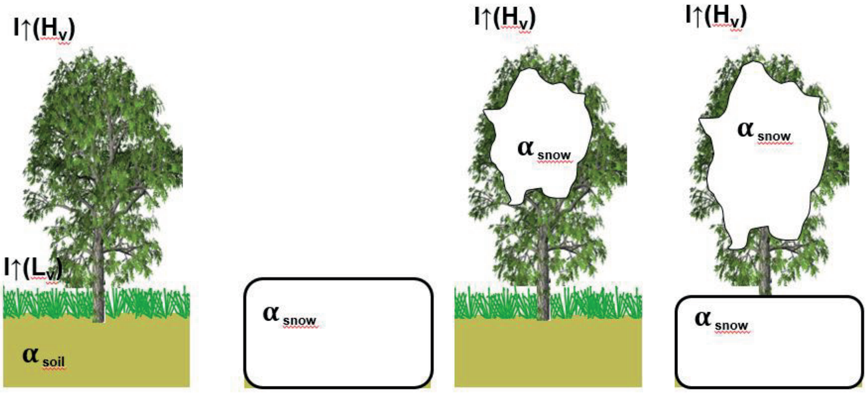

Figure 14: An illustration of the possible relations between snow depth and vegetation height, which are used to determine the value of surface albedos. Snow when it occurs is assumed to completely bury the *low-vegetation*, while it can be intercepted by the *high-vegetation* layer. When there is intercepted snow on the *high-vegetation*, snow is typically covering also the ground (right case). A similar scheme is also used for longwave radiation fluxes. These relations are applied to both the wavebands, $\Lambda 1$ and $\Lambda 2$, and separately for direct beam (μ) and diffuse radiation.

By analogy with the global shortwave radiation transfer scheme, the absorbed *Photosynthetically Active Radiation*, PAR_{abs} $[W\ m^{-2}]$, is partitioned into PAR absorbed by sunlit $PAR_{abs,sun}$ $[W\ m^{-2}]$ and shaded leaves $PAR_{abs,shd}$ $[W\ m^{-2}]$. This partition is realized taking into account the direct beam $I^{\mu}_{vis,abs}$ and diffuse fluxes $I_{vis,abs}$ $[-]$ absorbed by the vegetation canopies per unit incident flux in the UV/VIS waveband $[0.29\ \mu m \div 0.70\ \mu m]$. This band does not overlap perfectly with the *Photosynthetically Active Radiation* band $[0.40\ \div\ 0.70\ \mu m]$. However, errors arising due to the use of absorbed fractions in the UV/VIS waveband are considered negligible, as compared to other uncertainties.

$$PAR_{abs} = PAR_{abs,sun} + PAR_{abs,shd}\,, \tag{19}$$

$$PAR_{abs,sun} = (PAR_{dir} I^{\mu}_{vis,abs} + F_{sun} PAR_{dif} I_{vis,abs}) \frac{LAI}{PAI}\,, \tag{20}$$

$$PAR_{abs,shd} = (F_{shd} PAR_{dif} I_{vis,abs}) \frac{LAI}{PAI}\,, \tag{21}$$

where PAR_{dir} and PAR_{dif} are the incoming photosynthetically active radiation to the canopy, once shadow effect, S_h, and the sky view factor, S_{vf}, have been accounted for (see Section 3.3). Note that when the scheme includes the two vegetation layers, PAR_{dir} and PAR_{dif} for the *low-vegetation* layer (L_v) are obtained accounting for the transmission through the upper layer as done for total shortwave in Eq. (16)-(17). The terms $PAR_{abs,sun}$ and $PAR_{abs,shd}$ $[W\ m^{-2}]$ are used in the estimation of photosynthesis and stomatal resistance in Section 6.6.4 . The above equations assume the sunlit leaves absorb the direct beam radiation, that all leaves absorb diffuse radiation, and that leaves absorb $\frac{LAI}{LAI+SAI+LAI_{dead}}$ of the radiation absorbed by the vegetation. If $F_{sun} = 0$ all radiation is absorbed by the shaded leaves.

4.1.2 Non-vegetated surface

The total shortwave radiation flux absorbed by a non-vegetated surface (subscript "s"), such as bare soil, water, rock, ice, or snow is:

$$R_{abs,s} = \sum_{\Lambda} \left[R_{dir,\Lambda}(1 - S_{vf}\alpha^{\mu}_{s\Lambda}) + R_{dif,\Lambda}(1 - S_{vf}\alpha_{s,\Lambda}) \right] , \tag{22}$$

where $\alpha^{\mu}_{s,\Lambda}$ and $\alpha_{s,\Lambda}$ are the albedos for beam and diffuse radiation of the generic surface "s".

4.1.3 fPAR and NDVI

The fraction of absorbed photosynthetically active radiation $fPAR$ $[-]$ is a quantity typically observed through remote sensing product and is computed as:

$$fPAR = \frac{PAR_{abs}}{PAR_{dir} + PAR_{dif}} . \tag{23}$$

Variables estimated separately for each different land cover of a given basic element can be expressed as quantities averaged at the element-scale. The latter are composed through a linear combination of the relative contributions (proportional to the corresponding fractional areas) of all the land covers within a basic element. The contribution of the vegetated fraction is in turn obtained as a linear combination of all the *Crown Areas* (Section 2). The element-scale quantity of the *Normalized Difference Vegetation Index* $\overline{NDVI}$ can be obtained as:

$$\overline{NDVI} = \frac{\bar{r}_{nir} - \bar{r}_{vis}}{\bar{r}_{nir} + \bar{r}_{vis}} , \tag{24}$$

with:

$$\bar{r}_{\Lambda} = \frac{R\uparrow_{veg} + R\uparrow_{s}}{R_{dir,\Lambda} + R_{dif,\Lambda}} , \tag{25}$$

$$\begin{aligned} R\uparrow_{veg} = \sum_{i=1}^{n_c} \Bigg\{ C_{crown,i} \Bigg(& R_{dir,\Lambda}[S_{vf} I \uparrow^{\mu}_{\Lambda} (H_v, i)] \\ & + R_{dif,\Lambda}[S_{vf} I \uparrow_{\Lambda} (H_v, i)] \Bigg) \Bigg\} , \end{aligned} \tag{26}$$

$$R\uparrow_{s} = \sum_{s=1}^{n} \left\{ C_s \left[(S_{vf}\alpha^{\mu}_{s\Lambda}) R_{dir,\Lambda} + (S_{vf}\alpha_{s\Lambda}) R_{dif,\Lambda} \right] \right\} , \tag{27}$$

where C_{crown} $[-]$ are the fractions of the n_c *Crown Areas*, C_s $[-]$ are the fractions of the n possible non-vegetated surfaces, s, and $\alpha^{\mu}_{s\Lambda}$ and $\alpha_{s\Lambda}$ are the albedos for beam and diffuse radiation of a generic s surface.

The element-scale quantities may be useful for model verification/calibration, e.g., the $fPAR$ and $NDVI$ values estimated using Eq. (23) and (24) can be used to relate the model output to observations from remote sensing platforms (*Myneni et al.*, 2002).

4.1.4 Clumping factor

To be added.

4.2 Surface albedos

Six types of albedos can be considered within a computational element: vegetated, bare soil, snow, ice, rock, and water (Section 2). The vegetation albedos are parameterized using a canopy radiative transfer scheme, where biophysical properties of vegetation are considered (e.g., leaf and stem reflectances and transmittances, leaf orientation). Ground albedo for bare soil and understory bare ground is parameterized based on soil surface moisture content. The snow albedo is a function of snow age and phase composition of snow, e.g., freezing or melting conditions. The water albedo is parameterized based on the solar altitude, and rock and ice albedos are prescribed in this version of T&C.

4.2.1 Canopy radiative transfer scheme

The use of a canopy radiative transfer scheme is necessary in order to define the absorbed radiation and the albedos of a vegetated surface. The canopy radiative transfer scheme estimates, on the basis of leaf and stem optical characteristics (e.g., leaf and stem transmittances and reflectances, leaf angle) the variables $I\uparrow_{\Lambda}^{\mu}$, $I\uparrow_{\Lambda}$, $I\downarrow_{\Lambda}^{\mu}$, $I\downarrow_{\Lambda}$, ω_{vis}^{veg} and K_{opt} required for evaluation of $I_{\Lambda,abs}^{\mu}$, $I_{\Lambda,abs}$, and the shortwave energy balance of vegetated surfaces (Section 4.1.1). The terms $I\uparrow_{\Lambda}^{\mu}$ and $I\uparrow_{\Lambda}$ $[-]$ are the upward diffuse fluxes per unit incident direct beam and diffuse radiation, and ω_{vis}^{veg} is a canopy weighted scattering coefficient.

Among several popular radiation transfer schemes (*Goudriaan*, 1977; *Spitters et al.*, 1986; *Sellers et al.*, 1992; *Hanan*, 2001; *Zhao and Qualls*, 2005; *Dai and Sun*, 2006; *Dickinson*, 2008; *Widlowski et al.*, 2011), the two-stream approximation is used in T&C (*Dickinson*, 1983; *Sellers*, 1985; *Dai et al.*, 2004) because it combines both computational simplicity and accuracy. This method has been applied in several land surface schemes, as well as ecological and hydrological models with good results (*Sellers et al.*, 1986, 1996b; *Bonan*, 1996; *Dai et al.*, 2004; *Oleson et al.*, 2004, 2013; *Ivanov et al.*, 2008b). The two-stream approximation has been shown to perform better than the Goudriaan's radiation model and the Beer's law even when two different extinction coefficients for diffuse and direct radiation are used (*Wang*, 2003). The derivation of the governing equations for the two-stream model is based on the assumption that the incident sky diffuse radiation and the scattered radiation in the canopy are all isotropic in inclination, that the vertical structure of the canopy is uniform, and that the optical properties of the adaxial and abaxial leaf surfaces are the same (*Dai and Sun*, 2006). Although, caveats of the two-stream approximation have been reported (*Dai and Sun*, 2006), a comparison between the two-stream approximation model and a more complex multi-layer model has shown differences of absorbed fluxes negligible for hydrological applications (*Dai and Sun*, 2007).

The two-stream approximation equations are:

$$
\begin{aligned}
-\bar{\mu}\frac{dI\uparrow}{d(PAI)} + [1-(1-\beta)\omega]I\uparrow - \omega\beta I\downarrow &= \omega\bar{\mu}K_{opt}\beta_0 e^{-K_{opt}(PAI)}\,, && (28)\\
\bar{\mu}\frac{dI\downarrow}{d(PAI)} + [1-(1-\beta)\omega]I\downarrow - \omega\beta I\uparrow &= \omega\bar{\mu}K_{opt}(1-\beta_0) e^{-K_{opt}(PAI)}\,, && (29)
\end{aligned}
$$

where $I\uparrow$ and $I\downarrow$ $[-]$ are the upward and downward diffuse radiative fluxes per unit incident flux, $K_{opt} = G(\mu)/\mu$ $[-]$ is the optical depth of direct beam per unit plant area, μ is the cosine of the zenith angle of the incident beam or equivalent the sine of the solar altitude $\mu = \sin(h_S)$ (where h_S $[rad]$ is the solar altitude), $G(\mu)$ $[-]$ is the relative projected area of phytoelements in direction μ, $\bar{\mu}$ $[-]$ is the average inverse diffuse optical depth per unit plant area, ω $[-]$ is the scattering coefficient of phytoelements, β and β_0 $[-]$ are the upscatter parameters for diffuse and direct beam radiation, respectively. The optical parameters $G(\mu)$, $\bar{\mu}$, ω, β, and β_0 are calculated based on work of *Sellers* (1985) [see also *Oleson et al.* (2013)].

Once the vegetation optical properties, the direct beam albedo, $\alpha^{\mu}_{s\Lambda}$, and diffuse albedo, $\alpha_{s\Lambda}$, of the surface, s, underneath the vegetation are known, the equations (28)-(29) can be solved analytically and this allows to calculate the radiation fluxes. Considering a unit of incident direct and diffuse radiation, these are absorbed, reflected, and transmitted by the vegetation for ultraviolet/visible $[0.29 \div 0.70\ \mu m]$ and near-infrared $[0.70 \div 4.0\ \mu m]$ wavebands. The surface s underneath the *high-vegetation* (H_v) layer in case of a vertical composite vegetation is another vegetated surface. In this case, the albedos are obtained using the two-stream approximation in the *low-vegetation* layer (L_v).

The relative projected area of leaves and stems in the direction μ, $G(\mu)$ is computed by fitting a nonlinear expression from *Goudriaan* (1977) once the value of χ_L is given:

$$G(\mu) = \phi_1 + \phi_2\mu\,, \qquad (30)$$

where $\phi_1 = 0.5 - 0.633\chi_L - 0.33\chi_L^2$ and $\phi_2 = 0.877(1-2\phi_1)$ for $-0.4 < \chi_L < 0.6$. The term χ_L is an empirical parameter related to the leaf angle distribution (*Ross*, 1975). χ_L represents the departure of leaf angles from a spherical angle distribution and equals $+1$ for horizontal leaves, 0 for a spherical leaf angle distribution, and -1 for vertical leaves. The leaf angle distribution is a key parameter to characterize canopy structure and plays an important role in controlling energy and mass transfer in the soil-vegetation-atmosphere continuum (*Wang et al.*, 2007).

The average inverse diffuse optical depth per unit plant area $\bar{\mu}$ is:

$$\bar{\mu} = \int_0^1 \frac{\mu}{G(\mu)}d\mu = \frac{1}{\phi_2}\left[1 - \frac{\phi_1}{\phi_2}\ln\left(\frac{\phi_1+\phi_2}{\phi_1}\right)\right]\,, \qquad (31)$$

This integral is based on the assumptions: $\phi_1 \neq 0$ and $\phi_2 \neq 0$. There might be situations when ϕ_1 or ϕ_2 could be zero, consequently the integral (31) is no longer valid and *Dai et al.* (2004) provide supplementary solutions as follows:

$$\begin{aligned} \bar{\mu} &= 1/0.877 \;\; \text{if} \;\; \phi_1 = 0 && (32) \\ \bar{\mu} &= 1/[2\phi_1] \;\; \text{if} \;\; \phi_2 = 0 && (33) \end{aligned}$$

The optical parameters of vegetation, ω, β, and β_0 vary with wavelength (Λ) and are defined as:

$$\begin{aligned} \omega_\Lambda &= \omega_\Lambda^{veg} , \\ \omega_\Lambda \beta_\Lambda &= \omega_\Lambda^{veg} \beta_\Lambda^{veg} , \\ \omega_\Lambda \beta_{0,\Lambda} &= \omega_\Lambda^{veg} \beta_{0,\Lambda}^{veg} . \end{aligned} \tag{34}$$

For vegetation, $\omega_\Lambda^{veg} = \alpha_\Lambda + \tau_\Lambda$. α_Λ $[-]$ is a weighted combination of the leaf, stem, and dead-leaf reflectances ($\alpha_\Lambda^{leaf}, \alpha_\Lambda^{stem}, \alpha_\Lambda^{ldead}$):

$$\alpha_\Lambda = \alpha_\Lambda^{leaf} w_{leaf} + \alpha_\Lambda^{stem} w_{stem} + \alpha_\Lambda^{ldead} w_{ldead} , \tag{35}$$

where $w_{leaf} = LAI/(LAI + SAI + LAI_{dead})$, $w_{stem} = SAI/(LAI + SAI + LAI_{dead})$, and $w_{ldead} = LAI_{dead}/(LAI + SAI + LAI_{dead})$. τ_Λ $[-]$ is a weighted combination of the leaf, stem and dead-leaf transmittances ($\tau_\Lambda^{leaf}, \tau_\Lambda^{stem}, \tau_\Lambda^{ldead}$):

$$\tau_\Lambda = \tau_\Lambda^{leaf} w_{leaf} + \tau_\Lambda^{stem} w_{stem} + \tau_\Lambda^{ldead} w_{ldead} . \tag{36}$$

The upscatter for diffuse radiation is:

$$\omega_\Lambda^{veg} \beta_\Lambda^{veg} = \frac{1}{2} \left[\alpha_\Lambda + \tau_\Lambda + (\alpha_\Lambda - \tau_\Lambda) \left(\frac{1 + \chi_L}{2} \right)^2 \right] \tag{37}$$

and the upscatter for direct beam radiation is:

$$\omega_\Lambda^{veg} \beta_{0,\Lambda}^{veg} = \frac{1 + \bar{\mu} K_{opt}}{\bar{\mu} K_{opt}} a_s(\mu)_\Lambda , \tag{38}$$

where the single scattering albedo is:

$$\begin{aligned} \alpha_s(\mu)_\Lambda &= \frac{\omega_\Lambda^{veg}}{2} \int_0^1 \frac{\mu G(\mu)}{\mu G(\mu) + \mu G(\mu)} d\mu \\ &= \frac{\omega_\Lambda^{veg}}{2} \frac{G(\mu)}{\mu \phi_2 + G(\mu)} \left[1 - \frac{\mu \phi_1}{\mu \phi_2 + G(\mu)} \ln \left(\frac{\mu \phi_1 + \mu \phi_2 + G(\mu)}{\mu \phi_1} \right) \right] . \end{aligned} \tag{39}$$

The upward diffuse fluxes per unit incident direct beam and diffuse flux, i.e., the vegetated surface albedos are:

$$\begin{aligned} I\uparrow_{\Lambda}^{\mu} &= \frac{h_1}{\sigma} + h_2 + h_3\,, && (40)\\ I\uparrow_{\Lambda} &= h_7 + h_8\,. && (41)\end{aligned}$$

The downward diffuse fluxes per unit incident direct beam and diffuse radiation, respectively, are:

$$\begin{aligned} I\downarrow_{\Lambda}^{\mu} &= \frac{h_4}{\sigma} e^{-K_{opt}(LAI+SAI+LAI_{dead})} + h_5 s_1 + \frac{h_6}{s_1}\,, && (42)\\ I\downarrow_{\Lambda} &= h_9 s_1 + \frac{h_{10}}{s_1}\,. && (43)\end{aligned}$$

The estimation of parameters h_1 to h_{10}, σ, and s_1, strictly for $\sigma \neq 0$, follows *Sellers* (1985) and *Oleson et al.* (2004) and it is also reported in Appendix C of *Fatichi* (2010). *Dai et al.* (2004) give also the parametrization for $\sigma = 0$ together with new expressions for $I\uparrow_{\Lambda}$ and $I\downarrow_{\Lambda}$.

With the presence of snow in the canopy, as intercepted snow, the optical parameters ω, β, and β_0 are determined as a weighted combination between the vegetation and intercepted snow parameters:

$$\begin{aligned} \omega_{\Lambda} &= \omega_{\Lambda}^{veg}(1-d_{w,sno}) + \omega_{\Lambda}^{sno}(d_{w,sno})\,,\\ \omega_{\Lambda}\beta_{\Lambda} &= \omega_{\Lambda}^{veg}\beta_{\Lambda}^{veg}(1-d_{w,sno}) + \omega_{\Lambda}^{sno}\beta_{\Lambda}^{sno}(d_{w,sno})\,, && (44)\\ \omega_{\Lambda}\beta_{0,\Lambda} &= \omega_{\Lambda}^{veg}\beta_{0,\Lambda}^{veg}(1-d_{w,sno}) + \omega_{\Lambda}^{sno}\beta_{0,\Lambda}^{sno}(d_{w,sno})\,,\end{aligned}$$

where $d_{w,sno}$ is the fraction of canopy covered by snow (Section 5.3.1). The value of ω_{Λ}^{sno}, β_{Λ}^{sno}, and $\beta_{0,\Lambda}^{sno}$ for intercepted snow are taken from the Appendix *B* of *Sellers et al.* (1986), see also *Oleson et al.* (2013) (page 46).

The optical properties introduced, i.e., leaf, stem and dead-leaf reflectances, (α_{Λ}^{leaf}, α_{Λ}^{stem}, α_{Λ}^{ldead}); leaf, stem, and dead-leaf transmittances, (τ_{Λ}^{leaf}, τ_{Λ}^{stem}, τ_{Λ}^{ldead}), and the leaf angle distribution, χ_L, for different plant functional types and for VIS and NIR wavelengths were first provided by *Dorman and Sellers* (1989) and *Asner et al.* (1998) and can found in *Oleson et al.* (2013) (page 45).

4.2.2 Ground albedo

The direct beam, $\alpha_{soil,\Lambda}^{\mu}$ [$-$], and diffuse, $\alpha_{soil,\Lambda}$ [$-$], ground albedos depend on soil color class and moisture content at the soil surface (*Dickinson et al.*, 1993):

$$\alpha_{soil,\Lambda}^{\mu} = \alpha_{soil,\Lambda} = (\alpha_{sat,\Lambda} + \Delta) \leq \alpha_{dry,\Lambda}\,, \qquad (45)$$

where Δ [$-$] depends on the volumetric water content, θ_S [$-$], of the upper layer of the soil column (Section 12.1) through the equation: $\Delta = (0.11 - 0.40\,\theta_S)$ and $\Delta > 0$. The terms $\alpha_{sat,\Lambda}$ and $\alpha_{dry,\Lambda}$ [$-$] are the albedos for saturated and dry soil that depend in turn on color classes (assigned as in *Dickinson et al.* (1993), see also *Oleson et al.* (2013), page 48).

Since often the soil color class is unknown and its estimation is difficult, typical values: $\alpha_{sat,vis} = 0.11$, $\alpha_{dry,vis} = 0.22$, $\alpha_{sat,nir} = 0.225$ and, $\alpha_{dry,nir} = 0.45$ can be used. The ground albedos are assumed to be independent of the type of incident radiation (direct beam or diffuse), while they depend on the waveband.

4.2.3 Water albedo

Unfrozen water surfaces, lakes, and wetland albedos are parameterized as in *Bonan* (1996). The beam direct albedos are considered function of the cosine of the solar zenith angle, μ, or equivalent of the sine of the solar altitude, h_S $[rad]$, $\mu = \sin(h_S)$:

$$\alpha^{\mu}_{wat,vis} = \alpha^{\mu}_{wat,nir} = 0.06(\mu^{1.7} + 0.15)^{-1}. \tag{46}$$

The diffuse albedos are instead constant $\alpha_{wat,\Lambda} = 0.06$. Consequently, the water surface albedos are assumed to be independent of the waveband, while they are influenced by the type of radiation (direct beam or diffuse).

4.2.4 Rock albedo

Theoretically rock albedo depends on the type and mineral composition of the rock. For simplicity, rock albedo is assumed to be constant and equal for beam direct and diffuse radiation and for the two wavebands:

$$\alpha^{\mu}_{rock,\Lambda} = \alpha_{rock,\Lambda} = 0.25\,. \tag{47}$$

4.2.5 Ice albedo

Ice albedo is a function of ice age, dust, and debris cover (*Cuffey and Paterson*, 2010). For simplicity, ice albedo is assumed to be constant and equal for beam direct and diffuse radiation and for the two wavebands and is a model input, with typical value between 0.3 to 0.5.

$$\alpha^{\mu}_{ice\Lambda} = \alpha_{ice,\Lambda}\,. \tag{48}$$

4.2.6 Snow albedo

The parametrization of snow albedo is fundamental for the simulation of snowpack dynamics (Section 7.2). The partition between reflected and absorbed shortwave energy by a snow covered surface can vary by more than 50% depending on the condition of snow. Snow albedo has been shown to depend on many factors, such as precipitation history, snow depth, radiation type, sun angle, wavelength, grain size and type, liquid water content of the snowpack, meteorological conditions, and air pollution effects (*Wiscombe and Warren*, 1980; *Dickinson et al.*, 1993; *Melloh et al.*, 2002; *Aoki et al.*, 2003; *Pederson and Winther*, 2005; *Mölders et al.*, 2008; *Gardner and Sharp*, 2010).

A simple scheme is used in T&C to parameterize snow albedo. The approach was first proposed in the *ISBA* model by *Douville et al.* (1995). It includes a snow age dependence and distinguishes between melting and freezing periods. Typically refrozen snow albedo is lower than fresh snow albedo due to metamorphism effects inside the snowpack, liquid water content, and impurity content. In *Douville et al.* (1995), snow albedo of melting periods is parameterized as a time exponentially decreasing function to account for wet metamorphism. During cold days, a weak linear decrease function is imposed, according to an observational study of *Baker et al.* (1990). The snow albedos are assumed to be the same, regardless of the type of incident radiation (direct beam or diffuse) and wavebands $\alpha^{\mu}_{sno,\Lambda} = \alpha_{sno,\Lambda} = \alpha_{sno}$.

$$\begin{aligned} \alpha_{sno}(t+dt) &= \alpha_{sno}(t) - \tau_a \frac{dt}{\tau_1}\,, & \text{if } T_s < 0, \\ \alpha_{sno}(t+dt) &= [\alpha_{sno}(t) - \alpha^{m}_{sno}] \exp\left(-\tau_f \frac{dt}{\tau_1}\right) + \alpha^{m}_{sno}\,, & \text{if } T_s = 0, \end{aligned} \qquad (49)$$

where $\tau_a = 0.008$ $[-]$, $\tau_f = 0.24$ $[-]$, and $\tau_1 = 86400$ $[s]$ are parameters introduced by *Douville et al.* (1995); $\alpha^{m}_{sno} = 0.5$ $[-]$ is the minimum allowed albedo of snow; and T_s $[^{\circ}C]$ is the snowpack temperature. When a new snowfall occurs, the albedo of snow, α_{sno}, is reset to a maximum value, $\alpha^{M}_{sno} = 0.85$ $[-]$. Eq. (49) gradually modifies the albedo from the maximum of 0.85 to a minimum of 0.5 as the snow ages. In the original *ISBA* parameterization, a snowfall is considered to refresh the albedo when a threshold value of 10 $[mm]$ of snow water equivalent S_{WE} is exceeded, without a specification of the time step. Snow albedo modeling is very sensitive to this parameter. In this version, snowfall is accumulated over the previous 24 hours and is considered to reset snow albedo to the maximum, when it exceeds the threshold $Th_{Pr,sno}$, which is a model parameter. Values of $Th_{Pr,sno} = 8 - 20$ $[mm\ day^{-1}]$ have been found to give reasonable results in multiple locations.

When there is snow below canopy, shadow effects induced by vegetation and the modified surface reflectances are properly accounted for in the model, as sketched in Figure 14. The scheme used to calculate shortwave radiation fluxes absorbed by canopy and by understory snowpack provides the capability to model vegetation, energy, and water interactions in cold environments.

4.3 Longwave fluxes

In a general form, the net absorbed longwave radiation, L_{abs} $[W\ m^{-2}]$, is given as the difference between the incoming longwave radiation, $L\downarrow$ $[W\ m^{-2}]$, and the outgoing longwave radiation, $L\uparrow$ $[W\ m^{-2}]$. The latter depends on the radiative temperature of the surface, through the Stefan-Boltzmann law. At the land surface, the incoming longwave radiation is the downward atmospheric radiation, L_{atm} times the sky view factor S_{vf} $[-]$:

$$L_{abs} = S_{vf} L_{atm} - L\uparrow\ . \qquad (50)$$

The term L_{atm} $[W\ m^{-2}]$ can be provided as an input time series to T&C or can be computed internally based on the cloud cover fraction N $[-]$ and the atmospheric vapor pressure e_a $[Pa]$:

$$L_{atm} = \epsilon_{cs} K_N \, \sigma T_a^4 \,, \tag{51}$$

where T_a $[K]$ is the air temperature at the reference height, z_{atm} (Section 2), $\sigma = 5.6704 \; 10^{-8}$ $[W \; m^{-2} \; K^{-4}]$ is the Stefan-Boltzmann constant. Many different parameterizations of the cloudiness correction factor K_N and of the clear sky emissivity ϵ_{cs} have been presented in literature (*Brutsaert*, 1975; *Idso*, 1981; *Bras*, 1990; *Prata*, 1996; *Pirazzini et al.*, 2001; *Iziomon et al.*, 2003). Intecomparison studies suggest that the combination of *Dilley and O'Brien* (1998) parameterization of ϵ_{cs} and the *Unsworth and Monteith* (1975) parameterization of K_N generally provide better results (*Flerchinger et al.*, 2009; *Juszak and Pellicciotti*, 2013). These parameterizations are adopted in T&C, whenever L_{atm} is not available as input:

$$\epsilon_{cs} = \frac{\left(59.38 + 113.7 \left(\frac{T_a}{273.16}\right)^6 + 96.96\sqrt{\frac{w}{25}}\right)}{\sigma T_a^4} \,, \tag{52}$$

$$K_N = (1 - 0.84N) + 0.84 \frac{N}{\epsilon_{cs}} \,, \tag{53}$$

where $w = 4.65 e_a / T_a$ $[mm]$ is the precipitable water from *Prata* (1996).

4.3.1 Vegetated surface

The longwave radiation fluxes in the general case of two vegetation layers and partitioned between sunlit and shaded leaves are:

$$\begin{aligned} L \downarrow_{H_v} &= (1 - \alpha_{H_v}) S_{vf} L_{atm} + F_{sun}(H_v) \epsilon_{H_v} \sigma T_{v,sun}(H_v)^4 + \\ &\quad F_{shd}(H_v) \epsilon_{H_v} \sigma T_{v,shd}(H_v)^4 \,, \end{aligned} \tag{54}$$

$$\begin{aligned} L \downarrow_{L_v} &= (1 - \alpha_{L_v}) L \downarrow_{H_v} + F_{sun}(L_v) \epsilon_{L_v} \sigma T_{v,sun}(L_v)^4 + \\ &\quad F_{shd}(L_v) \epsilon_{L_v} \sigma T_{v,shd}(L_v)^4 \,, \end{aligned} \tag{55}$$

$$L \uparrow_s = (1 - \alpha_s) L \downarrow_{L_v} + \epsilon_s \sigma T_s^4 \,, \tag{56}$$

$$\begin{aligned} L \uparrow_{L_v} &= (1 - \alpha_{L_v}) L \uparrow_s + F_{sun}(L_v) \epsilon_{L_v} \sigma T_{v,sun}(L_v)^4 + \\ &\quad F_{shd}(L_v) \epsilon_{L_v} \sigma T_{v,shd}(L_v)^4 \,, \end{aligned} \tag{57}$$

$$\begin{aligned} L \uparrow_{H_v} &= (1 - \alpha_{H_v}) L \uparrow_{L_v} + F_{sun}(H_v) \epsilon_{H_v} \sigma T_{v,sun}(H_v)^4 + \\ &\quad F_{shd}(H_v) \epsilon_{H_v} \sigma T_{v,shd}(H_v)^4 \,, \end{aligned} \tag{58}$$

where $L \downarrow_{H_v}$ and $L \downarrow_{L_v}$ are downward longwave radiation from high and low vegetation and $L \uparrow_{L_v}$, $L \uparrow_{L_v}$, $L \uparrow_s$ are the corresponding upward longwave radiation from vegetation and the surface s underneath the canopy. The terms $T_{v,sun}$ and $T_{v,shd}$ $[K]$ are the radiative canopies temperature for sunlit and shaded leaves function of the vegetation layer H_v or L_v and T_s $[K]$ is the radiative temperature of the surface underneath the low canopy. The terms ϵ_{H_v}, ϵ_{L_v} are the vegetation emissivities and α_{H_v} and α_{L_v} are the vegetation absorptivities. ϵ_s is the emissivity of the underneath surface and α_s is the correspondent absorptivity. F_{sun} and F_{sun} are the sunlit and shaded portions of the canopy as described previously (Section 4.1.1).

In the above equations, it is assumed that leaves emit long-wave radiation from both sides. The scheme also assumes that a fraction $(1 - \alpha_{(H_v/L_v)})$ of long-wave radiation is transmitted through the canopy and the fraction $(1 - \alpha_s)$ of downward longwave radiation below the canopy is reflected by the underneath surface. The vegetation emissivity is computed as $\epsilon_v = 1 - e^{-(PAI)/\vec{\mu}}$, where PAI, SAI is the one-sided sum of leaf, stem and dead-leaves area indexes and $\vec{\mu} = 1$ is the average inverse optical depth for longwave radiation (*Bonan*, 1996). The absorptivities, α_v, are taken equal to the emissivities, ϵ_v, and all these quantities depend on the vegetation layer H_v or L_v.

According to the formulation described in Section 4.3 and Figure 15 the absorbed longwave radiation for the two vegetation layers and for sunlit and shadow fractions L_{abs,sun,H_v}, L_{abs,shd,H_v}, L_{abs,sun,L_v}, L_{abs,shd,L_v} $[W\ m^{-2}]$ and for understory surface $L_{abs,s}$ $[W\ m^{-2}]$ are:

$$\begin{aligned} L_{abs,sun,H_v} &= F_{sun}(H_v)[S_{vf}L_{atm} - L\downarrow_{H_v} - S_{vf}L\uparrow_{H_v} + L\uparrow_{L_v}]\,, &(59)\\ L_{abs,shd,H_v} &= F_{shd}(H_v)[S_{vf}L_{atm} - L\downarrow_{H_v} - S_{vf}L\uparrow_{H_v} + L\uparrow_{L_v}]\,, &(60)\\ L_{abs,sun,L_v} &= F_{sun}(L_v)[L\downarrow_{H_v} - L\downarrow_{L_v} - L\uparrow_{L_v} + L\uparrow_{s}]\,, &(61)\\ L_{abs,shd,L_v} &= F_{shd}(L_v)[L\downarrow_{H_v} - L\downarrow_{L_v} - L\uparrow_{L_v} + L\uparrow_{s}]\,, &(62)\\ L_{abs,s} &= L\downarrow_{L_v} - L\uparrow_{s}\ . &(63) \end{aligned}$$

Since it is impossible to distinguish which part of longwave energy is absorbed from the sunlit and shaded part of the canopy, the fraction F_{sun} and F_{shd} are also used to subdivide the absorbed longwave radiations. In the case of a single vegetation layer the system of equations (54)-(58) reduces to a three equations system, as described in *Bonan* (1996) and *Ivanov et al.* (2008b).

The presence of snowpack alters the longwave radiation exchange. In this case the snow depth is compared to the height of vegetation layer. The scheme is similar to the one used to compute snow effects for the shortwave radiation flux estimation (Figure 14). In this case, the temperature of the snowpack is used to compute longwave radiation emissions.

4.3.2 Non-vegetated surface

For a non-vegetated surface, s, the absorbed net longwave radiation takes the form:

$$\begin{aligned} L_{abs,s} &= \alpha_s\, S_{vf}L_{atm} - L\uparrow_s\,, &(64)\\ L\uparrow_s &= S_{vf}\, \epsilon_s \sigma T_s^4\,, &(65) \end{aligned}$$

where α_s $[-]$ is the absorptivity of the surface, s, ϵ_s $[-]$ is the emissivity of the surface, and T_s $[K]$ is the surface temperature (Section 5.1). In the most general case, water, ice, snow, rocks and bare soil net longwave radiation may be computed with Eq. (64) and have a different T_s. The above equation assumes that the fraction $(1 - \alpha_s)$ of the atmospheric longwave flux is reflected by a surface.

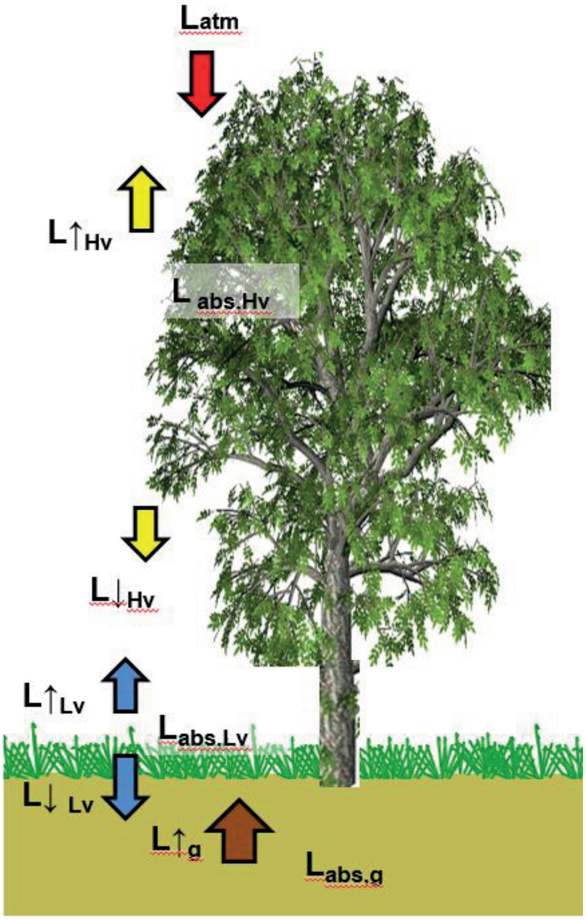

Figure 15: A sketch of long-wave radiation fluxes absorbed, transmitted, reflected, and emitted by vegetation and under-canopy surface. In the scheme the surface underneath the second vegetation layer L_v is bare ground ($s = g$). L_{atm} is the downward atmospheric longwave radiation flux, $L_v \downarrow_{(H_v/L_v)}$ is the downward longwave radiation flux from the vegetation canopy, $L \uparrow_g$ is the upward longwave radiation flux from the ground, and $L_v \uparrow_{(H_v/L_v)}$ is the upward longwave radiation fluxes from the canopy. L_{abs,H_v}, L_{abs,L_v}, $L_{abs,g}$ are the absorbed longwave radiation fluxes for high and low vegetation layers, and understory ground respectively.

The emissivity values used in the model are: $\epsilon_{sno} = \epsilon_{ice} = 0.97$ for snow and ice, $\epsilon_{soil} = 0.96$ for bare soil, $\epsilon_{wat} = 0.96$ for water surfaces, $\epsilon_{rock} = 0.95$ for rocks. The absorptivities, α_s, are taken equal to the emissivities ϵ_s.

4.4 Net radiation

The total net radiation, R_n $[W\ m^{-2}]$, absorbed at the element scale is the weighted sum of the net radiation absorbed by individual land cover fractions, i.e., vegetated areas, bare soil areas, water, rocks, ice, and snow:

$$\begin{aligned} R_n \quad = \quad & R_{n,sun,H_v} + R_{n,shd,H_v} + R_{n,sun,L_v} + R_{n,shd,L_v} + R_{n,ground} + \\ & R_{n,sno} + R_{n,wat} + R_{n,rock} + R_{n,ice}\,, \end{aligned} \tag{66}$$

where R_{n,sun,H_v}, R_{n,shd,H_v}, R_{n,sun,L_v} R_{n,shd,L_v}, and $R_{n,ground}$ $[W\ m^{-2}]$ are radiation fluxes absorbed by *high vegetation*, *low vegetation*, and bare ground at the element scale. The absorbed net radiation fluxes by snow, ice, rocks and water surfaces at the element scale are $R_{n,snow}$, $R_{n,ice}$, $R_{n,rock}$ and $R_{n,wat}$ $[W\ m^{-2}]$, respectively. Note that typically only one or few components of Eq. (66) are different from zero. For instance, the net radiation absorbed by vegetation only is:

$$R_{n,veg} = R_{n,sun,H_v} + R_{n,shd,H_v} + R_{n,sun,L_v} + R_{n,shd,L_v} \, . \tag{67}$$

The calculation of the various components of Eq. (66) is as follows:

$$\begin{aligned}
R_{n,sun,H_v} &= [1 - C_{sno}][1 - C_{ice}] \sum_{i=1}^{n_c} \Big(C_{crown,i} [R_{abs,sun,H_v,i} \\
&\quad + L_{abs,sun,H_v,i}] \Big) \, , && (68) \\
R_{n,shd,H_v} &= [1 - C_{sno}][1 - C_{ice}] \sum_{i=1}^{n_c} \Big(C_{crown,i} [R_{abs,shd,H_v,i} \\
&\quad + L_{abs,shd,H_v,i}] \Big) \, , && (69) \\
R_{n,sun,L_v} &= [1 - C_{sno}][1 - C_{ice}] \sum_{i=1}^{n_c} \Big(C_{crown,i} [R_{abs,sun,L_v,i} \\
&\quad + L_{abs,sun,L_v,i}] \Big) \, , && (70) \\
R_{n,shd,L_v} &= [1 - C_{sno}][1 - C_{ice}] \sum_{i=1}^{n_c} \Big(C_{crown,i} [R_{abs,shd,L_v,i} \\
&\quad + L_{abs,shd,L_v,i}] \Big) \, , && (71) \\
R_{n,ground} &= C_{bare} [R_{abs,bare} + L_{abs,bare}][1 - C_{sno}][1 - C_{ice}] \\
&\quad + \sum_{i=1}^{n_c} \Big(C_{crown,i} [R_{abs,s,i} + L_{abs,s,i}] \Big) \, , && (72) \\
R_{n,sno} &= C_{sno} \Big[R_{abs,sno} + L_{abs,sno} \Big] \Big[1 - \sum_{i=1}^{n_c} C_{crown,i} - C_{wat} \Big] \\
&\quad + C_{wat} C_{sno,w} [R_{abs,sno} + L_{abs,sno}] \, , && (73) \\
R_{n,ice} &= C_{ice} \Big[R_{abs,ice} + L_{abs,ice} \Big] [1 - C_{sno}] \Big[1 - \sum_{i=1}^{n_c} C_{crown,i} - C_{wat} \Big] \\
&\quad + C_{wat} C_{ice,w} [R_{abs,ice} + L_{abs,ice}] \, , && (74) \\
R_{n,wat} &= C_{wat} [R_{abs,wat} + L_{abs,wat}][1 - C_{sno,w}][1 - C_{ice,w}] \, , && (75) \\
R_{n,rock} &= C_{rock} [R_{abs,rock} + L_{abs,rock}][1 - C_{sno}][1 - C_{ice}] \, , && (76)
\end{aligned}$$

where the $C_{crown}\,, i = 1, ..., n_c$ $[-]$ represent the fractions occupied by vegetation patches, C_{bare} $[-]$ is the fraction occupied by bare soil, C_{wat} $[-]$ is the fraction occupied by water surfaces, C_{rock} $[-]$ is the fraction occupied by rocks, C_{sno} and C_{ice} $[-]$ are variables that assumes the value of *1* in presence of snow/ice and *0* otherwise, and $C_{ice,w}$ and $C_{sno,w}$ $[-]$ are variables that assumes the value of *1* when there is ice and snow above a water surface and *0* otherwise (see Section 2). For instance a frozen lake carrying some snow will have $C_{ice,w} = 1$ and $C_{sno,w} = 1$.

The subscript, s, may refer to the ground under canopy, i.e., $s = g$ in Eq. (18) and (63), and consequently $R_{abs,g}$ and $L_{abs,g}$ are the shortwave and longwave fluxes absorbed by the ground. Otherwise, s may refer to the snowpack under vegetation layers [$s = sno$ in equation (18) and (63)] or to ponding water below the vegetation ($s = wat$).

Note that in the case of snow cover and a fully or partially vegetated surface the net radiation absorbed by the ground snowpack can be computed as:

$$R_n = R_{n,ground} + R_{n,sno} \,. \tag{77}$$

This quantity is the result of radiation transfer through the canopy and thus accounts for the longwave radiation exchange between the plant and snow and vegetation shadow effects for shortwave radiation.

5 Soil-vegetation-atmosphere mass and heat transfer

In order to estimate sensible and latent heat fluxes between the ground and the reference height z_{atm}, the model employs a resistance analogy scheme (*Garratt*, 1992; *Arya*, 2001; *Brutsaert*, 2005). Such a theoretical framework is commonly used in land surface and hydrological models (*Sellers et al.*, 1986; *Choudhury and Monteith*, 1988; *Noilhan and Planton*, 1989; *Dickinson et al.*, 1993; *Ducoudré et al.*, 1993; *Viterbo and Beljaars*, 1995; *Braud et al.*, 1995; *Sellers et al.*, 1996b; *Noilhan and Mafhouf*, 1996; *Bonan*, 1996; *LoSeen et al.*, 1997; *Mengelkamp et al.*, 1999; *Cox et al.*, 1999; *Oleson et al.*, 2004; *Bertoldi et al.*, 2006b; *Ivanov et al.*, 2008b). For a remarkable summary of this type of approach the reader is referred to *Sellers et al.* (1997). In this section, numerical schemes and relevant assumptions for the estimation of sensible, latent, and ground heat fluxes are presented. A detailed description of the resistances and their computation is presented in Section 6. The estimation of energy and water fluxes from both non-vegetated surfaces and vegetated patches is discussed in the following.

5.1 Prognostic temperatures simplification

Generally, the energy balance closure requires a numerical solution of a system of highly non-linear equations, which unknowns are the different prognostic T_j temperatures, $j = 1, ..., n_T$, where n_T is the number of prognostic temperatures accounted for by a given model. The temperatures T_j may be dependent or independent, according to the adopted radiation transfer and resistance schemes, with the likely case of dependence among most of the T_j temperatures (e.g., Eq. 54-58). Even in the unrealistic case of independent T_j, single non-linear energy balance equations must be solved n_T times. In advanced models, multi-temperature schemes are typically implemented using two different temperatures, one for bare ground, T_g, and one for vegetation (leaf temperature), T_v, (*Braud et al.*, 1995; *Sellers et al.*, 1996b; *Anderson et al.*, 2000; *Oleson et al.*, 2004; *Ivanov et al.*, 2008b). Sometimes, a further differentiation between sunlit leaves, $T_{v,sun}$, and shaded leaves, $T_{v,shd}$, temperatures is accounted for in land-surface schemes which include biochemical models of photosynthesis. This solution leads to three prognostic temperatures (*Baldocchi and Harley*, 1995; *Wang and Leuning*, 1998; *Dai et al.*, 2004). More recently, multi-layer vegetation models have been implemented where the canopy is subdivided in various layers and sunlit and shaded leaf fractions (*Baldocchi and Wilson*, 2001; *Drewry et al.*, 2010; *Bonan et al.*, 2014; *Ryder et al.*, 2016). This configuration generates a much larger number of prognostic temperatures, which solution implies some degree of approximation or specific assumptions (*Ryder et al.*, 2016). When snow or other surfaces, such as rocks or water, are considered n_T can further increase making the energy balance estimation particularly challenging and computationally demanding. It should be noted that even the use of detailed models with three or more prognostic temperatures is still an approximation of the real-world. Leaf temperature can vary by 3-4 $[^{\circ}C]$ within the same leaf (*Stokes et al.*, 2006) and the temperature of bare ground below vegetation layers may be rather different when compared to the temperature of isolated patch of bare soil. Vegetation shadow effects can further induce important temperature differences within the canopy and in its surroundings.

A major simplification is adopted in T&C, which assumes, with an important exception detailed below, a single value of prognostic temperature, T_s. This value represents the homogeneous radiative temperature of the surface in a given computational element. This temperature T_s reflects the aggregated effect of energy partition in the n_c types of land cover in the absence of snow (Section 2). The single prognostic temperature simplification is a pragmatical choice uniquely related to the large computational efforts required to solve the energy budget with a multi-temperature scheme and does not have any other theoretical justification. In fact, the use of a unique value of T_s permits to reduce the system of equations to a single equation and thus allows to speed up the solution of the energy balance and further simplifies the computation of net radiation and photosynthesis. The reduction of the computational effort is remarkable. However, this has also practical limitations. For instance, all the components of absorbed net radiation are summarized in a single R_n (Eq. 66). This implies that for very dense canopies the net radiation absorbed by the leaves, may be counterbalanced by undercanopy ground evaporation or sensible heat, contrasting with the physical realization of the process. This shortcoming is only partially mitigated by the control exerted by terms such as the undercanopy resistance r'_a (Section 6.2). Another limitation, is related to longwave radiation exchanges between vegetation and ground, which are only related to emissivities and vegetation structural properties (e.g., LAI) but not to differences in temperature. In order to mitigate the implications of assuming a single prognostic temperature, T_s, it is strongly recommended to have basic computational elements of small dimension with a uniform land cover, (e.g., fully covered by vegetation, rocks or water).

In vegetated elements, when snow cover is present at the ground, i.e., $C_{sno} = 1$, and the vegetation is snow free, i.e., the intercepted snow cover less than half of the canopy $d_{w,sno} < 0.5$ (Section 7.3), the model computes two prognostic temperatures T_s and T_{veg}. The temperature T_s is assumed to represent the snowpack radiative temperature, while T_{veg} represents the temperature of snow-free vegetated surfaces, which is obtained from the balance between the net radiation absorbed by the vegetation layers (Eq. 67) along with sensible and latent heat produced by these layers. This solution allows to account for the substantial difference in temperature between vegetation and snow, which may occur in certain periods. For instance, in the melting season longwave radiation emitted by a warm evergreen canopy can significantly contribute to snowmelt (*Lundquist et al.*, 2013). When $d_{w,sno} > 0.5$ the energy budget of vegetation is not explicitly resolved and T_s represents the snowpack radiative temperature.

5.2 Numerical solution for surface temperature

The prognostic surface temperature T_s is the central variable for the estimation of heat fluxes to close the energy balance. In the adopted scheme T_s, in most cases, is the only considered prognostic temperature (Section 5.1). Net radiation, R_n, sensible heat, H, latent heat, λE, ground heat, G, and incoming heat with precipitation, Q_v, are calculated based on T_s. Including the heat consumed by CO_2 fixation in the photosyntehsis $\lambda_P A_C$, but neglecting the heat stored in the canopy and air between the surface and the reference height z_{atm} and any lateral advective term, the surface energy balance in the absence of snow and ice becomes:

$$R_n(T_s) - H(T_s) - \lambda E(T_s) - G(T_s) + Q_v(T_s) - \lambda_P A_C \quad = \quad 0\,. \tag{78}$$

Equation (78) is highly non-linear; for instance all of the resistance terms needed to compute the various fluxes theoretically depend on T_s, and thus its solution can be only found numerically. To solve Eq. 78 we used the Matlab "fzero" function, which uses a combination of bisection, secant, and inverse quadratic interpolation methods (*Forsythe et al.*, 1976). The closure of the energy balance in the presence of snow is described in Section 7.2 and in the presence of ice in Section 8. The energy budget of snow-free vegetated surfaces to compute T_{veg} is a simpler form of Eq. (78):

$$R_n(T_{veg}) - H(T_{veg}) - \lambda E(T_{veg}) - \lambda_P A_C \quad = \quad 0\,. \tag{79}$$

5.3 Sensible heat

The conceptual diagram of sensible heat flux with resistances is described in Figure 16 for a snow free vegetated patch and in Figure 17 when snow is present and it covers the *low-vegetation* layer.

The sensible heat flux at the patch scale H $[W\ m^{-2}]$ between the ground surface and the reference height z_{atm} is a weighted sum of different land cover fractions. It is assumed that the heat stored by the vegetation is negligible. Thus the sensible

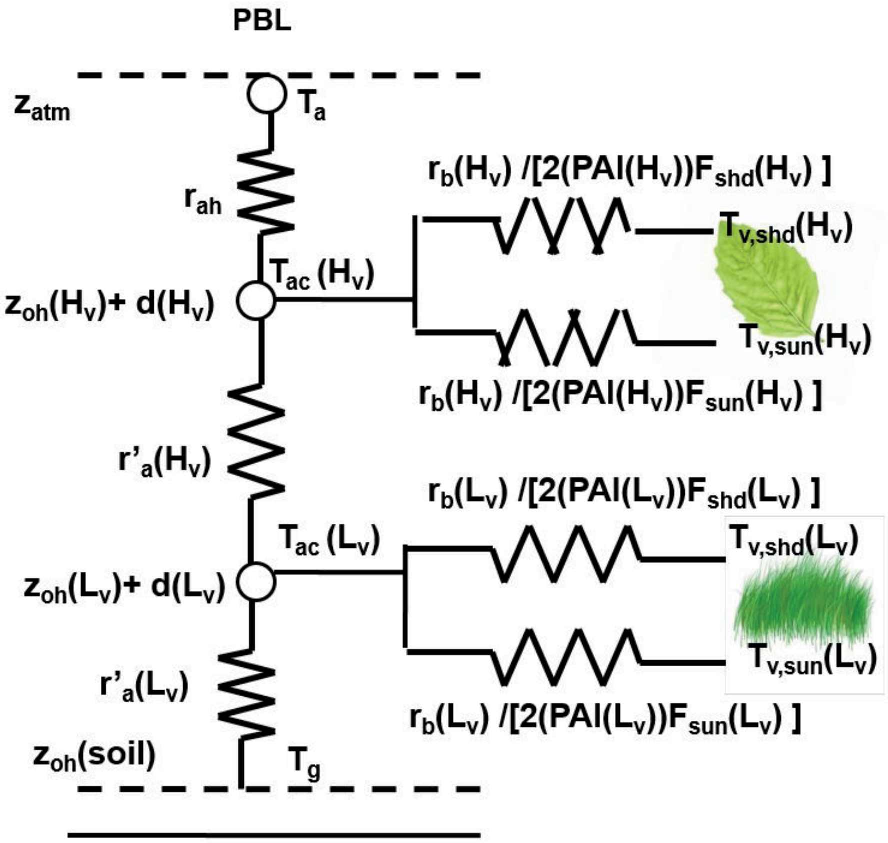

Figure 16: A conceptual diagram of sensible heat flux including resistances for a vegetated patch (*Crown Area*) without snow cover. For the definition of symbols refer to the text.

.

heat flux at the element scale is:

$$\begin{aligned} H \;=\; & \sum_{i=1}^{n_c} \big(C_{crown,i} [H_{H_v,sun,i} + H_{H_v,shd,i} + H_{L_v,sun,i} + H_{L_v,shd,i} + H_{g,i}] \big) + \\ & C_{bare} H_{bare} + C_{wat} H_{wat} + C_{rock} H_{rock} + C_{ice} (1 - (1 - C_{icew}) C_{wat}) H_{ice} + \\ & \left[d_{w,sno} \sum_{i=1}^{n_c} \big(C_{crown,i} \, [PAI(H_{v,i})] \big) + \big(1 - \sum_{i=1}^{n_c} C_{crown,i} - (1 - C_{snow}) C_{wat} \big) \right] H_{sno,f} + \\ & \sum_{i=1}^{n_c} \left(C_{crown,i} H_{sno,v,i} \right) \,, \end{aligned} \tag{80}$$

where $H_{H_v,sun}$, $H_{H_v,shd}$, $H_{L_v,sun}$, $H_{L_v,shd}$, and H_g $[W\ m^{-2}]$ are the sensible heat fluxes from the sunlit and shaded fractions of *high-vegetation*, *low-vegetation* layers, and understory ground. The terms H_{bare}, H_{wat}, H_{rock} and H_{ice} $[W\ m^{-2}]$ are the sensible heat fluxes from bare soil, water, rock and ice surfaces. The terms $H_{sno,f}$ and $H_{sno,v}$ $[W\ m^{-2}]$ are the sensible heat from snow in an open field and snow below the vegetation, respectively. Finally, the variable $d_{w,sno}$ $[-]$ is the fraction of *high-vegetation* covered by snow (Section 5.3.1). The *low-vegetation* layer is assumed to be entirely covered when snow is present (i.e., $C_{sno} = 1$). In this case the sensible heat flux from low-vegetation is assumed zero. However, the flux $H_{sno,v}$ of snow below high-vegetation is computed.

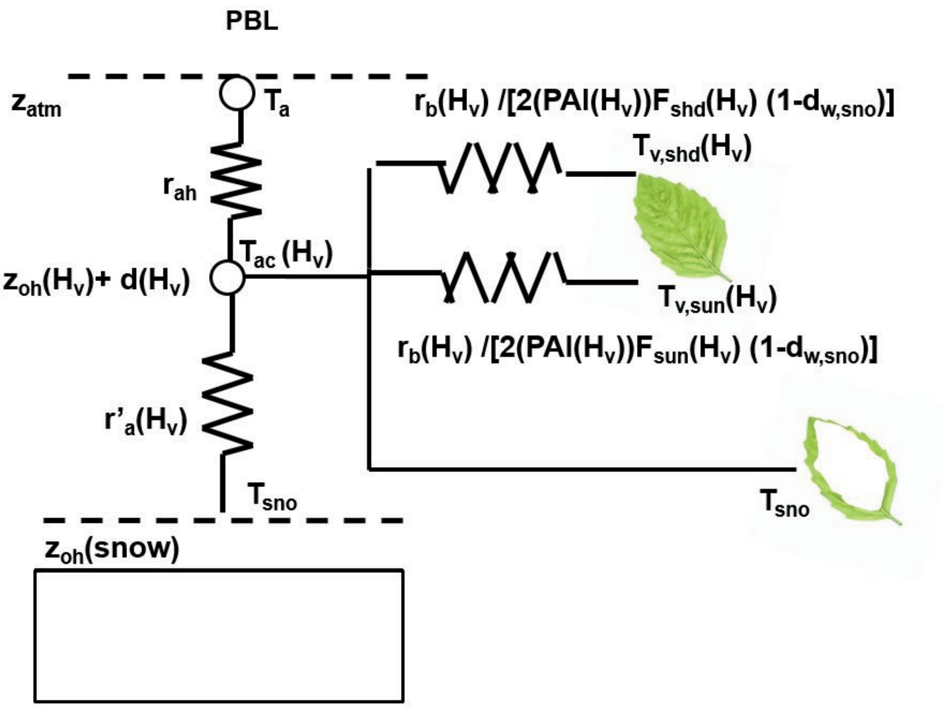

Figure 17: A conceptual diagram of sensible heat including resistances for a vegetated patch (*Crown Area*) in the presence of snow. For the definition of symbols refer to the text.

.

5.3.1 Vegetated surface

The sensible heat fluxes for different elements of a vegetated surface are estimated using the specific temperatures, which are all assumed to be equal to the surface temperature T_s [$°C$]:

$$
\begin{aligned}
H_{H_v,sun} &= [1-C_{ice}][1-C_{sno}]\rho_a C_p \, \frac{(T_{v,sun}(H_v)-T_a)}{r_{ah}+\frac{r_b(H_v)}{2[PAI(H_v)]F_{sun}(H_v)(1-d_{w,sno})}}, && (81)\\
H_{H_v,shd} &= [1-C_{ice}][1-C_{sno}]\rho_a C_p \, \frac{(T_{v,shd}(H_v)-T_a)}{r_{ah}+\frac{r_b(H_v)}{2[PAI(H_v)]F_{shd}(H_v)(1-d_{w,sno})}}, && (82)\\
H_{L_v,sun} &= [1-C_{ice}][1-C_{sno}]\rho_a C_p \, \frac{(T_{v,sun}(L_v)-T_a)}{r_{ah}+{r_a}'(H_v)+\frac{r_b(L_v)}{2[PAI(L_v)]F_{sun}(L_v)}}, && (83)\\
H_{L_v,shd} &= [1-C_{ice}][1-C_{sno}]\rho_a C_p \, \frac{(T_{v,shd}(L_v)-T_a)}{r_{ah}+{r_a}'(H_v)+\frac{r_b(L_v)}{2[PAI(L_v)]F_{shd}(L_v)}}, && (84)\\
H_g &= [1-C_{ice}][1-C_{sno}]\rho_a C_p \, \frac{(T_g-T_a)}{r_{ah}+{r_a}'(H_v)+{r_a}'(L_v)}, && (85)\\
H_{sno,v} &= [C_{sno}]\rho_a C_p \, \frac{(T_{sno}-T_a)}{r_{ah}+{r_a}'(H_v)}. && (86)
\end{aligned}
$$

The terms $T_{v,sun}$ and $T_{v,shd}$ $[°C]$ are the radiative canopies temperature for sunlit and shaded leaves function of the vegetation layer H_v or L_v. T_g $[°C]$ is the radiative temperature of the ground surface and T_{sno} $[°C]$ is the snow surface temperature. The term $C_p = 1005 + [(T_a + 23.15)^2]/3364$ $[J\, kg^{-1}\, K^{-1}]$ is the specific heat capacity of air at a constant pressure, ρ_a $[kg\, m^{-3}]$ is the air density, $PAI = LAI + SAI + LAI_{dead}$ is the plant area index including living and dead leaves and stem, r_{ah} $[s\ m^{-1}]$ is the aerodynamic resistance to heat flux, r_b, and $r_a{}'$ $[s\ m^{-1}]$ are the leaf boundary, and undercanopy resistances, which are functions of the vegetation type H_v or L_v. Further details on resistances can be found in Section 6. Note that equations (81)-(85) assume that both sides of the leaves can generate sensible heat.

The term $d_{w,sno} = \min[1, In_{S_{WE}}/In^M_{S_{WE}}]$ $[-]$ is the fraction of high-vegetation covered by intercepted snow (*Lee and Mahrt*, 2004). The term $In_{S_{WE}}$ $[mm]$ is the intercepted snow, and $In^M_{S_{WE}}$ $[mm]$ is the maximum intercepted snow (Section 7.3). The binary operators C_{sno}, and C_{ice} $[-]$ are used to determine the presence or absence of snow and ice, respectively.

When snow cover is present at the ground, i.e., $C_{sno} = 1$, the terms $H_{H_v,sun}$ and $H_{H_v,shd}$ would be zero. However, if the intercepted snow covers less than half of the canopy $d_{w,sno} < 0.5$, the sensible heat from snow-free vegetation is explicitly computed, since in this case two prognostic temperatures are used (Section 5.1). In such a case, the energy budget is solved twice once for the snowpack temperature and once for the snow-free vegetation temperature.

5.3.2 Non-vegetated surface

The sensible heat fluxes for non-vegetated land cover types are estimated as follows:

$$H_{bare} = [1 - C_{ice}][1 - C_{sno}]\rho_a C_p \frac{(T_g - T_a)}{r_{ah}}, \tag{87}$$

$$H_{wat} = [1 - C_{ice,w}][1 - C_{sno,w}]\rho_a C_p \frac{(T_{wat} - T_a)}{r_{ah}}, \tag{88}$$

$$H_{rock} = [1 - C_{ice}][1 - C_{sno}]\rho_a C_p \frac{(T_{rock} - T_a)}{r_{ah}}, \tag{89}$$

$$H_{ice} = [C_{ice}][1 - C_{sno}]\rho_a C_p \frac{(T_{ice} - T_a)}{r_{ah}}, \tag{90}$$

$$H_{sno,f} = [C_{sno}]\rho_a C_p \frac{(T_{sno} - T_a)}{r_{ah}}, \tag{91}$$

where T_{ice} T_{wat}, and T_{rock} $[°C]$ are the radiative temperatures of ice, water surfaces, and rocks and $C_{ice,w}$ and $C_{sno,w}$ $[-]$ are variables that assumes the value of *1* when there is ice and snow above a water surface and *0* otherwise.

5.4 Latent heat

The conceptual diagram of latent heat flux and related resistances is described in Figure 18 for a snow free vegetated patch.

The latent heat flux, λE $[W\ m^{-2}]$, or specifically, the energy flux of condensation,

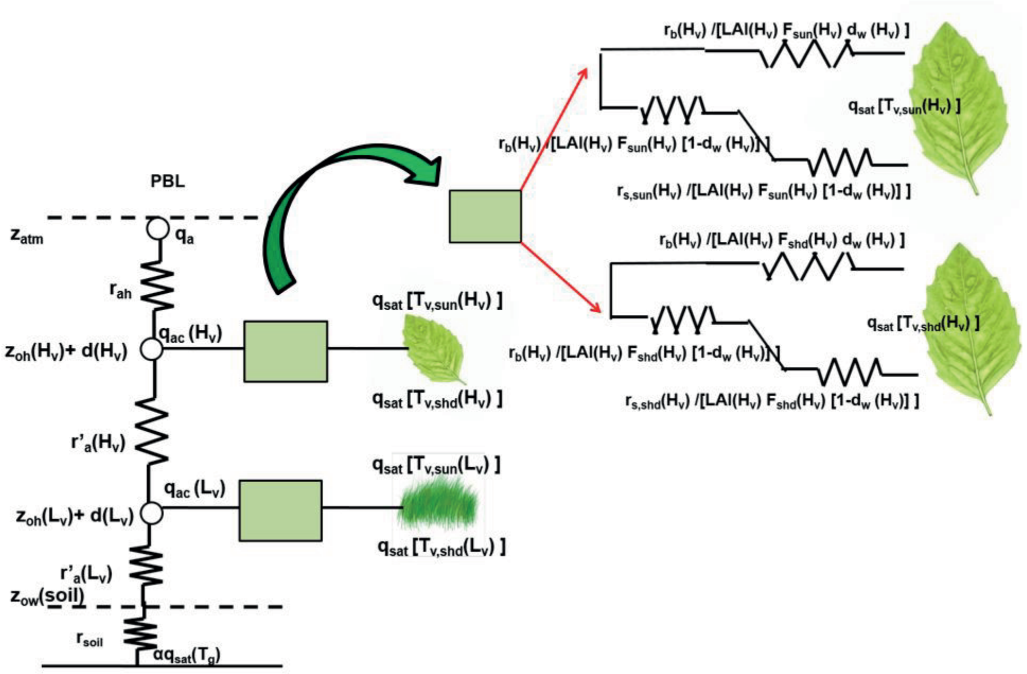

Figure 18: A conceptual diagram for latent heat including resistances in a vegetated patch (*Crown Area*) without snow cover. For the definition of symbols refer to the text.

.

sublimation, evaporation and transpiration fluxes of moisture between the surface and the reference height, z_{atm}, are calculated as the weighted sum of the different land cover fractions. It is assumed that the water vapor stored in the air is negligible. Thus, the latent heat flux at the element scale is:

$$\begin{aligned}\lambda E \;\; = \;\; & \lambda\Bigg[\sum_{i=1}^{n_c}\Big[C_{crown,i}\Big(T_{H_v,i}+T_{L_v,i}+E_{In,H_v,i}+E_{In,L_v,i}+E_{g,i}+C_{litter,i}E_{litter,i}\Big)\Big]+\\ & C_{bare}E_{bare}+C_{rock}E_{rock}+C_{wat}E_{wat}\Bigg]+\\ & \lambda_s\Bigg[\Big(d_{w,sno}\sum_{i=1}^{n_c}(C_{crown,i}[PAI(H_{v,i})])\Big)E_{sno,f}+\\ & \Big(1-\sum_{i=1}^{n_c}C_{crown,i}-(1-C_{sno,w})C_{wat}\Big)E_{sno,f}+\\ & \Big(C_{ice}(1-(1-C_{ice,w})C_{wat})\Big)E_{ice}+\sum_{i=1}^{n_c}(C_{crown,i}E_{sno,v,i})\Bigg],\end{aligned} \qquad (92)$$

where $\lambda = 1000[2501.3-2.361\ T_a]$ $[J\ kg^{-1}]$ $[J\ kg^{-1}]$ is the latent heat of vaporization, $\lambda_s = \lambda + \lambda_f$ is the latent heat of sublimation with $\lambda_f = 333700$ $[J\ kg^{-1}]$ being the latent heat of melting. The terms T_{H_v}, T_{L_v}, E_{litter} and E_g $[kg\ m^{-2}\ s^{-1}]$ are the transpiration fluxes from *high-vegetation*, *low-vegetation* layers, and the evaporation flux from the litter layer and ground under the vegetation canopy. The term C_{litter} $[-]$ is the fractional cover of litter in each C_{crown} and is different from zero only when the biogeochemistry module is activated (Section 6.5). The terms E_{bare}, E_{wat}, E_{rock} $[kg\ m^{-2}\ s^{-1}]$ are the evaporation fluxes from bare soil, water surfaces and intercepted water over rocks, respectively. The terms $E_{sno,f}$ and $E_{sno,v}$, $[kg\ m^{-2}\ s^{-1}]$ are the total evaporation/sublimation fluxes from snow in an open field and under vegetated canopy, and E_{ice} $[kg\ m^{-2}\ s^{-1}]$ is the evaporation/sublimation flux from ice. Finally, the terms E_{In,H_v} and E_{In,L_v} $[kg\ m^{-2}\ s^{-1}]$ are the evaporation fluxes from intercepted water in the *high* and *low-vegetation* layers.

All evaporation and transpiration terms are limited by the effective availability of water in the root zone, first soil layer, snowpack, icepack, ponding water and storages of interception. The terms E_g, E_{bare}, E_{litter} $E_{sno,f}$, $E_{sno,v}$, E_{ice}, E_{In,H_v}, and E_{In,L_v} are allowed to become negative when the specific humidity of the air at the reference height is higher than the specific humidity at saturation near the surface. These negative evaporation fluxes represent dew formation on the ground, litter, snow, ice, and vegetation.

Note the generally, only few terms of Eq. 92 are different from zero since the basic element composition is typically assumed to be homogenous (e.g., only vegetated surface or completely water covered).

5.4.1 Vegetated surface

Evaporation and transpiration fluxes from different parts of a vegetated element are estimated once the specific humidity at saturation q_{sat} $[-]$ at the surface s is computed with the corresponding temperature T_s $[°C]$, e.g., radiative canopies temperature for sunlit and shaded leaves $T_{v,sun}$ and $T_{v,shd}$, ground temperature T_g and snow temperature T_{sno}:

$$T_{H_v,sun} = [1 - C_{sno}][1 - C_{ice}] \cdot \frac{\rho_a(q_{sat}(T_{v,sun}(H_v)) - q_a)}{r_{aw} + \frac{r_b(H_v)}{LAI(H_v)F_{sun}(H_v)(1-d_{w,sno})(1-d_{w,H_v})} + \frac{r_{s,sun}(H_v)}{LAI(H_v)F_{sun}(H_v)(1-d_{w,sno})(1-d_{w,H_v})}}, \tag{93}$$

$$T_{H_v,shd} = [1 - C_{sno}][1 - C_{ice}] \cdot \frac{\rho_a(q_{sat}(T_{v,shd}(H_v)) - q_a)}{r_{aw} + \frac{r_b(H_v)}{LAI(H_v)F_{shd}(H_v)(1-d_{w,sno})(1-d_{w,H_v})} + \frac{r_{s,shd}(H_v)}{LAI(H_v)F_{shd}(H_v)(1-d_{w,sno})(1-d_{w,H_v})}}, \tag{94}$$

$$T_{H_v} = T_{H_v,sun} + T_{H_v,shd}\,, \tag{95}$$

$$T_{L_v,sun} = [1-C_{sno}][1-C_{ice}] \cdot \frac{\rho_a(q_{sat}(T_{v,sun}(L_v)) - q_a)}{r_{aw} + \frac{r_b(L_v)}{LAI(L_v)F_{sun}(L_v)(1-d_{w,L_v})} + \frac{r_{s,sun}(L_v)}{LAI(L_v)F_{sun}(L_v)(1-d_{w,L_v})} + r_a{}'(H_v)}, \quad (96)$$

$$T_{L_v,shd} = [1-C_{sno}][1-C_{ice}] \cdot \frac{\rho_a(q_{sat}(T_{v,shd}(L_v)) - q_a)}{r_{aw} + \frac{r_b(L_v)}{LAI(L_v)F_{shd}(L_v)(1-d_{w,L_v})} + \frac{r_{s,shd}(L_v)}{LAI(L_v)F_{shd}(L_v)(1-d_{w,L_v})} + r_a{}'(H_v)}, \quad (97)$$

$$T_{L_v} = T_{L_v,sun} + T_{L_v,shd}, \quad (98)$$

$$E_g = [1-C_{sno}][1-C_{ice}] \frac{\rho_a(\hat{\alpha}_{soil}\, q_{sat}(T_g) - q_a)}{r_{aw} + r_{soil} + r_a{}'(H_v) + r_a{}'(L_v) + r_{litter}}, \quad (99)$$

$$E_{litter} = [1-C_{sno}][1-C_{ice}] \frac{\rho_a(\alpha_{litter}\, q_{sat}(T_g) - q_a)}{r_{aw} + r_a{}'(H_v) + r_a{}'(L_v) + r_{litter}}, \quad (100)$$

$$E_{In,H_v} = [1-C_{sno}][1-C_{ice}] \cdot \left[\frac{\rho_a(q_{sat}(T_{v,sun}(H_v)) - q_a)}{r_{aw} + \frac{r_b(H_v)}{LAI(H_v)F_{sun}(H_v)d_{w,H_v}}} + \frac{\rho_a(q_{sat}(T_{v,shd}(H_v)) - q_a)}{r_{aw} + \frac{r_b(H_v)}{LAI(H_v)F_{shd}(H_v)d_{w,H_v}}}\right], \quad (101)$$

$$E_{In,L_v} = [1-C_{sno}][1-C_{ice}] \cdot \left[\frac{\rho_a(q_{sat}(T_{v,sun}(L_v)) - q_a)}{r_{aw} + \frac{r_b(L_v)}{LAI(L_v)F_{sun}(L_v)d_{w,L_v}} + r_a{}'(H_v)} + \frac{\rho_a(q_{sat}(T_{v,shd}(L_v)) - q_a)}{r_{aw} + \frac{r_b(L_v)}{LAI(L_v)F_{shd}(L_v)d_{w,L_v}} + r_a{}'(H_v)}\right], \quad (102)$$

$$E_{sno,v} = [C_{sno}] \frac{\rho_a(q_{sat}(T_{sno}) - q_a)}{r_{aw} + r_a{}'(H_v)}, \quad (103)$$

where $q_a = 0.622 e_a/(P_{atm} - 0.378 e_a)$ $[-]$ is the specific humidity of air at the reference height, z_{atm}, e_a $[Pa]$ is the air vapor pressure, P_{atm} $[Pa]$ is the atmospheric pressure, and r_{aw} $[s\ m^{-1}]$ is the aerodynamic resistance to vapor flux. The terms $r_{s,sun}$ and $r_{s,shd}$ $[s\ m^{-1}]$ are the stomatal resistances for sunlit and shaded portions of the canopy function of the vegetation type (Section 6.6). The terms $\hat{\alpha}_{soil}$ $[-]$ and r_{soil} $[s\ m^{-1}]$ are the relative humidity in the soil pores and the soil resistance (Section 6.4). The term α_{litter} and r_{litter} are the relative humidity in the litter and the litter resistance to evaporation. In case of dew formation, $\hat{\alpha}_{soil} = 1$, $r_{soil} = 0$, $\alpha_{litter} = 1$, and $r_{litter} = 0$.

The fraction of vegetation covered by intercepted water $d_w = \min(1, [In/In^M]^{2/3})$ $[-]$ follows *Deardorff* (1978), where In $[mm]$ is the intercepted water and In^M $[mm]$ is the maximum intercepted water (Section 9). The variable d_w, In and In^M are functions of vegetation type H_v or L_v. In the case of dew formation, d_w is assumed to be equal to one.

When snow cover is present at the ground, i.e., $C_{sno} = 1$, the terms T_{H_v} and E_{In,H_v}

would be zero, however, if the intercepted snow covers less than half of the canopy $d_{w,sno} < 0.5$, the latent heat from snow-free vegetation is explicitly computed, since in this case two prognostic temperatures are used (Section 5.1). In such a case, transpiration and evaporation fluxes from snow-free vegetation are also explicitly computed despite the presence of snow at the ground.

5.4.2 Non-vegetated surface

Evaporation fluxes from non-vegetated land cover types are estimated as follows:

$$\begin{aligned}
E_{bare} &= [1 - C_{sno}][1 - C_{ice}]\frac{\rho_a(\hat{\alpha}_{soil}\; q_{sat}(T_g) - q_a)}{r_{aw} + r_{soil}}\,, &(104)\\
E_{wat} &= [1 - C_{ice,w}][1 - C_{sno,w}]\frac{\rho_a(q_{sat}(T_{wat}) - q_a)}{r_{aw}}\,, &(105)\\
E_{rock} &= [1 - C_{sno}][1 - C_{ice}]\frac{\rho_a(q_{sat}(T_{rock}) - q_a)}{r_{aw}}\,, &(106)\\
E_{ice} &= [1 - C_{sno}]\frac{\rho_a(q_{sat}(T_{ice}) - q_a)}{r_{aw}}\,, &(107)\\
E_{sno,f} &= [C_{sno}]\frac{\rho_a(q_{sat}(T_{sno}) - q_a)}{r_{aw}}\,. &(108)
\end{aligned}$$

where T_{ice} T_{wat}, and T_{rock} are the surface temperatures of ice, water surfaces and rocks and all the symbols have been previously defined.

5.5 Ground heat

The flux of heat in the ground, G $[W\ m^{-2}]$, at a generic depth, z $[m]$, (definite positive upward) and time t $[s]$, once the coupling of water and heat transfer is neglected can be written as $G(z,t) = -\lambda_s \partial T_{soil}/\partial z_d$, where λ_s $[J\ K^{-1}\ m^{-1}\ s^{-1}]$ is the soil heat conductivity and $T_{soil}(z,t)$ $[^\circ C]$ is the soil temperature at time t and depth z. Combining the equation for the flux $G(z,t)$ with the conservation of energy, one can obtain the heat diffusion equation (*Hu and Islam*, 1995; *Hillel*, 1998; *Núnez et al.*, 2010):

$$cv_s \frac{\partial T_{soil}}{\partial t} = \frac{\partial}{\partial z_d}\Big(-G(z,t)\Big)\,, \tag{109}$$

where cv_s $[J\ K^{-1}\ m^{-3}]$ is the soil volumetric heat capacity. For each soil layer, homogeneous soil thermal properties (λ_s and cv_s) can be assumed and Eq. (109) can be written as:

$$\frac{\partial T_{soil}}{\partial t} = k_s \frac{\partial^2 T_{soil}}{\partial z^2}\,, \tag{110}$$

where $k_s = \lambda_s / cv_s$ $[m^2\ s^{-1}]$ is the soil heat diffusivity. The partial differential equation (110) has to be solved numerically (*Cox et al.*, 1999; *Cichota et al.*, 2004; *Bertoldi et al.*, 2006b) in a given spatial domain. When the soil temperature profile, $T_{soil}(z,t)$, is solved, the heat flux $G(z,t) = -\lambda_s \partial T_{soil}/\partial z$ at any depth and time is also known. The heat diffusion equation (Eq. 110) is solved in T&C using a finite volume approach with the method of lines, which discretizes the spatial domain and allows reducing the partial differential equation to a system of ordinary differential equations in time (*Lee et al.*, 2004), which is solved by means of an explicit Runge-Kutta (4,5) formula, the Dormand-Prince pair (*Dormand and Prince*, 1980). The spatial soil discretization is equivalent to the discretization used for computing soil moisture dynamics in Section 12.1. A clarification is necessary for the definitions of soil temperature, since there is some ambiguity in the literature. In T&C soil temperature, T_{soil}, refers to the average temperature of a certain soil layer, while ground surface temperature, T_g, refers to the skin temperature at the interface between the ground and the atmosphere.

5.5.1 Simplified solution: "force-restore" method

The solution of the partial differential Eq. (110) is generally computationally expensive (*Cox et al.*, 1999; *Cichota et al.*, 2004; *Bertoldi et al.*, 2006b). Therefore, approximate methods have been proposed to estimate $G(z,t)$ and especially the value of $G(0,t)$ at the interface between the soil surface and the air (*Lin*, 1980; *Dickinson*, 1988; *Noilhan and Planton*, 1989; *Hu and Islam*, 1995; *Wang and Bras*, 1999; *Liebethal and Foken*, 2007).

There is an option in T&C to avoid solving Eq. (110), which uses the "force-restore" method. The force-restore method approximates the partial differential equation with a single ordinary differential equation. The heat diffusion equation is solved in response to periodical forcing with the diurnal frequency ω_1. Different assumptions can be made with respect to the thickness of the soil slab, δ, used in the computation of T_g, and thus several versions of the force-restore method exist (*Hu and Islam*, 1995). A generic force-restore equation can be written as:

$$\frac{dT_g}{dt} = C_1 G - C_2(T_g - T_d)\,, \tag{111}$$

where C_1 $[m^2\ K\ J^{-1}]$, and C_2 $[s^{-1}]$ are coefficients of the force-restore method and T_d is the soil temperature at a certain dampening depth, d. The coefficients C_1 and C_2 depend on the thickness of upper soil layer, δ, the soil volumetric heat capacity cv_s $[J\ K^{-1}\ m^{-3}]$, and the dampening depth of the diurnal temperature wave $d = (2\lambda_s/(cv_s\,\omega_1)^{1/2}$ $[m]$, where $\omega_1 = 2\pi/\tau$ $[s^{-1}]$ and $\tau = 86400$ $[s]$ are the fundamental frequency and period. The *Deardorff* (1978) force-restore method is used in T&C, which assumes the limiting case $\lim_{\delta\to 0} T_{soil} = T_g$ and consequently $C_1 = 2/(cv_s d) = 2\sqrt{\pi/(\lambda_s cv_s \tau)}$ and $C_2 = \omega_1$. The equation for computing the soil heat flux $G(0,t)$ at the soil-air interface becomes:

$$G(t) = \frac{1}{C_1}\Big[\frac{2\pi}{\tau}[T_g(t) - T_d(t)] + \frac{T_g(t) - T_g(t-1)}{dt}\Big]\,. \tag{112}$$

The temperature at the dampening depth, T_d, is updated with the equation: $dT_d/dt = (T_g - T_d)/\tau$ (*Noilhan and Planton*, 1989).

5.5.2 Soil thermal properties

Generally, the volumetric heat capacity, cv_s, and the thermal conductivity, λ_s, depend on soil type, its water content, and the presence of ice content (*Peters-Lidard et al.*, 1998; *Boone et al.*, 2000; *Oleson et al.*, 2004, 2013). T&C does not include soil freezing and thawing processes and the water present in soil pores is always considered to be in a liquid state, therefore only dependencies on soil moisture, θ [$-$], and soil textural properties are considered. The thermal properties are assumed to be a weighted combination of the mineral and water phases in the soil (*Oleson et al.*, 2004, 2013). The volumetric heat capacity cv_s is:

$$cv_s = cv_{soil}(1-\theta_{sat}) + cv_{wat}\theta_S \, , \tag{113}$$

where cv_{soil} is the volumetric heat capacity of soil particles estimated from pedotransfer function as described below and $cv_{wat} = 4.186 \; 10^6$ [$J \; K^{-1} \; m^{-3}$] is the constant volumetric heat capacity of water. The variable θ_S should be the soil moisture averaged from the dampening depth, d, to the surface but it is assumed to be the soil moisture of the first soil layer, for simplicity.

The thermal conductivity λ_s is from *Farouki* (1981):

$$\begin{aligned} \lambda_s &= K_e\lambda_{sat} + (1-K_e)\lambda_{dry} \;\; \text{if } \theta_d/\theta_{sat} > 10^{-7} \; , \\ \lambda_s &= \lambda_{dry} \quad \text{if } \theta_d/\theta_{sat} \leq 10^{-7} \; , \end{aligned} \tag{114}$$

where λ_{dry} [$W \; m^{-1} \; K^{-1}$] is the thermal conductivity of dry soil, K_e is the Kersten number, which is a function of the relative saturation $K_e = \ln(\theta_S/\theta_{sat}) + 1 \geq 0$ and $\lambda_{sat} = \lambda_{soil}^{1-\theta_{sat}}\lambda_{wat}^{\theta_{sat}}$ is the saturated thermal conductivity with λ_{soil} thermal conductivity of solid soil and $\lambda_{wat} = 0.6$ [$W \; m^{-1} \; K^{-1}$] thermal conductivity of liquid water.

The thermal conductivity of solid soil λ_{soil} [$W \; m^{-1} \; K^{-1}$], the volumetric heat capacity of soil cv_{soil} [$J \; K^{-1} \; m^{-3}$], and the thermal conductivity of dry soil λ_{dry} [$W \; m^{-1} \; K^{-1}$] are estimated according to *de Vries* (1963); *Farouki* (1981) (see also *Oleson et al.* (2013) pages 130-132):

$$\lambda_{soil} = \left[8.8F_{san} + 2.92F_{cla}\right]/\left[F_{san} + F_{cla}\right] \; , \tag{115}$$

$$\lambda_{dry} = \left[0.135\rho_d + 64.7\right]/\left[2700 - 0.947\rho_d\right] \; , \tag{116}$$

$$cv_{soil} = 10^6 \left[2.128F_{san} + 2.385F_{cla}\right]/\left[F_{san} + F_{cla}\right] \; , \tag{117}$$

where F_{san}, F_{cla} [$-$] are the soil fractions of sand and clay, and $\rho_d = \rho_{ss}(1-\theta_{sat})$ [$kg \; m^{-3}$] is the bulk density of soil, with $\rho_{ss} = 2700$ [$kg \; m^{-3}$] soil solid density.

5.6 Incoming heat with precipitation

The heat flux incoming with precipitation Q_v [$W \; m^{-2}$] typically accounts only for a small fraction of the energy balance (*Douville et al.*, 1995; *Ivanov et al.*, 2008b) but can be non-negligible in some rain over snow event (*Bras*, 1990; *Wigmosta et al.*, 1994; *Tarboton and Luce*, 1996; *Essery et al.*, 1999; *Marks et al.*, 1999; *Williams and Tarboton*, 1999).

In order to estimate Q_v, both precipitation and its temperature must be known. In T&C, the temperature of rain is assumed to be the greater value between air temperature, T_a $[°C]$, and freezing point, $T = 0$ $[°C]$. The temperature of snow is assumed to be the smaller value between air temperature and freezing point (*Tarboton and Luce*, 1996). In reality, the temperature of the hydrometeor may differ appreciably from the air temperature, given its dependence on mesoscale meteorological patterns. However, the assumption of correspondence between the air and precipitation temperatures does not require the knowledge of other variables, such as the profile of temperature above the atmospheric surface layer. The incoming heat with precipitation, Q_v $[W\ m^{-2}]$, is defined herein as the energy required to convert the temperature of precipitated water to the temperature of the surface, T_s $[°C]$. The variable Q_v is thus calculated as:

$$Q_v \quad = \quad c_w P_{r,liq}\, \rho_w \big[\max(T_a, 0) - T_s\big] + c_i P_{r,sno}\, \rho_w \big[\min(T_a, 0) - T_s\big]\,, \qquad (118)$$

where $c_w = 4186$ $[J\ kg^{-1}\ K^{-1}]$ is the specific heat of water, $c_i = 2093$ $[J\ kg^{-1}\ K^{-1}]$ the specific heat of ice, $\rho_w = 1000$ $[kg\ m^{-3}]$ is the density of water and $P_{r,liq}$, $P_{r,sno}$ $[m\ s^{-1}]$ are the intensity of rain and snow respectively (Section7.1).

5.7 Energy consumed by photosynthesis

The energy consumed in the photosynthetic process $\lambda_P A_C$ $[W\ m^{-2}]$, by vegetation is simply the product between the specific energy consumed for unit of assimilated carbon $\lambda_P = 0.469$ $[J\ \mu mol CO_2^{-1}]$ and the gross assimilation A_C (Section 6.6.3) in the different C_{crown}:

$$\lambda_P A_C \quad = \quad \lambda_P \sum_{i=1}^{n_c} \Big(C_{crown,i} [A_{C,H_v,i} + A_{C,L_v,i}] \Big)\,. \qquad (119)$$

6 Energy and mass transfer resistances

The parameterization of vertical heat fluxes is based on an analogy with the Ohm's law. Serial and parallel resistances are used to mediate the transfer of heat, water vapor, and CO_2 between the land surface and the reference height z_{atm} in the planetary boundary layer, where observations are carried out. Various types of resistance are accounted for: the aerodynamic resistance r_a, the undercanopy resistance $r_a{}'$, the leaf boundary layer resistance r_b, the soil resistance r_{soil}, the litter resistance r_{litter}, the stomatal resistance r_s subdivided in sunlit and shaded fractions $r_{s,sun}$ and $r_{s,shd}$, the mesophyll resistance r_{mes} and the soil-to-root resistance r_{sr} or typically conductance g_{sr}. The resistances have dimensions of inverse velocities $[s\, m^{-1}]$ and depend on many factors including surface roughness (e.g., the canopy structure and leaf dimensions), wind speed, surface temperature, and atmospheric stability, to name a few. Note that often land surface and hydrological models neglect some or many resistance terms in order to simplify the entire scheme, typically retaining only r_a and r_s.

6.1 Aerodynamic resistance

The aerodynamic resistance is a measure of the capability of the atmospheric surface layer to impede or expedite turbulent transport of momentum, sensible and latent heat, and other scalars (e.g., CO_2). In the following, the derivation of the aerodynamic resistances to heat flux r_{ah} and water vapor r_{aw} are discussed.

The determination of the aerodynamic resistance r_{ah} has been mainly implemented in models using the Monin-Obukhov similarity theory (*Monin and Obukhov*, 1954; *Arya*, 2001). Starting with this theory many authors have proposed different parameterizations for the estimation of the aerodynamic resistances (*Louis*, 1979; *Mascart et al.*, 1995; *Launiainen*, 1995; *Abdella and McFarlane*, 1996; *van den Hurk and Holtslag*, 1997). These parameterizations can be differentiated in "direct" Monin-Obukohv similarity theory application, "empirical methods" and "semi-empirical parameterizations" (*Liu et al.*, 2007). In T&C the aerodynamic resistance can be calculated in two ways, with a direct solution of the Monin-Obukohv similarity theory or with the simplified method proposed by *Mascart et al.* (1995) for the *ISBA* model (*Noilhan and Mafhouf*, 1996). The simplified parameterizations is typically preferred because solving the complete Monin-Obukohv similarity theory is computationally demanding given the iterations involved in the problem. In any case, the two implemented methods provide fairly consistent results for r_{ah} (*Fatichi*, 2010).

The aerodynamic resistance to water vapor, r_{aw}, that is necessary in the latent heat flux estimation is assumed to be equal to the aerodynamic resistance to heat flux r_{ah}. This assumption allows, to use a single aerodynamic resistance $r_a = r_{aw} = r_{ah}$. This approximation is very common and it is made by most existent land surface and hydrological models (*Viterbo and Beljaars*, 1995; *Sellers et al.*, 1996b; *Noilhan and Mafhouf*, 1996; *Bertoldi et al.*, 2006b; *Ivanov et al.*, 2008b). The rationale of the assumption is given by the negligible differences in term of water vapor and heat transfer in turbulent conditions. As a consequence, there is an equality of roughness height for water vapor and sensible heat $z_{ow} = z_{oh}$.

6.1.1 Monin-Obukohv similarity solution

Following, the Monin-Obukhov similarity theory the fluxes of momentum, τ $[kg\ m^{-1}\ s^{-2}]$, sensible heat, H $[W\ m^{-2}]$, and water vapor, λE $[W\ m^{-2}]$, in the atmospheric surface layer, under the assumption of stationary and horizontally homogeneous conditions, can be written as functions of the friction velocity, u^* $[m\ s^{-1}]$, the potential temperature scale, θ^* $[K]$, and the specific humidity scale, q^* $[-]$:

$$\begin{aligned} \tau &= \rho_a {u^*}^2 \,, & (120) \\ H &= -\rho_a C_p u^* \theta^* \,, & (121) \\ \lambda E &= -\lambda \rho_a u^* q^* \,, & (122) \end{aligned}$$

where ρ_a $[kg\,m^{-3}]$ is the air density, C_p $[J\,kg^{-1}\,K^{-1}]$ is the specific heat of air at a constant pressure and λ is the latent heat of vaporization. The air temperature T_a $[°C]$ is observed at the reference height z_{atm} $[m]$. The turbulent scale quantities can be written as a function of the mean field variables (*Abdella and McFarlane*, 1996) using the integrated flux-profile relationship of *Dyer* (1974):

$$u^* = \frac{ku_a}{ln\left(\frac{z_{atm}-d}{z_{om}}\right) - \psi_m\left(\frac{z_{atm}-d}{\Lambda}\right) + \psi_m\left(\frac{z_{om}}{\Lambda}\right)}, \tag{123}$$

$$\theta^* = \frac{kPr^{-1}(\theta_a - \theta_s)}{ln\left(\frac{z_{atm}-d}{z_{oh}}\right) - \psi_h\left(\frac{z_{atm}-d}{\Lambda}\right) + \psi_h\left(\frac{z_{oh}}{\Lambda}\right)}, \tag{124}$$

$$q^* = \frac{kPr^{-1}(q_a - q_s)}{ln\left(\frac{z_{atm}-d}{z_{ow}}\right) - \psi_w\left(\frac{z_{atm}-d}{\Lambda}\right) + \psi_w\left(\frac{z_{ow}}{\Lambda}\right)}, \tag{125}$$

where $k = 0.4$ is the von Karman constant, Pr is the neutral turbulent Prandlt number, describing the ratio between the eddy diffusivity of momentum, K_m, and of heat, K_h, i.e. $Pr = K_m/K_h$ (*Grachev et al.*, 2007). The variables θ_s, and q_s are the potential temperature and specific humidity at the surface; z_{om}, z_{oh}, and z_{ow} $[m]$ are the roughness lengths for momentum, heat, and water vapor respectively; d $[m]$ is the zero-plane displacement; Λ $[m]$ is the Obukhov length and ψ_m, ψ_h, ψ_w $[-]$ are the non-dimensional integral stability function for momentum, heat, and water vapor respectively. Note that the apparent sinks for momentum, heat, and water vapor are theoretically in three different positions, i.e. $z_{om} + d$, $z_{oh} + d$, and $z_{ow} + d$, even though the assumption of equating turbulent transport of water vapor and heat gives $z_{ow} = z_{oh}$ and $\psi_w(\zeta) = \psi_h(\zeta)$. Additionally, the use of potential temperatures in Eq. (124) rather than virtual potential temperatures neglects the density stratification due to humidity gradients (*Brutsaert*, 2005, page 32).

The Obukhov length Λ is defined as:

$$\Lambda = \frac{u^{*2}\,T_a}{k\,g\,\theta^*} = \frac{-\rho_a C_p u^{*3} T_a}{k\,g\,H}, \tag{126}$$

where T_a $[K]$ is the air temperature at the reference height z_{atm} and $g = 9.81$ $[m\ s^{-2}]$ is the gravitational acceleration.

The aerodynamic resistance can be related to sensible heat flux, H $[W\ m^{-2}]$:

$$r_{ah} = \rho_a C_p \frac{(\theta_s - \theta_a)}{H}. \tag{127}$$

Therefore, $r_{ah} = (\theta_a - \theta_s)/(u^*\theta^*)$ and combining equations (120), (121), (123) and (124), the aerodynamic resistance r_{ah}, according to the Monin-Obukhov similarity theory we have:

$$\begin{aligned} r_{ah} = {} & \frac{Pr}{k^2 u_a}\left[\ln\left(\frac{z_{atm}-d}{z_{om}}\right) - \psi_m\left(\frac{z_{atm}-d}{\Lambda}\right) + \psi_m\left(\frac{z_{om}}{\Lambda}\right)\right] \cdot \\ & \left[\ln\left(\frac{z_{atm}-d}{z_{oh}}\right) - \psi_h\left(\frac{z_{atm}-d}{\Lambda}\right) + \psi_h\left(\frac{z_{oh}}{\Lambda}\right)\right]. \end{aligned} \tag{128}$$

The Prandtl number in equation (128) is assumed to be equal to *1* (*Noilhan and Mafhouf*, 1996; *van den Hurk and Holtslag*, 1997; *Liu et al.*, 2007), even though theoretically the value of Pr is related to the flow and stability conditions and its correct determination is challenging (*Grachev et al.*, 2007). In neutral condition the integral stability functions $\psi_m(x)$, $\psi_h(x)$ are equal to zero and the neutral aerodynamic resistance to heat transfer takes the expression:

$$r_{ah} = \frac{1}{k^2 u_a}\left[\ln\left(\frac{z_{atm} - d}{z_{om}}\right)\right]\left[\ln\left(\frac{z_{atm} - d}{z_{oh}}\right)\right], \tag{129}$$

and from equation (123), the wind profile in neutral condition is represented with the well-known logarithmic form:

$$u_a = \frac{u^*}{k}\ln\left(\frac{z_{atm} - d}{z_{om}}\right). \tag{130}$$

For non neutral condition the form of the stability functions $\psi_m(x)$, $\psi_h(x)$ must be specified. The differentiation between stable and unstable condition is accounted for calculating the bulk Richardson number Ri_B (*Mascart et al.*, 1995; *Abdella and McFarlane*, 1996; *van den Hurk and Holtslag*, 1997) including the correction proposed by *Kot and Song* (1998) to take into account that z_{om} and z_{oh} are different:

$$Ri_B = f^2\,\frac{g(\theta_a - \theta_s)(z_{atm} - d)}{0.5(\theta_a + \theta_s){u_a}^2}, \tag{131}$$

where $f^2 = [1 - z_{om}/(z_{atm} - d)]^2/[1 - z_{oh}/(z_{atm} - d)]$ (*Kot and Song*, 1998). Boundary layer stable conditions provide a bulk Richardson number $Ri_B > 0$ that in turn gives $\theta_s < \theta_a$, $H < 0$, and $\Lambda > 0$. Conversely, for unstable condition the bulk Richardson number is $Ri_B < 0$ that in turn gives $\theta_s > \theta_a$, $H > 0$, and $\Lambda < 0$ (Figure 19).

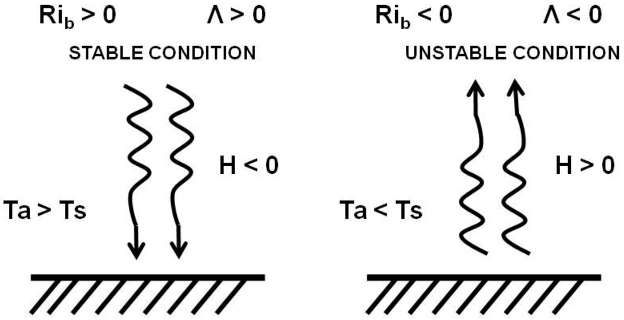

Figure 19: Signs of the involved quantities in case of stable or unstable conditions of the atmospheric surface layer. The potential temperatures, θ, are replaced with conventional temperatures T. This is possible since the reference height, z_{atm}, is relative close to the surface and changes in atmospheric pressure are negligible.

The stability functions $\psi_m(\zeta)$, $\psi_h(\zeta)$ for unstable conditions were obtained from experimental data by *Businger et al.* (1971) (see also *van den Hurk and Holtslag*

(1997)):

$$
\begin{aligned}
\psi_m(\zeta) &= \ln\Big[\Big(\frac{1+x}{2}\Big)^2\Big(\frac{1+x^2}{2}\Big)\Big] - 2\arctan(x) + \pi/2\,, \qquad (132)\\
\psi_h(\zeta) &= 2\ln\Big[\Big(\frac{1+x^2}{2}\Big)\Big]\,, \qquad (133)\\
x &= (1-\gamma\zeta)^{1/4}\,, \qquad (134)
\end{aligned}
$$

where $\gamma = 16$ both for momentum and heat as suggested by *Dyer* (1974) when $k = 0.4$. For stable condition *Businger et al.* (1971) assumed that $\psi_m(\zeta)$, $\psi_h(\zeta)$ are linear function of the argument ζ. *Louis* (1979) and others argued that the formulation of *Businger et al.* (1971) suppresses turbulent exchange too strongly, in particular under very stable conditions. The improved expression of *Beljaars and Holtslag* (1991) is adopted in T&C:

$$
\begin{aligned}
\psi_m(\zeta) &= -\Big[a\zeta + b\Big(\zeta - \frac{c}{d}\Big)\exp(-d\zeta) + \frac{bc}{d}\Big]\,, \qquad (135)\\
\psi_h(\zeta) &= -\Big[\Big(1+\frac{2a}{3}\zeta\Big)^{1.5} + b\Big(\zeta - \frac{c}{d}\Big)\exp(-d\zeta) + \Big(\frac{bc}{d} - 1\Big)\Big]\,, \qquad (136)
\end{aligned}
$$

where $a = 1$, $b = 0.667$, $c = 5$, and $d = 0.35$ are experimental coefficients.

An iterative procedure hypothesizing a initial value of Λ is necessary to solve for r_{ah}. The Obukhov length, $\Lambda = f(u^*, \theta^*)$, is a function of the friction velocity, $u^* = f(\Lambda)$, and of the potential temperature scale $\theta^* = f(\Lambda)$, that in turn are functions of the Obukhov length Λ. The initial value of Λ is chosen once the stability conditions of the atmospheric surface layer are known.

6.1.2 Simplified solution

The complete solution of the Monin-Obukhov similarity theory presented in Section 6.1.1 is computationally expensive. For this reason in T&C the approximate solution proposed by *Mascart et al.* (1995) following the study of *Louis* (1979) and applied in the *ISBA* land surface scheme (*Noilhan and Mafhouf*, 1996) is also implemented. This approach estimates the bulk transfer coefficient for heat $C_h = 1/(r_{ah}u_a)$. The coefficient C_h is expressed as a function of the neutral transport coefficient, C_n, and of an empirical equation, $F_h = f(Ri_B)$, function of the bulk Richardson number, Ri_B:

$$
C_h = \frac{1}{r_{ah}u_a} = C_n F_h(Ri_B)\,, \qquad (137)
$$

where the terms C_n and $F_h(Ri_B)$ are:

$$
C_n = \frac{k^2}{\ln\big[(z_{atm} - d)/z_{om}\big]^2}\,, \qquad (138)
$$

$$
\begin{aligned}
F_h(Ri_B) &= \left[1 - \frac{15 Ri_B}{1 + c_h\sqrt{|Ri_B|}}\right]\left[\frac{\ln[(z_{atm}-d)/z_{om}]}{\ln[(z_{atm}-d)/z_{oh}]}\right] \qquad \text{if } Ri_B \leq 0\,, \\
F_h(Ri_B) &= \left[\frac{1}{1 + 15 Ri_B\sqrt{1+5Ri_B}}\right]\left[\frac{\ln[(z_{atm}-d)/z_{om}]}{\ln[(z_{atm}-d)/z_{oh}]}\right] \text{ if } Ri_B > 0\,,
\end{aligned}
\tag{139}
$$

where c_h is calculate as follows:

$$c_h = 15 {c_h}^{*} C_n\left[(z_{atm}-d)/z_{oh}\right]^{p_h}\left[\frac{\ln[(z_{atm}-d)/z_{om}]}{\ln[(z_{atm}-d)/z_{oh}]}\right] \;, \tag{140}$$

$${c_h}^{*} = 3.2165 + 4.3431\mu + 0.5360\mu^2 - 0.0781\mu^3 \;, \tag{141}$$

$$p_h = 0.5802 - 0.1571\mu + 0.0327\mu^2 - 0.0026\mu^3 \;, \tag{142}$$

where $\mu = \ln(z_{om}/z_{oh})$. Note that the expression of $F_h(Ri_B)$ in equation (139) for stable condition is slightly different from the one originally proposed by *Mascart et al.* (1995). In equation (139) the enhancements first described by *Louis et al.* (1982) and introduced by *Noilhan and Mafhouf* (1996) (page 157) are taken into account [see also *van den Hurk and Holtslag* (1997) (page 132)].

Note that even though in the simplified solution of *Mascart et al.* (1995) the coefficient C_h is derived using the free convection limit, in completely windless condition, i.e. $u_a = 0$, the aerodynamic resistance $r_{ah} = \infty$, consequently there are not turbulent exchanges. In nature, such a condition is almost impossible since a free convection can guarantee a certain transport also in calm conditions (*Kondo and Ishida*, 1997). When $u_a < 0.05$ and conditions are unstable the aerodynamic resistance is computed as in *Beljaars* (1994):

$$C_h = \frac{1}{r_{ah}} = 0.15\left[\frac{g\,\nu}{0.5(\theta_s + \theta_a)Pr^2}\right]^{1/3}(\theta_s - \theta_a)^{1/3}\,, \tag{143}$$

where $\nu = 1.51\ 10^{-5}$ $[m^2\,s^{-1}]$ and $Pr = 0.71$.

6.1.3 Aerodynamic roughness

Further insights must be provided for the aerodynamic, thermal, and vapor roughness lengths z_{om}, and $z_{oh} = z_{ow}$, that are necessary for computing r_a. Scalar roughness height changes with the surface characteristics, atmospheric flow, and thermal dynamic state of the surface (*Su*, 2002; *Zhao et al.*, 2008). Mechanistic or semi-empirical models to evaluate z_{om}, z_{oh} together with the displacement height d have been proposed by different authors (*Raupach*, 1994; *Massman*, 1997; *Su et al.*, 2001; *Zeng and Wang*, 2007). These models are often based on complex parameterizations and an explicit calculation of the within-canopy turbulence profile. Such a complexity and the many required parameters make them less appealing for T&C. Therefore, the roughness lengths and displacement height are calculated with the relationships proposed by *Brutsaert* (1982), where only the height of vegetation (or a reference value for z_{om}) is required. The parameterization of *Brutsaert* (1982) has been widely used in hydrological models and land surface schemes. In case of vegetated surface the roughness are function of the canopy height H_c:

$$\begin{aligned} z_{om} &= 0.123 H_c \ , && (144)\\ z_{oh} &= z_{ow} = 0.1 z_{om} \ , && (145)\\ d &= 0.67 H_c \, . && (146) \end{aligned}$$

A detailed classification of roughness length parameters for different land uses can be found in *Wieringa* (1993). In T&C the following values are used $z_{om} = 0.003$ $[m]$ for bare soil, $z_{om} = 0.0002$ $[m]$ for water surfaces, $z_{om} = 0.001$ $[m]$ for snow and ice and $z_{om} = 0.0003$ $[m]$ for rocks. When multiple land-covers or vegetation occupy a given computational element the highest roughnesses and displacement height are used.

6.2 Under-canopy resistance

The aerodynamic resistance between the understory ground and the source for heat/vapor in the vegetation or between two levels of vegetation (when two vegetation layers are present) is called under-canopy resistance $r_a{}'$ $[s \ m^{-1}]$. Such a resistance depends on the turbulence profile and stability of the roughness sublayer. Both simplified relationships (*Choudhury and Monteith*, 1988; *Shuttleworth and Gurney*, 1990; *Bonan*, 1996; *LoSeen et al.*, 1997; *Zeng et al.*, 2005; *Ivanov et al.*, 2008a; *Sakaguchi and Zeng*, 2009) and detailed approaches to calculate the transfer of momentum within the canopy have been proposed (*Raupach*, 1989; *Massman*, 1997). T&C mostly followed the approach of *Mahat et al.* (2013), which combines logarithmic and exponential wind/eddy diffusion profiles, above- and below-canopy (Figure 20a). The logarithmic and exponential wind profiles are (*Bonan*, 1991; *Brutsaert*, 1982; *Mahat et al.*, 2013):

$$\begin{aligned} u(z) &= \frac{u^*}{k} \ln\Big(\frac{z-d}{z_{om}}\Big) && \text{for } z \geq H_c \text{ and } z < z'_{atm} \, , && (147)\\ u(z) &= u(H_c) \exp\left[-\alpha(1 - z/H_c)\right] && \text{for } z'_{atm} \geq z < H_c \, , && (148) \end{aligned}$$

where the superscript prime indicates the undercanopy quantities, $u(z)$ $[m \ s^{-1}]$ is the wind speed profile, $u(H_c) = \frac{u^*}{k} \ln\Big(\frac{H_c - d}{z_{om}}\Big)$ is the wind speed at canopy height, u^* $[m \ s^{-1}]$ is the friction velocity obtained inverting Eq. (130), d $[m]$ is the zero plane displacement, $k = 0.4$ $[-]$ is the Von Karman constant, H_c $[m]$ is the canopy height, z_{om} $[m]$ is the roughness height, and α $[-]$ is an attenuation coefficient. The above canopy wind speed u_a at the reference height z_{atm} is a model input. Different roughness properties are assumed for the undercanopy, where z'_{atm} $[m]$ is the reference height for below-canopy assumed to be 2 m or 2 m above the snowpack, z'_{om} $[m]$ is the undercanopy roughness height and the undercanopy displacement height is assumed to be zero.

Omitting the effect of atmospheric stability within and below the canopy, the under-canopy resistance can be expressed with the K-theory (*Choudhury and Mon-*

teith, 1988; *Shuttleworth and Gurney*, 1990; *Dolman*, 1993; *Mahat et al.*, 2013) as:

$$r_{an}{}' \;=\; \int_{z'_{atm}}^{d+z_{om}} \frac{dz}{K'_h(z)} + \int_{z'_{om}}^{z'_{atm}} \frac{dz}{K_h(z)} \;, \tag{149}$$

where the eddy diffusivity profiles within the canopy $K'_h(z)$ $[m^2\ s^{-1}]$, and below the canopy $K_h(z)$ $[m^2\ s^{-1}]$ are:

$$K'_h(z) \;=\; K_h(H_c)\exp\left[-\alpha\left(\frac{1-z}{H_c}\right)\right] \;, \tag{150}$$

$$K_h(z) \;=\; ku^*(z-d) \;, \tag{151}$$

where $K_h(H_c)$ is the eddy diffusion coefficient for the canopy at height H_c:

$$K_h(H_c) \;=\; \frac{k^2 u_a(H_c-d)}{\ln\left(\frac{z_{atm}-d}{z_{om}}\right)}) \;, \tag{152}$$

Substituting the values of $K'_h(z)$ and $K_h(z)$ and integrating Eq. (149) (*Mahat et al.*, 2013):

$$r'_{an} \;=\; \frac{H_c e^{\alpha}}{\alpha K_h(H_c)}\left[e^{-\alpha\frac{z'_{atm}}{H_c}} - e^{-\alpha\frac{d+z_{om}}{H_c}}\right] + \frac{1}{k^2 u'_a}\ln\left(\frac{z'_{atm}}{z'_{om}}\right)^2 \;, \tag{153}$$

where $u'_a = u(H_c)\exp\left[-\alpha(1 - z'_{atm}/H_c)\right]$ is the wind speed at the below canopy reference height z'_{atm} (Figure 20a).

Atmospheric stability adjustments to turbulent fluxes use the expressions suggested by *Choudhury and Monteith* (1988):

$$r'_a \;=\; \frac{r'_{an}}{(1-5Ri)^{3/4}} \qquad \text{if } Ri \leq 0\,,$$

$$r'_a \;=\; \frac{r'_{an}}{(1-5Ri)^{2}} \qquad \text{if } Ri > 0\,, \tag{154}$$

where Ri is the Richardson number within the canopy:

$$Ri \;=\; \frac{g(T_a - T_s)z'_{atm}}{(0.5(T_a + T_s) + 273.15){u'_a}^2} \,. \tag{155}$$

For $Ri > 0.16$, $Ri = 0.16$ is used.

A reference value of the attenuation coefficient $\alpha = 3$ was proposed by *Choudhury and Monteith* (1988). The coefficient α controls the vertical gradient of wind speed within the canopy that, in turn, controls enhancement of suppression of turbulent transfer at different canopy heights. In T&C, the coefficient α is evaluated assuming a point equivalence between Eq. (148) used to compute the exponential wind speed profile within the canopy and the logarithmic wind profile above the sink of momentum (Eq. 147). Specifically, the two wind profiles are forced to produce the same value of wind velocity not only at the reference height z_{atm} $[m]$, as implicitly required by the equations, but also at the canopy height H_c $[m]$ (Figure 20a). Under such an assumption the attenuation coefficient α becomes:

$$\alpha \;=\; \frac{\ln[u_a/u(H_c)]}{z_{atm}/H_c - 1}\,. \tag{156}$$

Values of α obtained under this assumption are similar to the range of values $\alpha \approx 2-4$ proposed by *Choudhury and Monteith* (1988) or used by other models (*Bonan*, 1996; *Ivanov et al.*, 2008b). With Eq. (156) the value assumed by α decreases with canopy height, as can be observed in Figure 20b. Such an outcome is consistent with the phenomenology of the physical process, where a lower canopy height is expected to exert a relatively smaller attenuation of wind.

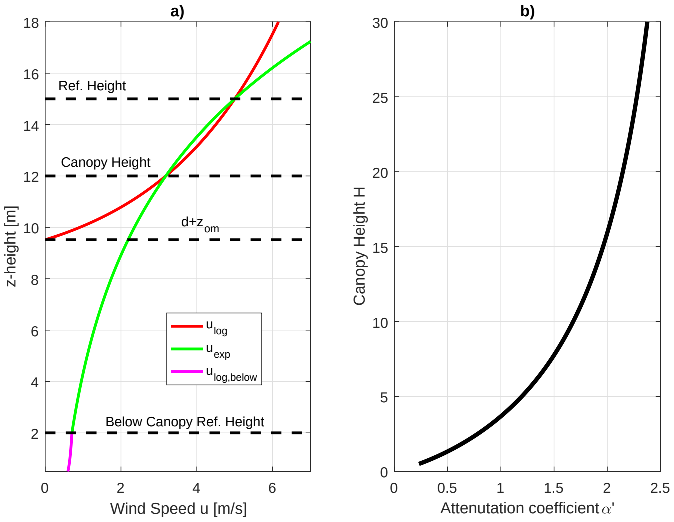

Figure 20: Representation of Eq.(156) used to compute α [$-$]. a.) Logarithmic and exponential profiles of wind speed are forced to produce the same value of wind speed u at the reference and canopy height H_c. b.) Values of α for different canopy heights. The reference height is placed 3 m above the canopy. A larger distance between z_{atm} and H_c reduces the value of α, i.e., it provides a lower attenuation.

The parametrization of α in Eq. 156 can be problematic for thick or very sparse canopy since it does not depend on the Leaf Area Index (*Zeng et al.*, 2005). The attenuation coefficient α is expected to increase rather than remain constant as LAI becomes larger and to exert a stronger control on turbulent exchanges. In T&C to improve the parametrization the computed α value is corrected to account for LAI:

$$\alpha = \alpha\, LAI\frac{0.5}{2}\,. \tag{157}$$

Eq. (157) exploits the linear α-LAI dependence derived by *Yi* (2008) (their Eq. 23), and assumes a characteristic value of $\alpha = 2$ before the LAI correction (Eq. 156).

In the case of two vegetation layers (H_v and L_v), two different undercanopy resistances are computed $r_a{}'(H_v)$, $r_a{}'(L_v)$ as required by the solution of sensible and latent heat fluxes (Section 5.3.1 and 5.4.1). In this case, the undercanopy roughness, undercanopy reference height, and undercanopy displacement height, for the high-vegetation H_v corresponds to the properties of the low vegetation and the undercanopy roughness and undercanopy reference height for the low-vegetation L_v corresponds to the one of the underneath ground or snow, when present.

6.3 Leaf boundary resistance

Exchanges of water vapor, carbon dioxide, and heat between plants and the atmosphere are also controlled by a thin layer of air between the leaf surfaces and the surrounding environment. It is observationally verified that the magnitude of temperature, wind velocity, water vapor, and CO_2 concentrations observed at the leaf surface and in the free atmosphere are different (*Vesala*, 1998). This is a consequence of a strong gradient of these quantities within a thin air layer in the immediate vicinity of the leaf surface. This thin layer is referred as the leaf boundary layer and its thickness δ $[mm]$ is defined as the distance from leaf surface where the flow velocity differs from the ambient value of only a small prescribed quantity (for instance 1%).

In land surface models, the leaf boundary layer is considered to compute the resistance r_b $[s\ m^{-1}]$ that such a layer exerts on the transfer of mass or heat. In still air, the leaf boundary resistance is related to the molecular diffusion. When air motion is enhanced as a consequence of wind, the transport in the leaf boundary layer becomes first laminar and then turbulent (*Jones*, 1983). The leaf boundary resistance has been shown to depend on several factors, such as leaf morphology (shape, size, roughness), leaf motion/orientation against the flow, and wind speed (*Jones*, 1983; *Schuepp*, 1993). Generally, the leaf boundary resistance, r_b, can be calculated empirically or from mathematical models (*Schuepp*, 1993).

The expression first proposed by *Jones* (1983) (also used by *Choudhury and Monteith* (1988) and *Shuttleworth and Gurney* (1990)) is adopted in T&C:

$$g_b(z) = a[u(z)/d_{leaf}]^{1/2}\,, \tag{158}$$

where $g_b(z)$ $[m\ s^{-1}]$ is the mean one-sided bulk leaf boundary conductance, $g_b(z) = 1/r_b(z)$, the term d_{leaf} $[m]$ is the characteristic leaf dimension, often referred to as leaf width, and $a = 0.01$ $[m\ s^{-1/2}]$ is an empirical coefficient (*Choudhury and Monteith*, 1988).

Using, for coherence, the same exponential profile of wind speed introduced in Eq. (148) and assuming a linear distribution of the Leaf Area Index, $L(z) = (LAI\ z)/H_c$, where $L(z)$ is the leaf area index varying with height (*Choudhury and Monteith*, 1988), the mean leaf conductance $g_{b,forc}$ is obtained as:

$$g_{b,forc} = \frac{\int_0^{LAI} g_b(z)dL'}{LAI} = \left(\frac{2a}{\alpha}\right)\left(\frac{u(H_c)}{d_{leaf}}\right)^{1/2}\left[1 - e^{-\alpha/2}\right]\ . \tag{159}$$

Eq. (159) is strictly valid for forced turbulence with $u_a > 0$, an expression for free convection can be added if $T_s > T_a$ (*Leuning et al.*, 1995; *Monteith*, 1973):

$$g_{b,free} = \frac{0.5 D_h \, G_r^{0.25}}{d_{leaf}} \, , \tag{160}$$

where $D_h = 1.9 \; 10^{-5}$ $[m^2 \; s^{-1}]$ is the molecular diffusivity for heat and $G_r = 1.6 \; 10^8 \, (T_s - T_a) \, d_{leaf}^3$ $[-]$ is the Grashof number. Finally, the mean one-sided resistance for unit leaf area is:

$$r_b = \frac{1}{g_{b,free} + g_{b,forc}} \, . \tag{161}$$

The expression (161) is used to compute r_b for all C_{crown} present in a given computational element. In the presented approach no attempt is made to distinguish between fluxes of vapor and heat in the determination of r_b. Slight differences due to the diffusion coefficients, in fact, are negligible across the laminar boundary layers of leaves, especially compared to other uncertainties (*Choudhury and Monteith*, 1988). Effects of stability conditions are also neglected in the evaluation of r_b. A sensitivity analysis of r_b $[s \; m^{-1}]$ to the leaf dimension d_{leaf} $[cm]$ and wind speed u_a $[m \; s^{-1}]$ is presented in Figure 21. The increase of r_b with larger leaf dimensions and with lower wind velocities is easily appreciable.

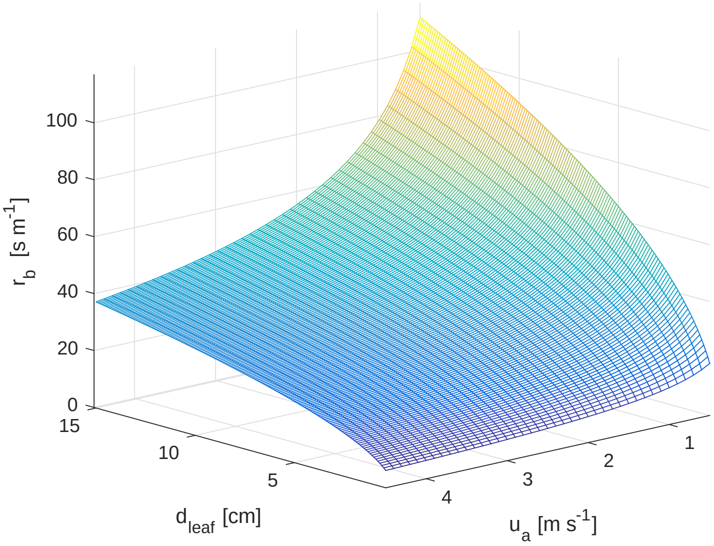

Figure 21: Sensitivity analysis of leaf boundary resistance, r_b $[s \; m^{-1}]$ to wind speed at the reference height, u_a $[m \; s^{-1}]$, and leaf dimension, d_{leaf} $[cm]$. The vegetation height is fixed to $H_c = 30$ $[m]$ and $LAI = 5$.

6.4 Soil resistance

Ground evaporation E, in T&C, corresponds to the quantities E_g and E_{bare} $[kg \; m^{-2} \; s^{-1}]$ (Section 5.4). Ground evaporation is controlled by atmospheric conditions, surface soil wetness, diffusion in the boundary layer at the soil surface, and moisture transport below the soil surface (*Kondo et al.*, 1990; *Mahfouf and Noilhan*, 1991; *He and Kobayashi*, 1998; *Wu et al.*, 2000; *Sakai et al.*, 2009; *Smits et al.*, 2011; *Or et al.*, 2013). The general expression for E is:

$$E = \frac{\rho_a[\hat{\alpha} q_{sat}(T_g) - q_{as}]}{r_{soil}}, \tag{162}$$

where ρ_a $[kg\ m^{-3}]$ is the air density, q_{as} $[-]$, and $q_{sat}(T_g)$ $[-]$ are the specific humidity at the roughness height for water vapor, z_{ow} (described in Section 6.1), and the specific humidity at saturation is calculated using the ground surface temperature T_g. Note that q_{as} is influenced by turbulent exchanges above the ground and therefore by the aerodynamic resistance and undercanopy resistance in presence of vegetation. The term $\hat{\alpha}$ is the relative humidity of air adjacent to water in the soil pore that is typically close to 1 and different from the relative humidity at the roughness height for water vapor.The term r_{soil} represents the resistance to the bulk transfer of water between the water in the soil pores and the air above the soil surface boundary layer.

Evaporation rates from ground are represented following the physically based analytical expression presented by *Haghighi et al.* (2013), which formulates a generalized top boundary condition for effective resistance to evaporation linking soil type, surface water content, and boundary layer characteristic. Specifically, the soil resistance to evaporation is separated in two water content-dependent mechanisms, one resistance r_{vbl} $[s\ m^{-1}]$ associated with the presence of a boundary layer around the discrete pores at the soil surface, which accounts for the resistance for vapor transport from the surface to the atmosphere just above the pore, and the soil internal capillary-viscous resistance, r_{sv} $[s\ m^{-1}]$, imposed on water transfer in the porous media and controlled by hydraulic properties (*Haghighi et al.*, 2013).

The soil boundary layer resistance r_{vbl} is expressed as:

$$r_{vbl} = \frac{\delta_m + P_{sz}\, f(\theta_S)}{Da}, \tag{163}$$

where Da $[m^2\ s^{-1}]$ is the water vapor molecular diffusivity, δ_m $[m]$ is the boundary layer thickness, P_{sz} $[m]$ is the size of the pore and $f(\theta_S)$ $[-]$ is a function reflecting the inherent coupling between the surface water content θ_S and the diffusive resistance. The boundary layer thickness $\delta_m = 2.26\, 10^{-3} u_a^{-0.5}$ is computed with the equation proposed by *Shahraeeni et al.* (2012) and derived from experimental data and theoretical considerations. The wind speed u_a $[m\ s^{-1}]$ is the wind speed at the reference height for bare soil or the under-canopy wind speed for vegetated landcovers (u'_a in Section 6.2). The size of pores P_{sz} can be roughly computed as one third of the particle size and is therefore correlated with the soil texture (*Haghighi et al.*, 2013). We estimate $P_{sz} = 11.12\, n^{3.28}\, 10^{-6}$, with n being the pore size distribution parameter in the van-Genuchten soil water retention curve (*Mualem*, 1976; *van Genuchten*, 1980). The expression is obtained correlating the values of P_{sz} and n provided by *Haghighi et al.* (2013). Finally, $f(\theta_S)$ is computed as a function of the water content θ_S $[-]$ in the shallowest layer of soil (*Haghighi et al.*, 2013). This layer is typically 10 $[mm]$ in T&C.

$$f(\theta_s) = \frac{2}{\pi} \frac{\left[\sqrt{\frac{\pi}{4\theta_S}} - 1\right]}{\sqrt{4\theta_S}} \, . \tag{164}$$

The internal capillary-viscous resistance r_{sv}, is expressed as a function of surface water content θ_S:

$$r_{sv} = \frac{\gamma}{4K(\theta_S)} \, , \tag{165}$$

where γ $[-]$ is a proportionality constant reconciling units for capillary liquid to vapor fluxes (*Haghighi et al.*, 2013) and K $[m \ s^{-1}]$ is the soil hydraulic conductivity computed for the water content θ_S, where the denominator of Eq. (165) represents an effective hydraulic conductivity supporting capillary flow between the drying front and the evaporating surface. The proportionality constant γ can be computed as:

$$\gamma = \frac{\hat{\alpha} e_{sat} - e_a}{\rho_w R_d T_g} \, , \tag{166}$$

where R_d $[J \ kg^{-1} \ K^{-1}]$ is the water vapor gas constant, ρ_w $[kg \ m^{-3}]$ is the water density, T_g $[K]$ is the soil temperature of the shallowest soil layer and e_{sat} and e_a $[Pa]$ are the water vapor pressure at saturation and in the air, respectively. The relative humidity of the air adjacent to the pores is calculated as in *Philip* (1957) using the theoretical definition of the humidity equilibrium value $\hat{\alpha}(\theta_S)$, for a given water potential Ψ_S $[m]$ corresponding to water content θ_S.

$$\hat{\alpha} = \exp\left[-\frac{g\Psi_S}{R_d T_g}\right] \, , \tag{167}$$

where g is the gravity acceleration constant.

Finally the soil resistance r_{soil} is the sum of the two resistances:

$$r_{soil} = r_{vbl} + r_{sv} \, . \tag{168}$$

Note that the above formulation of r_{soil} is mostly based on physical principles (*Haghighi et al.*, 2013) and therefore does not rely on empirically derived parameters as it is typically the case in other bare soil resistance formulations (*Camillo and Gurney*, 1986; *Kondo et al.*, 1990; *Mahfouf and Noilhan*, 1991; *Lee and Pielke*, 1992; *Oleson et al.*, 2008). Most of uncertainty is therefore confined to the definition of the soil texture and the discretization of the soil layers near the surface rather than on empirical parameters. A sensitivity analysis of r_{soil} for two soil types is presented in Figure 22.

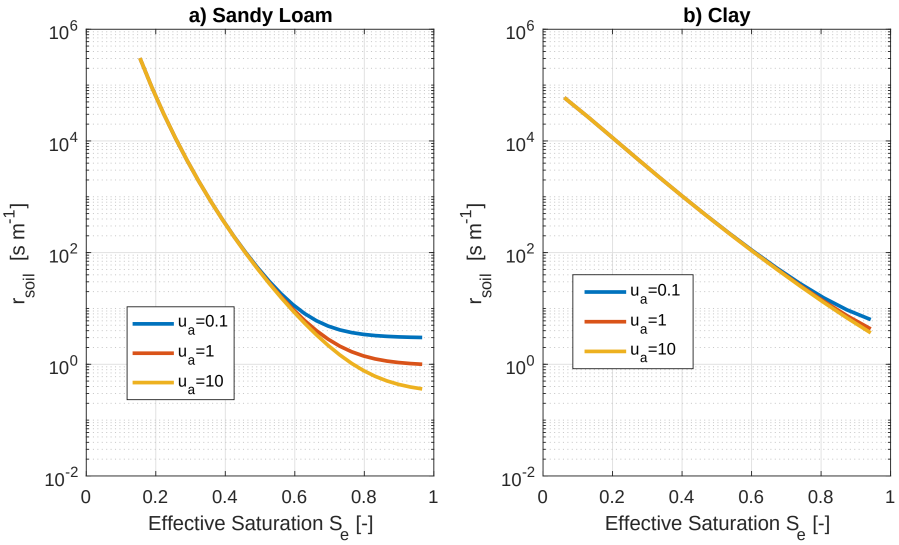

Figure 22: Soil resistance r_{soil} sensitivity to wind speed and soil moisture θ_S expressed as effective saturation S_e for a sand loam (a) and clay (b) soil. Soil temperature is assumed to be 20 $^{\circ}C$, the atmospheric pressure 101325 Pa and the vapour pressure 2000 Pa.

6.5 Litter resistance

Many vegetated patches have a developed litter layer above the soil surface due to accumulation of leaves, twigs, and woody debris. The litter layer has a significant effect on limiting soil water loss by evaporation and reducing the diurnal amplitude of soil temperature by providing daytime shade and nighttime reduction of heat loss (*Bristow et al.*, 1986; *Park et al.*, 1998; *Schaap and Bouten*, 1997). The resistance to soil water evaporation exerted by the litter layer is accounted for in T&C introducing a term r_{litter} $[s\ m^{-1}]$, which depends on the amount of litter B_{litter} $[kg\,DM\ m^{-2}]$ on the ground and on its water content θ_{Litter} $[-]$ (*Putuhena and Cordery*, 1996; *Park et al.*, 1998). The litter resistance to vapor diffusion is given by (*Kondo et al.*, 1993; *Park et al.*, 1998):

$$r_{litter} = L_{litter} \frac{F_0}{Da} \,, \tag{169}$$

where Da $[m^2\ s^{-1}]$ is the water vapor molecular diffusivity, $L_{litter} = S_{litter} B_{litter}$ $[m^2\,litter\ m^{-2} ground]$ is the litter area index, which is a linear function of the litter biomass times the litter specific area assumed $S_{litter} = 2$ $[m^2\,litter\ kg\,DM^{-1}]$. The term F_0 is the resistance of the litter layer from within the litter layer to its surface and depends on litter thickness and litter water content (*Kondo et al.*, 1990; *Park et al.*, 1998):

$$F_0 = 0.2731 \left[\frac{L_{thick}}{100} \left(1.609 \theta_{Litter}^{0.3952} \right) \right] \,. \tag{170}$$

The behavior of Eq. (170) is shown in Figure 23 and the numerical coefficients are fitted to reproduce Fig. 2 in *Park et al.* (1998). The litter water content is a function of the litter interception: $\theta_{Litter} = 0.4 In_{Litter}/L_{sto,cap,max}$, with a residual (minimum) water content of $\theta_{Litter} = 0.05$. The variable In_{Litter} $[mm]$ is computed in Section 9.5. The litter thickness is $L_{thick} = 1.6 B_{litter}$ $[cm]$, following observations in *Putuhena and Cordery* (1996). The maximum and minimum storage interception capacity are related to the litter biomass B_{litter} (*Putuhena and Cordery*, 1996; *Sato et al.*, 2004): $L_{sto,cap,max} = 0.8 B_{litter}$ and $L_{sto,cap,min} = 0.1 B_{litter}$. The relative humidity in the litter is always assumed to be $\alpha_{litter} = 1$, for simplicity.

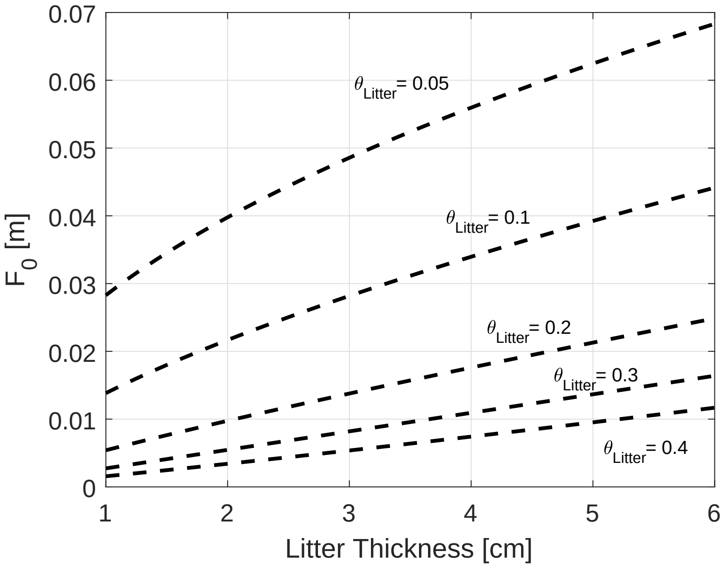

Figure 23: The resistance of the litter layer from the interior of the litter layer to its surface F_0 as a function of litter thickness L_{thick} and litter water content θ_{Litter} is presented.

The litter resistance r_{litter} is only used in Section 5.4.1 for the computation of evaporation from ground, while it is assumed that the litter layer does not affect the transfer of sensible heat flux from the soil to the air aloft (Section 5.3.1). Given the different thermal properties of litter and soil and the physical discontinuities, this assumption is quite strong and just made for sake of simplicity.

When the soil biogeochemistry module is not activated, then $B_{litter} = 0$ and $r_{litter} = 0$, thus the litter resistance parameterizations does not exert any role. In these conditions there is not litter evaporation, i.e., $E_{litter} = 0$. Model experience suggests that the sum of ground evaporation and litter evaporation when the soil biogeochemistry module is activated (i.e., with litter) is similar to the total ground evaporation when litter is absent. The effects on the other water vapour and energy fluxes are rather small.

6.6 Stomatal and photosynthesis

The framework used to estimate the stomatal resistance, r_s $[s\ m^{-1}]$, the net assimilation rate, A_{nC} $[\mu mol\, CO_2\ s^{-1}\ m^{-2}]$, and the leaf maintenance respiration R_{dC} $[\mu mol\, CO_2\ s^{-1}\ m^{-2}]$ is outlined in this section. These quantities are calculated using a biochemical model that couples photosynthesis and stomatal conductance.

The conceptual assumptions used in scaling from unit leaf to unit canopy are also described.

6.6.1 Canopy partition

In order to describe the fluxes of energy, water, and CO_2 for a vegetated surface, it is necessary to provide a scaling methodology from the leaf to the canopy scale because of several existing non-linear interactions (*de Pury and Farquhar*, 1997; *Wang and Leuning*, 1998; *Dai et al.*, 2004). These interactions involve absorbed energy, leaf temperature, and stomatal behavior at different levels of the canopy. Processes of photosynthesis and transpiration depend non-linearly on absorbed solar radiation and temperature of leaves, and generally the entire radiative balance is affected by the canopy partition (*Sinclair et al.*, 1976). A "big-leaf" approach is typically used to model canopies with properly scaled quantities used to calculate plant-scale fluxes (*Farquhar*, 1989; *Sellers et al.*, 1996b; *Bonan*, 1996; *Friend et al.*, 1997; *Dickinson et al.*, 1998; *Oleson et al.*, 2004). The big-leaf model requires assumptions about leaf properties, along with conceptualizations of the vertical profile of plant photosynthetic properties. The distribution of photosynthetic capacity of leaves is typically assumed to be related to an average profile of absorbed radiation. Consequently, the entire canopy photosynthesis is modeled using scaled equations that describe photosynthesis at the leaf level (*Sellers et al.*, 1992).

More detailed schemes, such as the "two big-leaves" approach, subdivide the canopy into sunlit and shaded fractions and model each fraction separately (*de Pury and Farquhar*, 1997; *Wang and Leuning*, 1998; *Dai et al.*, 2004). Multiple canopy layer models subdividing the canopy in a number of sunlit and shaded layers have been also proposed (*Leuning et al.*, 1995; *Baldocchi and Wilson*, 2001; *Drewry et al.*, 2010; *Bonan et al.*, 2014; *Ryder et al.*, 2016).

The subdivision into sunlit and shaded fractions is recommended because photosynthesis of shaded leaves has a linear response to absorbed PAR, while photosynthesis of sunlit leaves is often light saturated and so independent of absorbed PAR above a thrshold, furthermore sunlit leaves can be several degrees warmer than shaded leaves (*de Pury and Farquhar*, 1997; *Wang and Leuning*, 1998; *Dai et al.*, 2004). The "two big-leaves" approach is more complex than a big-leaf but it has been shown to give results comparable to those of multi-layers models and significantly better than those of the big-leaf model (*de Pury and Farquhar*, 1997; *Wang and Leuning*, 1998; *Dai et al.*, 2004).

This version of T&C adopts a two big leaves scheme, where sunlit and shaded leaves are treated separately when computing net assimilation and stomatal resistance even though a common single prognostic temperature is maintained (Section 5.1).

6.6.2 Scaling from leaf to canopy

Profiles of leaf properties have led to the hypothesis that leaves adapt or acclimate to their radiation environment such that plant nitrogen resources may be distributed to maximize daily canopy photosynthesis (*de Pury and Farquhar*, 1997; *Dewar et al.*, 2012). It has been further hypothesized that the optimal distribution of nitrogen occurs when nitrogen is distributed in proportion to the distribution of absorbed irradiance in the canopy.

The canopy nitrogen profile is assumed to decay exponentially controlled by a factor K_N $[-]$, in analogy with the penetration of the direct beam radiation in the canopy that is assumed to decay exponentially and controlled by a light extinction parameter K_{opt} (Section 4.2.1). Since the maximum photosynthetic capacity has been shown to depend linearly on leaf nitrogen content (*Schulze et al.*, 1994; *White et al.*, 2000; *Reich et al.*, 1997; *Wright et al.*, 2004), the instantaneous distribution of nitrogen and light in the canopy are used to scale photosynthesis from leaf to the two canopy levels. The scaling factor for photosynthetic capacity of the sunlit $F_{N,sun}$ and shaded $F_{N,shd}$ fractions of the leaf area index LAI are:

$$\begin{aligned} F_{N,sun} &= \int_0^{LAI} e^{-K_N\,x} e^{-K_{opt}\,x} dx = \frac{1-e^{-(K_N+K_{opt})\,LAI}}{K_N+K_{opt}} . \qquad (171) \\ F_{N,shd} &= \int_0^{LAI} e^{-K_N\,x}\left(1-e^{-K_{opt}\,x}\right) dx = \frac{1-e^{-(K_N\,LAI)}}{K_N} - \\ & \frac{1-e^{-(K_N+K_{opt})\,LAI}}{K_N+K_{opt}} . \qquad (172) \end{aligned}$$

The factors $F_{N,sun}$ and $F_{N,shd}$ are used to obtain the estimate of photosynthetic quantities scaled from leaf to canopy. It follows that the maximum Rubisco capacity at 25°C V_{max} for unit of leaf in the shaded and sunlit fractions $V_{max,sun}$, $V_{max,shd}$ $[\mu mol\,CO_2\ s^{-1}\ m^{-2} leaf]$ are:

$$\begin{aligned} V_{max,sun} &= V_{max}^T \frac{F_{N,sun}}{F_{sun} LAI} , \qquad (173) \\ V_{max,shd} &= V_{max}^T \frac{F_{N,shd}}{F_{shd} LAI} , \qquad (174) \\ & \qquad (175) \end{aligned}$$

where V_{max}^T $[\mu mol\,CO_2\ s^{-1}\ m^{-2}]$ is the maximum Rubisco capacity at 25°C at the top of the canopy, which is a model parameter. Theoretically, other quantities, such as the maximum electron transport capacity at 25°C at canopy top J_{max}^T $[\mu mol\,Eq\ s^{-1}\ m^{-2}]$ and the leaf maintenance respiration R_{dC} should be also scaled from the leaf to the canopy scale (*Wang and Leuning*, 1998; *Dai et al.*, 2004). Since in T&C J_{max}^T and R_{dC} are dependent on V_{max}^T, their scaling is implicit on the scaling of V_{max} (*Kattge and Knorr*, 2007). Note that F_{sun} and F_{shd} are computed similarly but not identically to Eq. (13) (Section 4.1.1) since living biomass LAI and not PAI is used.

The canopy scale quantities of net assimilation $\overline{A_{nC}}$ $[\mu mol\,CO_2\ s^{-1}\ m^{-2}]$ and the leaf maintenance respiration $\overline{R_{dC}}$ $[\mu mol\,CO_2\ s^{-1}\ m^{-2}]$ are finally obtained as the weighted sum of unit leaf sunlit and shaded fractions as:

$$\overline{A_{nC}} = A_{nC,sun}\, F_{sun} LAI + A_{nC,shd}\, F_{shd} LAI \,, \tag{176}$$
$$\overline{R_{dC}} = R_{dC,sun}\, F_{sun} LAI + R_{dC,shd}\, F_{shd} LAI \ . \tag{177}$$

The stomatal resistance for sunlit and shaded leaves $r_{s,sun}$, $r_{s,shd}$, $[s\ m^{-1}]$ are instead maintained at the leaf scale as required by Eq.(93)-(94).

6.6.3 Stomatal conductance

Plant metabolism depends on the photosynthetic reaction, in which photosynthetically active shortwave radiation energy is used to combine water and atmospheric CO_2 into sugars and other organic compounds. Plants allow the transfer of CO_2 from the atmosphere to the cellular sites of photosynthesis located in the chloroplasts inside the leaves. This flow requires an open pathway between the atmosphere and water-saturated tissues inside the leaf, which leads to an inevitable loss of water vapor over the same route (*Sellers et al.*, 1997). The opening of this pathway is regulated by the stomatal aperture. The complex mechanisms of stomatal movement depend on both plant physiology and environmental factors (*Daly et al.*, 2004; *Buckley*, 2005). A complete mechanistic model reproducing this function has not been yet developed, although several biochemical models have been proposed (*Jones*, 1998; *Jarvis and Davies*, 1998; *Dewar*, 2002; *Gao et al.*, 2002; *Katul et al.*, 2003; *Tuzet et al.*, 2003; *Buckley et al.*, 2003; *Sperry et al.*, 2002; *Buckley*, 2005; *Zweifel et al.*, 2007; *Vico and Porporato*, 2008). Generally, biochemical models show a consistently better performance compared to Jarvis-type schemes (*Niyogi and Raman*, 1997; *Lhomme*, 2001) or other methods used to compute photosynthesis (*Anderson et al.*, 2000; *LeRoux et al.*, 2001; *Arora*, 2002).

In T&C, a biochemical model describing the coupling between photosynthesis and stomatal resistance is employed. Simplifications are introduced in order to reduce the computational effort and to account for the limitations imposed by a single prognostic temperature (Section 5.1). Indeed, the necessity to solve iteratively for stomatal resistance ($r_{s,sun}$ and $r_{s,shd}$), which is a variable of the non-linear numerical scheme that determines the surface temperature T_s would require a large computational burden. In the biochemical model component of T&C, the leaf temperatures of sunlit and shaded canopy fractions $T_{v,sun}$ and $T_{v,shd}$ are approximated with the air temperature T_a and the value of aerodynamic resistance r_a used in Eq. (179) that depends implicitly on surface temperature, is approximated with the aerodynamic resistance for neutral conditions. These assumptions permit the estimation of photosynthesis and stomatal resistance outside the non-linear iterative equation used to calculate the surface temperature T_s. Such an approach diminishes the computational effort and is frequently used in numerical solution of stomatal resistance (*Noilhan and Planton*, 1989; *Nouvellon et al.*, 2000; *Daly et al.*, 2004; *Montaldo et al.*, 2005).

In order to avoid repetitions, in the following, the equations for stomatal resistance

r_s ($r_{s,sun}$ or $r_{s,shd}$) and net assimilation A_{nC} for a single leaf are presented, using a generic maximum Rubisco capacity at $25°C$ V_{max}, which corresponds to $V_{max,sun}$, for a sunlit leaf and to $V_{max,shd}$ for a shaded leaf.

The aperture of stomata has been experimentally shown to be related to the net assimilation rate of CO_2, A_{nC}, environmental vapor pressure deficit Δe $[Pa]$, and intercellular CO_2 concentration c_i $[Pa]$ (*Ball et al.*, 1987; *Leuning*, 1995; *Gao et al.*, 2002). It is important to note that all empirical stomatal conductance relationships give a linear dependence between the net assimilation rate A_{nC} and the stomatal conductance g_{s,CO_2}. Several empirical equations calculating stomatal conductance have been proposed in literature (*Ball et al.*, 1987; *Tardieu and Davies*, 1993; *Leuning*, 1990, 1995; *Tuzet et al.*, 2003). See also *Niyogi and Raman* (1997) and *Dewar* (2002) for comparisons of methods. The equation proposed by *Leuning* (1990, 1995) is used in T&C:

$$g_{s,CO_2} = g_{0,CO_2} + a\frac{A_{nC}}{(c_c - \Gamma^*)} f(\Delta e)\, P_{atm}\,, \qquad (178)$$

where g_{s,CO_2} $[\mu molCO_2\ m^{-2}\, leaf\ s^{-1}]$ is the stomatal conductance, $g_{s,CO_2} = 1/r_{s,co_2}$, a $[-]$ is an empirical parameter, Γ^* $[Pa]$ is the CO_2 compensation point, P_{atm} $[Pa]$ is the atmospheric pressure, and g_{0,CO_2} $[\mu mol\, CO_2\ m^{-2}\, leaf\ s^{-1}]$ is the minimum stomatal conductance when $A_{nC} \leq 0$, which includes cuticular conductance and imperfect stomatal closure. The sensitivity to vapor pressure deficit is expressed through an empirical function $f(\Delta e) = \left(\frac{1}{1+\Delta e/\Delta_0}\right)$, where Δe $[Pa]$ is the vapor pressure deficit, which is calculated with T_a, and Δ_0 $[Pa]$ is an empirical coefficient that expresses the value of vapor pressure deficit at which $f(\Delta e = \Delta_0) = 0.5$. Equation (178) is modified from the original formulation since the CO_2 concentration at the leaf surface, c_s $[Pa]$, is replaced with the CO_2 concentration at the chloroplast level c_c or the internal leaf concentration, c_i $[Pa]$, in case mesophyll conductance is not accounted for. This correction leads to a better agreement with observed stomatal response and to a more direct link with the CO_2 concentration sensed by the leaf (*Mott*, 1988; *Assmann*, 1999; *Dewar*, 2002).

The photosynthesis rates and stomatal conductance depend on chloroplast level partial pressure of CO_2, c_c $[Pa]$, that a priori is unknown (Section 6.6.4). An iterative procedure is thus required to estimate c_c, which is formulated as a problem of finding the zero of a non-linear equation. In order to solve the non-linear equation the resistance path between the leaf chloroplasts and the atmosphere must be calculated. The corresponding equation in terms of carbon fluxes is:

$$A_{nC} = \frac{c_a - c_c}{P_{atm}\,(1.64\, r_s + r_{mes} + 1.37 r_b + r_a)}\,, \qquad (179)$$

where c_a $[Pa]$ is the air atmospheric CO_2 concentration at the leaf surface, the coefficients 1.37 and 1.65 are the ratios between the resistances to transfer of CO_2 and water vapor across the leaf boundary layer (i.e., $r_{b,CO_2}/r_{b,H_2O} = 1.37$) and stomata (i.e., $r_{s,CO_2}/r_{s,H_2O} = 1.64$) (*vonCaemmerer and Farquhar*, 1981). The transfer of carbon through the aerodynamic surface layer is completely turbulent and $r_{a,CO_2} = r_{a,H_2O}$ (*Jones*, 1983). Note that throughout the rest of the document when the subscript in the resistance terms is omitted, the value always refer to water. The stomatal resistance r_s and the leaf boundary layer resistance r_b are at the leaf level. The term $r_{mes} = 1/g_{mes}$ $[m^2\ s^1\ \mu mol^{-1}\, CO_2\ ]$ is the mesophyll resistance (*Warren*, 2006), computed using a constant mesophyll conductance g_{mes}, which is a model input. Mesophyll conductance represents an additional resistance to the CO_2 path and has been shown to be a function of environmental variables and CO_2 itself (*Flexas et al.*, 2008, 2012). If these dependencies are accounted for mesophyll conductance can partially decouple water and carbon fluxes (*Warren*, 2008; *Sun et al.*, 2014), however, parameterizations of environmental dependencies are still very uncertain and are not accounted for in the current T&C version. When $g_{mes} = \infty$, its effect vanishes and Eq. (179) becomes equivalent to the classic formulation without mesophyll conductance. When the biochemical model is used to calculate photosynthesis of a low-vegetation (L_v) layer (located below high vegetation (H_v) layer), undercanopy resistance r'_a should be added to the denominator of Eq. (179).

The resistances in Eq. (179) are expressed in biochemical units of $[m^2\ s^1\ \mu mol^{-1}\, CO_2\ ]$. The conversion to hydrological units (i.e., $[s\ m^{-1}]$) is obtained using the gas molar volume, as in *Sellers et al.* (1996b):

$$r_x(s\ m^{-1}) \quad = \quad \frac{1}{0.0224}\frac{T_f\ P_{atm}}{(T+273.15)P_{atm,0}}10^6 r_x(m^2\ s\ \mu mol^{-1}\, CO_2)\,, \qquad (180)$$

where P_{atm} $[Pa]$ is the atmospheric pressure, $P_{atm,0} = 101325$ $[Pa]$ is the reference atmospheric pressure, $T_f = 273.15$ $[K]$ is the freezing temperature, T $[^\circ C]$ is the leaf temperature for r_s or air temperature for r_b and r_a, and $r_x(\diamond)$ is a generic resistance with unit of measurements $(\diamond)$.

6.6.4 Biochemical model of photosynthesis

Biochemical models of leaf photosynthesis describe CO_2 assimilation by chloroplasts of leaves as a process limited by rates of enzyme kinetics. Specifically, the amount and velocity of the carboxylating enzyme Rubisco, the electron transport, and the efficiency of leaf light-intercepting apparatus (chlorophyll) are considered as limiting factors (*Farquhar et al.*, 1980; *vonCaemmerer and Farquhar*, 1981; *Collatz et al.*, 1991, 1992; *Farquhar and Wong*, 1984; *Farquhar et al.*, 2001). The biochemical model of canopy photosynthesis implemented within T&C is based on *Farquhar et al.* (1980); *Collatz et al.* (1991, 1992) with modifications based on *Leuning* (1995); *Sellers et al.* (1996b); *Dai et al.* (2004); *Kattge and Knorr* (2007); *Bonan et al.* (2011). The model describes the net and gross photosynthetic rates, A_{nC}, and A_C, respectively, $[\mu mol\, CO_2\ s^{-1}\ m^{-2}]$, as a function of three limiting rates. Specifically, these rates describe the assimilation process as limited by the efficiency of the photosynthetic enzyme system (Rubisco-limited) J_c, the amount of PAR captured by the leaf chlorophyll J_e, that depends on the the electron transport rate J_m, and the capacity of the leaf to export or utilize the products of photosynthesis, J_s for C_3 plants or PEP-carboxylase, J_s for C_4 plants.

The RuBP-carboxylase (Rubisco enzyme) limited carboxylation rate is formulated as:

$$
\begin{aligned}
J_c &= V_m \left[\frac{c_c - \Gamma^*}{c_c + K_c(1 + O_i/K_o)} \right] , \quad && \text{for } C_3 \, , && (181) \\
J_c &= V_m \, , && \text{for } C_4 \, . && (182)
\end{aligned}
$$

The maximum rate of PAR captured by the leaf chlorophyll (i.e., the light-limited rate) is:

$$
\begin{aligned}
J_e &= J \left[\frac{c_c - \Gamma^*}{c_c + 2\Gamma^*} \right] , \quad && \text{for } C_3 \, , && (183) \\
J_e &= PPFD^* \, , && \text{for } C_4 \, , && (184)
\end{aligned}
$$

where J is the smaller root of the quadratic equation:

$$
\alpha_J J^2 - (PPFD^* + \frac{J_m}{4}) \, J + PPFD^* \, \frac{J_m}{4} \; = \; 0 \, , \qquad (185)
$$

The export-limited rate of carboxylation (for C_3 plants) and the PEP-carboxylase limited rate of carboxylation (for C_4 plants) are:

$$
\begin{aligned}
J_s &= 3 \, TPU \, , \quad && \text{for } C_3 \, , && (186) \\
J_s &= k_e \frac{c_c}{P_{atm}} \, , && \text{for } C_4 \, . && (187)
\end{aligned}
$$

In the above equations, c_c and O_i $[Pa]$ are the partial pressures of CO_2 and O_2 in the leaf chloroplasts. The quantity $PPFD^* = \epsilon \, \beta_Q \, PAR_{abs}$ $[\mu mol \, CO_2 \; s^{-1} \; m^{-2}]$ is the effective photosynthetic photon flux density of photosystem II, where ϵ $[\mu mol \, CO_2 \; \mu mol^{-1} \, photons]$ is the intrinsic quantum efficiency, and β_Q $[\mu mol \, photons \; J^{-1}]$ is a quanta-to-energy converting factor between the measurement units, that depends on the wavelength, λ, and thus on the type of radiation. *Dye* (2004) showed that a value of $\beta_Q = 4.57$ can be employed for a wide range of cloud conditions with little or no error. The term $\alpha_J = 0.7$ $[-]$ is a shape parameter (*Bonan*, 2002) and PAR_{abs} $[W \; m^{-2}]$ is the absorbed photosynthetically active radiation at the leaf scale computed from the canopy scale quantities in Section 4.1:

$$
\begin{aligned}
PAR_{abs} &= \frac{PAR_{abs,sun}}{F_{sun} LAI} \, , \quad && \text{for sunlit leaves} \, , \\
PAR_{abs} &= \frac{PAR_{abs,shd}}{F_{shd} LAI} \, , && \text{for shaded leaves} \, . && (188)
\end{aligned}
$$

The value of the intrinsic quantum efficiency, ϵ, depends on the photosynthesis pathway (C_3 or C_4). There are arguments about its variability among different plants (*Skillman*, 2008) but constant values of $\epsilon = 0.081$ $[\mu mol CO_2 \; \mu mol^{-1} \, photons]$ for C_3 and $\epsilon = 0.040$ $[\mu mol CO_2 \; \mu mol^{-1} \, photons]$ for C_4 plants are typically used (*Farquhar et al.*, 1980; *Collatz et al.*, 1991, 1992; *Cox*, 2001; *Arora*, 2002). The reader is referred to *Öquist and Chow* (1992) and *Singsaas et al.* (2001) for further discussions on ϵ.

The variables V_m $[\mu mol\, CO_2\ s^{-1}\ m^{-2}]$, J_m $[\mu mol\, Eq\ s^{-1}\ m^{-2}]$ and TPU $[\mu mol\, Eq\ s^{-1}\ m^{-2}]$ are the Rubisco capacity, electron transport capacity, and triose phosphate utilization, at the leaf scale, after the temperature dependence has been accounted for. The parameter Γ^* $[Pa]$ is the CO$_2$ compensation point (*Bonan et al.*, 2011):

$$\Gamma^* \quad = \quad \Gamma^*_{25} \exp\Big[\frac{37.83(T_v - T_{ref})}{(T_{ref}\, R T_v)}\Big] , \tag{189}$$

where $R = 8.314$ $[J\ mol^{-1}\ K^{-1}]$ is the universal gas constant, $T_{ref} = 273.15$ $[K]$ is a reference temperature, T_v $[K]$ is the leaf temperature in Kelvin, and $\Gamma^*_{25} = 42.75\, 10^{-6}\, P_{atm}$ $[Pa]$ is the CO$_2$ compensation point at $25°C$. The terms K_c and K_o $[Pa]$ are the Michaelis-Menten constants for CO$_2$ and O$_2$, respectively, expressed as functions of leaf temperature T_v $[K]$ (*Bonan et al.*, 2011):

$$K_c \quad = \quad K_{c,25} \exp\Big[\frac{79.43(T_v - T_{ref})}{(T_{ref}\, R T_v)}\Big] , \tag{190}$$

$$K_o \quad = \quad K_{o,25} \exp\Big[\frac{36.38(T_v - T_{ref})}{(T_{ref}\, R T_v)}\Big] , \tag{191}$$

where the reference values at $25°C$ are: $K_{c,25} = 404.9\ 10^{-6}\, P_{atm}$ $[Pa]$ and $K_{o,25} = 278.4\ 10^{-3}\, P_{atm}$ $[Pa]$.

The dependence of maximum catalytic capacity of Rubisco V_m, on temperature T_v, is accounted for as in *Kattge and Knorr* (2007):

$$V_m \quad = \quad V_{max} \exp\Big[\frac{H_a(T_v - T_{ref})}{(T_{ref}\, R T_v)}\Big] \frac{1 + exp\left(\frac{T_{ref}\Delta S - H_d}{T_{ref}\, R}\right)}{1 + exp\left(\frac{T_v \Delta S - H_d}{T_v\, R}\right)} , \tag{192}$$

where V_{max} $[\mu mol$ CO$_2$ $m^{-2}\ s^{-1}]$ is the value of Rubisco capacity at $25°C$, H_a $[kJ\ mol^{-1}]$ is the activation energy, and H_d $[kJ\ mol^{-1}]$ is the deactivation energy. The deactivation energy H_d is generally assumed to be constant, $H_d = 200$ $[kJ\ mol^{-1}]$ and describes the rate of decrease above the optimum temperature. The term ΔS $[kJ\ mol^{-1}\ K^{-1}]$ is the so-called "entropy factor". Reference values of $H_a = 72$ $[kJ\ mol^{-1}]$ and $\Delta S = 0.649$ $[kJ\ mol^{-1}\ K^{-1}]$ can be used in absence of specific information (*Kattge and Knorr*, 2007). More generally, these quantities are species dependent with typical ranges of $H_a = 45 - 95$ $[kJ\ mol^{-1}]$ and $\Delta S = 0.625 - 0.665$ $[kJ\ mol^{-1}\ K^{-1}]$. A generic illustration of temperature dependencies for various quantities including V_m and J_m is presented in Figure 24.

The parameterization of *Kattge and Knorr* (2007) improves the biochemical model of photosynthesis in comparison to the conventionally used Q_{10} function to account for temperature dependencies of photosynthetic parameters (*Collatz et al.*, 1991; *Sellers et al.*, 1996a; *Cox*, 2001). An equivalent expression to Eq. (192) but with different parameters has been also used by other authors (*Bernacchi et al.*, 2001, 2003; *Bonan et al.*, 2011). Besides, the parameter H_a and ΔS have a physical meaning and are not purely adjustment factors.

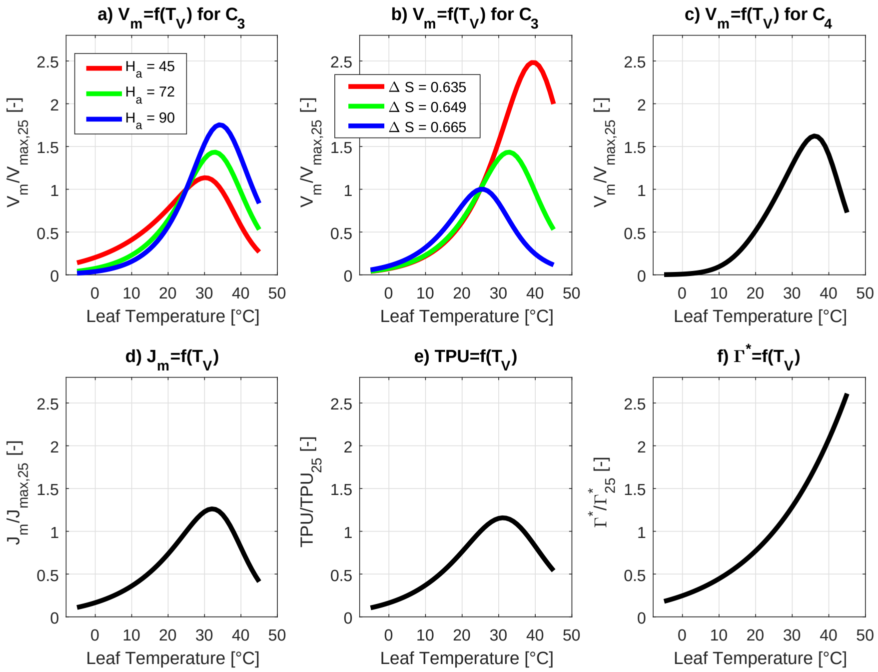

Figure 24: Leaf temperatures T_v [$^\circ C$] sensitivity of the maximum Rubisco capacity V_m/V_{max} for C_3 (a and b) and C_4 (c) photosynthesis patterns. The sensitivity to the activation energy, H_a [$kJ\ mol^{-1}$] (a), and entropy factor ΔS [$kJ\ mol^{-1}\ K^{-1}$] (b) are shown. Reference values of $\Delta S = 0.649$ is used in (a), and $H_a = 72$ in (b). Temperature sensitivities of maximum electron transport capacity J_m/J_{max} (d), Triose Phosphate Utilization TPU/TPU_{25} (e), and CO$_2$ compensation point Γ^*/Γ^*_{25} (f) are also shown.

The maximum electron transport capacity, J_m [$\mu mol\, Eq\ s^{-1}\ m^{-2}$], is also computed as in *Kattge and Knorr* (2007):

$$J_m \;=\; J_{max}\, \exp\Big[\frac{H_a(T_v - T_{ref})}{(T_{ref}\, R T_v)}\Big] \frac{1 + exp\left(\frac{T_{ref}\Delta S - H_d}{T_{ref}\, R}\right)}{1 + exp\left(\frac{T_v\Delta S - H_d}{T_v\, R}\right)}\,, \tag{193}$$

where J_{max} [$\mu mol\, Eq\ s^{-1}\ m^{-2}$] is the maximum electron transport capacity at $25°C$, computed from V_{max} as $J_{max} = r_{jv}\, V_{max}$ [$\mu mol\, Eq\ s^{-1}\ m^{-2}$], with r_{jv} [$\mu mol\, Eq\ \mu mol\, CO_2^{-1}$] an input parameter, with a typical range $r_{jv} = 1.6 - 2.6$, Reference values of $H_a = 50$ [$kJ\ mol^{-1}$], $H_d = 200$ [$kJ\ mol^{-1}$], $\Delta S = 0.646$ [$kJ\ mol^{-1}\ K^{-1}$], are used to compute J_m (*Kattge and Knorr*, 2007) (Figure 24).

The Triose Phosphate Utilization, TPU [$\mu mol\, Eq\ s^{-1}\ m^{-2}$], is computed as in *Bonan et al.* (2011):

$$TPU \;=\; TPU_{25}\, \exp\Big[\frac{H_a(T_v - T_{ref})}{(T_{ref}\, R T_v)}\Big] \frac{1 + exp\left(\frac{T_{ref}\Delta S - H_d}{T_{ref}\, R}\right)}{1 + exp\left(\frac{T_v\Delta S - H_d}{T_v\, R}\right)}\,, \tag{194}$$

where $TPU_{25} = 0.1182 V_{max}$ [$\mu mol\, Eq\ s^{-1}\ m^{-2}$] is the triose phosphate utilization at $25°C$ computed from V_{max} and the parameters of Eq. (194) are $H_a = 53.1$ [$kJ\ mol^{-1}$], $\Delta S = 0.490$ [$kJ\ mol^{-1}\ K^{-1}$], and $H_d = 150.65$ [$kJ\ mol^{-1}$] (Figure 24).

For C_4 species Eq. (192) is replaced with another expression to compute V_m (*Sellers et al.*, 1996b; *Dai et al.*, 2004; *Bonan et al.*, 2011):

$$V_m \;=\; V_{max}\, \left[2.1^{0.1(T_v-25)}\right] \left[\frac{1}{1+\exp[0.3(T_v-40)]}\right] \left[\frac{1}{1+\exp(0.2(15-T_v))}\right]\,, \tag{195}$$

where T_v [$°C$] is the leaf temperature in Celsius (Figure 24). The PEP Carboxylase coefficient k_e is computed as in *Bonan et al.* (2011):

$$k_e \;=\; k_{e,25}\, \left[2.1^{0.1(T_v-25)}\right]\,, \tag{196}$$

where T_v [$°C$] is the leaf temperature and $k_{e,25} = 20000\, V_{max}$ [$\mu mol\, Eq\ s^{-1}\ m^{-2}$] is the PEP Carboxylase coefficient at $25°C$.

The transition from one limiting rate to another (J_c, J_e, and J_s) is not abrupt. The coupling between the three processes leads to a continuous smooth function. *Collatz et al.* (1991) described it by combining the rate terms into two quadratic equations, which are then solved for their smaller roots:

$$\begin{aligned} \alpha_{ce} J_p^2 - J_p(J_c + J_e) + J_e J_c &= 0\,, \\ \alpha_{ps}(A^*)^2 - A^*(J_p + J_s) + J_p J_s &= 0\,, \end{aligned} \tag{197}$$

where the solution J_p [μmol $\mathrm{CO_2}$ $m^{-2}\ s^{-1}$] is the smoothed minimum of J_c and J_e, and the solution A^* [μmol $\mathrm{CO_2}\, m^{-2}\, s^{-1}$] is the gross assimilation rate for unit canopy before accounting for moisture stress, α_{ce} and α_{ps} are the coupling coefficients

(*Sellers et al.*, 1996a; *Bonan et al.*, 2011), with $\alpha_{ce} = 0.98$ for C_3 species and $\alpha_{ce} = 0.80$ for C_4 species, and $\alpha_{ps} = 0.95$.

The net assimilation rate at the leaf scale, A_{nC} [μmol CO$_2$ m^{-2} s^{-1}], is then given by:

$$A_{nC} \;=\; A_C - R_{dC}\,, \tag{198}$$

where $A_C = \beta_S\, A^*$ [μmol CO$_2$ m^{-2} s^{-1}] is the gross assimilation rate, and β_S is a water stress factor (Eq. 201). The term R_{dC} [μmol CO$_2$ m^{-2} s^{-1}] is the leaf maintenance respiration, which is assumed to be equal to the leaf dark respiration, even though this is a coarse assumption for respiration during daytime (*Villar et al.*, 1995; *Atkin et al.*, 1997), and is estimated following *Collatz et al.* (1991, 1992); *Bonan et al.* (2011). For C_3 species (Figure 25a):

$$R_{dC} \;=\; 0.015\, V_{max}\, \exp\Big[\frac{H_a(T_v - T_{ref})}{(T_{ref}\, R\, T_v)}\Big] \frac{1 + exp\left(\frac{T_{ref}\Delta S - H_d}{T_{ref}\, R}\right)}{1 + exp\left(\frac{T_v \Delta S - H_d}{T_v\, R}\right)}\;, \tag{199}$$

where T_v [K] is in Kelvin and reference values of $H_a = 46.39$ [$kJ\ mol^{-1}$], $H_d = 150.65$ [$kJ\ mol^{-1}$], and $\Delta S = 0.490$ [$kJ\ mol^{-1}\ K^{-1}$] are used. For C_4 species:

$$R_{dC} \;=\; 0.025\, V_{max}\, 2.0^{0.1(T_v - 25)}\, \Big[1 + e^{1.3\,(T_v - 55)}\Big]^{-1}\;, \tag{200}$$

where T_v [$^\circ C$] is in Celsius and the temperature inhibition functions are used to modulate respiration at elevated temperatures. Note that the relation between the leaf respiration, R_{dC}, and temperature, T_v, is likely more complex, because acclimation effects may play an important role (*Tjoelker et al.*, 2001; *Wythers et al.*, 2005; *Smith and Dukes*, 2013). Acclimation effects are, however, not accounted for in this version of T&C.

A β_S factor is introduced to reproduce the control of available moisture on transpiration and carbon assimilation. The factor β_S limits canopy photosynthesis based on leaf water potential Ψ_L [MPa] (Section 13) at the hourly scale (Figure 25b):

$$\beta_S \;=\; 1 - \frac{1}{1 + \exp(p_S \Psi_L + q_S)}\,, \tag{201}$$

where $p_S = \frac{3.89}{\Psi_{S,02} - \Psi_{S,50}}$ and $q_S = -p_S\, \Psi_{S,50}$ are two parameters computed from the knowledge of water potential thresholds where stomata closure begins (2%) and reaches the 50%, $\Psi_{S,02}$ and $\Psi_{S,50}$ [MPa], respectively, which are model parameters. Note that in the absence of a plant hydraulic module (Section 13) the leaf water potential Ψ_L, corresponds to the soil water potential Ψ_{sR} and Eq. (201) is only a proxy for the complex control of the entire root-xylem-leaf transfer process that regulates stomatal aperture and photosynthesis (*Tuzet et al.*, 2003; *Buckley et al.*, 2003; *Katul et al.*, 2003; *Bohrer et al.*, 2005; *Verbeeck et al.*, 2007; *Vico and Porporato*, 2008; *Feddes et al.*, 2001; *Sperry et al.*, 2003; *Kirkham*, 2005; *Sack and Holbrook*, 2006; *Nobel*, 2009). The factor β_S is applied to the assimilation rate, A^*, as proposed by

Daly et al. (2004) and not to the maximum Rubisco capacity, V_m, as proposed by other authors (e.g., *Ivanov et al.*, 2008b).

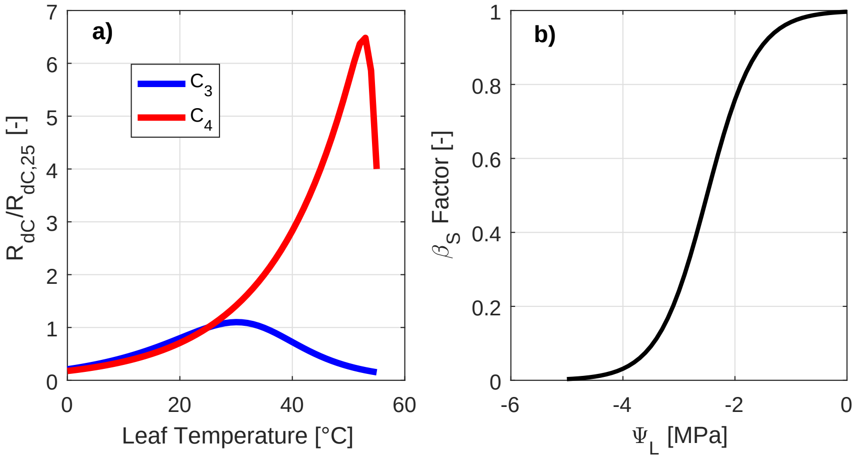

Figure 25: Sensitivity of the leaf maintenance respiration to leaf temperatures T_v $[°C]$, $R_{dC}/R_{dC,25}$ for C_3 and C_4 photosynthesis patterns (a). The value of the β_S factor for different leaf water potentials Ψ_L is also presented for the special case $\Psi_{S,00} = -0.8\ MPa$ and $\Psi_{S,50} = -2.5\ MPa$ (b).

An important parameter in the biochemical model is the maximum Rubisco capacity at $25°C$, V_{max} $[\mu mol\ \mathrm{CO_2}\ m^{-2}\ s^{-1}]$. Figure 26 shows the sensitivity to this parameter. The maximum photosynthetic capacity, A_{max} $[\mu mol\, CO_2\ s^{-1}\ m^{-2}]$, i.e. the gross assimilation rate, A_C, for optimal conditions, and the maximum stomatal resistance, $g_{s,CO_2,max}$ $[mmol\ \mathrm{CO_2}\ m^{-2}\ s^{-1}]$, are plotted against V_{max}. These quantities represent the rate of photosynthesis and the stomatal conductance when all the environmental conditions are non-limiting. The sensitivities of A_{max} and $g_{s,CO_2,max}$ to the atmospheric $\mathrm{CO_2}$ concentration, c_a $[ppm]$, and the empirical coefficient, a $[-]$, that indicates the linear link between assimilation rate and stomatal conductance are shown in Figure 26.

6.6.5 Chlorophyll fluorescence

The calculation of solar-induced chlorophyll fluorescence (SIF) follows the derivation of *Lee et al.* (2015). The flux of emitted fluorescence F can be expressed by an equation analogous to the expression for $PPFD^*$, $F = \epsilon_F\, \beta_Q\, PAR_{abs}$ $[\mu mol\, Eq\ s^{-1}\ m^{-2}]$ where ϵ_F $[\mu mol\, Eq\ \mu mol^{-1}\, photons]$ is the fluorescence yield (number of photons that fluoresce per absorbed photon) analogous to ϵ, and β_Q $[\mu mol\, photons\ J^{-1}]$ is again the converting factor between the measurement units.

The energy absorbed by excited chlorophyll must be transferred to one of: (i) photochemistry (photochemical quenching, i.e., the efficiency of electron transport per photon absorbed by photosystems), (ii) non-photochemical quenching (NPQ), that is, heat, or fluorescence (F). The non-photochemical quenching is partitioned as the sum of fractional heat loss in light-adapted conditions and in dark-adapted conditions. The corresponding rate coefficients of the different energy uses are: k_p

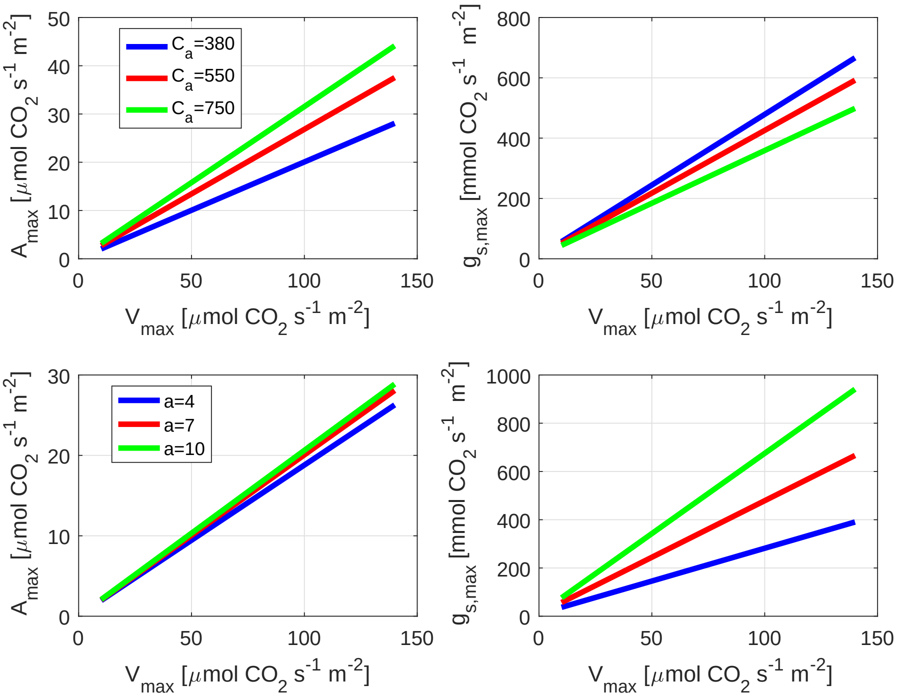

Figure 26: Values of maximum photosynthetic capacity, A_{max}, and maximum stomatal conductance, $g_{s,max}$, as a function of V_{max}. A sensitivity analysis to atmospheric CO_2 concentration, C_a $[ppm]$, and to the empirical coefficient, a $[-]$, is shown. The lines are calculated with $\epsilon = 0.081$ $[\mu molCO_2\ \mu mol^{-1}\, photons]$, $H_a = 72$ $[kJ\ mol^{-1}]$, $\Delta S = 0.649$ $[kJ\ mol^{-1}\ K^{-1}]$ for a C3 plant; $a = 7$ in the subplots (a) and (b); $c_a = 380$ ppm in the subplots (c) and (d).

(photochemical quenching), k_n (NPQ in light adapted conditions), k_d (NPQ in dark adapted conditions) and k_f (fluorescence) (*Lee et al.*, 2015). For a light-acclimated leaf when it is exposed to saturating irradiance $k_p = 0$, then, the fluorescence yield ϵ_F can be written as:

$$\epsilon_F = \frac{k_f}{k_f + k_d + k_n} (1 - \epsilon_P) , \tag{202}$$

where $\epsilon_P = 4\,\epsilon\, J_f / PPFD*$ $[\mu mol\, Eq\, \mu mol^{-1}\, photons]$, $k_d = max[0.03\, T_v{+}0.0773, 0.087]$, $k_f = 0.05$, and $k_n = (6.2473\, dls - 0.5944) dls$. The leaf temperature T_v $[^{\circ}C]$ is in Celsius and $dls = 1 - J_f/PPFD^*$ is the degree of light saturation (*Lee et al.*, 2013, 2015; *van der Tol et al.*, 2014). The term J_f is the actual electron transport rate calculated from the CO$_2$ exchange rate and $PPFD^*$ is the maximum possible electron transport rate for a given absorbed PAR. The term J_f is computed as (*Lee et al.*, 2015):

$$J_f = A^* \left[\frac{c_c + 2\Gamma^*}{c_c - \Gamma^*} \right] , \quad \text{for } C_3 , \tag{203}$$

$$J_f = A^* , \qquad \text{for } C_4 . \tag{204}$$

Since a spectrometer measures fluorescence as a power per solid angle, unit area, and wavelength range $[W \;\; m^{-2}\, sr^{-1}\, \mu m^{-1}]$, the flux of emitted fluorescence, F $[\mu mol\, Eq\;\, s^{-1}\;\, m^{-2}]$ must be converted to the proper units. The conversion would theoretically requires to run a full canopy radiative transfer model, fortunately conversion factors have been proposed to convert F in SIF at 755 nm (*Lee et al.*, 2015):

$$SIF_{755} = \frac{F}{k} , \tag{205}$$

where $k = 0.0375 V_{max} + 8.25$ accounts for the integration over all wavelengths in the fluorescence emission spectrum, observing angle, and for the unit conversion. Besides V_{max}, chlorophyll concentration also influences k but this is not accounted for in T&C. The value of SIF_{755} is computed separately for sunlit and shaded leaves and integrated at canopy scale identically to net assimilation (Eq. 176).

7 Snow hydrology

A suitable model of the hydrological cycle must account for snow accumulation and melt since the presence of snow modifies the energy and water mass balances.

7.1 Precipitation partition

The partition of incoming precipitation P_r $[mm\; h^{-1}]$ into rain $P_{r,liq}$ $[mm\; h^{-1}]$ and snow $P_{r,sno}$ $[mm\; h^{-1}]$ (in terms of liquid water depth) is considered to be regulated by air temperature, T_a $[^{\circ}C]$ at the reference height, z_{atm} $[m]$. This assumption is common in modeling snowpack dynamics (*Wigmosta et al.*, 1994; *Tarboton and Luce*, 1996), despite the fact that the partition between $P_{r,liq}$ and $P_{r,sno}$ depends on the actual profile of temperature in the lower troposphere, and on the weather system producing the precipitation event. The terms $P_{r,liq}$ and $P_{r,sno}$ are calculated as:

$$
\begin{aligned}
P_{r,sno} &= P_r\,, && \text{if } T_a \leq T_{min}, && (206)\\
P_{r,sno} &= P_r \frac{T_{max}-T_a}{T_{max}-T_{min}}\,, && \text{if } T_{min} < T_a < T_{max}, && (207)\\
P_{r,sno} &= 0\,, && \text{if } T_a \geq T_{max}, && (208)
\end{aligned}
$$

$$
P_{r,liq} = P_r - P_{r,sno}\,, \qquad (209)
$$

where T_{min} [$^\circ C$] is a threshold temperature below which all precipitation is in the form of snow, and T_{max} [$^\circ C$] is a threshold temperature above which all precipitation is rain. Between the threshold temperatures, precipitation is assumed to be a mix of rain and snow. The values of T_{min} and T_{max} are model parameter. Typical values of -1.1/-0.5 [$^\circ C$] and 2.5/3.3 [$^\circ C$] can be used for T_{min} and T_{max}, respectively (*USACE*, 1956).

7.2 Snowpack energy and mass balance

Two different storages of snow are considered: the snowpack at the ground, with the corresponding snow water equivalent S_{WE} [mm] and the intercepted snow in the *high-vegetation* canopy, with snow water equivalent $In_{S_{WE}}$ [mm]. Since a single prognostic surface temperature T_{sno} is computed for a given computational element, the energy balance of the two snow storages is combined.

The basic theory underlying all physically-based snowmelt models lies in balancing the energy budget for the snowpack and converting the excess energy into snowpack temperature change, metamorphism, or melt (*Williams and Tarboton*, 1999). The seasonal snowpack dynamics can be separated into the cooling phase, the warming phase, the ripening phase, and the output phase (*Dingman*, 1994). During the cooling/warming phases, the net energy input raises/decreases the temperature of snowpack, until a warming phase brings snow to the melting point. During the ripening and the output phases, the snowpack remains isothermal at the melting point temperature. Additional energy inputs cause some of the snow to change phase from ice to water. During the ripening phase, the liquid water is retained in the snowpack by surface-tension forces until the snow reaches its liquid holding capacity. Once snowpack voids are saturated, the output phase begins and meltwater flows out of the snowpack.

In cooling and warming phases, the temperature variation of snowpack is controlled by heat transfer as:

$$
dT_{sno} = \frac{1000\, dQ\, dt}{c_i\, \rho_w (S^b_{WE} + In^b_{S_{WE}})}\,, \qquad (210)
$$

where dQ [$W\ m^{-2}$] is the net energy flux input to the snowpack, c_i [$J\ kg^{-1}\ K^{-1}$]

is the specific heat of ice, ρ_w $[kg\ m^{-3}]$ is the density of water, and S^b_{WE} $[mm]$, $In^b_{S_{WE}}$ $[mm]$ are the water mass equivalent of ground snowpack and intercepted snow before accounting for melting. The term dt $[s]$ is the time step, and $dT_{sno} = T_{sno}(t) - T_{sno}(t - dt)$ $[°C]$ is the change in the average temperature of the snowpack. Note that in Eq. (210) the temperature change dT_{sno} can be positive or negative depending on the sign of dQ that implicitly depends on T_{sno}.

During the ripening and output phases, snowpack remains isothermal at the temperature of melting point $T_{sno} = 0$ $[°C]$. Additional energy inputs cause some of the snow to change phase from ice to water:

$$S_m = \frac{1000 dQ}{\lambda_f \rho_w}, \tag{211}$$

where $\lambda_f = 333700$ $[J\ kg^{-1}]$ is the latent heat of melting of ice at 0 $[°C]$, and S_m $[mm]$ is the snow water equivalent converted to water. The total flux S_m is partitioned into snowmelt S_{m1} $[mm]$, occurring in snowpack at the ground (i.e., mass released from S^b_{WE}), and snowmelt S_{m2} $[mm]$, occurring in the intercepted snowpack (i.e., mass released from $In^b_{S_{WE}}$) weighting the relative masses:

$$S_{m1} = \frac{S^b_{WE}}{S^b_{WE} + In^b_{S_{WE}}} S_m, \tag{212}$$

$$S_{m2} = \frac{In_{S^b_{WE}}}{S^b_{WE} + In^b_{S_{WE}}} S_m. \tag{213}$$

The net energy flux input to the snowpack, dQ $[W\ m^{-2}]$, is calculated by considering all significant sources of incoming and outgoing heat in the energy balance equation (*Anderson*, 1968; *Bras*, 1990; *Wigmosta et al.*, 1994; *Dingman*, 1994; *Tarboton and Luce*, 1996; *Williams and Tarboton*, 1999; *Liston and Elder*, 2006):

$$\begin{aligned} dQ(T_{sno}) &= R_n(T_{sno}) + Q_v(T_{sno}) + Q_{fm}(T_{sno}) \\ &\quad - H(T_{sno}) - \lambda E(T_{sno}) - G(T_{sno}), \end{aligned} \tag{214}$$

where R_n $[W\ m^{-2}]$ is net radiation energy absorbed by snow, Q_v $[W\ m^{-2}]$ is incoming heat with precipitation, G $[W\ m^{-2}]$ is ground heat flux into the soil, H $[W\ m^{-2}]$ is sensible heat flux from snow, λE $[W\ m^{-2}]$ is latent heat flux from snow and Q_{fm} $[W\ m^{-2}]$ is heat release from melting (negative) or freezing (positive) of liquid water held by snow (Section 7.4). Note that all of the above quantities implicity or explicitly depend on the surface snow temperature T_{sno}.

Snowpack mass S_{WE} $[mm]$ is updated conserving the mass balance:

$$S^b_{WE}(t) = S_{WE}(t - dt) + P_{r,u,sno}(t) - E_{sno}(t) dt, \tag{215}$$

$$S_{WE}(t) = S^b_{WE}(t) - S_{m1}(t), \tag{216}$$

where $P_{r,u,sno}$ $[mm]$ is snow precipitation that reaches the ground, E_{sno} $[mm\ h^{-1}]$ is evaporation-sublimation from the snowpack, and dt $[h]$ is the time step. The term $P_{r,u,sno}$ is the total snow precipitated in the land area, less the newly intercepted snow $In_{S_{WE}}^{N}$ $[mm]$, plus the snow unloaded from the snow interception storage $U_{In_{S_{WE}}}$ $[mm]$ (Eq. 217). Further details are given in Section 7.3. The term E_{sno} is from Eq. (92) and accounts for evaporation-sublimation from the whole snowpack.

$$\begin{aligned} P_{r,u,sno} &= P_{r,sno}\, dt \left[1-(1-C_{sno,w})C_{wat}\right] - In_{S_{WE}}^{N} + U_{In_{S_{WE}}} \,, && (217) \\ E_{sno} &= \Big(1-\sum_{i=1}^{n_c} C_{crown,i} - (1-C_{sno,w})C_{wat}\Big) E_{sno,f} + \\ & \sum_{i=1}^{n_c} \big(C_{crown,i}\, E_{sno,v,i}\big) \,, && (218) \end{aligned}$$

where the symbols in Eq. (218) are defined in Section 5.4.

All of the quantities in Eq. (214) are functions of the surface temperature T_{sno} that is an unknown. Further, T_{sno} depends also on the snow mass balance since it influences snowmelt and liquid water content of the snowpack. An iterative numerical solution has been developed to solve for T_{sno} that satisfies the energy and mass balances. First, an initial value of T_{sno}^{1} is assumed and then Eq. (214) is solved iteratively until the equality $T_{sno}^{i} = T_{sno}^{i+1}$ is satisfied.

7.3 Canopy interception of snow

Interception by forest canopies can store up to 60% of cumulative snowfall by midwinter in cold boreal forests, which may result in a significant loss of snow through sublimation (*Pomeroy et al.*, 1998a). Most of intercepted snow remains in the canopy where it is exposed to a relatively warm and dry atmosphere. Underestimation of interception will result in a shorter exposure time for sublimation/evaporation and thus in a decrease in seasonal sublimation (*Pomeroy et al.*, 1998a). Intercepted snow also alters the surface albedo. A significant decrease of albedo occurs once the intercepted snow is unloaded from canopies.

In T&C only the *high-vegetation* layer (H_v) is parameterized to have a storage of intercepted snow. A single value of intercepted snow water equivalent, $In_{S_{WE}}$ $[mm]$ is considered for any given element and it represents the average of intercepted snow between different crown areas ($C_{crown,i}$) that can be present within a basic computational element. In the *low-vegetation* layer, there is no storage for snow interception. When snow falls on the *low-vegetation* layer, snow is assumed to increment the ground snow layer and its contribution is added to the snow water equivalent S_{WE}. The presence of snow on the ground is assumed to completely hide the *low-vegetation* layer. In such a situation, the latent and sensible heat fluxes are estimated directly from the snow surface.

The snow interception model developed by *Hedstrom and Pomeroy* (1998) is applied to calculate the intercepted snow mass $In_{S_{WE}}$. *Hedstrom and Pomeroy* (1998) provide a physically-based formulation of snow interception, where $In_{S_{WE}}$ is related to snowfall characteristics, leaf area index, tree species, canopy density, air temperature, and wind speed (*Hedstrom and Pomeroy*, 1998; *Pomeroy et al.*, 1998b, 2002; *Gelfan et al.*, 2004). Further adaptations presented by *Gelfan et al.* (2004);

Lee and Mahrt (2004); *Liston and Elder* (2006) are also accounted for and implemented in T&C. The model of snow interception permits the calculation of several quantities such as the newly intercepted snow $In_{S_{WE}}^{N}$ $[mm]$, the actual intercepted snow $In_{S_{WE}}(t)$, and the unloaded snow $U_{In_{S_{WE}}}$ $[mm]$ from standard meteorological variables.

$$\begin{aligned} In_{S_{WE}}^{b}(t) &= In_{S_{WE}}(t-dt) + In_{S_{WE}}^{N}(t) - E_{In_{S_{WE}}}(t)dt\,, & (219) \\ In_{S_{WE}}(t) &= In_{S_{WE}}^{b}(t) - U_{In_{S_{WE}}}(t) - S_{m2}(t)\,, & (220) \end{aligned}$$

where $In_{S_{WE}}^{b}(t)$ $[mm]$ is the intercepted snow before unloading, $E_{In_{S_{WE}}}$ $[mm\ h^{-1}]$ is the sublimation/evaporation from intercepted snow, S_{m2} $[mm]$ is the snowmelt of the intercepted snow (Section 7.2), and dt $[h]$ is the time step. Sublimation/evaporation from intercepted snow $E_{In_{S_{WE}}}$ is taken from Eq. (92):

$$E_{In_{S_{WE}}} = \Big(d_{w,sno} \sum_{i=1}^{n_c} \big(C_{crown,i}[PAI(H_{v,i})]\big)\Big) E_{sno,f}\,, \qquad (221)$$

where $E_{sno,f}$ is in $[mm\ h^{-1}]$, $d_{w,sno} = \min\left(1, In_{S_{WE}}/In_{S_{WE}}^{M}\right)$ $[-]$ is the fraction of vegetation in the *high-vegetation* layer covered by intercepted snow (*Lee and Mahrt*, 2004). The term, $d_{w,sno}$, is averaged on the n_c *crown areas*, and $In_{S_{WE}}^{M}$ $[mm]$ is the total (on the *crown areas*) snow interception capacity. This equation is equivalent to the one describing evaporation from a water surface, once the snowpack temperature and the latent heat of sublimation are considered. This is a simplification when compared to more accurate approaches that compute sublimation losses accounting for ice and canopy exposure coefficients (*Pomeroy et al.*, 1998b). However, this simplification is considered to be adequate in the context of T&C.

The newly intercepted snow, $In_{S_{WE}}^{N}$, depends on the difference between canopy snow interception capacity $In_{S_{WE}}^{M}$ $[mm]$, and the initial snow load $In_{S_{WE}}(t-1)$ $[mm]$. It is further related through an exponential function to snowfall and canopy coverage and density (*Hedstrom and Pomeroy*, 1998):

$$In_{S_{WE}}^{N} = c\Big(In_{S_{WE}}^{M} - In_{S_{WE}}(t-1)\Big)\left(1 - e^{-\varsigma_p \frac{P_{r,sno}dt}{In_{S_{WE}}^{M}}}\right)\,, \qquad (222)$$

where ς_p $[-]$ is the canopy-leaf contact area per unit area of ground, which for no wind condition is proportional to canopy coverage and in high wind speeds is 1 (*Pomeroy et al.*, 1998b). For simplicity, $\varsigma_p = 1$ is assumed for any condition. The term $P_{r,sno}$ $[mm\ h^{-1}]$ is the snowfall on the canopy (considered equal to the open-area snowfall) (Section 7.1). The coefficient c $[-]$ represents the immediate unload of the newly intercepted snow. A value of $c = 0.7$ was found to be appropriate for hourly time-step (*Pomeroy et al.*, 1998a; *Hedstrom and Pomeroy*, 1998).

The snow unloaded from the canopy $U_{In_{S_{WE}}}$ $[mm]$, at each time step is calculated using a linear reservoir model as first proposed by *Hedstrom and Pomeroy* (1998).

The value of $U_{In_{SWE}}$ for cold conditions is:

$$U_{In_{SWE}}(t) \quad = \quad \left(1 - e^{-\overline{u}dt}\right) In^{b}_{SWE}(t)\,. \tag{223}$$

where $\overline{u} = 4.1\ 10^{-3}\ h^{-1}$ is a reference parameter obtained from the sensitivity analysis of *Hedstrom and Pomeroy* (1998). Eq. (223) is valid for cold conditions and the wind speed is not considered in the unloading process (*Hedstrom and Pomeroy*, 1998). All the mechanisms for unloading of intercepted snow increase dramatically for wet-snow conditions. Therefore, when the atmospheric dew point temperature, T_{dew} $[°C]$, exceeds 0 $°C$ and the wind speed, u_a is greater than 0.5 $m\ s^{-1}$ the intercepted snow in the canopy is considered to be sufficiently ventilated to be isothermal at 0 $°C$ and as suggested by *Gelfan et al.* (2004) is completely unloaded, i.e., $U_{In_{SWE}}(t) = In^{b}_{SWE}(t)$. This mechanism is consistent with the unloading criteria underlined by *Storck et al.* (2002), it is physically meaningful and computationally simple.

The canopy snow interception capacity In^{M}_{SWE} $[mm]$ is calculated following *Hedstrom and Pomeroy* (1998). The interception capacity of snow, In^{M}_{SWE}, depends on the plant area index PAI and on the maximum snow load per unit of plant area, $Sp_{sno,In}$ $[kg\,m^{-2}]$ or equivalently $[mm]$:

$$In^{M}_{SWE} \quad = \quad Sp_{sno,In} \sum_{i=1}^{n_c} \Big[C_{crown}[PAI(H_v)]\Big]\,, \tag{224}$$

where $Sp_{sno,In}$ is composed of a mean specie value $\widehat{Sp}_{sno,In}$ corrected by a function that depends on snow density, ρ_{sno} $[kg\,m^{-3}]$. Since the snow density of the intercepted snow is not explicitly resolved, it is always assumed to be the that of a theoretical new snowfall, ρ^{new}_{sno} (Section 7.5):

$$Sp_{sno,In} \quad = \quad \widehat{Sp}_{sno,In} \left(0.27 + \frac{46}{\rho^{new}_{sno}}\right)\,. \tag{225}$$

Field observations have suggested values of $\widehat{Sp}_{sno,In}$ between 5.9-6.6 $[mm\ m^2\ ground\ area\ m^{-2}\ leaf\,area]$ (*Schmidt and Gluns*, 1991).

7.4 Snowpack water content

During the ripening phase, liquid water is retained in snowpack by surface-tension forces until snow reaches its liquid holding capacity. Generally, the outflow rate from snowpack W_{rs} $[mm]$, is determined through Darcy's law accounting also for capillary forces (*Tarboton and Luce*, 1996; *Essery et al.*, 1999; *Zanotti et al.*, 2004). In order to avoid excessive computational efforts, a simple "bucket" model to describe the dynamics of the water content in the snowpack, Sp_{wc} $[mm]$ is used. The bucket approach provides outflow W_{rs}, when the maximum holding capacity Sp^{M}_{wc} $[mm]$, is exceeded (*Wigmosta et al.*, 1994; *Belair et al.*, 2003). The maximum holding capacity of the snowpack Sp^{M}_{wc} is calculated as a function of snow water equivalent,

S_{WE} $[mm]$ and specific holding capacity coefficient c^R $[-]$ that, in turn, depends on snow density ρ_{sno} $[kg\,m^{-3}]$. The equations first proposed by *Belair et al.* (2003) are used:

$$\begin{aligned}
Sp_{wc}^M &= c^R\, S_{WE}\,, && (226)\\
c^R &= c^R_{min}\Big(\rho_{sno} \geq \rho_e\Big) + \\
&\Big(c^R_{min} + (c^R_{max} - c^R_{min})\frac{\rho_e - \rho_{sno}}{\rho_e}\Big)\Big(\rho_{sno} < \rho_e\Big)\,, && (227)
\end{aligned}$$

where the snow density is defined in Section 7.5, the minimum specific holding capacity coefficient is $c^R_{min} = 0.03$ $[-]$, the corresponding maximum is $c^R_{max} = 0.1$ $[-]$, and the density threshold is $\rho_e = 200$ $[kg\,m^{-3}]$. The release of water from snowpack starts when snowpack water content Sp_{wc} exceeds Sp^M_{wc}. Once the process reaches this threshold, the output phase begins and melted water W_{rs} flows out of snowpack. The released water is: $W_{rs} = (Sp_{wc} - Sp^M_{wc})$.

The balance of snowpack water content Sp_{wc} results from the sum of snowmelt and liquid precipitation entering the snowpack, less W_{rs}:

$$\begin{aligned}
Sp_{wc}(t) &= Sp_{wc}(t-dt) + S_m + P_{r,liq}(t)dt\Big[1 - (1 - C_{sno,w})C_{wat} \\
&-\Big[\sum_{i=1}^{n_c} C_{crown}C_{fol,H_v}\Big]\big(1 - d_{w,sno}\big)\Big] - W_{rs}\,, && (228)
\end{aligned}$$

where C_{fol,H_v} $[-]$ is the fractional vegetation cover for the *high-vegetation* layer (Section 9.1).

The snowpack water content is considered to be in a liquid state, when the surface temperature T_{sno} is larger than -0.01 $°C$, where -0.01 is used instead to avoid numerical instability of jumping at every time step between liquid and frozen snowpack water. It is in a frozen state otherwise, i.e., no intermediate states are considered. Consequently, the heat released from the melting (negative) or the freezing (positive) of this water, Q_{fm} $[W\ m^{-2}]$, is estimated as:

$$\begin{aligned}
Q_{fm}(t) &= f_{sp}\frac{\lambda_f\,\rho_w\,Sp_{wc}(t-dt)}{1000\,dt}\,,\\
&\qquad \text{if } T_{sno}(t) < -0.01 \text{ and } T_{sno}(t-dt) \geq -0.01\,, && (229)\\
Q_{fm}(t) &= f_{sp} - \frac{\lambda_f\,\rho_w\,Sp_{wc}(t-dt)}{1000\,dt}\,,\\
&\qquad \text{if } T_{sno}(t) \geq -0.01 \text{ and } T_{sno}(t-dt) < -0.01\,, && (230)
\end{aligned}$$

where $\rho_w = 1000$ $[kg\ m^{-3}]$ is the density of water, $\lambda_f = 333700$ $[J\ kg^{-1}]$ is the latent heat of melting-freezing, dt $[s]$ is the time step and $f_{sp} = 5/S_{WE}$ $[-]$ with $f_{sp} \leq 1$ is the fraction of snowpack water content involved in freezing/melting transformations, assumed to be the total water for snowpack less than 5 $[mm]$ and a smaller fraction for thick snowpacks. This solution avoids creating huge and and unrealistic energy fluxes when a large amount of water is present in a deep snowpack. Without any phase change, the flux $Q_{fm} = 0$.

7.5 Snow depth and density

The density of snow is assumed to be constant with depth to avoid complex depth-dependent parameterizations and be consistent with the single snowpack layer (*Douville et al.*, 1995). The snow density, ρ_{sno} $[kg\ m^{-3}]$, evolves in time according to the conceptual formulation first proposed by *Verseghy* (1991) (see also *Douville et al.*, 1995; *Essery et al.*, 1999). The original procedure has been successively improved by *Belair et al.* (2003). In this modified formulation, snow density increases due to gravitational settling, following an exponential function of time and is updated when fresh snow falls on the snowpack. The mechanism of compaction due to the weight of new snow falling in the existing snowpack is neglected (*Anderson and Crawford*, 1964) .

The snow density is calculated as:

$$\begin{aligned} \rho'_{sno} &= \rho^{M}_{sno} - \left[\rho^{M}_{sno} - \rho_{sno}(t-dt)\right] e^{\left(-\tau_f \frac{dt}{\tau_1}\right)} \,, \text{ if } \rho_{sno}(t-dt) < \rho^{M}_{sno} \,, && (231) \\ \rho'_{sno} &= \rho_{sno}(t-dt) \,, \qquad \text{if } \rho_{sno}(t-dt) \geq \rho^{M}_{sno} \,, && (232) \end{aligned}$$

where ρ'_{sno} $[kg\ m^{-3}]$ is an intermediate value of snow density, ρ^{M}_{sno} $[kg\ m^{-3}]$ is the maximum snow density, $\tau_f = 0.24$ $[-]$, and $\tau_1 = 86400$ $[s]$ are parameters proposed by *Verseghy* (1991) (see also Section 4.2.6), and dt $[s]$ is the time step. The maximum density of snow ρ^{M}_{sno} depends on snow depth and melting conditions (*Belair et al.*, 2003):

$$\begin{aligned} \rho^{M}_{sno} &= \frac{1000}{\rho_w}\left[\rho^{M1}_{sno} - \frac{20.47}{S_{dep}}\left(1 - e^{-\frac{S_{dep}}{0.0673}}\right)\right] \,, \quad \text{if } S_{m1} > 0 \,, && (233) \\ \rho^{M}_{sno} &= \frac{1000}{\rho_w}\left[\rho^{M2}_{sno} - \frac{20.47}{S_{dep}}\left(1 - e^{-\frac{S_{dep}}{0.0673}}\right)\right] \,, \quad \text{if } S_{m1} = 0 \,, && (234) \end{aligned}$$

where $\rho_w = 1000$ $[kg\ m^{-3}]$ is the density of water, S_{dep} $[m]$ is the snow depth, S_{m1} $[mm]$ is the snow melt from the snowpack and ρ^{M1}_{sno}, ρ^{M2}_{sno} $[kg\ m^{-3}]$ are the maximum density allowed for snow in melting and freezing conditions, respectively. Typical values for these parameters are $\rho^{M1}_{sno} = 500 - 600$ and $\rho^{M2}_{sno} = 300 - 450$ (*Dingman*, 1994; *Essery et al.*, 1999; *Belair et al.*, 2003). Values of $\rho^{M1}_{sno} = 580$ and $\rho^{M2}_{sno} = 300$ are typically used in T&C. The intermediate value of snow density, ρ'_{sno}, is used to update the snow density. When a new snowfall occurs, snow density decreases due to fresh snow. The updated value of ρ_{sno} becomes:

$$\rho_{sno} = \frac{\rho^{new}_{sno} P_{r,sno}(t)dt + \rho'_{sno} S_{WE}(t-dt)}{P_{r,sno}(t)dt + S_{WE}(t-dt)} \,, \tag{235}$$

where $P_{r,sno}$ $[mm\ h^{-1}]$ is the snow precipitation, S_{WE} $[mm]$ is the snow water equivalent in the snowpack, dt in $[h]$, and the fresh snow density, ρ^{new}_{sno} $[kg\ m^{-3}]$, is calculated as (*Bras*, 1990):

$$\rho^{new}_{sno} = 1000\left[0.05 + \left(\frac{1.8\,T_a + 32}{100}\right)^2\right] \,, \tag{236}$$

where T_a is in $[^\circ C]$. Note that without a new snowfall, ρ_{sno} is simply equal to ρ'_{sno}.

The snow depth, S_{dep} $[m]$, is calculated from the snow water equivalent and snow density as:

$$S_{dep} = 0.001\, S_{WE}(t)\, \frac{\rho_w}{\rho_{sno}} \,. \tag{237}$$

Finally, presence of snow on the ground also changes the roughness of the surface z_{om} $[m]$, (Section: 6.1.3). A new roughness length, z_{om}, in the presence of snow is re-evaluated as in *Strack et al.* (2004), weighting vegetation and snow roughness on the basis of snowpack and plant heights:

$$z_{om} = z_{om,veg} \max\left[0, \left(1 - \frac{S_{dep}}{H_c}\right)\right] + z_{om,sno} \min\left[1, \frac{S_{dep}}{H_c}\right] , \tag{238}$$

where $z_{om,veg}$ $[m]$ and $z_{om,sno}$ $[m]$ are the roughness of vegetation and snow in a open field (Section 6.1.3), H_c $[m]$ is the vegetation height, and S_{dep} in $[m]$. The relationship $z_{oh} = z_{ow} = 0.1 z_{om}$ continues to hold true.

8 Ice hydrology

8.1 Ice energy and mass balance

Ice cover ($C_{ice} = 1$) is either caused by the presence of a glacier or because a water surface freezes ($C_{ice,w} = 1$). Note that C_{ice} is a model variable and not a parameter, therefore another land-cover (e.g., bare soil or rocks) must be specified underneath the ice layer. Ice is considered as a unique storage of water equivalent I_{WE} $[mm]$ with a single prognostic surface temperature T_{ice} computed for each element covered by ice. The energy and mass budget follows identical physical principles of the snowpack energy and mass budget (Section 7.2). Ice melted water cumulates in a ice water storage Ip_{wc}, $[mm]$ and can be released in form of water flux W_{ri} $[mm]$ at the bottom of the ice layer.

The temperature variation of the ice in absence of melting is controlled by heat transfer as:

$$dT_{sno} = \frac{1000\, dQ\, dt}{c_i\, \rho_w I^b_{WE}} \,, \tag{239}$$

where dt $[s]$ is the time step, dQ $[W\ m^{-2}]$ is the net energy flux input to the ice, c_i $[J\ kg^{-1}\ K^{-1}]$ is the specific heat of ice, ρ_w $[kg\ m^{-3}]$ is the density of water, and I^b_{WE} $[mm]$, is the water mass equivalent of ice before accounting for melting. Note that in glaciers the water mass of ice in a given point could be several meters (even hundreds of meters) and since we do not solve the ice profile temperature, we need to consider only the upper part of the ice layer, which contributes to the surface energy budget. Therefore, an upper limit to I^b_{WE} equal to 2000 mm is imposed in the model for convenience. This implies that only the upper 2 m of ice water equivalent in a glacier contributes to energy exchanges, which is a realistic approximation considering that temperature fluctuations below this depth are minor. The difference $dT_{ice} = T_{ice}(t) - T_{ice}(t - dt)$ $[°C]$ is the change in the average temperature of the ice layer (or approximately upper 2 m of ice, if $I^b_{WE} > 2000$).

During ice melting periods, the ice remains isothermal at the temperature of melting point, $T_{ice} = 0$ $[°C]$. Therefore, additional energy inputs cause some of the ice to change phase from ice to water:

$$I_m = \frac{1000dQ}{\lambda_f \rho_w}, \tag{240}$$

where $\lambda_f = 333700$ $[J\ kg^{-1}]$ is the latent heat of melting of ice at 0 $[°C]$, and I_m $[mm]$ is the ice water equivalent converted to liquid water. During the melting phase, liquid water is retained in the ice and can be released either because the cracks in the ice pack are saturated or through fractures in the ice (e.g., moulins and crevasses). In this case the melt-water flows out of the ice.

The net energy flux input to the ice, dQ $[W\ m^{-2}]$, is calculated by considering the sources of incoming and outgoing heat in the energy balance equation:

$$dQ(T_{ice}) = R_n(T_{ice}) + Q_v(T_{ice}) - H(T_{sno}) - \lambda E(T_{ice}) - G(T_{ice}), \tag{241}$$

where R_n $[W\ m^{-2}]$ is net radiation energy absorbed by the ice, Q_v $[W\ m^{-2}]$ is incoming heat with precipitation, G $[W\ m^{-2}]$ is ground heat flux from ice to the soil or at the bottom of the 2 m ice if $I^b_{WE} > 2000$, H $[W\ m^{-2}]$ is the sensible heat flux from ice, λE $[W\ m^{-2}]$ is the latent heat flux from ice. The heat released from melting or freezing of liquid water held in the ice is not accounted for, since melted water is considered to percolate deep enough to avoid re-freezing near the surface.

Ice mass I_{WE} $[mm]$ is updated conserving the mass balance:

$$I^b_{WE}(t) = I_{WE}(t - dt) + {I_{WE}}^N(t) - \tilde{E}_{ice}(t)dt, \tag{242}$$

$$I_{WE}(t) = I^b_{WE}(t) - I_m(t), \tag{243}$$

where ${I_{WE}}^N$ $[mm]$ is the new ice mass formed at the time step dt $[h]$, $\bar{E}_{ice}$ $[mm\ h^{-1}]$ is evaporation-sublimation from the ice. The term $\tilde{E}_{ice}$ is from Eq. (92) and accounts for evaporation-sublimation from ice:

$$\tilde{E}_{ice} = C_{ice}(1 - (1 - C_{ice,w})C_{wat})E_{ice}, \tag{244}$$

where the symbols are defined in Section 5.4. Note that ice evaporation can occur from a water surface if it is frozen ($C_{ice,w} = 1$).

New ice I^N_{WE} can be generated in two ways, (i) if there is old snow and snow density is above a prescribed threshold $\rho_{ice,th}$ $[kg\ m^{-3}]$; (ii) if a water surface freezes. In the first case the new ice is subtracted from the snowpack water equivalent S_{WE}. A threshold $\rho_{ice,th} = 500$ is typically assumed, which correspond to a snow to firn transition (*Cuffey and Paterson*, 2010). Additionally, the conversion occurs with a constant rate of 0.037 $[mm\ h^{-1}]$, which is derived from long-term observations of ice formation processes (*Cuffey and Paterson*, 2010):

$$I_{WE}{}^{N} = \min\bigl[S_{WE}, 0.037dt\bigr]\,, \text{ if } \rho_{sno} > \rho_{ice,th}\,, \quad (245)$$

$$I_{WE}{}^{N} = 0\,, \qquad \text{if } \rho_{sno} \leq \rho_{ice,th}\,. \quad (246)$$

Alternatively, I_{WE}^{N} can be generated when a lake freezes and it is subtracted from the water storage WAT (Section 10). In this second case:

$$I_{WE}{}^{N} = C_{wat}\,\Delta z_{ice}\,dt\,, \qquad \text{if } S_{dep} < 0.1 \text{ and } T_{ice} < 0\ \ , \quad (247)$$

$$I_{WE}{}^{N} = C_{wat}\,\frac{\Delta z_{ice}}{5}\,dt\,, \qquad \text{if } S_{dep} \geq 0.1\,, \quad (248)$$

where S_{dep} is in m and Δz_{ice} $[mm\ h^{-1}]$ is a ice formation rate, with a typical value $\Delta z_{ice} = 0.54$ (*Yang et al.*, 2012). Note that ice formation process is assumed to be five time slower when the frozen water is covered by a insolating layer of snow. Eq. (247) is a coarse conceptualization of the ice formation process over a lake, which computation would require the solution of the lake temperature profile (e.g., *Subin et al.*, 2012).

All of the quantities in Eq. (241) are functions of the surface temperature, T_{ice} that is an unknown and T_{ice} also depends on the ice mass balance. Equivalently to the computation of the snow energy budget in Section 7.2, an iterative numerical solution has been developed to solve for T_{ice} that satisfies the energy and mass balances.

8.2 Ice water content and depth

A linear reservoir model is used to describe the dynamics of the water content in the ice Ip_{wc} $[mm]$. The linear reservoir approach generates outflow W_{ri} proportionally to Ip_{wc} and when the maximum holding capacity Ip_{wc}^{M} $[mm]$ is exceeded. The maximum holding capacity of the ice $Ip_{wc}^{M} = c^{R2} I_{WE}$ is a function of the ice water equivalent I_{WE} $[mm]$, and of a specific holding capacity coefficient c^{R2} $[-]$, which is a model parameter, typically $c^{R2} = 0.01$, i.e., storage capacity in the ice pack is expected to be 1% of the ice water equivalent.

The balance of the ice water content Ip_{wc} is the sum of ice-melt and liquid precipitation minus the water released by the snowpack W_{ri} $[mm]$ that is the sum of saturation excess of the ice pack and of a reservoir outflow:

$$\begin{aligned} Ip_{wc}(t) &= Ip_{wc}(t-dt) + I_m + P_{r,liq}(t)dt[1 - C_{sno}]\,\cdot \\ &\quad \Bigl(1 - (1 - C_{ice,w})C_{wat} - \sum_{i=1}^{n_c} C_{crown} C_{fol,H_v}\Bigr) - W_{ri}\,, \end{aligned} \quad (249)$$

where the symbols have been previously defined (Section 5 and 9.1). The release of water from ice can occur when the water content, Ip_{wc}, exceeds Ip_{wc}^{M}, and through a linear reservoir outflow I_{out} $[mm\,h^{-1}]$ of the liquid water in the ice:

$$\begin{aligned} W_{rs} &= (Sp_{wc} - Sp_{wc}^{M}) + I_{out}dt\,, && (250)\\ I_{out} &= \frac{Ip_{wc}}{K_{ice}}\,, && (251) \end{aligned}$$

where $K_{ice} = I_{WE}/1000$ $[h]$ is the reservoir constant assumed to be proportional to the ice storage. An average percolation velocity of 1 $m\,h^{-1}$ is used as temporal scale to transfer water vertically through the entire ice column. The ice melted water, W_{ri}, flows out of snowpack and can eventually infiltrate or run off in the underlying soil or rock, which must be parameterized, since glaciers are not a prescribed land-cover but they occur above another land-cover when $I_{WE} > 0$ and therefore $C_{ice} = 1$.

The density of ice is assumed to be constant with depth and equal to $\rho_{ice} = 916.2$ $[kg\ m^{-3}]$. Therefore, the ice depth, I_{dep} $[m]$, is calculated from the ice water equivalent as:

$$I_{dep} = 0.001\,I_{WE}(t)\,\frac{\rho_w}{\rho_{ice}}\,. \qquad (252)$$

9 Interception and water influx to the soil

The interception of rainfall by vegetation canopies has long been considered as a significant hydrological process (*Horton*, 1919). This process modifies the water balance at the surface, since water retained on leaves evaporates back into the atmosphere in the form of latent heat (*Mahfouf and Jacquemin*, 1989). Interception can be an important fraction of precipitation in temperate humid climates with frequent drizzles (*Link et al.*, 2004; *Savenije*, 2004; *Gerrits et al.*, 2007).

Interception can be partitioned into canopy, and forest floor interception storages (even though traditionally, the term refers only to the former type). Canopy interception considers water retained by leaves and stems; forest floor interception considers water trapped by litter and dead vegetation biomass.

Both types of interception are calculated in T&C. Additionally, since up to two vertical layers of vegetation are considered, canopy interception is simulated for both *high-vegetation* and *low-vegetation.*

9.1 Throughfall

Precipitation can be either intercepted by canopy or it can fall on the ground as throughfall flux and stem flow. In order to distinguish between intercepted precipitation and free fall, a fractional vegetation cover is introduced. The fractional vegetation cover C_{fol} $[m^2\ obstracted\ area\ m^{-2}\ \ VEG\,area]$, represents the fraction $[0-1]$ of the area occupied by leaves, dead-leaves and stems projected on the ground in the vertical direction and is different from C_{crown} or LAI. The fractional cover of litter C_{litter} $[m^2\ litter\ area\,m^{-2}\ \ VEG\,area]$ is a variable $[0-1]$, which indicates how much area is actually covered by litter and it is different from the litter area index $L_{litter} = S_{litter}B_{litter}$ $[m^2 litter\ m^{-2} ground]$. The terms C_{fol} and C_{litter} are computed for each C_{crown} and are used for the evaluation of canopy and litter interception. C_{litter} is different from zero only when the biogeochemistry module is activated. The variable C_{fol} is a function of plant area index, $PAI = LAI + SAI + LAI_{dead}$ $[m^2 \; plant \; area \; m^{-2} \; VEG \, area]$. Following *Mahfouf and Jacquemin* (1989), we use the following empirical relationships:

$$C_{fol} = 1 - e^{-\kappa(PAI)}, \tag{253}$$

$$C_{litter} = 1 - e^{-\kappa(L_{litter})}, \tag{254}$$

with $\kappa = 0.75$ $[-]$ as suggested by *Ramírez and Senarath* (2000).

Once C_{fol} is defined, the fraction of rain that falls through canopy gaps is $P_r(1 - C_{fol})$ $[mm \; h^{-1}]$, and the intercepted fraction is $P_r \; C_{fol}$ $[mm \; h^{-1}]$. According to Figure 27, rainfall reaching vegetated surface in the *high* and *low-vegetation* layers, respectively, are P_{r,H_v} and P_{r,L_v} $[mm \; h^{-1}]$:

$$P_{r,H_v} = C_{crown} P_{r,liq}(1 - d_{w,sno}), \tag{255}$$

$$P_{r,L_v} = [1 - C_{sno}][1 - C_{ice}][(1 - C_{fol,H_v})P_{r,H_v} + Dr_{H_v}], \tag{256}$$

where the respective intercepted fluxes can be calculated by multiplying P_{r,H_v} and P_{r,L_v} by C_{fol,H_v} and C_{fol,L_v}, respectively, (see Figure 27). Later in the text, the terms P_{r,H_v} and P_{r,L_v} are generally indicated as $P_{r,fol}$ (i.e., without specifying the layer). The quantity Dr_{H_v} $[mm \; h^{-1}]$ is the total drainage from *high-vegetation* layer (Section 9.3).

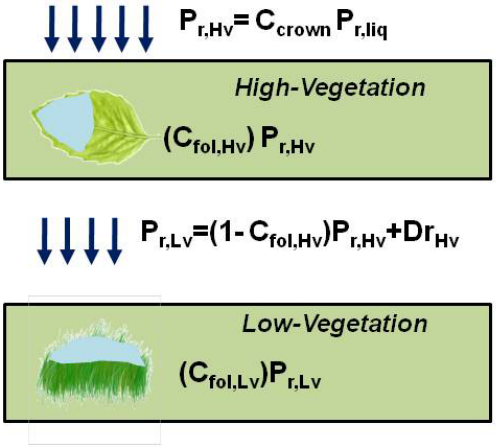

Figure 27: An illustration of rainfall interception with two vegetation layers, *high* and *low-vegetation*, in the absence of snow. The terms P_{r,H_v} and P_{r,L_v} represent precipitation reaching the two layers. All of the other terms are defined in the text.

It must be added that since n_c different *Crown Areas* can be simultaneously present within a computational element, the calculation of interception is made independently for each *Crown Area*.

9.2 Canopy storage capacity

The maximum possible water interception in a leaf layer, called also canopy storage capacity, In^M [mm] is calculated with the approach proposed by *Dickinson et al.* (1993):

$$In^M = S_{p,In}(LAI + SAI + LAI_{dead}) \,, \tag{257}$$

where $S_{p,In}$ [$mm\, m^2\, VEG\, area\, m^{-2}\, plant\, area$] is the specific water retained by a vegetated surface function of the specific vegetation type. The assumption made in Eq. (257) is that a plant cannot retain more than In^M of liquid water. This relation is perhaps oversimplified because other factors such as wind speed can influence the interception (*Mahfouf and Jacquemin*, 1989). Nevertheless, Eq. (257) has been widely applied in land surface and hydrological models (*Noilhan and Mafhouf*, 1996; *Oleson et al.*, 2004; *Ivanov et al.*, 2008b). Typical values of $S_{p,In}$ between 0.1-0.4 [mm] with a reference value of 0.2 [mm] have been proposed in the literature (*Rutter et al.*, 1975; *Mahfouf and Jacquemin*, 1989).

9.3 Model of interception

Canopy interception, In [mm], in each *Crown Area*, C_{crown}, and separately for two vegetation layers is estimated using the Rutter model (*Rutter et al.*, 1971, 1975; *Mahfouf and Jacquemin*, 1989; *Eltahir and Bras*, 1993; *Ivanov et al.*, 2008b). The equation describing interception storage dynamics is:

$$\frac{dIn}{dt} = P_{r,fol} - Dr - E_{In} \,. \tag{258}$$

Equation (258) is a non-linear ordinary differential equation that cannot be solved analytically. In order to avoid the efforts of the numerical integration, a finite difference approximation of Eq. (258) is used, where the numerical updates due to precipitation and evaporation are considered first and successively the drainage term is added:

$$In_t(t) = In(t - dt) + P_{r,fol}(t)dt - E_{In}(t)dt \,, \tag{259}$$

$$In(t) = In_t(t) - Dr(t)dt \,, \tag{260}$$

where dt [h] is the time step, In and In_t [mm] are the intercepted water, and a temporary value of intercepted water, respectively. The flux E_{In} [$mm\ h^{-1}$] is the evaporation rate from wetted fraction of canopy estimated using equations (100)-(102). When E_{In} is negative, it is considered as dew on the foliage. The quantity $P_{r,fol}$ [$mm\ h^{-1}$] is the rainfall rate falling in the vegetation. $P_{r,fol}$ is a function of the vegetation layer, i.e., $P_{r,fol} = P_{r,H_v}$ or $P_{r,fol} = P_{r,L_v}$ (Section 9.1). The flux Dr [$mm\ h^{-1}$] is the canopy drainage, sum of the dripping from the canopy Dr_d [$mm\ h^{-1}$] and of the drainage from saturation excess Dr_s [$mm\ h^{-1}$]. Dripping from canopy Dr_d is calculated as in the Rutter model:

$$Dr_d = K_c e^{g_c(In_t - In^M)}, \tag{261}$$

where K_c $[mm\ h^{-1}]$ and g_c $[mm^{-1}]$ are the drainage rate coefficient and exponential decay parameter, and In^M $[mm]$ is the is the maximum interception capacity (Section 9.2). Since the drainage rate coefficient and the exponential decay parameter have a limited range of variability, prescribed values, i.e. $K_c = 0.06$ $[mm\ h^{-1}]$ and $g_c = 3.7$ $[mm^{-1}]$ are used (*Rutter et al.*, 1971; *Mahfouf and Jacquemin*, 1989). Note that the intercepted water In $[mm]$, must be always inferior to the maximum interception capacity In^M. Consequently, when this value is exceeded a storage excess drainage, Dr_s $[mm\ h^{-1}]$, is computed:

$$Dr_s = \frac{(In_t - In^M)}{dt}(In > In^M), \tag{262}$$

with dt $[h]$ time step.

9.4 Influx of water to soil

The influx of water q_{ins} $[mm\ h^{-1}]$ at the soil surface can be a sum of several components: direct rainfall in non-vegetated areas, throughfall below two vegetation layers, water released from snowpack, drainage of intercepted water, and dew. An external flux, the runon q_{runon} $[mm\ h^{-1}]$ is another possible contribution to the flux q_{ins}. Furthermore, q_{ins} can be partitioned in the influx of water to soil in vegetated areas $q_{ins,veg}$ and in bare-soil areas $q_{ins,bs}$, with $q_{ins} = q_{ins,veg} + q_{ins,bs}$. It follows that:

$$\begin{aligned}
q_{ins,veg} &= [1 - C_{sno}][1 - C_{ice}]\sum_{i=1}^{n_c}\Big[\big(P_{r,liq}C_{crown,i}(1 - C_{fol,H_v,i}) + Dr_{H_v,i}\big)\big(1 - C_{fol,L_v,i}\big) + Dr_{L_v,i}\Big] + \\
&\quad \sum_{i=1}^{n_c} C_{crown,i}\big(\frac{W_{rs}}{dt}(1 - C_{ice}) + \frac{W_{ri}}{dt}\big)[1 - C_{rock} - C_{wat}] + \\
&\quad \sum_{i=1}^{n_c}(Dr_{H_v,i} + Dr_{L_v,i})\, max[C_{sno}, C_{ice}] + \sum_{i=1}^{n_c} C_{crown,i}\, q_{runon}\, dt[1 - C_{rock} - C_{wat}]\,. \qquad (263)\\
q_{ins,bs} &= P_{r,liq}C_{bare}[1 - C_{sno}][1 - C_{ice}] + \\
&\quad \big(1 - \sum_{i=1}^{n_c} C_{crown,i}\big)\big(\frac{W_{rs}}{dt}(1 - C_{ice}) + \frac{W_{ri}}{dt}\big)[1 - C_{rock} - C_{wat}] + \\
&\quad \big(1 - \sum_{i=1}^{n_c} C_{crown,i}\big) q_{runon}\, dt[1 - C_{rock} - C_{wat}]\,. \qquad (264)
\end{aligned}$$

If there is still liquid canopy drainage Dr in the presence of snow or ice, this is contributing directly to the influx of water to the soil ($q_{ins,veg}$) as a necessary condition to conserve mass. Runon for a given element is estimated as the sum of surface runoff produced in neighboring elements that contribute their flow to a considered element following the imposed drainage pattern and is considered to be distributed in vegetated and non-vegetated areas proportionally to their sizes.

9.5 Litter interception

The litter intercepted water In_{Litter} $[mm]$ is replenished by the influx of water in the vegetated patches, which falls in the fractional area occupied by litter at the element scale $\overline{C_{litter}} = \left(1 - \sum_{i=1}^{n_c} C_{crown,i} C_{litter}\right)$ and depleted by the evaporation from litter E_{Litter}:

$$In_{Litter}(t) = In_{Litter}(t-dt) + \overline{C_{litter}} q_{ins,veg}(t) - E_{Litter}(t)dt \,. \qquad (265)$$

Intercepted water on the litter has an upper limit, which is the maximum litter interception capacity In_{Litter}^{M} $[mm]$ and is calculated as the difference between the maximum and minimum litter storage $L_{sto,cap,max}$ and $L_{sto,cap,min}$.:

$$In_{Litter}^{M} = \sum_{i=1}^{n_c} C_{crown,i} \left(L_{sto,cap,max} - L_{sto,cap,min}\right) \,. \qquad (266)$$

The maximum and minimum storage capacity of litter are related to the litter biomass B_{litter} (*Putuhena and Cordery*, 1996; *Sato et al.*, 2004): $L_{sto,cap,max} = 0.8B_{litter}$ and $L_{sto,cap,min} = 0.1B_{litter}$. Note that the litter intercepted water, In_{Litter} must be always inferior to the maximum interception capacity In_{Litter}^{M}. Consequently, when this value is exceeded a litter storage excess drainage, SE_{Litter} $[mm\ h^{-1}]$, is computed. Therefore in presence of litter the q_{ins} becomes:

$$q_{ins} = SE_{Litter} + (1 - \overline{C_{litter}}) q_{ins,veg} + q_{ins,bs} \,, \qquad (267)$$

When the biogeochemistry module is deactivated $B_{litter} = 0$, $\overline{C_{litter}} = 0$, and there is not litter interception $In_{Litter} = 0$.

9.6 Water logging and ponding

Even in absence of an explicit water surface (i.e., $C_{wat} = 0$), there could be a storage of water at the land-surface in ponds, puddles, surface micro-depressions (*Kamphorst et al.*, 2000), or simply because surface runoff is generated during an intense storm. The presence of runon at the previous time step $q_{runon}(t-dt)$ identifies this type of situations and modifies the evaporation fluxes. In fact, if $q_{runon}(t-dt) > 0$ at the ground, then priority is given to evaporation from this ponding water and the term E_{wat} is computed even if $C_{wat} = 0$. Concurrently, the evaporation fluxes E_{Litter}, E_{bare}, and E_g are suppressed until there is water above the surface.

The presence of ponding water also changes the roughness of the surface z_{om} $[m]$. A new roughness length z_{om} in the presence of ponding water is re-evaluated as done for snow (Section 7.5), weighting vegetation and water roughness on the basis of water and plant heights:

$$z_{om} = z_{om,veg} \max\left[0, \left(1 - \frac{y_{dep}}{H_c}\right)\right] + z_{om,wat} \min\left[1, \frac{y_{dep}}{H_c}\right] \,, \qquad (268)$$

where $z_{om,veg}$ $[m]$ and $z_{om,wat}$ $[m]$ are the roughness of vegetation and water (Section 6.1.3), H_c $[m]$ is the vegetation height, and y_{dep} is the ponding water in $[m]$. The relationship $z_{oh} = z_{ow} = 0.1 z_{om}$ continues to hold true.

10 Rocks and Water

In case of exposed rocks ($C_{rock} > 0$) a film of water can be intercepted by rock surfaces In_{rock} $[mm]$. Incoming water is supplied by precipitation, water released by the snowpack W_{rs} or ice W_{ri} and runon, q_{runon} and depleted by the evaporation from rocks E_{rock} and leakage $L_{k,rock}$ $[mm\ h^{-1}]$ if the rock is fractured:

$$\begin{aligned} In_{rock}(t) &= In_{rock}(t-dt) + C_{rock}[1-C_{sno}][1-C_{ice}]P_{r,liq}dt + \\ &\left(\frac{W_{rs}}{dt}(1-C_{ice}) + \frac{W_{ri}}{dt}\right)[C_{rock}] + q_{runon}dt[C_{rock}] - E_{rock}dt - L_{k,rock}dt\,. \end{aligned} \tag{269}$$

The interception capacity of rocks, In^M_{rock} is a model parameter, with typical values of $In^M_{rock} = 0.05 - 0.2$ mm. When this value is exceeded, standing water is consider to run off from rocks as SE_{rock} $[mm\ h^{-1}]$. The leakage from rocks $L_{k,rock}$ is simply computed as the minimum between the intercepted water in rocks In_{rock}/dt and the hydraulic conductivity of rocks K_{rock} a constant model parameter, which value is basically zero for compacted rocks and can be different from zero for fractured rocks. A free drainage condition can be also given, in that case In_{rock} is completely infiltrated in the fractured rock and no water remains on the rock surface.

The rock leakage $L_{k,rock}$ supplies the fractured rock water storage F_{rock} $[mm]$. This volume is used for distributed T&C applications to supply water in specified catchment location through $\overline{Q_{sub}}$ and represents a conceptualization of water sources from deep fractured rocks (Section 14). At the plot scale, F_{rock} continuously increases because there is not a sink in Eq. (270). The volume F_{rock} is computed also in absence of exposed rocks (i.e., when $C_{rock} = 0$) and collects the deep leakage from soil L_{kb} (Section 14) and from the bottom of water surfaces (e.g., lakes) $L_{k,water}$:

$$F_{rock}(t) = F_{rock}(t-dt) + (L_{k,rock} + L_{kb} + L_{k,water} - \overline{Q_{sub}})dt\,, \tag{270}$$

where $L_{k,water}$ $[mm\ h^{-1}]$ is computed equally to $L_{k,rock}$ but only when the land-cover is a water-surface $C_{wat} > 0$.

In case of exposed water surfaces ($C_{wat} > 0$), for instance over a lake column, the mass budget of this water WAT $[mm]$ is explicitly computed:

$$\begin{aligned} WAT(t) &= WAT(t-dt) - E_{wat}dt + \left(\frac{W_{rs}}{dt}(1-C_{ice}) + \frac{W_{ri}}{dt}\right)[C_{wat}] + \\ &([P_{r,liq} + P_{r,sno}]dt[1-C_{sno,w}][1-C_{ice,w}])[C_{wat}] + q_{runon}dt[C_{wat}] - L_{k,water}\,. \end{aligned} \tag{271}$$

Open water surface can freeze in the model. Once water is frozen, this is identified by the variable $C_{ice,w} = 1$. For lakes to freeze the condition $T_{wat} < 0$ $[°C]$ is necessary but not sufficient, in fact, surface freezing depends not only on the skin surface but also on the temperature profile and wind speed conditions. To simplify these complex processes, T&C conceptualize ice formation whenever $T_{wat} < \overline{T_{wat,fz}}$, where $\overline{T_{wat,fz}}$ $[°C]$ is a prescribed threshold for water freezing, typically in the order of 0/-10 $[°C]$. Once the water is frozen, snow can accumulate over the ice layer, in this case $C_{sno,w} = 1$. Note that such a conceptualization may be regarded appropriate for small lakes but it can completely fail for large water bodies.

11 Rainfall induced erosion

The evaluation of rainfall induced erosion can be useful in specific model applications since the material displaced by splash erosion is one of the components that contributes to the sediment transport. A module of T&C is dedicated to the evaluation of the erosion rate, E_r $[mm\ h^{-1}]$ or in mass units $[kg\ h^{-1}\ m^{-2}]$. At the element scale only erosion due to rainfall detachment is considered. Other possible erosion mechanisms, such as sheetflow, gully, and river erosion are mostly meaningful at larger scales (e.g., *Francipane et al.*, 2012) and are not implemented yet in the model.

Rainfall detachment is related to the kinetic energy of rainfall. A distinct effect of leaf drainage, and direct throughfall is considered to estimate soil detachment by raindrop impact. This permits to explicitly account for the effects of different vegetation characteristics such as height H_c $[m]$ and fractional vegetation cover C_{fol} $[-]$. It further meets the purpose of including the multiple feedbacks of vegetation at the Earth surface within the model. The free throughfall $P_{r,TR}$ $[mm\ h^{-1}]$ and the drainage from plant $P_{r,LD}$ $[mm\ h^{-1}]$ that reach the ground are:

$$\begin{aligned}
P_{r,TR} &= [1 - C_{sno}] \sum_{i=1}^{n_c} \Big[[1 - C_{litter,i}] P_{r,liq} C_{crown,i} (1 - C_{fol,H_v,i})(1 - C_{fol,L_v,i}) \Big] + \\
&\quad P_{r,liq} C_{bare} (1 - C_{sno}) \,, && (272) \\
P_{r,LD,H_v,i} &= [1 - C_{sno}][1 - C_{litter,i}] \Big[Dr_{H_v,i} (1 - C_{fol,L_v,i}) \Big] \,, && (273) \\
P_{r,LD,L_v,i} &= [1 - C_{sno}][1 - C_{litter,i}] \Big[Dr_{L_v,i} \Big] \,, && (274)
\end{aligned}$$

where $P_{r,LD}$ is subdivided between *low* and *high vegetation* layers. It is further assumed that the water released by the snowpack and icepack, given their natural slow dynamics do not induce erosion, even though this is probably a coarse approximation. The specific kinetic energy of rainfall reaching the ground as direct throughfall, $K_{E,TR}$ $[J\ m^{-2}\ mm^{-1}]$, is assumed to be the same as that of the natural rainfall. This term depends on rainfall intensity and raindrop size. Following *Brandt* (1990) which assumes a raindrop size distribution as described by *Marshall and Palmer* (1948), $K_{E,TR}$ can be evaluated as:

$$K_{E,TR} = 8.95 + 8.44 \log_{10}(P_{r,TR}) \,. \qquad (275)$$

The specific kinetic energy of the leaf and stem drainage, $K_{E,LD}$ $[J\ m^{-2}\ mm^{-1}]$, is estimated using the equation developed experimentally by *Brandt* (1990):

$$K_{E,LD} = 15.8\sqrt{H_c} - 5.87\,, \tag{276}$$

where H_c $[m]$ is the effective plant canopy height. Such a simple relationship is considered valid because, for a wide range of plants, the drop-size distribution of leaf drainage has been found invariant (*Brandt*, 1989). This statement is further reinforced by recent studies where it has been observed that plant architecture does not play an important role in soil detachment due to dripping (*Foot and Morgan*, 2005). This means that the variations in the energy of leaf drainage are solely a function of the impact velocity of the raindrops, which depends on the height of fall. The kinetic energy of leaf drainage is set to zero when the canopy height is less than $H_c < 0.14$ $[m]$ in order to avoid negative values, as suggested by *Morgan et al.* (1998). The total flux of kinetic energy K_E $[J\ m^{-2}\ h^{-1}]$ of rainfall can be calculated multiplying the specific energies obtained from Eq. (275) and (276) by the respective intensities. These *"rainfall"* intensities are the direct throughfall and the leaf drainage from *low* and *high vegetation* layers:

$$\begin{aligned} K_E &= K_{E,TR}P_{r,TR} + \sum_{i=1}^{n_c} K_{E,LD,H_v,i}P_{r,LD,H_v,i} +\,, \\ &\sum_{i=1}^{n_c} K_{E,LD,L_v,i}P_{r,LD,L_v,i}\,. \end{aligned} \tag{277}$$

The same formulation of kinetic energy (Eq. 278) is used in the *LISEM* (*DeRoo et al.*, 1996) and *EUROSEM* (*Morgan et al.*, 1998) models. The total erosion rate, E_r $[kg\ h^{-1}\ m^{-2}]$, due to raindrop detachment in a basic computational element is:

$$E_r = K_E K_{ero}\Big[P_{r,TR} + \sum_{i=1}^{n_c} P_{r,LD,H_v,i} + \sum_{i=1}^{n_c} P_{r,LD,L_v,i}\Big]\,, \tag{278}$$

where K_{ero} $[kg\ h\ J^{-1}\ mm^{-1}]$ is an erodibility factor (Section 12.5) that needs to be multiplied again for the total rainfall intensity. The erosion rate, E_r, can be expressed in height of lost soil $[mm\ h^{-1}]$ dividing per the bulk density of soil, $\rho_d = \rho_{ss}(1-\theta_{sat})$ $[kg\ m^{-3}]$: $E_r = E_r\ 1000/\rho_d$; where θ_{sat} is the soil water content at saturation, and $\rho_{ss} = 2650$ $[kg\ m^{-3}]$ is the solid soil density (Section 12.5). Note that the erodibility factor, K_{ero}, is scaled with the intensity of the rainfall. Since this intensity is already accounted for in the estimation of K_E it would be probably better in successive version of T&C to consider a detachability coefficient, K_{det} $[g\ J^{-1}\ ]$, valid for every rainfall intensity as proposed in other studies (*Morgan*, 2001; *Gumiere et al.*, 2009). Corrections due to the presence of a possible thin sheet of water on the surface that reduces the erosive power of the drops are neglected (*Torri et al.*, 1987; *Wicks and Bathurst*, 1996; *Morgan et al.*, 1998). The uncertainties in the determination of a water depth correction factor are indeed quite large (*Parsons et al.*, 2004).

12 Vadose zone dynamics

The profile of soil moisture $\theta(z)$, where z is the depth, directly influences energy and mass exchanges at the land surface through processes such as ground evaporation, infiltration, runoff generation, lateral subsurface flow, aquifer recharge, and vegetation water uptake.

The influx of water, q_{ins} $[mm\ h^{-1}]$ at the soil surface is the sum of several components as described in Section 9.4. Depending on the magnitude of q_{ins}, the intensity of incoming flux and antecedent soil moisture conditions, the flux may either infiltrate or be excluded, partially or entirely, as surface runoff (*Panday and Huyakorn*, 2004; *Brutsaert*, 2005; *Kollet and Maxwell*, 2006; *Maxwell and Kollet*, 2008).

12.1 Formulation

The 1-D Richards equation (*Hillel*, 1998) is solved in T&C, which assumes locally homogeneous, uniform soil characteristics, and describes the flow of liquid water in variably saturated soils under gravity and capillary forces in isothermal conditions. The basic equation, using the one-dimensional approximation written for the vertical direction, was derived by *Richards* (1931) by combining the Darcy's law with the continuity equation, as:

$$\frac{\partial \theta}{\partial t} = \frac{\partial}{\partial z}\left[K_v(\theta)\frac{\partial \Psi_S(\theta)}{\partial z} + K_v(\theta)\right] - S\,, \qquad (279)$$

where θ $[-]$ is the soil moisture content, $K_v(\theta)$ $[mm\ h^{-1}]$ is the hydraulic conductivity in the vertical direction, $\Psi_S(\theta)$ $[mm]$ is the soil water potential, S $[h^{-1}]$ is the sink term accounting for transpiration, evaporation and lateral transfer fluxes, and t $[h]$ is time.

The Richards equation is a highly nonlinear partial differential equation and its numerical solution is time consuming even in the one-dimensional formulation (*Celia et al.*, 1990; *vanDam and Feddes*, 2000; *Ross*, 2003; *Varado et al.*, 2006; *Miller et al.*, 2006). The 1-D Richards equation is solved in T&C using a finite volume approach with the method of lines (*Lee et al.*, 2004), which discretizes the spatial domain and allows reducing the partial differential equation to a system of ordinary differential equations in time. In order to evaluate soil moisture content θ_i $[m^3\ m^{-3}]$, the soil column is subdivided in $i = 1, ..., n_s$ finite volumes, i.e., the layers (Figure 28). Each layer i is characterized by the depth from the surface to a layer upper boundary, $Z_{s,i}$ $[mm]$, the layer thickness, $d_{z,i}$ $[mm]$, and a distance between the layer center and the preceding layer center, $D_{z,i}$ $[mm]$. The depth Z_{n_s+1} $[mm]$ is the maximum soil depth simulated in the model and can be often assumed to encompass the regolith up to the bedrock boundary. The resulting ordinary differential equations are of the following general form:

$$\begin{aligned} d_{z,i}\frac{d\theta_i}{dt} &= q_{i-1} - q_i - \left(\sum_{j=1}^{n_c} T_{H_v,j}\, r_{H_v,i,j}\right) - \left(\sum_{j=1}^{n_c} T_{L_v,j}\, r_{L_v,i,j}\right) \\ &- \left(\sum_{j=1}^{n_c} E_{g,j}\right) - E_{bare} + Q_{l,in,i} - Q_{l,out,i}\,. \end{aligned} \tag{280}$$

where q_i $[mm\ h^{-1}]$ is the vertical outflow from a layer i, the terms in parentheses quantify moisture sinks in vegetation patches, and n_c is the number of different *crown areas* in a given element. The sinks at the soil surface and in the root zone are due to evapotranspiration process. They can be subdivided into the following components: evaporation from bare soil E_{bare} $[mm\ h^{-1}]$, evaporation from the soil under the canopy E_g $[mm\ h^{-1}]$, and transpiration from high- and low-vegetation layers T_{H_v}, and T_{L_v} $[mm\ h^{-1}]$. The fluxes E_g and E_{bare} are assumed to have access to moisture only in the first $(i = 1)$ soil layer.

The treatment of the fraction of the root biomass contained in a given soil layer, r_i $[-]$ is described in Section 12.2. The lateral outflows $Q_{l,out,i}$ $[mm\ h^{-1}]$, are calculated according to the soil moisture content and the kinematic approximation of lateral head gradient (Section 14). The incoming lateral subsurface fluxes $Q_{l,in,i}$ $[mm\ h^{-1}]$ are the sum of subsurface water fluxes originating in neighboring elements and flowing toward the cell of interest.

In Eq. (279), the vertical outflow from a layer i is:

$$q_i = \overline{K_{v,i}}\left(1 + \frac{\Psi_{S,i} - \Psi_{S,i+1}}{Dz_{i+1}}\right), \tag{281}$$

where $\overline{K_{v,i}}$ $[mm\ h^{-1}]$ is the unsaturated hydraulic conductivity arithmetically averaged between the layers i and $i + 1$, and $\Psi_{S,i}$ $[mm]$ is the soil water potential of layer i. In heterogenous soil conditions, the value of the soil hydraulic properties, at a given depth z_i, are also a function of the layer depth.

Note that the number of computed fluxes q_i is $n_s - 1$ because the inflow to the first soil layer is calculated as infiltration, I_f $[mm\ h^{-1}]$, and the vertical outflow from the deepest soil layer is considered as leakage to the underlying bedrock, L_{kb} (Section 14). Consequently, in the last equation of the system described in Eq. (280), the term q_{n_s} is replaced with L_{kb} $[mm\ h^{-1}]$. There may be cases where the last layer n_s (for example when an impermeable bottom is specified) or some intermediate layer become saturated. In these conditions the water in excess is considered to saturate progressively the *"unsaturated"* zone starting from the interested layer toward the surface. This mechanism leads to the formation of a shallow water table depth, Z_{wt} $[mm]$ and of a saturated zone within the soil column (Section 12.4).

The adopted numerical method operates on a mesh that is supposed to resolve the vertical variability of soil moisture. Since the numerical discretization permits a variable resolution, the soil profile is resolved with a higher detail near the surface, which allows one to account for the high-frequency variability in the atmospheric

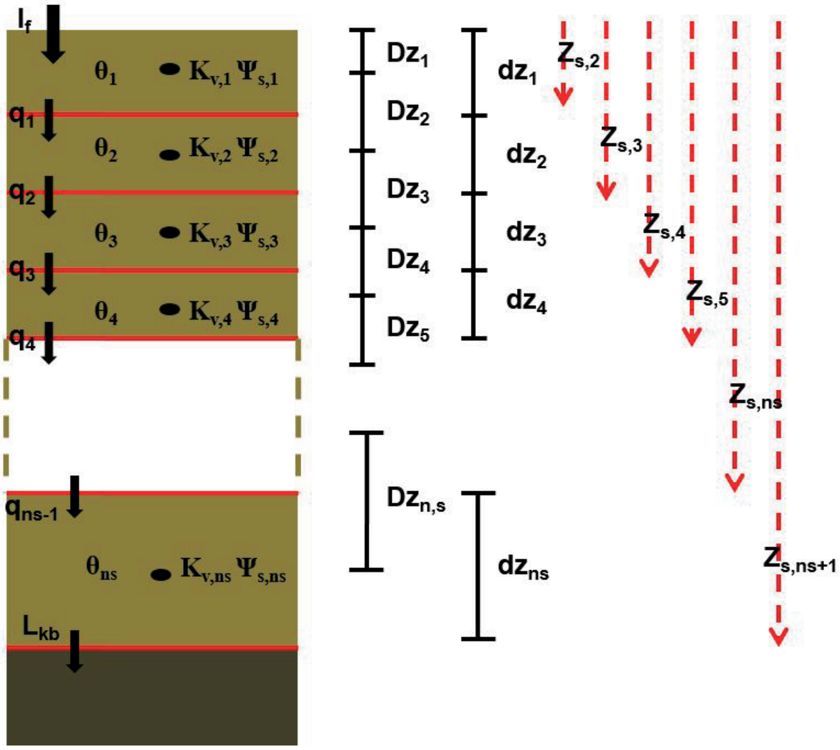

Figure 28: A graphical scheme illustrating a soil column representation and the principal variables used in the computation of subsurface water dynamics. The subscript i identifies a soil layer. The term $\Psi_{S,i}$ $[mm]$ is the soil water potential in the center of the layer, $K_{v,i}$ $[mm\ h^{-1}]$ is the saturated conductivity at the center of layer, L_{kb} $[mm\ h^{-1}]$ is the bottom leakage flow, θ_i $[-]$ is the soil water content, q_i $[mm\ h^{-1}]$ is the vertical outflow from layer i, $Z_{s,i}$ $[mm]$ is the depth from the surface to the layer upper boundary, $d_{z,i}$ $[mm]$ is the layer thickness, and $D_{z,i}$ $[mm]$ is a positive distance between the layer center and the preceding layer center. Note that the first value of Z_s is always zero, corresponding to the surface. Typically, between 8 and 30 layers are used with a coarser mesh resolution at greater depths for computational efficiency.

forcing. The mesh has a coarser resolution at greater depths for computational efficiency. Typical mesh resolutions adopted in the model permit 10-30 layers with layer depths varying from 10 to 500 $[mm]$.

The solution of the system of ordinary differential equations (280) is carried out numerically with a modified Rosenbrock formula of order 2 that can solve stiff numerical problems (*Shampine and Reichelt*, 1997). Since all of the evaporation and transpiration fluxes depend on soil water content, the solution of the system (280) requires the solution of energy balance at each internal time step. In order to reduce the computational burden, the transpiration and evaporation fluxes of equation (280) are determined with the soil water content calculated at the preceding time step. Similarly, the lateral incoming fluxes $Q_{l,in,i}$ represent outflows from neighboring elements at the preceding time step.

12.2 Soil water sinks

Since the soil column is resolved with layers covering multiple depths, the root biomass profile can be explicitly represented in the numerical scheme. The fractions of root biomass at different depths are identified as r_i $[-]$, with $i = 1 \dots n_s$. The terms r_i can be calculated from the soil layer discretization (e.g., the depth of the layer upper boundary $Z_{s,i}$ $[mm]$) and the root profile distribution. Specifically, four options are available in T&C to define the root profile distribution (Figure 29): (i) an exponential root profile (*Arora and Boer*, 2005; *Ivanov et al.*, 2008a) that requires only the knowledge of the rooting depth that contains 95% of fine root biomass, $Z_{R,95}$ $[mm]$; (ii) a profile following a linear dose response model (*Schenk and Jackson*, 2002; *Collins and Bras*, 2007) that requires knowledge of $Z_{R,95}$ and the rooting depth that contains 50% of fine root biomass $Z_{R,50}$ $[mm]$; (iii) a constant root profile, which requires knowledge of $Z_{R,95}$; (iv) a linear dose response profile with tap roots, which beyond $Z_{R,95}$ and $Z_{R,50}$ requires also the knowledge of the maximum rooting depth $Z_{R,max}$ $[mm]$. The terms r_i for the exponential root profile are computed as:

$$r_i = e^{-\eta\,(Z_{s,i})} - e^{-\eta\,(Z_{s,i+1})}\,, \quad \text{if} \quad Z_{R,95} > Z_{s,i+1}\,, \tag{282}$$

$$r_i = e^{-\eta\,(Z_{s,i})} - e^{-\eta\,Z_{R,95}}\,, \quad \text{if} \quad Z_{s,i} \leq Z_{R,95} \leq Z_{s,i+1}\,, \tag{283}$$

$$r_i = 0\,, \quad \text{if} \quad Z_{R,95} < Z_{s,i}\,, \tag{284}$$

where the decay rate of root biomass, $\eta = 3/Z_{R,95}$ $[mm^{-1}]$, is a model parameter for each C_{crown} (Section 2.2).

The terms r_i for the linear dose response profile are:

$$r_i = \frac{1}{1+\left(\frac{Z_{s,i+1}}{Z_{R,50}}\right)^{c_R}} - \frac{1}{1+\left(\frac{Z_{s,i}}{Z_{R,50}}\right)^{c_R}}\,, \quad \text{if} \quad Z_{R,95} > Z_{s,i+1}\,, \tag{285}$$

$$r_i = \frac{1}{1+\left(\frac{Z_{R,95}}{Z_{R,50}}\right)^{c_R}} - \frac{1}{1+\left(\frac{Z_{s,i}}{Z_{R,50}}\right)^{c_R}}\,, \quad \text{if} \quad Z_{s,i} \leq Z_{R,95} \leq Z_{s,i+1}\,, \tag{286}$$

$$r_i = 0\,, \quad \text{if} \quad Z_{R,95} < Z_{s,i}\,, \tag{287}$$

where $c_R = 2.94/\log(Z_{R,50}/Z_{R,95})$ $[-]$. Finally for a constant root profile the terms r_i are:

$$r_i = \frac{Z_{s,i+1} - Z_{s,i}}{Z_{R,95}}, \qquad \text{if} \quad Z_{R,95} > Z_{s,i+1}, \tag{288}$$

$$r_i = \frac{Z_{R,95} - Z_{s,i}}{Z_{R,95}}, \qquad \text{if} \quad Z_{s,i} \leq Z_{R,95} \leq Z_{s,i+1}, \tag{289}$$

$$r_i = 0, \qquad \text{if} \quad Z_{R,95} < Z_{s,i}. \tag{290}$$

In order to preserve the water mass budget the fractions of the root biomass, r_i, are corrected to obtain a sum exactly equal to 1 (i.e., it should be $\sum_i^{n_s} r_i = 1$), rather than 0.95 as would imply from the exponential and linear dose response root profiles (Figure 29). The fractions r_i for the linear dose response profile with tap roots can be computed as for the linear dose response profile imposing that the remaining 5% of roots is distributed with a constant profile between $Z_{R,95}$ and $Z_{R,max}$, rather than correcting r_i to sum to 1.

Note that the rooting depth that contains 95% of fine roots, Z_{R95} $[mm]$ or $Z_{R,max}$ (if the fourth option is chosen) should be always shallower than Z_{s,n_s+1}. This is a necessary assumption given that the soil profile below Z_{s,n_s+1} is not solved. The fractions of root biomass, r_i, are used as numerical representations of plant water uptake. Since we selected to use fractions proportional to the fine root biomass, we assume a static distribution of uptake. It has been argued that plants have the capability to compensate for water stress and uptake water from wetter layers (*Guswa et al.*, 2002; *Teuling et al.*, 2006; *Javaux et al.*, 2008). Since numerous uncertainties still remain regarding this behavior, dynamic adaptations of root fractions are not accounted for in T&C. However, there is a modification to the static strategy related to the possible lack of moisture in one or more soil layers. In this case, the transpiration rate is reduced, due to smaller uptake of water from drier layers; therefore, in these conditions the partition of transpiration in the root zone does not follow the imposed fine root distribution.

12.3 Infiltration flux and infiltration excess runoff

The infiltration term in T&C is computed by using a technique that first imposes a "hypothetical" Dirichlet boundary condition at the soil surface, under which the surface soil water potential is equal to zero. This is done in order to estimate the upper limit for infiltration flux, i.e., the infiltration capacity, I_f^C $[mm\ h^{-1}]$. When the total water influx q_{ins} is less than I_f^C the situation corresponds to the Neumann-type flux boundary condition and q_{ins} enters the soil. Once ponding occurs (under which condition q_{ins} is higher than I_f^C), the condition corresponds to a Dirichlet-type boundary condition, with the soil water potential assigned to be equal to the hydrostatic head induced by the ponding at the soil surface.

Surface sealing and soil crust mechanisms can be accounted for in T&C and their

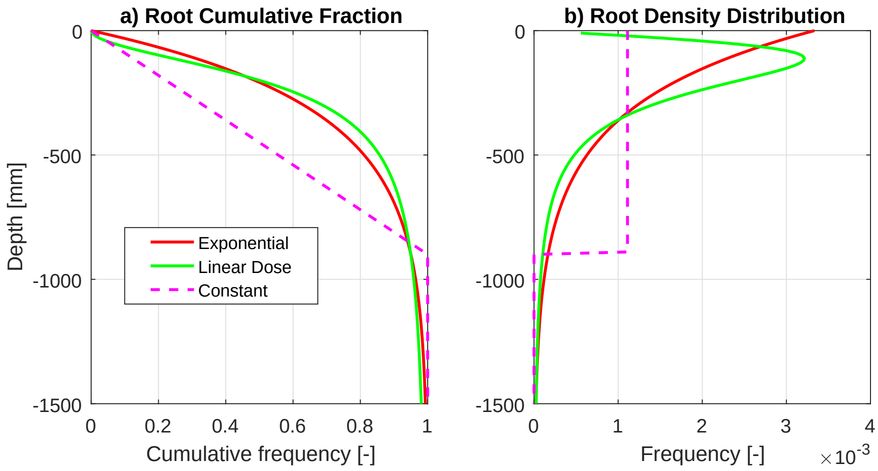

Figure 29: (a) Cumulative distribution function and (b) probability density function for three different root profiles: exponential (red lines), linear-dose (green lines) and constant (magenta lines). Values of $Z_{R,95} = 900\ mm$ $Z_{R,50} = 200\ mm$ have been used.

conceptualization is described in Section 12.6. Soil sealing decreases the infiltration rate, reduces the available water to the plants in the root zone, diminishes the natural recharge of aquifers, and increases runoff and soil erosion (*Assouline*, 2004). Therefore, considering soil sealing effects can be of paramount importance in eco-hydrological modeling, especially when arid and semiarid environments with large portions of bare soil are investigated. Although it has also been shown that vegetation density and distance from vegetation can be important factors in determining the soil infiltration capacity (*Bhark and Small*, 2003; *Madsen et al.*, 2008; *Bedford and Small*, 2008), the corresponding mechanisms are neglected, except in specific applications (*Paschalis et al.*, 2016).

Infiltration excess runoff, also called the *Hortonian* runoff is calculated as the difference between the water influx to soil, q_{ins}, and the actual infiltration rate I_f $[mm\ h^{-1}]$, R_H $[mm\ h^{-1}]$.

$$R_H = q_{ins} - I_f\,. \tag{291}$$

The actual infiltration rate is the minimum between infiltration capacity, I_f^C $[mm\ h^{-1}]$, and q_{ins}: $I_f = \min\left(q_{ins}, I_f^C\right)$ $[mm\ h^{-1}]$, where "min" is the minimum operator. In case of exposed rocks ($C_{rock} > 0$) the run off SE_{rock} $[mm\ h^{-1}]$ produced by incoming water exceeding the maximum interception capacity is also considered as infiltration excess runoff and its contribution is added to R_H.

12.4 Saturation excess runoff

A soil layer i of the soil column becomes saturated, once it reaches the soil saturation content θ_{sat} $[-]$. If this occurs when inflow to the layer i is larger than the outflow, a saturated zone within the soil column is formed with the water table depth located at Z_{wt} $[mm]$, where Z_{wt} represents the depth of the upper side of the shallowest saturated layer. In this case there is a surplus of water that the layer i is unable to store. As anticipated in Section 12.1, the model assumption is that the exceeding water, W_{TR} $[mm\ h^{-1}]$, is transferred to the upper layer $i-1$. Consequently, the formation of a saturated zone in deeper soil layers starts to progressively saturate the soil toward the surface. When the upward flux, W_{TR} $[mm\ h^{-1}]$, exfiltrates from the surface through the top layer, this component becomes surface runoff, namely, saturation excess runoff R_D $[mm\ h^{-1}]$. Numerically the fluxes $W_{TR,i}$ are estimated at each time step after solving equation (280), and checking progressively from the bottom if the layer are over-saturated (Section 12.1).

12.5 Soil hydraulic properties

Soil texture and hydraulic properties are very important components of the coupled dynamics between climate, soil, and vegetation. Suitable relationships to link soil textural properties to hydraulic characteristics are thus required (*Saxton et al.*, 1986; *Mayr and Jarvis*, 1999; *Schaap and van Genuchten*, 2006) to define the hydraulic conductivity curve relating unsaturated hydraulic conductivity K $[mm\ h^{-1}]$ with soil moisture content, θ $[-]$ or $[mm^3\ mm^{-3}]$ and the soil water retention curve relating the soil water potential Ψ_s $[MPa]$ to θ $[-]$. Different parameterizations have been proposed in literature for the hydraulic conductivity function $K(\theta)$ and soil water retention curve $\Psi_s = f(\theta)$ (e.g., *Brooks and Corey*, 1964; *Campbell*, 1974; *Clapp and Hornberger*, 1978; *van Genuchten*, 1980; *Assouline and Or*, 2013).

T&C is flexible and can use either the *van Genuchten* (1980) or the *Saxton and Rawls* (2006) parameterizations of soil-water-relationships. The parameters required in the calculation of the characteristics soil hydraulic curves are the saturated water content θ_{sat} $[-]$, the residual or hygroscopic moisture content θ_r, the saturated hydraulic conductivity K_{sat} $[mm\ h^{-1}]$, and parameters characterizing the intercept and shape of the soil water retention curve as the air-entry bubbling pressure Ψ_e $[MPa]$ and the pore-size distribution index $\lambda_\circ$ $[-]$. Additionally, the moisture content at field capacity θ_{fc}, i.e., the water content at which the gravitational drainage becomes negligible can be also required by specific modules (e.g., Section 21.5).

The value of the parameters θ_r and θ_{fc} can be obtained from the soil water retention curve imposing a water potential equal to -10 $[MPa]$ for the residual water content, i.e., $\theta_r = \theta(\Psi = -10\ [MPa])$, and an unsaturated conductivity of 0.2 $[mm\ h^{-1}]$ for the field capacity, i.e., $\theta_{fc} = \theta(K = 0.2\ [mm\ h^{-1}])$ (*Laio et al.*, 2001). Generally, the characterization of these parameters is uncertain, and other threshold values can be chosen. The other parameters must be evaluated using pedotransfer functions that provides soil hydraulic parameters as a function of textural composition of the soil. Typically, the fractions of sand, F_{san} $[-]$, and clay F_{cla} $[-]$, and the percentage of organic material, P_{org} $[-]$, are required to compute the soil hydraulic parameters. In T&C the pedotransfer functions published by *Saxton and Rawls* (2006) as an update of the *Saxton et al.* (1986) database are internally implemented and can be used to compute soil hydraulic parameters. Alternatively, if the *van Genuchten* (1980) parameterization is used, soil hydraulic parameters have to be provided as inputs. The soil column can have a variable texture composition with depth and therefore variable hydraulic properties. For instance, an exponential decline with depth of the unsaturated hydraulic conductivity, can be assumed in the model (*Beven*, 1982; *Sivapalan et al.*, 1987; *Wigmosta et al.*, 1994). The implemented pedotransfer equations are described in page 1571 of *Saxton and Rawls* (2006).

Hydraulic conductivity, K, can be different in the horizontal and vertical direction because of heterogeneities in the soil, such a difference is accounted for with an anisotropy factor a_r $[-]$ (*Garrote and Bras*, 1995; *Assouline and Or*, 2006), defined as the ratio between the hydraulic conductivity in the directions parallel to the slope K_h and the hydraulic conductivity normal to the slope K_v:

$$a_r = \frac{K_h}{K_v} . \qquad (292)$$

Typically $a_r > 1$ (*Assouline and Or*, 2006). Sometime, the value of K_h can be parameterized to be one order of magnitude larger then K_v, and it represents a simple way to include preferential lateral flows in hydrological models. Anytime the subscript h or v is omitted in the text, K refers to the hydraulic conductivity normal to the slope.

Another useful definition is the effective saturation S_e $[-]$. The effective saturation of a soil layer i, S_e $[-]$ is defined as:

$$S_e = \frac{\theta_i - \theta_r}{\theta_{sat} - \theta_r} . \qquad (293)$$

12.6 Soil sealing and crust

The formation of a seal at the soil surface can result from different causes, such as rainfall, fire, biological activity. In T&C we account only for rainfall-induced surface sealing as described in *Assouline* (2004). Structural seals are formed at the soil surface by destruction of soil aggregates exposed to direct impact of rain drops. Under the impact of raindrops, weaker soil aggregates break down, soil undergoes a compaction and its pores are filled and clogged by wash-in of fine material. Consequently, soil develops a surface seal that alters the surface hydraulic properties (*Assouline*, 2004). Subsequently, seals after drying become crusts. In arid and semiarid environments with large fractions of soil directly exposed to raindrop impacts, soil sealing plays an important role decreasing the infiltration capacity (*Morin et al.*, 1989; *Robinson and Phillips*, 2001; *Assouline and Mualem*, 2001; *Assouline*, 2004; *Assouline and Mualem*, 2006). For this reason, surface sealing effects are accounted for.

A conceptual model used to describe the surface seal layer follows *Mualem and Assouline* (1989). They suggested that seal is a nonuniform layer at the soil surface. It results from the rearrangement and compaction of soil particles in the disturbed upper zone due to raindrop impact and from fine soil particles percolating to larger depth during infiltration. Consequently, the seal bulk density ρ_{cr} $[kg\ m^{-3}]$ is highest at the surface and decreases exponentially with depth z $[mm]$ converging to the density of the undisturbed soil, i.e., $\rho_d = \rho_b(1-\theta_{sat})$ $[kg\ m^{-3}]$, where θ_{sat} is the soil water content at saturation, and ρ_b $[kg\ m^{-3}]$ is the density of solid soil:

$$\rho_{cr}(z) = \rho_d + \Delta\rho \exp(-\gamma_{cr} z)\,, \tag{294}$$

where $\Delta\rho$ $[kg\ m^{-3}]$ is the maximum change of bulk density at the soil surface ($z = 0$), and γ_{cr} $[mm^{-1}]$ is a characteristic parameter of soil-rainfall interaction. The seal thickness d_{cr} $[mm]$ is identified as the depth at which the changes in hydraulic properties are insignificant, namely, where $\Delta\rho(z) \leq 0.001\Delta\rho$. It follows that $\gamma_{cr} = -\ln(0.001)/d_{cr}$. While the model of *Mualem and Assouline* (1989) is theoretical, it has been recently tested to be valid against accurate measurements (*Assouline*, 2004).

The main purpose of including seal modeling in T&C is the possibility to simulate infiltration into a seal-topped profile. In order to simulate infiltration for a sealed soil, the seal hydraulic properties must be calculated. The calculation of hydraulic properties is carried out using the undisturbed soil properties and the modified seal bulk density, ρ_{cr}. The seal density in turn depends on the depth z according to Eq. (294). The undisturbed soil parameters are the saturation moisture content, θ_{sat} $[-]$, the residual moisture content, θ_r $[-]$, the pore-size distribution index, $\lambda_\circ$ $[-]$, the air entry bubbling pressure, Ψ_e $[mm]$, and the vertical saturated hydraulic conductivity, $K_{sat\,v}$ $[mm\ h^{-1}]$ (Section 12.5, Figure 30). The correspondent parameters modified by the seal effect are indicated with the subscript *cr* and are calculated according to *Mualem and Assouline* (1989):

$$\begin{aligned}
\theta_{sat,cr}(\rho_{cr}) &= \theta_{sat} - \big[\rho_{cr}(z_d) - \rho_d\big]/\rho_{ss}\,, && (295)\\
\theta_{r,cr}(\rho_{cr}) &= \theta_r\big[1 + (\rho_{cr}(z_d) - \rho_d)/\rho_d\big]\,, && (296)\\
\Psi_{e,cr}(\rho_{cr}) &= \Psi_e\big[1 + (\rho_{cr}(z_d) - \rho_d)/\rho_d\big]^{3.72}\,, && (297)\\
\lambda_{\circ,cr}(\rho_{cr}) &= \lambda_\circ - \mathcal{C}\big[\rho_{cr}(z_d) - \rho_d\big]\,, && (298)\\
K_{sat\,v,cr}(\rho_{cr}) &= K_{sat\,v}\left[\frac{\theta_{sat,cr} - \theta_{hy,cr}}{\theta_{sat} - \theta_{hy}}\right]^{2.5}\left[\frac{\Psi_e}{\Psi_{e,cr}}\right]^2\left[\frac{\lambda_{\circ,cr}(1+\lambda_\circ)}{\lambda_\circ(1+\lambda_{\circ,cr})}\right]^2\,, && (299)
\end{aligned}$$

where $\mathcal{C}$ $[m^3\ kg^{-1}]$ is a fitting parameter. A value $\mathcal{C} = 2.5\,10^{-4}$ $[m^3\ kg^{-1}]$ is used, when no specific information for its calibration is available (*Assouline and Mualem*, 1997).

In order to calculate the hydraulic properties in a nonuniform seal, the seal must be characterized by maximum change of the bulk density at the soil surface $\Delta\rho$ $[kg\ m^{-3}]$ and the seal thickness d_{cr} $[mm]$. These two variables are the result of soil and rainfall interaction. They evolve in time according to the seal development. The conceptual model of *Mualem et al.* (1990) of seal formation is implemented in T&C. The model is based on Eq. (294) and accounts dynamically for the transfer of kinetic energy from the rainfall to the soil. The maximum increase in the soil bulk density at the soil surface $\Delta\rho$ and the seal thickness d_{cr} are considered to be function of the rainfall cumulative kinetic energy E_K $[J\ mm^{-2}]$. The cumulative kinetic energy can be estimated from the total flux of direct throughfall and leaf drainage kinetic energy K_E $[J\ m^{-2}\ h^{-1}]$, calculated in Section 11. The variable, E_K, is simply the time integral of K_E.

$$\begin{aligned}\Delta\rho(E_K) &= \Delta\rho^*\left[1-\exp(-\eta_{cr}E_K)\right], &(300)\\ d_{cr}(E_K) &= d^*_{cr}\left[1-\exp(-\zeta_{cr}E_K)\right], &(301)\end{aligned}$$

where $\Delta\rho^*$ $[kg\ m^{-3}]$ and d^*_{cr} $[mm]$ are the maximal values of $\Delta\rho$, and d_{cr} reached after a long exposure to rainfall. The parameters η_{cr}, and ζ_{cr} depend on soil-rainfall characteristics. Theoretically, the values of $\Delta\rho^*$, d^*_{cr}, η_{cr}, and ζ_{cr} must be estimated from observations of seal formation (*Assouline*, 2004). Here, literature values of $\Delta\rho^* = 400$ $[kg\ m^{-3}]$, $d^*_{cr} = 10$ $[mm]$ $\eta_{cr} = 7000$ $[mm^2\ J^{-1}]$, and $\zeta_{cr} = 3500$ $[mm^2\ J^{-1}]$ are assumed as representative for every soil and rainfall type (*Mualem et al.*, 1990). A more accurate model of seal formation has been also proposed (*Assouline and Mualem*, 1997). It includes a characterization of raindrop size distribution and soil mechanical properties. Nevertheless, given the scarcity of laboratory experiments to estimate the required parameters, the *Mualem et al.* (1990) model is preferred.

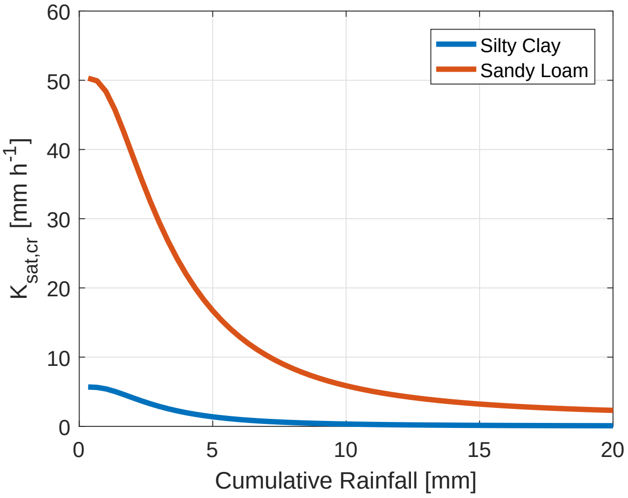

Figure 30: Values of saturated hydraulic conductivity, $K_{sat\,v,cr}$ $[mm\ h^{-1}]$, of a sealed soil for a sandy-loam and a silty-clay subject to a 20 $[mm\ h^{-1}]$ rainfall lasting one hour in a bare-soil. The effects of cumulative rainfall is shown at a depth $z_d = 0.25$, which is used in the model to compute the seal properties.

Models and applications of seal formation and related changes of soil hydraulic properties have been developed and used at the event scale (*Mualem et al.*, 1990; *Mualem and Assouline*, 1989; *Assouline and Mualem*, 1997, 2001, 2006). Their extension to longer time scales is obtained by re-starting the accumulation of cumulative kinetic energy, E_K $[J\ mm^{-2}]$ for each event, i.e., when a seal formation event is considered to be concluded, $E_K = 0$. The latter is assumed when the kinetic energy flux has been zero for more than one hour. Otherwise, E_K evolves in time as the time integration of fluxes of kinetic energy. The proposed simplification neglects long-lasting effects of the seal layer, i.e., the formation of an enduring soil crust when the surface dries, or the maintenance of a seal between two consecutive precipitation events (*Sela et al.*, 2015). Little information, if any, exists on the surface seal breaking and reversal to the initial undisturbed conditions or conversely on its persistence with time. The study of such effects could be important both for infiltration and soil evaporation dynamics. Nonetheless, given the large uncertainties in measuring and understanding this phenomenon, no attempt is made to model the long-term seal/crust evolution in T&C.

The effect of soil sealing is confined to a thin superficial layer (*Assouline*, 2004; *Fatichi*, 2010). Because of that, surface seal is considered to modify only infiltration flux and keep the subsurface soil-water dynamics unchanged (Section 12.1). After the formation of a seal layer, soil hydraulic properties, required in the calculation of infiltration, are obtained as the average of the properties at the seal surface $z = 0.25$ mm and those of the undisturbed first soil layer, except for $K_{sat\,v}$ which is assumed to correspond to the seal surface (Figure 30). This is a further simplification of the method, however the implementation of a non-uniform seal would require a very fine spatial discretization of the soil column at the surface, which is infeasible for long-term simulations. Furthermore, *Assouline and Mualem* (2001) show that assuming a uniform seal layer does not affect significantly the estimated infiltration curve, when the dynamic phase of seal formation is simulated.

13 Plant water relations

13.1 Root zone soil moisture, water potential and temperature

The average soil moisture content θ_R $[-]$ available to a given plant root is computed using the fractions of root biomass r_i described in Section 12.2 as $\theta_R = \sum_{i=1}^{n_s} r_i \theta_i$ where n_s is the number of soil layers. The average value of water content available to roots θ_R is then used to compute the soil water potential felt by the roots Ψ_{sR} $[MPa]$, using the soil water retention curve $\Psi_s = f(\theta)$. The term Ψ_{sR} correspond to the water potential in the soil, while T&C uses the leaf water potential Ψ_L $[MPa]$ to compute various water-stress variables, generally indicated as β $[-]$ factors (Section 6.6.4, 17.3.7, 17.4.1, and 20.1.1). The evaluation of leaf water potential Ψ_L starting from Ψ_{sR} requires the solution of water movement within the plant from the absorbing roots up to the leaves, including the evaluation of the xylem water potential Ψ_X $[MPa]$. Plant hydraulics are currently not simulated by T&C, which therefore assumes an equivalence between $\Psi_{sR} = \Psi_X = \Psi_L$.

In analogy with the average soil moisture content in the root zone, the average soil temperature in the root zone is computed as $T_R = \sum_{i=1}^{n_s} r_i T_{soil,i}$, where $T_{soil,i}$ is the temperature of the soil layer i.

13.2 Plant hydraulics

A plant-hydraulic component is not implemented in T&C yet.

13.3 Plant water uptake and soil-to-root conductance

Since plant-hydraulics are not resolved in this version of T&C, the water flux from soil to xylem J_{sx} $[mm\,h^{-1}]$ and from xylem to leaf J_{xl} $[mm\,h^{-1}]$ are just assumed to be the same of the transpiration fluxes T_H and T_L computed in Section 5.4.1 for each vegetation unit and for high and low vegetation layers. Therefore the magnitude of the plant-water uptake J_{sx} is dictated by the transpiration demand as far as there is enough water in a given soil layer or the water uptake is not limited by the hydraulic resistance between the soil and the root (see below). The $J_{sx,i} = r_i J_{sx}$ is distributed in the different soil layers following the fractions of root biomass r_i described in Section 12.2.

The soil-to-root conductance g_{sr} $[mmol\,H_2 0\ s^{-1}\,MPa^{-1}\,m^{-2}\,ground]$ represents the resistance to water movement from the bulk soil to the fine-root interior (*Sperry et al.*, 1998; *Hölttä et al.*, 2009) and theoretically depends on the micro-gradient of soil water potential on the rhizosphere around fine roots as well as on the radial root hydraulic conductivity (*Doussan et al.*, 1998; *Steudle and Peterson*, 1998). An approximated method (*Newman*, 1969; *Deckmym et al.*, 2008) is used in T&C to compute $g_{sr,i}$ for each soil layer and for each vegetation unit using the value of root length density R_L for unit of vegetation (Eq. 403) and the fraction of root biomass in each layer r_i. The root length density for unit of ground in a given soil layer is $R_{L,i} = r_i C_{crown} R_L$ $[m\,root; m^{-2}\,ground]$ and is combined with the average radius of fine roots, assumed to be $r_{root} = 0.5\ mm$, the average radius of the cylinder of soil to which root has access to, assumed to be $r_{cyl} = 2.0\ mm$, and the soil hydraulic conductivity in the layer i, $K_v(\theta_i)$ $[m\ s^{-1}]$, function of the water content θ_i (Section 12.5):

$$g_{sr,i} \quad = \quad \kappa K_v(\theta_i)\, R_{L,i}\, 2\pi\ \log\left[\frac{r_{cyl}}{r_{root}}\right]\,, \tag{302}$$

where $\kappa = 5.66\,10^9$ is a unit conversion factor to pass to $[mmol\,H_2 0\ s^{-1}\,MPa^{-1}$ $m^{-2}\,ground]$. The total soil-to-root conductance can be computed in analogy to parallel conductances as $g_{sr} = \sum_i g_{sr,i}$. The soil-to-root conductances $g_{sr,i}$ are used to compute the maximum root-uptake capacity $RWU_{max,i}$ $[mm\,h^{-1}]$ in each soil layer as:

$$RWU_{max,i} \quad = \quad \tilde{\kappa} g_{sr,i} |\Psi_s - \Psi_{min}|\,, \tag{303}$$

where $\tilde{\kappa} = 0.0648$ is a unit conversion factor to obtain $[mm\,h^{-1}]$, Ψ_s $[MPa]$ is the soil water potential of layer i and $\Psi_{min} = \min[\Psi_{X,50}, \Psi_{L,50}]$, is the minimum water potential allowed in the xylem or leaf before having a 50% reduction of hydraulic conductivity and represents a lower limit to the gradient of water potential that can be imposed between the soil and the plant to extract water. From Eq. (303) it follows that low values of $g_{sr,i}$ can prevent water uptake from one or more soil layers when they approach dry conditions. The plant water uptake in each layer is then the minimum between $J_{sx,i}$ and $RWU_{max,i}$.

14 Subsurface water flow

Water transferred sideways from the soil column in a given element, $Q_{l,out}$ $[mm\ h^{-1}]$, represents lateral subsurface flow. It is assumed in T&C that the slope of the hydraulic head is parallel to the soil surface (kinematic wave approximation), an assumption that is commonly made in several topographic subsurface routing methods (*Beven and Kirkby*, 1979; *Sivapalan et al.*, 1987; *Beven and Freer*, 2001; *Ciarapica and Todini*, 2002). The assumption validity is violated in shallow terrains (e.g., floodplain), especially when a portion or the entire soil column becomes saturated. A hydraulic head gradient formulation would be preferable (*Wigmosta and Lettenmaier*, 1999; *Panday and Huyakorn*, 2004; *Kollet and Maxwell*, 2008) and is regarded as a potential future improvement of the model.

The subsurface kinematic wave is solved in a discretized space domain (a lattice of square cells) for each soil layer. The lateral flow from a layer i, $Q_{l,out,i}$, moves along a pre-defined drainage flow direction(s) into the neighboring element(s):

$$Q_{l,out,i} = \frac{T_{r,i}\ \sin\beta_T}{a_T}\ , \tag{304}$$

where β_T $[rad]$ is the maximum surface slope of an element, a_T $[mm]$ is the element area per unit contour length that drains through the location (*Quinn et al.*, 1995; *Sivapalan et al.*, 1987), and $T_{r,i}$ $[mm^2\ h^{-1}]$ is the total transmissivity of the layer i, which is obtained multiplying the hydraulic conductivity of a given layer $K_H(\theta_i, z_i)$ in direction parallel to the slope, with the layer thickness dz_i $[mm]$. The total lateral subsurface flow from an element, $Q_{l,out}$, $[mm\ h^{-1}]$, is calculated by integrating Eq. (304) over n_s layers. When dealing with a cell containing a channel element, the subsurface flow, $Q_{l,out}$, is added to channel flow of that grid cell. In this unidirectional operation, the effect of seepage flow is mimicked.

An artificial time lag is used in the subsurface routing, since the routing is made at the end of each time step: for a given cell the inflow is the outflow of the preceding time step. This artificial time lag allows the model to be easily parallelized and run on multiple processors. Incoming lateral flow is then applied as a source term in the 1-D Richards equation in each vertical layer (Section 12.1), while outgoing lateral flow is computed as in Eq. (304).

Soil-bedrock leakage flow has been regarded as an important process of the subsurface dynamics (*Weiler and McDonnell*, 2004; *Tromp-van Meerveld and Weiler*, 2008). According to Figure 28, the last layer of the soil column is drained through the bottom resulting in leakage flow L_{kb} $[mm\ h^{-1}]$. This term represents the percolation flux from the soil column (i.e., the regolith) to the bedrock. This flux is considered to be equal to the conductivity of bedrock, $L_{kb} = K_{bot}$ $[mm\ h^{-1}]$, when the last n_s-th layer of soil is saturated. No unsaturated flow to the bedrock is assumed. Another possible condition $K_{bot} = 0$ implies an impermeable bedrock, which precludes recharge to deeper aquifers. A free-gravitational drainage condition can also be assumed in T&C, as another type of the bottom boundary condition.

Note that non-zero vertical subsurface flow L_{kb} provides a recharge to a deep aquifers, schematized as a volume of water in fractured rocks (see Section 10). The fractured rock water storage F_{rock} $[mm]$ represents a reservoir with a relatively long residence time and can be conceptualized as a lumped component at the watershed or sub-watershed scales. This deep aquifer can return a baseflow flux, $\overline{Q_{sub}}$ $[mm\ h^{-1}]$, that can be distributed throughout the stream network or added at specific locations, which represents the water sources from deep rock aquifers in a given watershed. A linear reservoir scheme is assumed in T&C, where the baseflow $Q_{sub} = k_{res} F_{rock}$, is a function of the reservoir volume and of a parameter k_{res} $[h^{-1}]$.

In order to maintain continuity of the water lateral exchanges, the soil depth and the vertical discretization in soil layers should be equal in all the cells of the domain. This allows every flux $Q_{l,out,i}$ to have a downstream soil layer or a channel as outlet. This strong limitation can be partially by-passed assigning for each cell nearly impermeable soil properties to all soil layers below the depth that is expected to contribute marginally to subsurface water dynamics.

15 Surface water flow

The numerical scheme adopted for representing surface flow in T&C is a function of topographic representation of the domain (Section 3). The runoff depth, R_{tot} $[mm]$, in a given computational element is the sum of infiltration excess runoff R_H $[mm\ h^{-1}]$ and saturation excess runoff R_D $[mm\ h^{-1}]$. The flow depth of locally produced runoff y $[mm]$ is then approximated with the assumption of a sheet flow, i.e., for overland flow, $y = R_{tot}$. Channel is conceptualized as a sub-grid element with the rectangular cross-section of width w_{ch} $[m]$. The width w_{ch} is parameterized as a function of the upstream contributing area according to regional geomorphological relationships (*Orlandini*, 2002; *Camporese et al.*, 2010) and it is independent of the discharge. A cell containing a channel area can have both overland and channel flow components. Channels are assumed to both receive subsurface flow (Section 14) and overland flow. The water depth in the channel is $y_{ch} = R_{ch}\, dx/w_{ch}$, where dx $[m]$ is the grid cell size and R_{ch} $[mm]$ is the runoff in the channel, expressed per unit of cell area.

Surface and channel flows are successively routed using the kinematic wave approach, i.e., assuming the momentum equation $S_{fl} = \sin\beta_T$, where S_{fl} $[-]$ is the the energy gradient and β_T $[rad]$ is the slope of the element (*Chow*, 1988; *Bras*, 1990; *Chanson*, 2004; *Brutsaert*, 2005). The water surface is therefore assumed to be parallel to the cell bed at a given location. Further, assuming locally uniform flow and the Manning equation as the flow depth-discharge relationship, it is possible to calculate the overland and channel flow velocities U and U_{ch} $[m\ s^{-1}]$

and, consequently, the respective time t_R and t_{ch} $[s]$ needed to move water from a computational element to downstream element(s) (*Kollet and Maxwell*, 2006):

$$U_{ch} \;=\; \frac{1}{n_{ch}} R_{hy}^{2/3} {S_{fl}}^{1/2}\,, \tag{305}$$

where $R_{hy} \approx y_{ch}$ $[m]$ is the hydraulic radius approximated with the flow depth, and n_{ch} $[s\ m^{-1/3}]$ is the channel Manning's coefficient that characterizes river bed roughness. Consequently, the routing time is $t_{ch} = dx\, n_{ch}\, y^{-2/3} \sin {\beta_T}^{-1/2}$. Equivalent equations can be written for overland flow routing. The distance between the centers of two cells is always assumed to be equal to the cell size dx. The runoff depths R_{ch} (or R_{tot}) $[mm]$ present at any time in a given element are thus routed according to the time t_{ch} (or t_R), following the flow directions calculated from the topography (Sections 3).

At the end of a given time step, a fraction of the produced runoff R_{tot} may remain in a hillslope element and is indicated as runon q_{runon} $[mm\ h^{-1}]$. At the successive time step this runoff fraction can be re-infiltrated (Section 12). Finally, the rate at which overland and channel flows leave the domain or pass trough a specific location is the sum of overland flow and channel discharge, $Q = \overrightarrow{R_{tot}}/dt$ $[mm\ h^{-1}]$ and $Q_{ch} = \overrightarrow{R_{ch}}/dt$ $[mm\ h^{-1}]$, where $\overrightarrow{R_{tot}}$ and $\overrightarrow{R_{ch}}$ $[mm]$ represent the routed fractions of R_{tot} and R_{ch}. In order to respect the Courant condition (*Chanson*, 2004; *Martin and Gorelick*, 2005), a fine time step must be used to route the water flow across the domain. The present version of T&C adopts an adaptive time step for channel and overland flow (*Sulis et al.*, 2010). The model starts from a reference value of $2s$ and increases or decreases the time-step to respect the Courant condition at each iteration based on the previous field of flow velocity in channels and hillslopes. It must be noted that this only improves the correctness of the flow routing, since runoff generation and runon re-infiltration are still computed at the hourly time scale from Section 12.

16 Gravitational snow redistribution

Avalanches can be an important process for re-distributing snow in steep terrains and they can considerably affect hydrology at high-elevations (*Gruber*, 2007; *Bernhardt and Schulz*, 2010). Gravitational snow redistribution is simulated assigning to each cell a maximum terrain snow storage capacity S_{dep}^M $[m]$, which is a function of the slope of the surface S_{sno} $[degree]$ that sum the terrain and the snow depth (*Bernhardt and Schulz*, 2010):

$$S_{dep}^M = C \exp(-a_{sno} S_{sno})\,, \tag{306}$$

where $C = 99.05$ $[m]$ and $a_{sno} = 0.1012$ $[degree^{-1}]$ are parameters introduced by *Bernhardt and Schulz* (2010) in their Fig. 2b and the minimum S_{dep}^M is assumed to be 0.05 m (Figure 31). The slope S_{sno} is computed adding the actual snow depth S_{dep} $[m]$ to the reference elevation of the DEM, the same surface is used to compute flow directions for routing the snow flux.

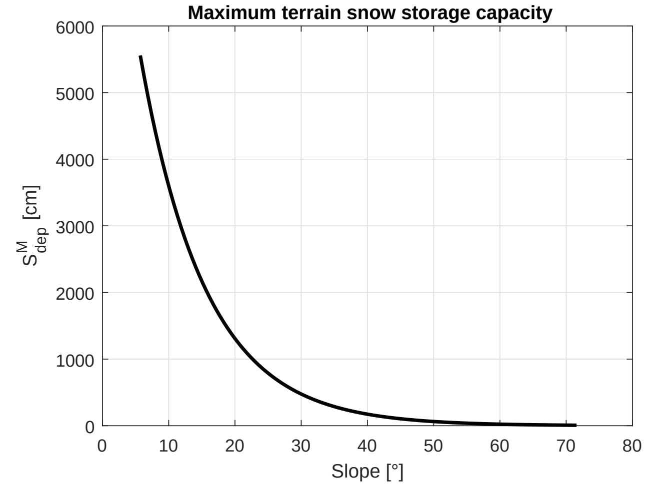

Figure 31: The maximum terrain snow storage capacity S_{dep}^{M} $[cm]$, as a function of the slope of the surface S_{sno} $[degree]$ as inferred from *Bernhardt and Schulz* (2010).

An avalanche can be triggered by a snowfall, variable melting rates or a preceding avalanche that increase the local snow depth above the maximum terrain snow storage capacity, i.e., $S_{dep} > S_{dep}^{M}$. A fraction of snow in excess of the local storage capacity $f_{snr} = (S_{dep} - S_{dep}^{M})/S_{dep}$ is computed, and used to route the corresponding snow water equivalent $f_{snr}\, S_{WE}$. Generally, the avalanche triggering is expected to increase the snow density, when compared to the original snowpack. The density of the re-deposited material is assumed to be $\rho_{ava} = max[\rho_{sno}, 400]$ $[kg\ m^{-3}]$, where the reference value of 400 $kg\ m^{-3}$ is derived from observations of avalanche deposit density (*Sovilla et al.*, 2006).

The avalanche is finally routed following the flow direction and the redistributed snow is assumed to mix perfectly with the original snow cover to produce an overall snow density that is the weighted average between the density of the present snow and the avalanche deposit. Based on this snow density value, we updated the snow depth on the entire domain and we recompute S_{sno}. For each time step, the routing process is repeated until there is some cell in the domain where $S_{dep} > S_{dep}^{M}$, which means that an avalanche can travel a long distance within a single time step, and that at the end of the time step snow is stable in the entire domain. Note that the implemented method assumes an instantaneous redistribution of snow, for instance immediately following a snowfall, and has nothing to do with the real temporal occurrence of avalanches, which is a much more complex process to describe related to snow metamorphisms (*Sovilla et al.*, 2006). Nonetheless, this simple method is expected, on average, to provide a realistic gravitational snow redistribution and to significantly improve the prediction of spatially distributed snow patterns in steep terrain. For instance, avoiding unrealistic deep snow cover in steep high-elevation slopes.

17 Plant carbon dynamics

Carbon dynamics are represented by seven carbon pools for each vegetation type. The budget of the carbon pools is the difference between the carbon gained as a result of photosynthesis and its consumption through maintenance and growth respiration, tissue turnover, and reproduction. The represented carbon pools are: green aboveground biomass (leaves) C_{leaf} $[g\,C\ m^{-2}\,VEG]$, living sapwood (woody plants only) C_{sapw} $[g\,C\ m^{-2}\,VEG]$, fine roots C_{root} $[g\,C\ m^{-2}\,VEG]$, carbohydrate reserves C_{hydr} $[g\,C\ m^{-2}\,VEG]$, flower and fruits, C_{flfr} $[g\,C\ m^{-2}\,VEG]$, heartwood (woody plants only) C_{heaw} $[g\,C\ m^{-2}\,VEG]$, and standing dead leaves C_{ldea} $[g\,C\ m^{-2}\,VEG]$. The carbohydrate reserve pool roughly corresponds to what it is often indicated as non-structural carbohydrates (NSC), i.e., glucose, fructose, sucrose and starch, but it is also meant to include lipids and sugar alcohols (*Hoch et al.*, 2003; *Gough et al.*, 2009). The flower and fruit carbon pool C_{flfr} takes into account the reproduction cost of the plant. The C_{heaw} pool accounts for the turnover of living sapwood and its conversion into structural wood in the trunk and coarse roots. Even though in the following is indicated as heartwood carbon pool for brevity, it also includes dead sapwood and it exists also for those species than never form a properly defined heartwood. The partition between aboveground and belowground C_{heaw} is controlled by a model parameter f_{ab}, which corresponds to the fraction of structural wood and reserves that are physically located aboveground. Note that the terms C_{leaf}, C_{sapw}, C_{root}, C_{hydr}, C_{flfr}, C_{heaw} C_{ldea} refers only to the area occupied by a given vegetation type and not to the total ground area, i.e., they are for units of vegetation *VEG* corresponding to the *Crown area* extent (H_v or L_v) in a basic computational element.

Vegetation structure evolves dynamically, since the carbon in the different pools varies responding to environmental conditions, stress, and phenological state. These dynamics directly influence vegetation attributes, such as leaf and stem areas, canopy height, root profile, and leaf dimension. Although all of the described attributes of vegetation are time-varying, only LAI, grass height, and root length index are dynamically updated in this version of T&C, which does not consider forest demography (Section 18). An exception is represented by plantations for which other structural attributes can be dynamically updated.

In order to describe the dynamics of other vegetation attributes an explicit representation of forest demography would be necessary. This would require the use of allometric relations to link the size of carbon pools to plant dimensional attributes (Section 18) such as tree density, height, diameter at breast height, and crown area (*Cox*, 2001; *Niklas and Enquist*, 2001; *Sitch et al.*, 2003; *Levis et al.*, 2004; *Deckmyn et al.*, 2006; *Sato et al.*, 2007; *Cheng and Niklas*, 2007; *Enquist et al.*, 2007). Such a capability will be included in future versions of T&C based on ongoing research and novel solutions in forest growth modeling (*Kirschbaum*, 199; *Lischke et al.*, 2006; *Strigul et al.*, 2008; *West et al.*, 2009; *Enquist et al.*, 2009; *Weng et al.*, 2015). Given this limitation, typical T&C applications are expected to cover mature vegetation, where forest structural changes can be considered minor, allowing the approximation of static structural vegetation parameters during the simulation period.

Each vegetation considered in T&C belongs to a broad category of vegetation types. Specifically, T&C distinguishes between four vegetation categories identified with the symbol Ξ: normal evergreen plants ($\Xi = 0$), seasonally deciduous plants ($\Xi = 1$), grass species ($\Xi = 2$) and evergreen tropical plants ($\Xi = 3$). This separation is necessary because different vegetation categories have substantially different phenology and carbon allocation and translocation dynamics and must use different model structures and not only model parameters.

17.1 Net Primary Production and plant respiration

The net primary production NPP $[g\,C\ m^{-2}\,VEG\ day^{-1}]$, is defined as the gross plant photosynthesis, or gross primary production GPP $[g\,C\ m^{-2}\,VEG\ day^{-1}]$, less autotrophic respiration R_A $[g\,C\ m^{-2}\,VEG\ day^{-1}]$ (*Ruimy et al.*, 1996; *Knorr*, 2000; *Arora*, 2002; *Sitch et al.*, 2003; *Levis et al.*, 2004; *Krinner et al.*, 2005):

$$NPP = GPP - R_A\,, \qquad (307)$$

$$GPP = \kappa(\overline{A_{nC}} + \overline{R_{dC}})\,, \qquad (308)$$

where $\kappa = 1.0368$ $[g\,C\ s\ \mu mol\,CO_2^{-1}\ day^{-1}]$ is used to convert the unit of canopy-scale net assimilation rate $\overline{A_{nC}}$ $[\mu mol\,CO_2\ s^{-1}\ m^{-2}]$ and leaf maintenance respiration $\overline{R_{dC}}$ $[\mu mol\,CO_2\ s^{-1}\ m^{-2}]$, from the photosynthesis module (Section 6.6). Vegetation autotrophic respiration R_A $[g\,C\ m^{-2}\,VEG\ day^{-1}]$ is estimated as the sum of maintenance respiration R_m, growth respiration R_g, and idling respiration R_i rates:

$$R_A = R_m + R_g + R_i\,, \qquad (309)$$

$$R_m = R_{mF} + R_{mS} + R_{mR} + R_{mH}\,, \qquad (310)$$

$$R_g = \max\left[0, \omega_{grw}(GPP - R_m)\right]\,, \qquad (311)$$

where ω_{grw} $[-]$ is the growth respiration fraction. The maintenance respiration R_m is typically subdivided into different fractions corresponding to living plant compartments (*Thornley*, 1970; *McCree*, 1970; *Ryan*, 1991; *LeRoux et al.*, 2001). The terms R_{mS}, R_{mR}, and R_{mH} $[g\,C\ m^{-2}\,VEG\ day^{-1}]$ are the maintenance respiration rates for living sapwood, fine roots, and carbohydrate reserves respectively, $R_{mF} = \kappa\overline{R_{dC}}$ $[g\,C\ m^{-2}\,VEG\ day^{-1}]$ is the rate of foliage maintenance respiration and is computed at the hourly scale in the photosynthesis module (Section 6.6).

17.1.1 Growth respiration

In order to grow, plants require carbohydrates both for their plant-body construction and biosynthesis (*Sato et al.*, 2007). Usually, the amount of growth respiration costs can be estimated by combining data on biochemical composition of organs with the knowledge on biochemical costs of synthesis of all the major compounds, including cellulose, hemicellulose, lignin, protein, lipids, and organic acids (*Poorter*, 1994; *Poorter and Villar*, 1997; *Lambers et al.*, 1998). Since an exact physiological estimation of growth respiration cost is challenging, vegetation models approximate this cost as a constant fraction ω_{grw} of the carbon potentially allocated to growth, i.e., the gross primary production less maintenance respiration (*Ryan*, 1991; *Sitch et al.*, 2003; *Levis et al.*, 2004; *Ivanov et al.*, 2008b). The values assumed by the growth respiration fraction ω_{grw} $[-]$ are usually quite constrained $(0.15-0.30)$ (*Ryan*, 1991; *LeRoux et al.*, 2001; *Sitch et al.*, 2003; *Krinner et al.*, 2005; *Ivanov et al.*, 2008b). Very often, a value of $\omega_{grw} = 0.25$ is assumed (*Ryan*, 1991; *Cox*, 2001; *Bonan et al.*, 2003; *Sitch et al.*, 2003), which corresponds to an average cost for tissue construction (*Poorter*, 1994).

17.1.2 Idling respiration

When the soil biogeochemstry component is activated, an additional respiration flux R_i, the idling respiration, can be added to the total respiration cost and represents the carbon that cannot be allocated to grow plant tissues because of insufficient nutrient availability, i.e., when the nutrient reserve pools are not able to satisfy minimal stoichiometric ratios. Therefore, the term R_i is different from zero only in cases of severe nutrient limitations. This fluxes is computed as the difference between the theoretical NPP in absence of nutrient limitations and NPP after nutrient limitations have been accounted for (see Section 17.3.5). Mechanistically this respiration cost can be triggered by futile cycles and alternative pathways that leads to the waste of the excess carbon that cannot be used (*Cannell and Thornley*, 2000).

17.1.3 Maintenance respiration

The maintenance respiration is defined as that required for maintenance and turnover of existing biomass (*Amthor*, 1984, 2000; *Cannell and Thornley*, 2000; *LeRoux et al.*, 2001). The maintenance respiration R_m for living plant compartments is calculated as a function of temperature and biomass, once the nitrogen/carbon ratio of each tissue is known (*Ruimy et al.*, 1996; *Sitch et al.*, 2003; *Krinner et al.*, 2005). For a wide variety of plant organs, the maintenance respiration rate is assumed to be linearly related to the nitrogen content of a living tissue (*Ryan*, 1991; *Ruimy et al.*, 1996), even though more recent evidence suggests an exponential dependence between nitrogen content and respiration rates (*Reich et al.*, 1998b, 2006). Furthermore, the maintenance respiration coefficient increases with temperature (air temperature is used for aboveground plant tissues; root-zone temperature is used for belowground biomass) (*Sitch et al.*, 2003; *Krinner et al.*, 2005). Maintenance respiration for the different carbon pools is calculated as:

$$R_{mS} = r_m \left[f_{ab} \frac{C_{sapw}}{CN_s} g(T_a) + (1 - f_{ab}) \frac{C_{sapw}}{CN_s} g(T_{root}) \right] , \tag{312}$$

$$R_{mR} = r_m \frac{C_{root}}{CN_r} g(T_{root}) , \tag{313}$$

$$R_{mH} = r_m \left[f_{ab} \frac{C_{hydr}}{CN_s} g(T_a) + (1 - f_{ab}) \frac{C_{hydr}}{CN_s} g(T_{root}) \right] , \tag{314}$$

where T_{root} $[^\circ C]$ is the daily averaged temperature in the root zone from Section 13.1, T_a $[^\circ C]$ is the daily averaged air temperature at the reference height z_{atm} (Section 5). The parameter r_m $[g\,C\ g\,N^{-1}\ day^{-1}]$ is the respiration rate coefficient (uses a $10^\circ C$ base) that is species specific. The value of r_m typically accounts for observational evidences that plants from warmer environments have lower respiration rates than plants from cooler environments (*Ryan*, 1991; *Reich et al.*, 1998b; *Sitch et al.*, 2003); r_m typically ranges between 0.020 and 0.070 $[g\,C\ g\,N^{-1}\ day^{-1}]$ (*Sitch et al.*, 2003; *Bonan et al.*, 2003). The terms CN_s, and CN_r $[g\,C\ g\,N^{-1}]$ are the living sapwood and fine root carbon-nitrogen C:N mass ratios, where carbohydrate reserves are assumed to have the same C:N ratio of living sapwood. The temperature dependence $g(T)$ $[-]$ is expressed with a modified Arrhenius equation, with T in $[^\circ C]$:

$$g(T) = e^{308.56\left(\frac{1}{56.02} - \frac{1}{T+46.02}\right)} . \tag{315}$$

The use of the modified Arrhenius equation instead of a fixed Q_{10} (*Nouvellon et al.*, 2000; *Arora*, 2002; *Deckmym et al.*, 2008) is preferred because of the evidence for a constant decline in the apparent Q_{10} of autotrophic respiration with temperature (*Sitch et al.*, 2003).

Note that when T&C solves the ground heat flux with the “force-restore method”, i.e., without explicitly resolving the soil thermal profile (Section 5.5), the temperature at the dampening depth T_d, is used as a proxy of the rooting depth temperature.

Foliage respiration R_{mF} is estimated as the daily sum of maintenance respiration, R_{dC}, that is estimated at the hourly scale in the photosynthesis and stomatal resistance module (Section 6.6). The carbon-nitrogen C:N mass ratios for living sapwood and fine roots CN_s, CN_r, can be explicitly assigned for a given species or they can be estimated from a fixed ratio between these quantities and the reference foliage carbon-nitrogen C:N mass ratio CN_l $[g\,C\ g\,N^{-1}]$, as proposed by *Friend et al.* (1997):

$$CN_s = CN_l/0.145 , \tag{316}$$

$$CN_r = CN_l/0.860 . \tag{317}$$

Values of C:N mass ratio for leaves and grasses, CN_l, can be found in literature for different species (*White et al.*, 2000; *Wright et al.*, 2004). Typical values are $CN_l = 20 - 50$ $[g\,C\ g\,N^{-1}]$.

As can be observed from Eq.(307), the net primary production is positive when carbon uptake from photosynthesis exceeds autotrophic respiration, a situation characteristic of favorable daily meteorological conditions. The value of NPP is negative at night or when environmental stresses, such as soil moisture deficit, do not allow vegetation to effectively photosynthesize and maintenance costs are higher than gross carbon uptake.

17.2 Carbon budget

The mass balance of the carbon pools: C_{leaf}, C_{sapw}, C_{root}, C_{hydr}, C_{flfr}, C_{heaw}, and C_{ldea} is simulated using a system of ordinary differential equations (*Dickinson et al.*, 1998; *Arora and Boer*, 2005; *Ivanov et al.*, 2008b). When Net Primary Production NPP (Section 17.1) is positive, the carbon changes in the pools are:

$$
\begin{aligned}
\frac{dC_{leaf}}{dt} &= f_l\, NPP - S_{leaf} + Tr_l\,, && (318)\\
\frac{dC_{sapw}}{dt} &= f_s\, NPP - S_{sapw}\,, && (319)\\
\frac{dC_{root}}{dt} &= f_r\, NPP - S_{root} + Tr_r\,, && (320)\\
\frac{dC_{hydr}}{dt} &= f_h\, NPP - Tr_C - R_{exmy} + Add_{AR}\,, && (321)\\
\frac{dC_{flfr}}{dt} &= f_f\, NPP - S_{flfr}\,, && (322)\\
\frac{dC_{heaw}}{dt} &= S_{sapw} - S_{wood}\,, && (323)\\
\frac{dC_{ldea}}{dt} &= S_{leaf} - S_{ldea}\,, && (324)
\end{aligned}
$$

where f_x are the five allocation fractions corresponding to green aboveground biomass (f_l), living sapwood (f_s), fine roots (f_r), carbohydrate reserves (f_h), and fruit and flowers (f_f) (Section 17.3.1). The terms S_{leaf}, S_{sapw}, S_{root}, S_{flfr} and S_{ldea} $[g\,C\ m^{-2}\ VEG\ day^{-1}]$ are the tissue turnover rates; S_{wood} $[g\,C\ m^{-2}\,VEG\ day^{-1}]$ is the conversion of living sapwood into heartwood or dead sapwood; Tr_C $[g\,C\ m^{-2}\,VEG\ day^{-1}]$ is the rate of translocation from carbohydrate reserves, which is subdivided into translocation to green aboveground biomass Tr_l, and fine roots Tr_r. The term R_{exmy} and Add_{AR} $[g\,C\ m^{-2}\,VEG\ day^{-1}]$ are the total carbon exudated and exported from the roots (Section 17.3.2), and the additional allocation to reserves in case of occurrence of environmental constraints on growth (Section 17.3.7).

When NPP is negative, gross primary production GPP, less eventually growth respiration rate R_g, is partitioned among the various pools. The respective maintenance respiration costs R_m, are then subtracted from the specific carbon pools:

$$\begin{aligned}
\frac{dC_{leaf}}{dt} &= f_l(GPP - R_g) - \kappa R_{dC} - S_{leaf} + Tr_l\,, && (325)\\
\frac{dC_{sapw}}{dt} &= f_s(GPP - R_g) - R_{mS} - S_{sapw}\,, && (326)\\
\frac{dC_{root}}{dt} &= f_r(GPP - R_g) - R_{mR} - S_{root} + Tr_r\,, && (327)\\
\frac{dC_{hydr}}{dt} &= f_h(GPP - R_g) - R_{mH} - Tr_C - R_{exmy}\,, && (328)\\
\frac{dC_{flfr}}{dt} &= f_f(GPP - R_g) - S_{flfr}\,, && (329)\\
\frac{dC_{heaw}}{dt} &= S_{sapw} - S_{wood}\,, && (330)\\
\frac{dC_{ldea}}{dt} &= S_{leaf} - S_{ldea}\,, && (331)
\end{aligned}$$

In order to avoid that maintenance respiration is consuming leaf biomass directly, when $f_l(GPP - R_g)$ is less than κR_{dC} an amount of carbon is transferred from the carbohydrate reserves to support the leaf maintenance respiration, without affecting C_{leaf} directly. This precaution is necessary to avoid unrealistic drops in leaf biomass caused by maintenance respiration rather than stress turnover when NPP is negative.

The system of ordinary differential equations (318)-(324) or (325)-(331) is solved with an explicit *Runge-Kutta(4,5)* formulation.

Another important characteristic of productivity is the Above-Ground Net Primary Production $ANPP$ [$gC\ m^{-2}\,VEG\ day^{-1}$]. The term $ANPP$ represents the aboveground productivity and provides a value that can be compared with in situ measurements, since estimates of $ANPP$ are generally more frequently available than NPP or GPP measurements:

$$ANPP = \frac{dC_{leaf} + f_{ab}\,dC_{sapw} + f_{ab}\,dC_{hydr} + dC_{flfr}}{dt} + S_{leaf} + f_{ab}S_{sapw} + S_{flfr}\,. \qquad (332)$$

Note that Eq. (332) implies that a fraction f_{ab} of carbohydrate reserves and living sapwood are located in the aboveground. For the grass category ($\Xi = 2$), carbohydrate reserve are assumed to be completely stored belowground and ANPP is compute only through changes in C_{leaf} and C_{flfr}.

17.2.1 Carbon starvation

A note must be dedicated to the possibility for the model to simulate tree mortality. Among the possible mechanisms proposed to explain tree mortality (*McDowell et al.*, 2008; *Sala*, 2009) solely carbon starvation is simulated. Carbon starvation may occur after an extended period of environmental stress, mainly drought, where negative NPP induces a deprivation of carbon in the various pools. When carbon content in the various compartments, especially in the carbohydrate reserve pool, is extremely reduced, new favorable environmental conditions cannot be sufficient for the plant to recover and when $C_{hydr} = 0$ the vegetation dies. The possibility that plants can die of hydraulic failure due to cavitation in the xylem (*Pockman and Sperry*, 2000; *McDowell et al.*, 2008), is not foreseen in T&C since the plant hydraulic functions are not currently explicitly solved (Section 13.2).

17.3 Carbon allocation and translocation

Carbon assimilated through photosynthetic process is allocated to the different carbon pools. Carbohydrate allocation currently represents a central and poorly constrained component in terrestrial biosphere models. Physiological and biochemical mechanisms that control the allocation of photosynthate under resource stresses are only partially understood (*Friedlingstein et al.*, 1998). Hence, a mechanistic formulation of allocation remains a thorny issue (*LeRoux et al.*, 2001; *Niklas and Enquist*, 2002; *Litton et al.*, 2007; *Franklin et al.*, 2012; *Mäkelä*, 2012; *Fatichi et al.*, 2014a).

Carbon allocation in T&C is strongly based on *Friedlingstein et al.* (1998) and *Krinner et al.* (2005), who provide an allocation scheme that responds dynamically to time variability of resources. The use of dynamic, stress-dependent scheme permits more flexible patterns of carbon redistribution (*Arora and Boer*, 2005; *Ivanov et al.*, 2008b). The basic hypothesis in the model of *Friedlingstein et al.* (1998) is that a plant will allocate carbon to different compartments in response to external limitations due to water, light, and nitrogen. The allocation is also made dependent on the phenological state that a plant experiences. For instance, carbon is allocated entirely to leaves during the maximum growth state and predominantly to carbohydrate reserves during senescence (Section 20). Carbon allocation is finally regulated by allometric constraints. T&C uses two fundamental allometric constraints: a minimum root:shoot ratio, i.e., the ratio of fine root carbon to foliage carbon; and an upper limit for storage of carbohydrate reserves. The latter limit is parameterized as a constant fraction of living sapwood biomass (or of fine root biomass for herbaceous species). First, constraint-free allocation coefficients are estimated. A subsequent procedure modifies these allocations, so that allometric limits are satisfied.

17.3.1 Allocation fractions

The original allocation scheme presented by *Friedlingstein et al.* (1998) calculates the allocation fractions for three compartments (leaves, stems, roots). A modification implemented in the *ORCHIDEE* model (*Krinner et al.*, 2005) considers eight biomass compartments, among which carbon can be allocated to six. In T&C this scheme is further modified to allocate to five carbon pools. The five allocation fractions correspond to green aboveground biomass (f_l), living sapwood (f_s), fine roots (f_r), carbohydrate reserves (f_h), and fruit and flowers (f_f). There is no allocation to tree heartwood pool as the latter is produced by the slow conversion of living sapwood, as well as dead-standing leaves are produced by the turnover of alive leaves.

The limiting factors for allocation are preliminarily computed and they account for root zone soil moisture availability A_H $[-]$, light availability A_L $[-]$, and nitrogen availability A_N $[-]$:

$$\begin{aligned} A_H &= \max\left[0.1, \min\left(1, \beta_{R,all}\right)\right] \;, && (333) \\ A_L &= \max\left[0.1, e^{-K_e\, LAI}\right] \;, && (334) \\ A_N &= \max\left[0.1, F_{NC}\right] \;, && (335) \end{aligned}$$

where $\beta_{R,all}$ $[-]$ is the daily averaged soil moisture stress factor in the root zone for the carbon allocation calculated using the leaf water potential Ψ_l $[MPa]$ as described in Eq. (384) (see description of $\beta_{R,all}$ in Section 17.3.7). The LAI $[m^2\ leaf\ area\ m^{-2}\ VEG\,area]$ is the living leaf area index and $K_e = 0.15$ is a constant light extinction coefficient used in the allocation module. The nitrogen availability factor F_{NC} is 1 when there are not nutrient limitations and less than 1 otherwise. It is computed as the average number of days, nutrient concentration was minimal in the plant tissues in the last 90 days.

The belowground availabilities A_N and A_H are combined to a single belowground availability, $A_B = \min(A_N, A_H)$. The belowground and light availabilities are finally used to calculate preliminary allocation fractions to leaves, $\widetilde{f_l}$ $[-]$, fine roots, $\widetilde{f_r}$ $[-]$, and living sapwood, $\widetilde{f_s}$ $[-]$:

$$\begin{aligned} \widetilde{f_r} &= \max\left[r_{min},\ r_0 \frac{3A_L}{A_L + 2A_B}\right] \;, && (336) \\ \widetilde{f_s} &= \min\left[0,75,\ s_0 \frac{3A_B}{2A_L + A_B}\right] \;, && (337) \\ \widetilde{f_l} &= \max\left[a_{min}, \min\left(a_{max}, 1 - \widetilde{f_r} - \widetilde{f_s}\right)\right] \;, && (338) \end{aligned}$$

where $r_{min} = 0.15$, $a_{min} = 0.2$, $a_{max} = 0.5$, and r_0 and s_0 are coefficients that indicate the theoretically unstressed allocation to leaves, fine roots, and living sapwood. The coefficients r_0 and s_0, for woody plants, are a function of the tree biomass, which is typically related to the total stand biomass and tree density (*Niklas and Enquist*, 2002; *Wolf et al.*, 2011b,a). However, since forest demography is not currently simulated in T&C, constant values $r_0 = s_0 = 0.3$ are assumed following *Krinner et al.* (2005). The preliminary root allocation fraction is then recalculated as: $\widetilde{f_r} = 1 - \widetilde{f_l} - \widetilde{f_s}$, that gives $\widetilde{f_l} + \widetilde{f_r} + \widetilde{f_s} = 1$.

For grasses species ($\Xi = 2$) there is no allocation to the living sapwood, in this case the computed $\widetilde{f_s}$ is partitioned among $\widetilde{f_l}$ and $\widetilde{f_r}$ proportionally to their previous values with $\widetilde{f_s} = 0$.

For tropical evergreen species ($\Xi = 3$), the preliminary carbon allocation fraction to leaves is computed as $\widetilde{f_l} = 1 - d_{LO}/A_{cr}$ where A_{cr} $[days]$ is the critical leaf age and d_{LO} $[days]$ is a phenological index counting the days after the beginning of the new season (see Section 17.4.1 and 20). The remaining assimilated carbon is partitioned among $\widetilde{f_r}$ and $\widetilde{f_s}$ proportionally to their previous values . Tropical evergreen forests do not experience proper senescence and dormant phases and carbon is allocated to reproductive organs year-round. This change in the preliminary allocation is necessary to reproduce the light-phenological cycle of tropical evergreen plants with maximal allocation to leaf at the beginning of the dry season (*Wu et al.*, 2016).

Generally, the scheme to calculate preliminary allocation fractions provides more carbon allocation to roots when soil moisture or nitrogen are limiting in order to increase the belowground biomass (Figure 32). More carbon is provided to sapwood when foliage significantly limits light penetration to lower levels of the canopy, in order to increase the canopy supporting structure (Figure 32).

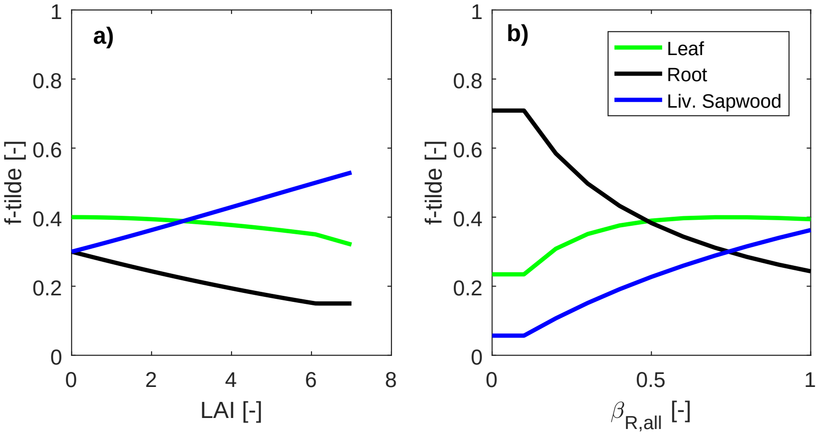

Figure 32: Preliminary allocation fractions to leaves, $\widetilde{f_l}$, fine roots, $\widetilde{f_r}$, and living sapwood, $\widetilde{f_s}$ as a function of LAI with $\beta_{R,all} = 1$ and $F_{NC} = 1$ (a); and as a function of $\beta_{R,all}$ with $LAI = 2$ and $F_{NC} = 1$ (b).

The reproduction costs, i.e., the carbohydrates allocated to produce reproductive organs and propagules typically range between 5% and 20% (*Larcher*, 2001) of the assimilated carbon. In T&C, an allocation fraction to reproductive organs f_f is used during the maximum growth and normal growth phenological phases (Section 20), $f_f = 0$ otherwise. During senescence or dormant phenological phases it is assumed that the plant does not produce fruit or flowers, i.e. does not invest in reproduction. This assumption is reasonable if we consider that the allocable carbon during the senescence and dormant phenological phases is rather small. Tropical evergreen species ($\Xi = 3$) do not experience proper senescence and dormant phases and therefore they always allocate carbon to reproductive organs. A typical value of $f_f = 0.1$ is used for natural plants and grasses, however these value can increase considerably ($f_f = 0.5 - 0.65$) for crops and plantations.

During the maximum growth phenological phase (see Section 20), all of the preliminary fractions are modified to allocate all the synthesized carbon to C_{leaf}, i.e., $\widetilde{f_l} = 1$ and $\widetilde{f_r} = 0$, $\widetilde{f_s} = 0$. Combined with translocation of carbon from reserves, this assumption permits a rapid attainment of a relatively dense leaf cover at the beginning of the season, which would be impossible to realize with newly assimilated carbon only.

The allocation toward the carbohydrate reserves f_h, is tentatively computed as a function of the sum of the preliminary allocation fractions $\widetilde{f_l}$ and $\widetilde{f_r}$ (as the carbohydrate reserves will later be translocated toward the leaves and roots) (*Krinner et al.*, 2005):

$$f_h = (1 - C)(1 - f_f)\,, \tag{339}$$

where

$$C = \frac{1}{1 + \varepsilon_{al}(\widetilde{f_l} + \widetilde{f_r})}\,. \tag{340}$$

The term ε_{al} $[0-1]$ is a parameter controlling carbohydrate reserve allocation (*Krinner et al.*, 2005). Typically, $\varepsilon_{al} = 1$ for seasonal plants ($\Xi = 1$) and grasslands ($\Xi = 1$) and $\varepsilon_{al} < 1$ for evergreen plants ($\Xi = 0$ and $\Xi = 3$). Note that when $\varepsilon_{al} = 0$, $C = 1$, i.e., there is not allocation toward reserves. Therefore also evergreen plants must have $\varepsilon_{al} > 0$ to allow the existence of a carbohydrate reserve pool that can be used during leaf onset and for root exudation and mycorrhiza export (*Hansen and Beck*, 1990; *Chapin III et al.*, 1990; *Kobe*, 1997). Typical values of $\varepsilon_{al} = 0.2 - 0.5$ have been found to provide realistic results for evergreen species.

For seasonal plants outside of the growing season i.e., when a plant is in the senescence or dormant phenological states (Section 20), carbon is not allocated to leaves, roots, or living sapwood but only to reserves. The plant is assumed to save carbon for the next season and all assimilated products are allocated to the carbohydrate reserves: $f_h = 1$. All the other allocation fractions are set to zero (*Krinner et al.*, 2005). Note that during the senescence or dormant phenological phases, carbon available for allocation is scarce due to unfavorable environmental conditions and leaf shedding.

Temperate and tropical evergreens ($\Xi = 0$ and $\Xi = 3$) are an exception to the above behavior and for these plants carbon is allocated to all of the compartments, including reserves throughout the entire year. For evergreens, senescence and the dormant phenological phases are treated differently from other species (see also Section 20) and are similar to the normal growth phase from a carbon allocation point of view. For tropical evergreens ($\Xi = 3$) they are in fact identical to normal growth and for general evergreens ($\Xi = 0$) the only difference is the lack of allocation to the fruit and flower pool. Finally, for all of the vegetation categories during the phenological phase of maximum growth (Section 20), allocation to carbohydrate reserves is set equal to zero ($f_h = 0$), imposing $C = 1$.

The final allocation fractions f are calculated as:

$$f_l = \widetilde{f_l}(1 - f_f)\, C\,, \tag{341}$$

$$f_r = \widetilde{f_r}(1 - f_f)\, C\,, \tag{342}$$

$$f_s = \widetilde{f_s}(1 - f_f)\, C\,, \tag{343}$$

subject to the condition $f_l + f_r + f_s + f_f + f_h = 1$.

17.3.2 Root exudation, transfer to mycorrhizal fungi, and carbon cost of biological N fixation

The evaluation of root exudation, carbon export to mycorrhiza, and carbon allocated to the root-nodules for biological fixation is inspired by the rationale of the FUN2.0 model presented by *Fisher et al.* (2010) and *Brzostek et al.* (2014). The original FUN2.0 model builds a resistor network for the cost of nitrogen acquisition, corresponding to the amount of nitrogen needed to support net primary production. The model computes the integrated carbon costs across a series of pathways, where the amount of carbon spent on each pathway depends on the resistance through that pathway (*Brzostek et al.*, 2014). Specifically, the model includes costs related to non-mycorrhizal, ectomycorrhizal, and arbuscular mycorrhizal active nitrogen uptake, which depends on soil nitrogen and fine root biomass, the cost of biological nitrogen fixation, which depends on soil temperature, and the cost of retranslocation, which depends on the amount of foliar nitrogen. The original FUN2.0 model operates at an annual time step.

In T&C foliar nutrient re-translocation is already accounted for at the plant-level (Section 19) and is therefore excluded from this carbon cost computation. Additionally, the overall scheme is modified for coherence with the plant nutrient uptake formulation described in Section 19.2 and the daily time step of T&C, and it is extended to include phosphorus and potassium.

The sum of the carbon exudated and exported R_{exmy} $[gC\ m^{-2}\,day^{-1}]$ from the roots is the maximum between the cost of N, P, and K acquisition:

$$R_{exmy} = \max([C_{acq,N}\,N_{upI}], [C_{acq,P}\,P_{upI}], [C_{acq,K}\,K_{upI}])\,, \tag{344}$$

where N_{upI} $[gN\ m^{-2}\,day^{-1}]$, P_{upI} $[gP\ m^{-2}\,day^{-1}]$, K_{upI} $[gK\ m^{-2}\,day^{-1}]$ are the uptake rates of nitrogen, phosphorus, and potassium, averaged over the previous 365 days. The terms $C_{acq,N}$ $[gC\ gN^{-1}]$, $C_{acq,P}$ $[gC\ gP^{-1}]$, $C_{acq,K}$ $[gC\ gK^{-1}]$ are the costs of nitrogen, phosphorus, and potassium acquisition, respectively. These are computed assuming the costs of nutrient acquisition as resistors in parallel using Ohm's law in analogy to electric circuits (*Brzostek et al.*, 2014):

$$C_{acq,N} = \left(\frac{1}{C_{acq,R_N}} + \frac{EM}{C_{acq,EM_N}} + \frac{1-EM}{C_{acq,AM_N}} + \frac{1}{C_{fix,N}}\right)^{-1}\,, \tag{345}$$

$$C_{acq,P} = \left(\frac{1}{C_{acq,R_P}} + \frac{EM}{C_{acq,EM_P}} + \frac{1-EM}{C_{acq,AM_P}}\right)^{-1}\,, \tag{346}$$

$$C_{acq,K} = \left(\frac{1}{C_{acq,R_K}} + \frac{EM}{C_{acq,EM_K}} + \frac{1-EM}{C_{acq,AM_K}}\right)^{-1}\,, \tag{347}$$

where EM $[-]$ is the fraction of ectomycorrhizal fungi and $1-EM$ corresponds to the fraction of arbuscular mycorrhizal fungi in a given computational element. The terms $C_{acq,R}$, $C_{acq,EM}$, $C_{acq,AM}$, $C_{fix,N}$ are the carbon costs for nutrient acquisition of the non-mycorrhizal, ectomycorrhizal, arbuscular mycorrhizal and biological N-fixation pathways, respectively. In the following, fine root costs are denoted by subscript (1), mycorrhizal costs by subscript (2) and biological N fixation by subscript (3). The cost of biological N fixation is present only for nitrogen acquisition and is disabled whenever biological N fixation does not occur.

In a general form, the cost of acquisition $C_{acq,X}$ $[gC\, gX^{-1}]$ of a generic nutrient X $[g\, X\ m^{-2}]$ is proportional to the carbon investment R_{ex} $[gC\ m^{-2}\, day^{-1}]$ made for its acquisition through a given pathway (e.g., for fine roots $R_{ex,1}$, for mycorrhizae $R_{ex,2}$, and for root-nodules associated with biological N fixation $R_{ex,3}$) and inversely proportional to the amount of nutrient taken up X_{up} $[g\, X\ m^{-2}\, day^{-1}]$ in that pathway in a given period:

$$C_{acq,X} = \frac{R_{ex}}{X_{up}}. \tag{348}$$

Uptake functions for ectomycorrhizal fungi, arbuscular mycorrhizae and fine roots are defined in Section 19.2 (e.g., Eq. 438) and can be generally written as:

$$X_{up} = V_D \frac{X\, B_{root}^{3/2}}{r_r}, \tag{349}$$

$$X_{up} = V_D \frac{X\, C_{EM}^{3/2}}{r_{em}}, \tag{350}$$

$$X_{up} = V_D \frac{X\, C_{AM}^{3/2}}{r_{am}}, \tag{351}$$

Substituting X_{up} in Eq. 348 allows to compute carbon costs as a function of nutrient amount in the soil X and fine root or mycorrhizal fungi biomass. Furthermore, considering that mycorrhizal biomass is solely fed by R_{ex}, in a steady-state condition, the carbon export to mycorrhizae must sustain mycorrhizal biomass. Then, carbon export can be related to its biomass through the turnover coefficient m_r $[day^{-1}]$, i.e., $C_{EM} = m_r\, R_{ex,2}$ or $C_{AM} = m_r\, R_{ex,2}$, where m_r is potentially different for ectomycorrhizal and arbuscular mycorrhizal fungi (Table 5). It follows that nutrient acquisition costs can be summarized as:

$$C_{acq,R} = \frac{k_R}{X B_{root}^{3/2}}, \tag{352}$$

$$C_{acq,EM} = \frac{k_{EM}}{X C_{EM}^{1/2}}, \tag{353}$$

$$C_{acq,AM} = \frac{k_{AM}}{X C_{AM}^{1/2}}, \tag{354}$$

where $k_R = (R_{ex,1}\, r_r)/(V_D)$, $[g\, C^{5/2}\ m^{-5}]$, $k_{EM} = r_{em}/(V_D\, m_r)$ $[g\, C^{3/2}\ m^{-3}]$, and $k_{AM} = r_{em}/(V_D\, m_r)$ $[g\, C^{3/2}\ m^{-3}]$ embeds all the dependencies on other parameters such as diffusion coefficient at the root or hypha interfaces and uptake resistance terms (Section 19.2). The parameter k_R is also dependent on the carbon investment in the non-mycorrhizal pathway itself $R_{ex,1}$. The expressions in Eq. 352 to 354 are a consequence of the formulation of nutrient uptake rates (Section 19.2) and differ from the original FUN 2.0 equation $C_{acq} = \frac{kx}{X} + \frac{kc}{B_{root}}$, where cost functions responded to a change in the amount of root biomass also for ectomycorrhizal and arbuscular mycorrhizal fungi but conversely they do not depend on mycorrhizal biomasses.

The expressions in Eq. 352 to 354 can be used separately for the three nutrients considered in T&C. Therefore, the costs of nitrogen acquisition are:

$$
\begin{aligned}
C_{acq,R_N} &= \frac{k_{R,N}}{\overline{N_{avI}} B_{root}^{3/2}} \,, && (355)\\
C_{acq,EM_N} &= \frac{k_{EM,N}}{\overline{N_{avI}} C_{EM}^{1/2}} \,, && (356)\\
C_{acq,AM_N} &= \frac{k_{AM,N}}{\overline{N_{avI}} C_{AM}^{1/2}} \,, && (357)
\end{aligned}
$$

where $\overline{N_{avI}}$ $[gN\ m^{-2}]$ is the minimum between the average mineral nitrogen in the soil in the previous year and the nitrogen uptake N_{upI} averaged over the previous year, B_{root} $[gC\ m^{-2}\,VEG]$ is the amount of root biomass, and the nitrogen cost coefficients ($k_{R,N}$, $k_{EM,N}$, and $k_{AM,N}$) are given in Table 1. Equivalent expressions are written for the costs of phosphorus and potassium. Mineral nutrient availability in Eq. 355- 357 is capped with the previous year nutrient uptake to avoid an unrealistic feedback, where nutrient availability increases, decreasing uptake costs and allocation to mycorrhizal fungi, which in turn leads to an even larger increase in soil nutrient content. In this case, unrealistic plant nutrient limitations would develop due to minimal amounts of mycorrhizal fungi and low nutrient uptake capacity, despite a relatively high nutrient availability. The trade-offs imposed by equations 355-357 are summarized in Figure 33.

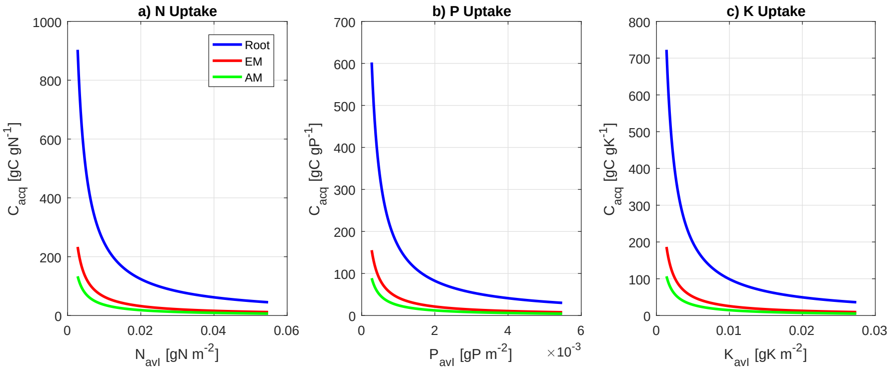

Figure 33: Costs of nitrogen, phosphorus, and potassium acquisition $C_{acq,R}$, $C_{acq,EM}$,and $C_{acq,AM}$, for different values of nutrient availability in the soil. Root biomass $B_{root} = 200\ gC\ m^{-2}$, ectomycorrhizal biomass $C_{EM} = 30\ g\,C\ m^{-2}$ and arbuscular mycorrhizal biomass $C_{AM} = 30\ g\,C\ m^{-2}$ are fixed in this figure.

The coefficients k_R, k_{EM}, and k_{AM} of Eq. (352) to (354) can be directly computed from the resistances and diffusion coefficient parameters defined in Section 19.2. However, variability in nutrient availability X, and potentially different costs of ectomycorrhizal and arbuscular mycorrhizal fungi would not be accounted for by such a direct computation. This implies that k_R, k_{EM} and and k_{AM} must be selected to provide reasonable carbon costs of nitrogen acquisition that are also comparable

Root of hyphae	**N coefficients**	**P coefficients**	**K coefficients**
Root	$k_{R,N} = 7000$	$k_{R,P} = k_{R,N}/15$	$k_{R,K} = k_{R,N}/2.5$
EM	$k_{EM,N} = 3.5$	$k_{EM,P} = k_{EM,N}/15$	$k_{EM,K} = k_{EM,N}/2.5$
AM	$k_{AM,N} = 2.0$	$k_{AM,P} = k_{AM,N}/15$	$k_{AM,K} = k_{AM,N}/2.5$

Table 1: Cost parameters that control the carbon allocation to arbuscular mycorrhizal (subscript AM) and ectomycorrhizal fungi (subscript EM) and the investment in root exudates (subscript R). The units of $k_{R,N}$ are $[g\,C^{5/2}\ m^{-5}]$, for $k_{EM,N}$ and $k_{AM,N}$ are $[g\,C^{3/2}\ m^{-3}]$.

with the original FUN2.0 model (*Brzostek et al.*, 2014). Concurrently, the costs for nitrogen, phosphorus, and potassium must scale roughly proportionally to the plant stoichiometric composition for these nutrients to preserve a balance in the acquisition costs. On the basis of these considerations, cost coefficients are defined in Table 1.

Note that the value selected for $k_{AM,N}$ is matching $r_{em}/(V_D\, m_r)$, which reinforces the coherence between the expressions used to compute root exudation and carbon export to mycorrhizae (Eq. 355 to 357) and the expressions for root, ectomycorrhizal, and arbuscular mycorrhizal nutrient uptake rates (Section 19.2). Furthermore, the cost parameters in Table 1 are such that arbuscular mycorrhizal or ectomycorrhizal fungi are much more beneficial to the plant in acquiring nutrients than roots (*Brzostek et al.*, 2014). This is especially true for medium and low nitrogen availability because roots have limited ability to produce enzymes and have a much lower surface area-to-volume ratio than fungal hyphae (e.g., *Smith and Smith*, 2011). This characteristic becomes less important at higher levels of soil nutrients, where fine roots can take up a sufficient amount of nutrients, regardless of mycorrhizae (Figure 34). In such a condition, the cost-to benefit ratio of supporting mycorrhizae decreases (*Brzostek et al.*, 2014). The ability of arbuscular mycorrhizal fungi to act as scavengers is accounted for by assigning the lowest cost for a given nutrient availability (i.e., $k_{AM} < k_{EM}$). Increasing k_{EM} in ectomycorrhizal fungi means that they are more costly to maintain for the same nutrient availability in the soil. However, ectomycorrhizal fungi are able to produce oxidative enzymes (e.g., *Baskaran et al.*, 2017) and this can contribute to nutrient mineralization and therefore increased nutrient availability (as accounted for in T&C, see Section 21.4.2). This should also favor shifts in the abundance of arbuscular mycorrhizal and ectomycorrhizal fungi and plants across fertility and latitudinal gradients, as it was observed (*Phillips et al.*, 2013).

The carbon cost of biological nitrogen fixation, $C_{fix,N}$ $[g\,C\ g\,N^{-1}]$, follows *Brzostek et al.* (2014) and is a function of the soil temperature T_{bg} $[°C]$ in the soil biogeochemically active zone:

$$C_{fix,N} = s\left[\exp\left(a + b\,T_{bg}\left[1 - 0.5\frac{T_{bg}}{c}\right]\right) - 2\right], \tag{358}$$

where $a = -3.62$, $b = 0.27$, $c = 25.14$, $s = -30$ are empirical curve-fitting parameters

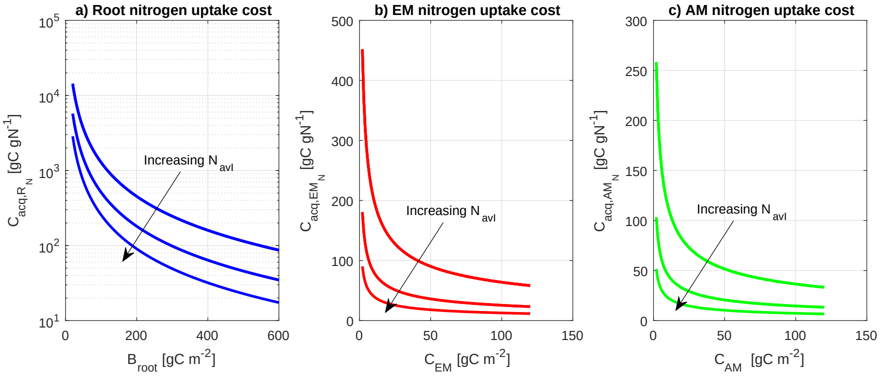

Figure 34: Costs of nitrogen acquisition C_{acq,R_N}, C_{acq,EM_N}, and C_{acq,AM_N}, for different values of fine root biomass, B_{root}, ectomycorrhizal biomass C_{EM} and arbuscular mycorrhizal biomass C_{AM}. Three different values of $\overline{N_{avI}}$, 0.0055, 0.0137, and 0.0274 $g\,N; m^{-2}$ are used for the representation. Note the different scales on the y-axes and the logarithmic axes for C_{acq,R_N}.

(Figure 35).

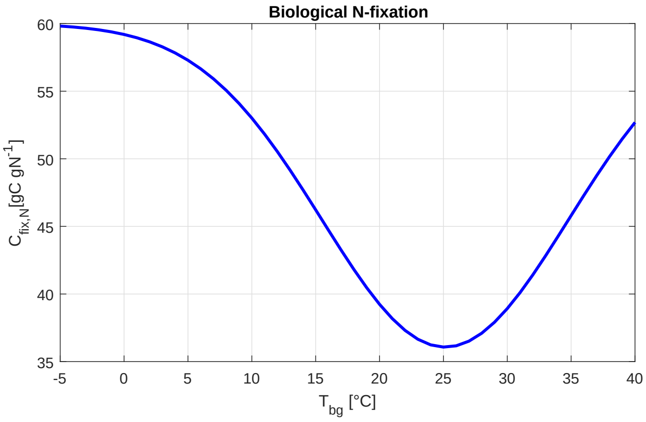

Figure 35: Change in the carbon cost of biological nitrogen fixation, $C_{fix,N}$ $[g\,C\;g\,N^{-1}]$, with soil temperature T_{bg} $[^{\circ}C]$ in the soil biogeochemically active zone.

Finally, the total carbon exported from roots R_{exmy} $[gC\;\;m^{-2}\,day^{-1}]$ needs to be partitioned among root exudation $R_{ex,1}$, export to arbuscular mycorrhizal and ectomycorrhizal fungi $R_{ex,2}$, and carbon allocated to root nodules for biological N fixation $R_{ex,3}$.

$$R_{ex,1} = R_{exmy}\frac{X_{ut,ex}}{X_{ut,tot}}\,, \tag{359}$$

$$R_{ex,2} = R_{exmy}\frac{X_{ut,em}+X_{ut,am}}{X_{ut,tot}}\,, \tag{360}$$

$$R_{ex,3} = R_{exmy}\frac{X_{ut,bnf}}{X_{ut,tot}}\,, \tag{361}$$

This is done computing the theoretical nutrient uptake for each pathway corresponding to the estimated cost. The theoretical total nutrient uptake rate $X_{ut,tot}$

$[gX\ m^{-2}\, day^{-1}]$ is:

$$X_{ut,tot} = X_{ut,bnf} + X_{ut,ex} + X_{ut,am} + X_{ut,em}\,, \tag{362}$$

where $X_{ut,bnf}$, $X_{ut,ex}$, $X_{ut,am}$, $X_{ut,em}$ $[gX\ m^{-2}\, day^{-1}]$ are the theoretical nutrient uptake rates following the cost functions defined above for biological nitrogen fixation, non-mycorrhizal, arbuscular mycorrhizal and ectomycorrhizal fungi. For nitrogen:

$$N_{ut,bnf} = \frac{R_{exmy}}{C_{fix,N}}\,, \tag{363}$$

$$N_{ut,ex} = \frac{R_{exmy}}{C_{acq,R_N}}\,, \tag{364}$$

$$N_{ut,am} = (1 - EM)\,\frac{R_{exmy}}{C_{acq,AM_N}}\,, \tag{365}$$

$$N_{ut,em} = EM\,\frac{R_{exmy}}{C_{acq,EM_N}}\,. \tag{366}$$

The term $X_{ut,tot}$ is computed using the cost corresponding to the most difficult nutrient to take up as estimated from the maximum cost in Eq. (344), if P or K are the least available nutrient $X_{ut,bnf} = 0$. Note, that $X_{ut,tot}$ is simply a theoretical nutrient uptake capacity, which serves the purpose of computing carbon exudation and allocation to mycorrhizal fungi. While there is a correspondence, it does not exactly match the actual nutrient uptake in T&C, which is computed following the procedure described in Section 19.2.

The sum of the carbon exported and exudated from the roots R_{exmy} is computed only for days where Net Primary Production NPP is positive and the term is subtracted from the carbohydrate reserves. If $NPP \leq 0$, there is no root carbon export and $R_{exmy} = 0$.

If the soil biogeochemistry component is not enabled then nutrient uptakes (e.g., N_{upI}, P_{upI}, K_{upI}) will be equal to zero, leading to a trivial solution of $R_{exmy} = 0$. In such a case, R_{exmy} is simply computed as fraction of NPP according to Eq. (367):

$$R_{exmy} = d_{exmy}\, NPP\,, \tag{367}$$

where $d_{exmy} = 0.04$ $[-]$ is the unstressed fraction of NPP going into root carbon export. In such a case, $R_{exmy,1} = 0.2R_{exmy}$, $R_{exmy,2} = 0.8R_{exmy}$ and $R_{exmy,3} = 0$, following *Farrar et al.* (2003) for the C fraction partitioning between root exudation and export to mycorrhizae.

17.3.3 Allometric constraints

In addition to the allocation processes described above, two allometric constraints are imposed to refine allocation dynamics. The first one concerns the maximum capacity to store carbohydrate reserves. The constraint on the size of carbohydrate reserves C_{hydr} is parameterized following *Friend et al.* (1997). The maximum value for C_{hydr} is assumed to be 0.67 of the living sapwood biomass C_{sapw} or fine root biomass C_{root} for herbaceous species. Note that this value is consistent with estimates of the fraction of labile carbon in sapwood that are typically around 2-10% of the dry matter (*Hoch et al.*, 2003; *Körner*, 2003; *Gough et al.*, 2009). Considering that on average about 10% of sapwood is alive and the conversion factor 0.5 $[gC\ gDM^{-1}]$ (*Kozlowski and Pallardy*, 1997; *Friend et al.*, 1997), the fraction of carbohydrate reserves to living sapwood is around $0.4 - 2$. These values are generally higher than 0.67. However, the latter is considered to be a realistic approximation considering that a portion of reserves could be sequestered rather than stored in plants and thus not available for translocation (*Körner*, 2003; *Millard and Grelet*, 2010). When the value of 0.67 is exceeded, the carbon theoretically allocated to reserves is partitioned among all of the other carbon pools during normal growth or it is transferred to living sapwood during the senescence and dormancy phenological states. This is valid for vegetation categories, $\Xi = 0,\ 1\ 3$. For grasses ($\Xi = 2$), the maximum of carbohydrate reserves is assumed to be 0.67 of the fine root carbon pool C_{root}. Herbaceous species lack the living sapwood component and all carbohydrates are assumed to be stored in the roots.

The second allometric constraint concerns the leaf-to-root or shoot-to-root ratio, R_{ltr} $[-]$. Vegetation models typically introduce a constant allometric relation on the shoot:root ratio, since leaf biomass needs to be supported by a sufficient amount of transporting tissue (*Lüdeke et al.*, 1994; *Bonan et al.*, 2003; *Sitch et al.*, 2003; *Deckmym et al.*, 2008). In T&C, this value is just a maximum threshold. The allocation to C_{leaf} is constrained when $C_{leaf} > R_{ltr}\ C_{root}$. In this case, $f_l = 0$ and its value is partitioned between f_s and f_r proportionally to their biomasses. The range of variability of R_{ltr} proposed in literature is around $0.2 - 1.5$ with higher values for woody species as compared to grass species (*Sitch et al.*, 2003; *Bonan et al.*, 2003; *Sato et al.*, 2007).

17.3.4 Carbon translocation

Knowledge of dynamics of carbon storage and mobilization from reserves is mainly qualitative (*LeRoux et al.*, 2001). There is evidence that carbohydrate reserves are formed through storage in late summer and fall, they are partially depleted during winter through maintenance respiration and a massive mobilization of reserves occurs in spring to enhance leaf onset and permit plant to photosynthesize more efficiently (*Chapin III et al.*, 1990; *Dickinson et al.*, 2002; *Pregitzer*, 2003; *Krinner et al.*, 2005; *Gough et al.*, 2009). Some studies analyzing non-structural carbohydrates concentration found minor evidence of such dynamics, and identified a mobilization of carbohydrate reserves only after strong environmental stresses (*Körner*, 2003).

In T&C, all of the vegetation categories Ξ have a carbon storage compartment, and thus translocation occurs also for evergreen species. Since few quantitative carbon translocation analyses have been carried out so far (*Gough et al.*, 2009, 2010), mechanistic parameterizations are also lacking. A simple scheme is adopted in T&C. Carbohydrate translocation is modeled to occur during the phenological state of maximum growth (see Section 20) with a prescribed constant rate, Tr_C $[g\,C\ m^{-2}\,VEG\ day^{-1}]$, which is species-dependent. The rate Tr_C is a parameter of the model and suitable values have been found in the range of 0.5-8 $[g\,C\,m^{-2}\,VEG\,day^{-1}]$, with higher values for plants that attain rapidly a high LAI after leaf onset (grasses, temperate deciduous species). Assuming T_{rC} constant, as opposed to be dependent on the reserve size, has shown better results and LAI growth has been observed to be fairly linear during leaf onset in the maximum growth phenological phase. This is likely due to the fact that translocation is a sink- and not source- driven process (*Millard and Grelet*, 2010). The total carbohydrate translocation is then subdivided between translocation to green aboveground biomass Tr_l $[g\,C\ m^{-2}\,VEG\ day^{-1}]$ and fine roots Tr_r $[g\,C\ m^{-2}\,VEG\ day^{-1}]$, inversely proportional to their biomasses.

$$Tr_l = Tr_C \frac{C_{root}}{C_{leaf} + C_{root}}, \tag{368}$$

$$Tr_r = Tr_C \frac{C_{leaf}}{C_{leaf} + C_{root}}. \tag{369}$$

Another potential occurrence of translocation is during maximum or normal growth phenological phases, when the maintenance respiration of leaves is higher than the assimilation rate, i.e., $NPP < 0$. This can be a result of unexpectedly harsh environmental conditions, e.g., a late frost or a very dry period. In this case translocation is considered to compensate the leaf maintenance respiration, in order to avoid a premature and unrealistic drop of leaves because of maintenance respiration costs.

17.3.5 Plant stoichiometric constraints and flexibility

Each plant tissue (carbon pool in the model abstraction) has a corresponding quantity of nutrients, which is necessary for its construction. Nutrients can be also stored in the plant as reserves and stoichiometric ratios of different tissues have been shown to be flexible and to respond to nutrient availability (*Magill et al.*, 2004; *Sistla and Schimel*, 2012; *Zaehle et al.*, 2014). The target stoichiometric ratios are prescribed quantities in the model and define the nutrients required for a given amount of carbon for a plant with a balanced nutrient status (Table 2). Stoichiometric flexibility is explicitly modeled as a two-step process. First, nutrient reserves can buffer uptake and demand for nutrient without modifying the nutrient concentration of structural and non-structural tissues. Second, tissue concentration in the non-structural compartments can be modified to respond to excess or deficit of nutrients, allowing for an actual stoichiometric flexibility. Structural tissues have a fixed stoichiometry.

The maximum plant storages of nitrogen N_{sto} $[g\,N\ m^{-2}\ VEG]$, phosphorus P_{sto} $[g\,P\ m^{-2}\ VEG]$, and potassium K_{sto} $[g\,K\ m^{-2}\ VEG]$ are computed considering a hypothetical stoichiometric flexibility of the carbon reserve pool, which defines a

Pool	C:N $[g\,C\ g\,N^{-1}]$	C:P $[g\,C\ g\,P^{-1}]$	C:K $[g\,C\ g\,K^{-1}]$	Lignin $[g\,Lig\ g\,DM^{-1}]$
C_{leaf}	CN_l	CP_l	CK_l	$Lig_{fr,l}$
C_{sapw}	CN_s	CP_s	CK_s	-
C_{root}	CN_r	CP_r	CK_r	$Lig_{fr,r}$
C_{hydr}	CN_c	CP_c	CK_c	-
C_{flfr}	CN_f	CP_f	CK_f	$Lig_{fr,lf}$
C_{heaw}	CN_h	CP_h	CK_h	$Lig_{fr,h}$

Table 2: List of parameters used to indicate the target stoichiometric mass-ratio of nitrogen, phosphorus, potassium, and lignin in the carbon pools. Note that these ratios are constant, but tissue stoichiometry is flexible thanks to varying relative nutrient concentration (e.g., Eq. 373 and 374). Many of the parameters can be assigned knowing CN_l only and exploiting some proportionality between the other parameters and CN_l (e.g., *Friend et al.*, 1997), as described in Section 17.1.3.

storage size:

$$N_{sto} = \phi_s C_{hydr}\left(\frac{1}{CN_l} - \frac{1}{CN_c}\right), \tag{370}$$

$$P_{sto} = \phi_s C_{hydr}\left(\frac{1}{CP_l} - \frac{1}{CP_c}\right), \tag{371}$$

$$K_{sto} = \phi_s C_{hydr}\left(\frac{1}{CK_l} - \frac{1}{CK_c}\right), \tag{372}$$

where ϕ_s is a scaling parameter. When $\phi_s = 1$, the current option in T&C, the maximum nutrient storage size is simply the size of the carbohydrate reserves with a stoichiometric range that goes from the nutrient content of leaves to the one of heartwood. These can be regarded as the upper and lower extremes of nutrient concentration in the different plant tissues. An increase of nutrient content without exceeding the maximum storage size does not affect the actual nutrient concentration of the different pools. Note that this assumption does not necessarily imply that nutrients are changing in association with the carbon reserve pool but simply that nutrient reserves are changing somewhere within the plant without affecting the nutrient concentration of non-structural pools (leaves, fine roots, fruit and flowers pools). However, if nutrient concentration in the reserves exceeds the maximum nutrient storage or becomes less than zero, i.e., there are not enough nutrients to preserve the targeted stoichiometric relations, the relative nutrient concentration of non-structural tissues is modified (Fig. 36a).

At each time step nutrient reserves (e.g., $N_{reserve}$ for nitrogen) are computed as indicated in Equation (408) and the plant relative nutrient concentration of nitrogen r_{N_c} $[-]$, phosphorus r_{P_c} $[-]$, and potassium r_{K_c} $[-]$ can be computed as:

$$r_{N_c} = 1 + \frac{N_{reserve}}{TNS_N}, \tag{373}$$

if $N_{reserve} < 0$ and therefore the r_{N_c} is less than 1.

Alternatively, when $N_{reserve} > N_{sto}$ the r_{N_c} is larger than 1 and it is computed as:

$$r_{N_c} = 1 + \frac{N_{reserve} - N_{sto}}{TNS_N} \,. \tag{374}$$

Whenever $N_{reserve}$ ranges from 0 to N_{sto} the relative nutrient concentration r_{N_c} remains equal to 1, because of the buffering effect of changes in the nutrient storage (Fig. 36a). Equations equivalent to (373) and (374) are used to compute r_{P_c} and r_{K_c}. Such a modeling solution is adopted to avoid having tissue nutrient concentrations oversensitive to fluctuations in plant nutrient status, which can be a problem in terrestrial biosphere models that introduce stoichiometric flexibility (*Zaehle and Dalmonech*, 2011; *Zaehle et al.*, 2014) and usually it is not observed in nature. The non-structural nitrogen TNS_N, phosphorus TNS_P and potassium TNS_K are computed as indicated in Section 19.

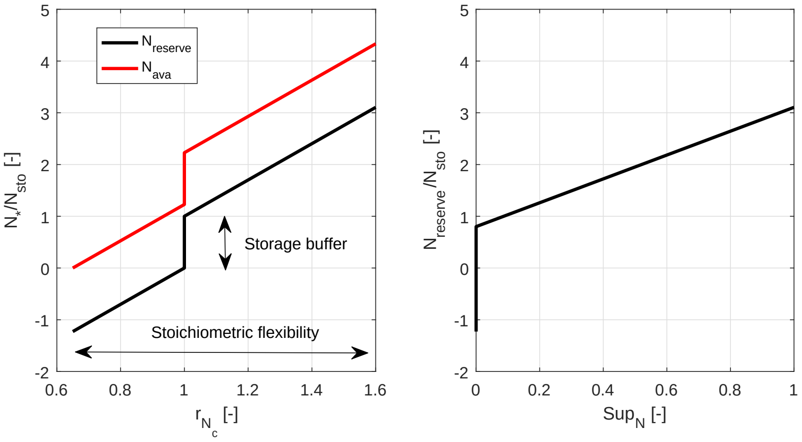

Figure 36: (a) Changes in $N_{reserve}$ and N_{ava} normalized by N_{sto} as a function of relative nitrogen concentration r_{N_c}. The role of N_{sto} in buffering changes in nutrient concentration is highlighted. If $N_{reserve}$ is larger than N_{sto} or lower than zero r_{N_c} is changing. The actual available nitrogen N_{ava} is also reported and it is simply a shifted quantity from $N_{reserve}$. (b) Changes in $N_{reserve}$ normalized by N_{sto} as a function of the nutrient uptake suppression function between 1 (total suppression) and 0 (no suppression).

Since nutrient uptake (Section 19.2) and carbon allocation depend on the plant internal nutrient budget, the relative concentrations r_{N_c} $[-]$, r_{P_c} $[-]$ and r_{K_c} $[-]$, are typically constrained between 0.65 and 1.60 (Fig. 36a), which represent the observed stoichiometric flexibility of non-structural tissues such as leaves and fine roots (*Meyerholt and Zaehle*, 2015).

At each time step the availability of nitrogen N_{ava} $[g\,N\;m^{-2}\;VEG]$, phosphorus P_{ava} $[g\,P\;m^{-2}\;VEG]$, and potassium K_{ava} $[g\,K\;m^{-2}\;VEG]$ to construct new tissue is given by:

$$N_{ava} = N_{reserve} + 0.35 TNS_N \,, \tag{375}$$

$$P_{ava} = P_{reserve} + 0.35 TNS_P \,, \tag{376}$$

$$K_{ava} = K_{reserve} + 0.35 TNS_K \,. \tag{377}$$

Eq. (375)-(377) are imposing a stoichiometric constraint on tissue construction, i.e., they can limit allocation of NPP, whenever the relative nutrient concentration of non-structural tissues r_{N_c}, r_{P_c} or r_{K_c} is dropping at the 0.65 level, a level of stoichiometric flexibility, which is rarely exceeded in reality. In other words, when nutrient reserves in the model, $N_{reserve}$, are negative and equal -0.35 of TNS_N, plant growth is nutrient limited. Note that the negative sign in $N_{reserve}$ is a modeling convenience and simply means a depletion of nutrient in non-structural tissues (e.g., $r_{N_c} < 1$).

The nitrogen required, N_{req} $[g\,N\ m^{-2}\ VEG\ day^{-1}]$ for the allocation of the unconstrained NPP is given by the allocation fraction to the different tissues minus the nutrient retained during tissue turnover:

$$\begin{aligned} N_{req} \ = \ & f_l \frac{NPP}{CN_l} + f_f \frac{NPP}{CN_f} + f_c \frac{NPP}{CN_c} + f_r \frac{NPP}{CN_r} + f_s \frac{NPP}{CN_s} + \\ & \frac{Tr_l}{CN_l} + \frac{Tr_r}{CN_r} + \frac{S_{sapw}}{CN_h} - f_{transf,l} \frac{S_{leaf}}{CN_l} - f_{transf,r} \frac{S_{root}}{CN_r} \\ & - \frac{T_{rC}}{CN_c} - \frac{S_{sapw}}{CN_s} - \frac{R_{exmy}}{CN_c} + \frac{Add_{AR}}{CN_c}, \end{aligned} \tag{378}$$

where f_x $[-]$ are the allocation fractions for NPP (with $x = l, f, c, r, s$ for leaves, flower and fruits, carbohydrate reserves, fine roots, and living sapwood respectively, R_{exmy} is the carbon exudated from roots and exported to mycorrhizal fungi (Section 17.3.2), Add_{AR} is the additional allocation to carbon reserve due to environmental constraints on growth (Section 17.3.7), and S_{sapw} $[g\,C\ m^{-2}\,VEG\ day^{-1}]$, Tr_l and Tr_r $[g\,C\ m^{-2}\,VEG\ day^{-1}]$ are previously defined (Section 17.2). The terms $f_{transf,l}$ and $f_{transf,r}$ are the resorbed fractions of nutrient in the leaves and fine roots. The nutrient resorption fractions $f_{transf,l}$ and $f_{transf,r}$ are introduced to describe translocation of nutrients from senescent leaves and fine roots (*Thomas and Stoddart*, 1980; *Chapin III et al.*, 1990; *Reed et al.*, 2012; *Vergutz et al.*, 2012; *Cleveland et al.*, 2013). This mechanism partially prevents the loss of nutrients for tissue turnover (Section 19.1). Equivalent expressions to Eq. (378) can be written to compute phosphorus P_{req} $[g\,P\ m^{-2}\ VEG\ day^{-1}]$, and potassium K_{req} $[g\,K\ m^{-2}\ VEG\ day^{-1}]$ requirements. If N_{ava}, P_{ava}, and K_{ava} are larger than N_{req}, P_{req}, and K_{req} (the typical case), there are enough nutrients to allocate entirely NPP to the different tissues, otherwise a reduction factor f_{red} $[-]$ is computed for each nutrient (e.g., for nitrogen) as:

$$f_{red} \ = \ \frac{N_{ava}/dt}{N_{req}}, \tag{379}$$

where dt is the time step in days and NPP is corrected as $NPP = f_{red}\,NPP$. The remaining fraction of unallocated NPP is lost through autotrophic respiration as idling (or overflow) respiration $R_i = 1 - f_{red}\,NPP$, because there is insufficient nutrient availability to build tissues. This case should be regarded as rare, in natural conditions, but can occur in nutrient poor soils or for crops where large quantities of nutrients are subtracted through fruit and seed harvesting.

17.3.6 Nitrogen control on photosynthesis and respiration

In several models, leaf nitrogen content is linked to leaf photosynthetic capacity correlating linearly the maximum Rubisco capacity (V_{max}) to nitrogen concentration for unit of leaf area (*Friend and Kiang*, 2005; *Zaehle and Friend*, 2010; *Bonan et al.*, 2011; *Clark et al.*, 2011; *Oleson et al.*, 2013). Some models decompose V_{max} into its fundamental components as specific activity of Rubisco, nitrogen content of Rubisco protein, fraction of leaf nitrogen in Rubisco and leaf nitrogen content (*Niinemets and Tenhunen*, 1997; *Thornton and Zimmermann*, 2007; *Niinemets et al.*, 2015). In T&C, a relative photosynthetic efficiency factor $e_{rel,N}$ is applied to scale V_{max} to account for changes in the relative nitrogen content in the leaves r_{N_c} as:

$$e_{rel,N} \quad = \quad \nu(r_{N_c} - 1) + 1\,, \tag{380}$$

where $\nu = 0.5$ is a smoothing factor to account for the fact that changes in leaf nitrogen content do not directly imply a proportional change of nitrogen content in the Rubisco protein (e.g., *Ainsworth and Long*, 2005). Note that since leaf maintenance respiration is related to V_{max}, a change in $e_{rel,N}$ has also consequences in terms of leaf respiration. Maintenance respiration in the other living tissues is also related to the nitrogen concentration through the carbon-nitrogen mass ratios CN_s and CN_r (Section 17.1.3). The effects of these ratios for respiration are modified using the relative nitrogen concentration coefficient for respiration R_{rN_c}, which is:

$$R_{rN_c} \quad = \quad min\left[1.85, \nu(r_{N_c} - 1) + 1\right]\,, \tag{381}$$

where the smoothing factor ν is still accounting for the fact that changes in nitrogen content related to changes in plant-nutrient status do not directly imply a proportional change in respiration. Furthermore, we assume that respiration costs for unit of nitrogen cannot increase beyond 85% of the base respiration coefficient to avoid unrealistic respiration costs at very high nutrient concentrations.

17.3.7 Environmental constraints

There is evidence from plant physiological literature suggesting that direct control of carbon sinks (defined as growth in the sense of carbon investment on plant tissue expansion) via environmental factors could be more important than indirect control via photosynthesis, the carbon source (*Fatichi et al.*, 2014a). For example, water- or temperature-limited plants tend to reduce growth but increase carbon storage (*Körner*, 2003; *Sala and Hoch*, 2009; *Woodruff and Meinzer*, 2011; *Sala et al.*, 2012), which suggests that environmental controls act first on sink activity rather than source activity (*Körner*, 2015). An option to introduce these environmental constraints acting directing on plant growth is made available in T&C. When this option is enabled a potential growth factor GF [$gC\ m^{-2}\ day^{-1}$] is computed for each day and it is compared with the NPP value of that day (Section 17.1). The potential growth factor GF [$gC\ m^{-2}\ day^{-1}$] accounts for temperature and water limitations:

$$GF = \sum (g_{coef}\, k_T\, \beta_{R,all}) \,, \tag{382}$$

where g_{coef} $[gC\ m^{-2}\ h^{-1}]$ is the maximum allocation capacity in unstressed conditions at a reference temperature $T_{ref} = 20\ ^{\circ}C$. The term k_T $[-]$ is a temperature modulation coefficient and $\beta_{R,all}$ $[-]$ is the water stress factor that decreases the potential growth achievable in a given day and is computed in Eq. (384). The sum operator integrates the hourly values throughout the day. When NPP is lower than GF, the environmental conditions constrain carbon allocation to structural tissues and a reduction factor $f_{red} = GF/NPP$ is computed to reduce the fraction of NPP allocated to leaves, fruits, fine roots, and living sapwood. The remaining carbon $Add_{AR} = (1 - f_{red})NPP$ is allocated to the carbohydrate reserve pool and can be subsequently used by the plant when environmental conditions become favourable again.

The temperature control is introduced because temperature influences several metabolic processes (e.g., cell doubling time), determining the potential growth rate of organs in the absence of other growth limiting factors (*Pantin et al.*, 2012). Most temperature-controlled processes of plant growth have been summarized by Boltzmann-Arrhenius type equations, which describe a decrease in growth rates at suboptimal and supra-optimal temperatures (*Parent et al.*, 2010). Furthermore, a 5-6 $^{\circ}C$ threshold has often been identified to limit growth in cold adapted species, irrespective of photosynthetic activity, which typically ceases only at freezing point (*Körner*, 2008). The temperature modulation coefficient k_T is therefore adapted from *Parent et al.* (2010):

$$k_T = \exp\Big[\frac{H_a(T_v - T_{ref})}{(T_{ref}\, R T_v)}\Big] \frac{1 + exp\left(\frac{T_{ref}\Delta S - H_d}{T_{ref}\, R}\right)}{1 + exp\left(\frac{T_v \Delta S - H_d}{T_v\, R}\right)} \,, \tag{383}$$

where $R = 8.314$ $[J\ mol^{-1}\ K^{-1}]$ is the universal gas constant, $H_a = 76$ $[kJ\ mol^{-1}]$ is the activation energy, and $H_d = 285$ $[kJ\ mol^{-1}]$ is the deactivation energy, which describes the rate of decrease above the optimum temperature. The term $\Delta S = 0.933$ $[kJ\ mol^{-1}\ K^{-1}]$ is the so-called "entropy factor", $T_{ref} = 273.15$ $[K]$ is a reference temperature, and T_v $[K]$ is the canopy temperature in Kelvin. Additionally, in order to account for the observed cessation of growth activity below 5 $^{\circ}C$ (*Körner*, 2008), k_T is assumed to be equal to zero when $T_v < 5\ ^{\circ}C$.

When water limitations occur, there is evidence that cambial and leaf growth are inhibited at much lower levels of water stress (higher water potentials) than photosynthesis (*Muller et al.*, 2011; *Tardieu et al.*, 2011). A decrease in xylem- or leaf water potential implies a reduction in cell turgor and in the capacity to transport sugars (*Woodruff et al.*, 2004; *Sala et al.*, 2011; *Woodruff and Meinzer*, 2011). Specifically, lower cell turgor has the potential to limit cell wall expansion, cell wall synthesis and protein synthesis (*Lockhart*, 1965; *Hsiao*, 1973; *Sala et al.*, 2011). In order to account for these effects, the water limitation control $\beta_{R,all,i}$ $[-]$

is adapted from (*Muller et al.*, 2011) and it is computed as function of leaf water potential Ψ_L $[MPa]$ at the hourly scale (Section 13):

$$\beta_{R,all,i} = 1 - \frac{1}{1+\exp(p_G \Psi_L + q_G)}, \tag{384}$$

with p_G and q_G two parameters computed from the knowledge of water potential thresholds where hydraulic growth is impaired of 50% and 99%, $\Psi_{G,50}$ and $\Psi_{G,99}$, respectively. The daily average value $\beta_{R,all}$ is then computed as average of the hourly $\beta_{R,all,i}$ values.

17.4 Tissue turnover

A parametrization of transformation of dead leaves, fine roots, fruits and flowers, and heartwood pools into litter, and a conversion of living sapwood to dead sapwood/heartwood and living leaves to dead leaves is necessary to account for processes of organic matter turnover and plant structural growth. The turnover rates of green aboveground biomass, S_{leaf} $[g\,C\ m^{-2}\,VEG\ day^{-1}]$, fine root biomass S_{root} $[g\,C\ m^{-2}\,VEG\ day^{-1}]$, fruit and flowers biomass S_{flfr} $[g\,C\ m^{-2}\,VEG\ day^{-1}]$, and heartwood S_{wood} $[g\,C\ m^{-2}\,VEG\ day^{-1}]$ are linear functions of biomass. The amount of sapwood biomass converted to heartwood S_{sapw} $[g\,C\ m^{-2}\,VEG\ day^{-1}]$ and the leaf abscission rate S_{ldea} $[g\,C\ m^{-2}\,VEG\ day^{-1}]$ are also linear functions of their biomasses. These turnover and conversion rates are parameterized based on tissue longevity. The leaf turnover rate and leaf abscission are also related environmental controls, such as drought and cold stresses. The equations used to calculate the tissue turnover are:

$$S_{leaf} = \left[d_{leaf,a} + d_{leaf,c} + d_{leaf,d}\right] C_{leaf}, \tag{385}$$

$$S_{sapw} = d_{sapw}\, C_{sapw}, \tag{386}$$

$$S_{root} = d_{root}\, C_{root}, \tag{387}$$

$$S_{wood} = W_m\, C_{heaw}, \tag{388}$$

$$S_{flfr} = M_f\, C_{flfr}, \tag{389}$$

$$S_{ldea} = d_{ldead}\, C_{ldea}, \tag{390}$$

where d_{sapw} $[day^{-1}]$ is the living sapwood conversion rate to heartwood, d_{root} $[day^{-1}]$ is the turnover rate for fine roots, $d_{leaf,a}$, $d_{leaf,c}$, and $d_{leaf,d}$ $[day^{-1}]$ represent the turnover rates of green aboveground biomass due to ageing, cold stress, and drought stress, respectively (*Levis et al.*, 2004; *Arora and Boer*, 2005; *Ivanov et al.*, 2008b). The term d_{ldead} $[day^{-1}]$ is the abscission rate of standing dead-leaves, which is a function of the age of dead leaves and for grass ($\Xi = 2$) also of air temperature. The term M_f $[day^{-1}]$ is a coefficient that accounts for fruits and flowers abscission and W_m $[day^{-1}]$ is the dead-wood turnover to litter. The W_m coefficient embeds all the processes that lead to structural wood turnover from tree self-pruning, forest self-thinning, and other external factors that can cause plant mortality such as diseases or insect attacks (*Hawkes*, 2000). Catastrophic natural disturbances such as wildfire, windthrow, and management actions as forest logging or thinning are instead dealt with in the management module (Section 22).

The coefficients d_{sapw}, d_{root}, M_f, and W_m are parameters of the model and are assumed to be constant, even though there is evidence suggesting that W_m can be a function of the age or standing biomass (*Bugmann and Bigler*, 2011; *Manusch et al.*, 2012). Typical values for living sapwood conversion to dead sapwood/heartwood are $d_{sapw} = 1/365{-}1/900$ $[day^{-1}]$. The turnover rate of fine roots d_{root} has typical values of $d_{root} = 1/240 - 1/1500$ $[day^{-1}]$ (*Foley et al.*, 1996; *Kucharik et al.*, 2000; *Gill and Jackson*, 2000; *Bonan et al.*, 2003; *Arora and Boer*, 2005; *Wramneby et al.*, 2008), even though field observed turnover rates tend to overestimate the values of d_{root} needed in the model to obtain more realistic amounts of fine roots.

Values for W_m can be derived using global relationships between ANPP $[g\,DM\ m^{-2}\,yr^{-1}]$ and standing aboveground biomass AGB $[Mg\,DM\ ha^{-1}]$ (*Keeling and Phillips*, 2007; *Keith et al.*, 2009; *Pan et al.*, 2013; *Michaletz et al.*, 2014; *Chu et al.*, 2016). The scatter in these global relationships is considerable (Figure 37a). For a given level of ANPP, different values of standing biomass can be observed as a consequences of different demographic, climatic, and edaphic factors as well as occurrence of various type of disturbances. When an upper envelope of the ANPP-AGB relationship is selected (e.g., the 80th percentile), this can be assumed to roughly correspond to the maximum standing biomass at a given ANPP value, when disturbances and other external limiting factors to biomass accumulation are not predominant. If the fraction of ANPP allocated to aboveground wood is known or computed with T&C, one can approximate the value of wood turnover time W_m, in absence of catastrophic disturbances (Figure 37b).

There is not much literature evidence for the average turnover rate of fruits and flowers M_f, which determines how long they reamain on the plant and it is likely to strongly depend on the specific species. Realistic values are typically assumed $M_f = 1/50 - 1/200$ $[day^{-1}]$.

17.4.1 Leaf turnover, shedding, and environmental stresses

A fraction of green aboveground biomass leaves (or grass plus stalks) is lost every time step as a function of leaf age. This is based on the fact that even though meteorological conditions may remain favorable, plants (in particular evergreen trees) have to renew their leaves simply because old leaves become inefficient. The dynamics of leaf age, Ag_L $[day]$, are tracked explicitly and $d_{leaf,a}$ is parameterized according to Ag_L with a modification of the approach first proposed by *Krinner et al.* (2005). This is a relatively different modeling solution since, typically, terrestrial biosphere models do not calculate explicitly leaf age, and they use a constant turnover rate, $d_{leaf,a}$ (*Bonan et al.*, 2003; *Arora and Boer*, 2005; *Ivanov et al.*, 2008b).

The equation used to determine the turnover rate, $d_{leaf,a}$, as a function of leaf age depends on the vegetation type (Ξ). For deciduous plants ($\Xi = 1$) turnover rate follows a fourth power equation of leaf-age as proposed by *Krinner et al.* (2005) (Eq. 392). For evergreen and grass types the fourth power equation was found to be

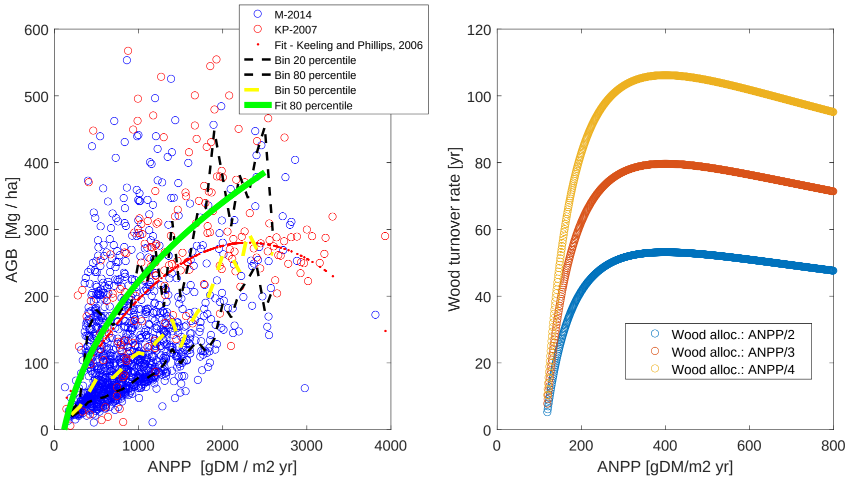

Figure 37: Observed relation between aboveground standing biomass (AGB) and aboveground net primary production ANPP in the *Keeling and Phillips* (2007) and *Michaletz et al.* (2014) datasets, the fit of *Keeling and Phillips* (2007) is reported along with the 20-50-80 percentiles for binned value of ANPP (bins are 100 $gDM\,m^{-2}\,year^{-1}$]), the line fitted to the 80th percentile is shown (subplot a). Wood turnover rate assuming maximum aboveground biomass corresponding to the 80th percentile envelope and aboveground long-term allocation to wood equal to 1/2, 1/3 and 1/4 of the total ANPP (subplot b).

inadequate, since it produces a too rapid biomass loss when the critical age threshold, A_{cr}, is exceeded and, conversely, a rather slow turnover for relatively young leaves. For these reasons, a simpler linear expression is proposed to estimate turnover for evergreen ($\Xi = 0$, Eq. 391) and grass species ($\Xi = 2$, Eq. 393). For grass species an upper limit to the turnover rate is imposed to account for a general resilience of old grass to turn over when favorable conditions are lasting toward the end of the growing season. Finally, for seasonal tropical evergreens ($\Xi = 3$), the turnover rate of leaves is assumed to be proportional to the ratio of newly produced leaves to the total biomass (NB_{Leaf}/C_{leaf}), thus generating faster turnover times during leaf production and mimicking the observed behavior of shedding old leaves to create space for new ones (*Wu et al.*, 2016). For an aseasonal forest $\frac{NB_L(t)}{C_L(t)} = \frac{1}{A_{L,cr}}$ and d_L becomes equal to the Eq. 391 for ($\Xi = 0$).

$$d_{leaf,a} = \frac{Ag_L}{A_{cr}^2}\,, \qquad \text{if} \;\; \Xi = 0\,, \tag{391}$$

$$d_{leaf,a} = \min\left[0.99, \frac{1}{A_{cr}}\left(\frac{Ag_L}{A_{cr}}\right)^4\right], \qquad \text{if} \;\; \Xi = 1\,, \tag{392}$$

$$d_{leaf,a} = \min\left[\frac{1}{A_{cr}}, \frac{Ag_L}{A_{cr}^2}\right], \qquad \text{if} \;\; \Xi = 2\,, \tag{393}$$

$$d_{leaf,a} = \frac{NB_{Leaf}A_{cr}}{C_{leaf}}, \frac{Ag_L}{A_{cr}^2}\,, \qquad \text{if} \;\; \Xi = 3\,, \tag{394}$$

where Ag_L [day] is the average leaf age, NB_{Leaf} [$g\,C\,m^{-2}\,VEG\,day^{-1}$] is the amount of carbon corresponding to leaves created in the previous time step (both described in Section 20.4), and A_{cr} [day] is the critical leaf age or leaf lifespan, which is a species dependent parameter. Typical values proposed in literature for A_{cr} range from 120 $[day]$ for grasses species to more than a 1000 $[day]$ for evergreen trees (*Foley et al.*, 1996; *Bonan et al.*, 2003; *Krinner et al.*, 2005; *Arora and Boer*, 2005; *Wramneby et al.*, 2008; *Wright et al.*, 2004; *Sato et al.*, 2007). The graphical behavior of the four turnover-age functions, in relative terms, is shown in Figure 40.

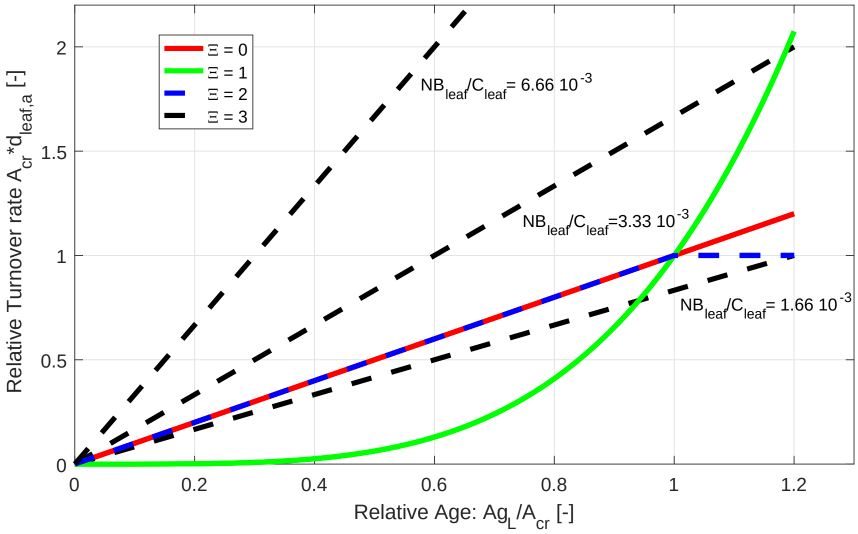

Figure 38: Relative leaf age turnover, $d_{leaf,a} \cdot A_{cr}$ $[-]$, function of the normalized average leaf age, Ag_L/A_{cr} $[-]$, for normal evergreen ($\Xi = 0$), deciduous ($\Xi = 1$), grass ($\Xi = 2$) and seasonal tropical evergreens ($\Xi = 3$) for three levels of NB_{Leaf}/C_{leaf}.

Environmental and meteorological conditions may impose additional controls on the loss of green aboveground biomass (*Kozlowski and Pallardy*, 2002; *Ivanov et al.*, 2008b). Two further turnover rates are introduced to account for drought and cold stress. Leaf foliage losses due to the severity of a drought or the effect of chilling are not well understood neither from first principle physiological mechanisms nor quantitatively. However, they are occurring and they need to be included in models through conceptual parameterizations. The drought-induced foliage loss rate, $d_{leaf,d}$ $[day^{-1}]$, is parameterized similarly to *Arora and Boer* (2005); *Ivanov et al.* (2008b). The rate $d_{leaf,d}$ is a function of the species-dependent, maximum drought loss rate $d_{d\,max}$ $[day^{-1}]$ and of a daily averaged soil moisture stress factor in the root zone (Section 13) for leaf shedding, β_R $[-]$.

$$d_{leaf,d} \;=\; d_{d\,max}(1-\beta_R)^3\,, \tag{395}$$

with:

$$\beta_R \;=\; 1-\frac{1}{1+\exp(p_D\Psi_L+q_D)}\,, \tag{396}$$

where Ψ_L $[MPa]$ is the leaf water potential and p_D and q_D are two parameters computed from the knowledge of water potential thresholds where leaf hydraulic conductivity start to be hydraulic limited and where it loses 50% of conductivity,

$\Psi_{L,0}$ and $\Psi_{L,50}$, respectively. The daily average value β_R is computed as an average of the hourly $\beta_{R,i}$ values. Given the shape of Eq. (396), the value of β_R would be always smaller than one, implying that the plant is never completely unstressed, to avoid this problem when $\beta_R > 0.95$, it is assumed to be equal to 1. Note that β_R is not equal to $\beta_{R,all}$ (Eq. 384) since different water potential thresholds are used. The power exponent 3 of Eq. (395) reflects the sensitivity of leaf shedding to drought and is taken from *Arora and Boer* (2005). The parameter $d_{d\,max}$ $[day^{-1}]$ is difficult to determine, because it is a conceptual representation of a poorly understood mechanism. Model experience suggests values of $d_{d\,max} = 1/10 - 1/40$ for drought decidous plant and grasses that allow plants to shed their leaves when unfavourable soil moisture conditions occur without having to spend a large amount of carbon in tissue maintenance with negative NPP. Values of $d_{d\,max} = 1/200 - 1/365$ $[day^{-1}]$ are more typical of deciduous and evergreen plants that preserve their leaf cover investment during relatively short drought periods with negative NPP, waiting for favourable conditions.

The rate of foliage loss due to cold stress, $d_{leaf,c}$ $[day^{-1}]$, is assumed to be a linear function of air temperature below a certain threshold temperature (*Cox*, 2001):

$$d_{leaf,c} \;=\; d_{cold}(T_{cold} - T_a)(T_a \leq T_{cold})\,, \tag{397}$$

where d_{cold} $[day^{-1}\ ^{\circ}C^{-1}]$ is a linear coefficient, species-dependent, for foliage loss due to cold temperatures and T_a $[^{\circ}C]$ is the air temperature. The temperature threshold, T_{cold} $[^{\circ}C]$, is a species-dependent parameter that demarcates the temperature below which cold temperatures start the leaf shedding. This parametrization assumes that leaf shedding due to cold stress increases linearly with temperature once the threshold T_{cold} is exceeded (towards lower values). As stated for leaf shedding induced by drought, the underlaying physiological mechanisms governing these processes are not understood and no mechanistic model exists. Consequently, the assumption behind Eq. (397) is only indirectly tested through satisfactory model performance. The threshold T_{cold} is, indeed, higher for cold intolerant plants, for vegetation located in warmer climates and for deciduous species compared to evergreen ones. Note that foliage loss due to cold stress is mostly playing a role in seasonally temperate climates, where leaf loss of deciduous species and partially of evergreens occur before winter. Boreal or high-elevation species are parameterized with extremely low thresholds, which are never exceeded, as well as tropical plants never experience cold leaf stress because of the warm climate throughout the entire year. The parameter d_{cold} is correlated to T_{cold} and has been found to be mostly a function of the vegetation category and climate. For example, $d_{cold} = 1/10 - 1/15$ is used for winter deciduous species, $d_{cold} = 1/50$ for temperate grass species, $d_{cold} = 1/5$ for boreal evergreens, $d_{cold} = 1/120 - 1/150$ for evergreens with partial winter leaf shedding.

Finally, the equation used to determine the abscission of the standing dead-leaves

d_{ldead}, is a function of the average dead-leaf age Ag_{DL}:

$$d_{ldead} \quad = \quad \min\left[0.99, K_{Lf}\left(\frac{Ag_{DL}}{K_{lf}}\right)^4\right] \,, \tag{398}$$

where K_{Lf} $[day^{-1}]$ is a dead-leaf abscission parameter, which is assumed constant for all broad vegetation categories except grass species ($\Xi = 2$), where $K_{Lf} = K_{Lf}2^{0.1(T_a-20)}$ is a function of the air temperature T_a (*Lazzarotto et al.*, 2009). In grass, the transition between dead-standing biomass and litter is in fact regulated by air temperature with a faster transition during warmer periods than colder periods, where dead-standing grass plus stalks can persist for long-time. The fourth power dependence of d_{ldead} on dead-leaf age assures that a rapid conversion of dead-standing leaves into litter is achieved once the dead leaves are ageing and before a new growing season begins. Typical values of $K_{Lf} = 1/15 - 1/80$ $[day^{-1}]$ are used with faster leaf-abscission rates in tropical environments.

18 Plant biophysical relations

Each vegetation unit is characterized by several structural vegetation attributes, such as canopy height H_c $[m]$, leaf area index LAI $[m^2\ leaf\ area\, m^{-2}\, VEG\, area]$, stem area index SAI $[m^2\ stem\ area\, m^{-2}\ \ VEG\, area]$, leaf area index of standing dead leaves LAI_{dead} $[m^2\, leaf\ \ area\, m^{-2}\, VEG\, area]$, root length density R_L $[m\, root\ m^{-2}\, VEG]$. All these attributes are expressed for unit of *Crown Area*, i.e., for $m^{-2}\, VEG\, area$.

Although all the attributes of vegetation are dynamic components (time-varying) only LAI, R_L, and grass canopy height are dynamic components in this version of T&C, while the other attributes are assumed to be constant and they must be specified as model inputs for each vegetation unit. Vegetation properties can be obtained from literature: for instance *Jackson et al.* (1996) provide a comprehensive study of the root distributions for a variety of species. *Bonan* (1996) provides typical values of leaf dimension for various plant types, and *Simard et al.* (2011) provide a global map of canopy height just to cite a few examples.

18.1 Leaf and Stem Area Index

In each vegetation unit, LAI $[m^2\, leaf\ area\, m^{-2}\, VEG\, area]$, is related to the green aboveground biomass carbon pool:

$$LAI \quad = \quad C_{leaf}\, S_{LAI} \,. \tag{399}$$

The term S_{LAI} $[m^2\, LAI\ g\, C^{-1}]$ is the specific leaf area of biomass, which is a species-dependent parameter. Vegetation models are quite sensitive to the values of S_{LAI}, since it represents the ability of plants to invest in leaf cover and therefore additional photosynthetic potential. It has been found that S_{LAI} generally increases with photosynthetic capacity and leaf nitrogen content and decreases with leaf life span

(*Schulze et al.*, 1994; *Reich et al.*, 1997; *Wright et al.*, 2004). Reference values of S_{LAI} are relatively easy to find in literature and typical values of S_{LAI} range between 0.005-0.050 $[m^2\, LAI\; g\, C^{-1}]$ (*Schulze et al.*, 1994; *Foley et al.*, 1996; *Kaduk and Heimann*, 1996; *Friend et al.*, 1997; *Reich et al.*, 1997, 1998a; *Kucharik et al.*, 2000; *Cox*, 2001; *Bonan et al.*, 2003; *Wright et al.*, 2004; *Sato et al.*, 2007; *Wramneby et al.*, 2008).

There is evidence that S_{LAI} is not constant throughout the canopy but tend to decrease at the top of the canopy, which has thicker leaves (lower S_{LAI}), while at the bottom of the canopy there are thinner leaves (higher S_{LAI}) (*Niinemets and Kull*, 1998; *Koch et al.*, 2004; *Niinemets et al.*, 2015). This vertical gradient of S_{LAI} can be accounted for in the computation of LAI (*Thornton and Zimmermann*, 2007), as $S_{LAI}(x) = S_{LAI,0} + m_{SL}\, x$, if S_{LAI} is assumed to be a linear function of the canopy depth x expressed as overlying leaf area index and of $S_{LAI,0}$, the specific leaf area at the top of the canopy. *Thornton and Zimmermann* (2007) provide the solution of LAI as a function of leaf biomass integrating through the canopy profile:

$$LAI = S_{LAI,0} \left(\frac{\exp\left(m_{SL}\, C_{leaf}\right) - 1}{m_{SL}} \right) , \qquad (400)$$

where m_{SL} $[m^2\, LAI\; g\, C^{-1}\;\; m^2\, VEG\; (m^2\, LAI)^{-1}]$ is a scaling factor that account for the linear decrease of S_{LAI} with increasing LAI. *Thornton and Zimmermann* (2007) also provide the expressions to compute the S_{LAI} of shaded and sunlit portion of the canopy.

While Eq. (400) is theoretically more appealing than using a constant S_{LAI} (Eq. 399), it has been tested and found to create unrealistic cheap investments in leaf biomass at high value of LAI, where S_{LAI} progressively increases. For this reason, while both options are available in T&C, the option with a constant S_{LAI} is preferred and can be simply obtained imposing $m_{SL} = 0$. Another potential issue in using Eq. (400) is that the maximum Rubisco capacity at $25°C$ V_{max}^L at the top of the canopy (Section 6.6.2) cannot depend anymore on the nitrogen content profile, because with this option nitrogen content for unit of mass is assumed constant and nitrogen for unit of area is scaled coherently with the profile of S_{LAI}. While generally, nitrogen content for unit of mass does not vary much with canopy profile (*Dewar et al.*, 2012; *Niinemets et al.*, 2015), the assumption of scaling leaf to canopy photosynthetic capacity based solely on S_{LAI} has been found restrictive and to provide worse result than using an exponential profile of nitrogen content (Section 6.6.2).

Equivalently to the LAI of living green aboveground biomass, the LAI_{dead} $[m^2\, leaf\; area\; m^{-2}\, VEG\, area]$ of standing dead leaves is related to its biomass carbon pool using the specific leaf area index:

$$LAI_{dead} = C_{ldea}\, S_{LAI} \, . \qquad (401)$$

The specific leaf area index of dead biomass is assumed equal to the green biomass while the optical properties of LAI_{dead} are parameterized differently from living biomass as explained in Section 4.2.1. If $m_{SL} \neq 0$ then an equation similar to Eq.

(400) is used also to compute LAI_{dead}.

The stem area index SAI [m^2 *stem area* m^{-2} *VEG area*] is a structural attribute and can be theoretically computed as:

$$SAI = \left((1-f_v)(DH_c)+(f_v)\frac{\pi D^2}{4}\right)\frac{T_\rho}{C_{crown}}, \qquad (402)$$

where the coefficient f_v [$-$] is the fraction of stem and branches that can be regarded as prevalently vertical, T_ρ is the tree density [*number of individuals* m^{-2} *ground*], D [m] is the average wood trunk diameter and H_c [m] is the canopy height. Since tree diameter and canopy height are not dynamically evolved, SAI [$m^2\, SAI\ m^{-2}\, VEG$] remains constant through time in T&C.

18.2 Root profile and length density

While fine root biomass C_{root} is dynamically updated in the model, the root profile distribution with $Z_R(z)$ is constant throughout the simulation. The root biomass profile is explicitly represented using the fractions of root biomass at different depths r_i [$-$], for each layer of soil i in the soil profile (Section 12.2) . Four different options are available in T&C to define the root profile distribution (*Jackson et al.*, 1996; *Feddes et al.*, 2001; *Schenk and Jackson*, 2002; *Arora and Boer*, 2003; *Collins and Bras*, 2007) and they are described in Section 12.2. In the most general case, the rooting depth that contains 50% $Z_{R,50}$ [mm] and 95% $Z_{R,95}$ [mm] of fine root biomass and the maximum rooting depth $Z_{R,max}$ [mm] are required to completely define the root profile. The root profile corresponds to the distribution of fine roots responsible for water uptake. Since usually no differentiation is made between fine and coarse root distributions the two profiles are considered equivalent.

The root length density R_L [$m\,root\ m^{-2}\,VEG$], is computed from the fine root biomass C_{root} as:

$$R_L = \frac{C_{root}}{\rho_{root}\,\pi r_{root}^2}, \qquad (403)$$

where $\rho_{root} = 122$ [$kgC\,m^{-3}$] is the carbon root density and $r_{root} = 0.5$ [mm] is an average radius of fine roots, assumed to be constants in T&C. The root length density R_L is then used in the computation of the soil-to-root resistance (Section 13.3).

18.3 Canopy height

Canopy height, H_c [m], represents the distance between the ground surface and the top of the canopy and is a constant in this version of T&C for tree and shrub plant forms, while it changes in time for grass species ($\Xi = 2$).

Grass height is computed from LAI, using the *Allen et al.* (1989, 1998) equation, $H_{veg} = 24\,LAI^*$, where H_{veg} [m] is the grass height, limited to 1.2 m and $LAI^* = LAI + LAI_{dead}/3$ is an equivalent LAI that accounts for the fact that dead leaf biomass does not contribute as much as alive biomass to grassland height. Different empirical equations exist and provide similar LAI for heights of less than 20 cm (*Pocock et al.*, 2010).

18.4 Leaf dimension

The characteristic leaf dimension d_{leaf} $[cm]$ is a model input, which affects the computation of the leaf boundary layer resistance (Section 6.3). The value of d_{leaf} is considered time-invariant in the model even though in reality it changes with leaf-age for a few days/weeks after leaf-onset.

18.5 Additional structural attributes

From a theoretical point of view, for woody species there is a number of other structural attributes (including H_c) that can evolve dynamically in time. This is only enabled in particular applications of T&C (e.g., plantations, crops), which otherwise does not account for structural changes beyond the ones described earlier in this Section. The carbon pools that form the woody part of the aboveground plant are the aboveground heartwood carbon pool, $f_{ab}C_{heaw}$ $[g\,C\ m^{-2}\,VEG]$, the aboveground sapwood, $f_{ab}C_{sapw}$, $[g\,C\ m^{-2}\,VEG]$ and the aboveground carbohydrate reserve $f_{ab}C_{hydr}$ $[g\,C\ m^{-2}\,VEG]$ (Section 17.2). Considering the woody part of the plant halfway between a cylinder and a cone:

$$
\begin{aligned}
V_{tree} &= \frac{C_{crown}}{T_\rho}\left(\frac{f_{ab}C_{heaw}}{\rho_{heaw}} + \frac{f_{ab}C_{sapw}}{\rho_{sapw}} + \frac{f_{ab}C_{hydr}}{\rho_{sapw}}\right), & (404)\\
V_{tree} &= \frac{\pi D^2 H_c}{6}, & (405)
\end{aligned}
$$

where V_{tree} $[m^3\,,\ number\,of\,individuals^{-1}]$ is the volume of wood of an average representative tree, ρ_{heaw} and ρ_{sapw} $[g\,C\ m^{-3}]$ are the heartwood and sapwood carbon wood density respectively, D $[m]$ is the average wood trunk diameter, T_ρ $[number\,of\,individuals\ \ m^{-2}\ ground]$ is the tree population density, C_{crown} is the *Crown Area* fraction, expressed by $C_{crown} = T_\rho A_{crown}$ $[m^2\ VEG\,m^{-2}\ ground]$, with $C_{crown} \leq 1$; and A_{crown} $[m^2\ VEG\,,\ \ number\,of\,individuals^{-1}]$ is the average crown extension of an individual. Equations (404) and (405) contain several implicit assumptions about the shape of the tree and the density of different tissues. Equations (404) and (405), are in essence a single independent equation with four unknowns: D, A_{crown}, H_c, and T_ρ. Therefore, further allometric relations are necessary to estimate the vegetation structural parameters. Equations relating A_{crown} and H_c to D are of the form:

$$
\begin{aligned}
A_{crown} &= k_1 D^{k_3}\,, & (406)\\
H_c &= k_2 D^{k_4}\,, & (407)
\end{aligned}
$$

where k_1 $[m^{2-k_3}]$, k_2 $[m^{1-k_4}]$, k_3 $[-]$, and k_4 $[-]$ are allometric constants, species dependent (e.g., *Falster et al.*, 2015). Typical values assumed by the allometric constants are: $k_1 = 100 - 200$, $k_2 = 28 - 40$, $k_3 = 1.6$, $k_4 = 0.5 - 0.83$, (*Sitch* *et al.*, 2003; *Sato et al.*, 2007). For the scaling parameter k_3 and k_4, theoretical values of $k_3 = 1.33$ and $k_4 = 0.66$ based on universal scaling in tree and vascular plant allometry have been also calculated (*Enquist*, 2002; *West et al.*, 2009). Substituting Eq. (406) and (407) in (404)-(405) allows to solve iteratively for D if T_ρ is known. Consequently, a dynamic structural representation of the canopy including a time varying canopy fraction, C_{crown}, can be achieved. When $T_\rho A_{crown} \geq 1$ only (407) is substituted into (404). The knowledge of the population density, T_ρ $[number\, of\, individuals\ m^{-2}\ ground]$ is a critical element, and while T_ρ is roughly a constant for plantations or managed forests, it changes through time in natural ecosystems. In order to obtain a dynamic evolution of vegetation T_ρ should also evolve in time as a consequence of forest demography (species competition, mortality, establishment), which is not currently simulated in T&C. A possibility exist of computing T_ρ using the self-thinning law (*Yoda et al.*, 1963; *Wolf et al.*, 2011a), but this is not currently implemented in T&C. In any case, the above parameterization is solely valid for ecosystems composed by trees of similar size, as plantations, and cannot handle the large variability in tree size and height that is observed in forest with frequent disturbances.

19 Plant nutrient budget

The nutrient budget of the plant is obtained by computing changes in nutrient reserves of nitrogen $N_{reserve}$ $[g\, N\ m^{-2}\ VEG]$, phosphorus $P_{reserve}$ $[g\, P\ m^{-2}\ VEG]$, and potassium $K_{reserve}$ $[g\, K\ m^{-2}\ VEG]$. “Nutrient reserve” is a modeled quantity that accounts for real reserves and for stoichiometric flexibility as explained in Section 17.3.5. The term $N_{reserve}$ (nitrogen is used as an example but the model also considers P and K) can, in fact, become negative when nitrogen tissue concentration falls below the targeted stoichiometry. More generally, $N_{reserve}$ should range from $-0.35\, TNS_N$ to $N_{sto} + 0.60\, TNS_N$, which accounts for both maximum nutrient reserve size N_{sto} and stoichiometric flexibility (Section 17.3.5). The term TNS_N $[g\, N\ m^{-2}\ VEG]$ is the non-structural content of nitrogen as described below. The reserve budgets are expressed as:

$$\frac{dN_{reserve}}{dt} = N_{uptake} - \frac{dTS_N}{dt} - N_{export,l}\,, \tag{408}$$

$$\frac{dP_{reserve}}{dt} = P_{uptake} - \frac{dTS_P}{dt} - P_{export,l}\,, \tag{409}$$

$$\frac{dK_{reserve}}{dt} = K_{uptake} - \frac{dTS_K}{dt} - K_{export,l}\,, \tag{410}$$

where $N_{export,l}$, $P_{export,l}$, and $K_{export,l}$ $[g\, X\ m^{-2}\, VEG\ day^{-1}]$ are the nutrients exported from living tissue through tissue turnover and N_{uptake}, P_{uptake}, and K_{uptake} $[g\, X\ m^{-2}\, VEG\ day^{-1}]$ are the fluxes of nutrients taken up from soil. The changes in total nutrient content in the plant (e.g., dTS_N/dt) are a consequence of changes in carbon content of the various pools. The total nutrient content of nitrogen TS_N $[g\, N\ m^{-2}\ VEG]$, phosphorus TS_P $[g\, P\ m^{-2}\ VEG]$ and potassium TS_K

$[g\,K\ m^{-2}\ VEG]$ are given by:

$$TS_N = \frac{C_{leaf}}{CN_l} + \frac{C_{sapw}}{CN_s} + \frac{C_{root}}{CN_r} + \frac{C_{hydr}}{CN_c} + \frac{C_{flfr}}{CN_f} + \frac{C_{heaw}}{CN_h}\,, \tag{411}$$

$$TS_P = \frac{C_{leaf}}{CP_l} + \frac{C_{sapw}}{CP_s} + \frac{C_{root}}{CP_r} + \frac{C_{hydr}}{CP_c} + \frac{C_{flfr}}{CP_f} + \frac{C_{heaw}}{CP_h}\,, \tag{412}$$

$$TS_K = \frac{C_{leaf}}{CK_l} + \frac{C_{sapw}}{CK_s} + \frac{C_{root}}{CK_r} + \frac{C_{hydr}}{CK_c} + \frac{C_{flfr}}{CK_f} + \frac{C_{heaw}}{CK_h}\,, \tag{413}$$

Even in absence of tissue turnover a transfer of carbon among the pools or an increase in the total amount of carbon must be accompanied by a change in the total nutrient content of the plant. This can be supported by a change in the nutrient reserves or by nutrient uptake (Eq. 408-410). An excess of nutrient uptake with respect to use may lead to an increase in nutrient tissue concentration (e.g., $N_{reserve} > N_{sto}$), an insufficient uptake with respect to use may lead to a decrease in nutrient tissue concentration (e.g., $N_{reserve} < 0$), which can ultimately lead to stoichiometric limitations on growth as described in Section 17.3.5.

The non-structural nutrient content of nitrogen TNS_N, phosphorus TNS_P and potassium TNS_K are given by equivalent expressions of Eq. (411) to (413) but without accounting for the nutrients contained in C_{sapw} and C_{heaw}, which are the structural pools. The quantities TNS_N, TNS_P and TNS_K are used in Section 17.3.5 to compute the plant relative nutrient concentrations for nitrogen r_{N_c} $[-]$, phosphorus r_{P_c} $[-]$, and potassium r_{K_c} $[-]$.

19.1 Plant nutrient export

The total flux of nutrients exported from living plant tissues $N_{export,l}$, $P_{export,l}$, and $K_{export,l}$ $[g\,X\ m^{-2}\,VEG\ day^{-1}]$ are:

$$\begin{aligned} N_{export,l} &= r_{N_c}(1-f_{transf,l})\frac{S_{leaf}}{CN_l} + r_{N_c}\frac{S_{flfr}}{CN_f} + \\ &\quad r_{N_c}(1-f_{transf,r})\frac{S_{root}}{CN_r} + \frac{S_{wood}}{CN_h}\,, \end{aligned} \tag{414}$$

$$\begin{aligned} P_{export,l} &= r_{P_c}(1-f_{transf,l})\frac{S_{leaf}}{CP_l} + r_{P_c}\frac{S_{flfr}}{CP_f} + \\ &\quad r_{P_c}(1-f_{transf,r})\frac{S_{root}}{CP_r} + \frac{S_{wood}}{CP_h}\,, \end{aligned} \tag{415}$$

$$\begin{aligned} K_{export,l} &= r_{K_c}(1-f_{transf,l})\frac{S_{leaf}}{CK_l} + r_{K_c}\frac{S_{flfr}}{CK_f} + \\ &\quad r_{K_c}(1-f_{transf,r})\frac{S_{root}}{CK_r} + \frac{S_{wood}}{CK_h}\,, \end{aligned} \tag{416}$$

where S_{leaf}, S_{root}, S_{flfr}, S_{wood} $[g\,C\ m^{-2}\,VEG\ day^{-1}]$ are the turnover rates of green aboveground biomass, fine roots, fruit and flowers, and wood, and $f_{transf,l}$ and $f_{transf,r}$ are the resorbed fractions of nutrient in the leaves and fine roots defined previously. The nutrient export simply follows the target stoichiometry of the different tissues (CN_l, CN_r, CN_f and CN_h), which for non-structural tissues can be modified according to the relative nutrient concentrations: r_{N_c}, r_{P_c}, and r_{K_c}. Nutrient resorption in leaves and fine roots occurs before these nutrient rich tissues are turned over in order to preserve nutrient within the plant, given the relatively large cost of their acquisition (*Reed et al.*, 2012; *Vergutz et al.*, 2012; *Cleveland et al.*, 2013). Theoretically these fractions are a function of environmental conditions and plant nutrient status (*Brzostek et al.*, 2014; *Shi et al.*, 2016; *Zhang et al.*, 2018), however in T&C $f_{transf,l}$ and $f_{transf,r}$ are assumed to be constant when nutrient reserves are below the maximum nutrient storages (N_{sto}, P_{sto}, K_{sto}). Whenever the relative nutrient concentrations exceed 1 the fractions of nutrient resorption in the leaf and fine root $f_{transf,l}$ and $f_{transf,r}$ are set equal to zero, because the plant has an excess of nutrients and does not need to resorb them. Such a modeling solution allows for some flexibility in the long-term nutrient resorption.

19.2 Plant nutrient uptake

Plant uptake of mineral nutrients can occur directly from fine roots and it can be passive, i.e., following the transpiration flow, or active, i.e., regulated and against concentration gradients (e.g., *Haynes*, 1990; *Porporato et al.*, 2003). Additionally, mycorrhizal symbiosis can also contribute to nutrient acquisition (*Marschner and Dell*, 1994; *Smith and Smith*, 2011; *Hinsinger et al.*, 2011). The nutrient uptake rates (e.g., $NH4_{up}$) are computed for unit of ground area and they are converted to unit of vegetated areas (e.g., N_{uptake} $[g\,X\ m^{-2}\,VEG\ day^{-1}]$) for being used in the plant nutrient budget (e.g., Eq. 408).

$$\begin{aligned} N_{uptake} &= (NH4_{up} + NO3_{up})(1 - Sup_N)/C_{crown}\,, & (417)\\ P_{uptake} &= P_{up}(1 - Sup_P)/C_{crown}\,, & (418)\\ K_{uptake} &= K_{up}(1 - Sup_K)/C_{crown}\,, & (419)\end{aligned}$$

where Sup_N, Sup_P, Sup_K $[-]$ are nutrient uptake suppression functions bounded between 1 (total suppression) and 0 (no suppression). These functions are essential to decrease the nutrient uptake of the plant based on its nutrient status. Specifically, they are computed as linear functions of the amount of nutrient reserves and they also account for total nutrient content in non-structural tissues:

$$\begin{aligned} Sup_N &= \frac{N_{reserve} - 0.8N_{sto}}{0.6\,TNS_N + 0.2N_{sto}}\,, & (420)\\ Sup_P &= \frac{P_{reserve} - 0.8P_{sto}}{0.6\,TNS_P + 0.2P_{sto}}\,, & (421)\\ Sup_K &= \frac{K_{reserve} - 0.8K_{sto}}{0.6\,TNS_K + 0.2K_{sto}}\,. & (422)\end{aligned}$$

The suppression of nutrient uptake starts when $N_{reserve}$ are 80% of the nutrient maximum storage capacity N_{sto} and reaches its maximum for a relative nutrient concentration of 1.6 (Fig. 36b). These coefficients prevent plants from taking up nutrients when their tissue concentrations are already very high, i.e., 60% in excess of the targeted nutrient concentration. However, this does not imply that relative nutrient concentrations cannot exceed this threshold as a result of a shift in the distribution of carbon among the pools. The total nutrient content is indeed computed as a single quantity, Eq. (411) to (413).

The actual nutrient uptake rates per unit of ground area $NH4_{up}$, $NO3_{up}$, P_{up}, and K_{up} are computed as the maximum between passive uptake occurring through the transpiration stream and active uptake influenced by the amount of fine roots C_{root}, ectomycorrhizae C_{EM}, and arbuscular mycorrhizae C_{AM}. The expressions below are in absence of uptake suppression; once uptake suppression takes place, the $NH4_{up}$, $NO3_{up}$, P_{up}, and K_{up} are down-regulated using Sup_N, Sup_P, and Sup_K as described in Eq. (417) to (419).

$$\begin{aligned} NH4_{up} &= max[NH4_{up,a}, NH4_{up,p}] \,, && (423)\\ NO3_{up} &= max[NO3_{up,a}, NO3_{up,p}] \,, && (424)\\ P_{up} &= max[P_{up,a}, P_{up,p}] \,, && (425)\\ K_{up} &= max[K_{up,a}, K_{up,p}] \,. && (426) \end{aligned}$$

Of course, nutrient uptake rates are also limited by the actual availability of ammonium, nitrate, and mineral available phosphorus and potassium in the soil.

Passive uptake rates $NH4_{up,p}$, $NO3_{up,p}$, $P_{up,p}$, and $K_{up,p}$ $[g\,X\ m^{-2}\,day^{-1}]$ are computed as:

$$\begin{aligned} NH4_{up,p} &= a_{NH4}\,NH4\,\frac{T}{VT} \,, && (427)\\ NO3_{up,p} &= a_{NO3}\,NO3\,\frac{T}{VT} \,, && (428)\\ P_{up,p} &= a_P\,P_{min}\,\frac{T}{VT} \,, && (429)\\ K_{up,p} &= a_K\,K_{min}\,\frac{T}{VT} \,, && (430) \end{aligned}$$

where $NH4$, $NO3$, P_{min}, and K_{min}, $[g\,X\ m^{-2}]$ are the ammonium, nitrate, and mineral available phosphorus and potassium in the soil, T $[mm\,day^{-1}]$ is the transpiration flux from the biogeochemically active depth, VT $[mm]$ is the total volume of water in the biogeochemically active depth, and a_{NH4}, a_{NO3}, a_P, and a_K $[-]$ are the solubility coefficients for ammonium, nitrate, phosphorus, and potassium (Table 8).

Active uptake $[g\,X\ m^{-2}\,day^{-1}]$ is the sum of uptake rates given by fine roots, ectomycorrhizae, and arbuscular mycorrhizae:

$$\begin{aligned} NH4_{up,a} &= NH4_{up,r} + EM\,NH4_{up,em} + (1-EM)NH4_{up,am} \,, && (431)\\ NO3_{up,a} &= NO3_{up,r} + EM\,NO3_{up,em} + (1-EM)NO3_{up,am} \,, && (432)\\ P_{up,a} &= P_{up,r} + EM\,P_{up,em} + (1-EM)P_{up,am} \,, && (433)\\ K_{up,a} &= K_{up,r} + EM\,K_{up,em} + (1-EM)K_{up,am} \,, && (434) \end{aligned}$$

where EM is the ground area covered by plants associated with ectomycorrhizal fungi and $1 - EM$ corresponds to the fraction of plants associated with arbuscular mycorrhizae in a given computational element.

The active uptake rate X_{up} $[g\,X\ m^{-2}\,day^{-1}]$ of a generic nutrient with concentration C_X $[g\,X\ m^{-3}]$ is computed in analogy to Fick's laws of diffusion, considering the nutrient concentration in the soil and a characteristic length L_X $[m]$ representing the average distance between the nutrient in the soil and the fine root or mycorrhizal hypahe taking up nutrients. This is a highly simplified approach that ignores nutrient concentration variability in the rhizosphere and complex biochemical processes involved in the solute uptake (e.g., *Haynes*, 1990). However, it is intended to link uptake rates to the major controls of nutrient uptake at the ecosystem scale. Uptake rates for unit of root or hypahe are upscaled using the amount of roots or hypahe actually present in the soil (e.g., expressed through the fine root areal index, RAI $[m^2 root\, m^{-2} ground]$).

$$X_{up} \quad = \quad V_D \frac{C_X}{L_X} RAI\,, \tag{435}$$

where V_D $[m^2\,day^{-1}]$ is a diffusion coefficient at the root or hypha interface, the concentration gradient ΔC_X is approximated with the concentration C_X in bulk soil and the characteristic length L_X is computed as (*Daly et al.*, 2004; *Manzoni et al.*, 2014):

$$L_X \quad = \quad \sqrt{\frac{2Z_{biog}}{R_L}}\,, \tag{436}$$

where Z_{biog} $[m]$ is in this case the depth of the biogeochemically active zone and R_L is the root length density $[m\,root\ m^{-2}\,ground]$, which is related to RAI as $R_L = RAI/r_{root}$, where r_{root} $[m]$ is the average radius of fine roots. The root length density can be expressed as a function of of the root biomass B_{root} $[g\,C\ m^{-2}]$, root radius r_{root}, and tissue density ρ_r $[g\,C\ m^{-3}]$ as:

$$R_L \quad = \quad \frac{B_{root}}{\rho_r\, r_{root}^2}\,. \tag{437}$$

Re-arranging Eq. 435 with the nutrient expressed for unit of ground area $X = C_X\,Z_{biog}$ $[g\,X\ m^{-2}]$ and using the definition of L_X, RAI, and R_L, we obtain:

$$X_{up} \quad = \quad V_D \frac{X\,B_{root}^{3/2}}{\sqrt{2}\,r_{root}^2\,Z_{biog}^{3/2}\,\rho_r^{3/2}}\,, \tag{438}$$

if the denominator is expressed as a single resistance term:

$$r_r \quad = \quad \sqrt{2}\,r_{root}^2\,Z_{biog}^{3/2}\,\rho_r^{3/2}\,, \tag{439}$$

with r_r in $[g\,C^{3/2}\,m^{-1}]$, one can re-cast Eq. 438 as:

$$X_{up} \quad = \quad V_D \frac{X\,B_{root}^{3/2}}{r_r}\,. \tag{440}$$

Equivalent expressions can be written for ectomycorrhizal fungi and arbuscular mycorrhizae:

$$X_{up} = V_D \frac{X\, C_{AM}^{3/2}}{r_{am}} , \qquad (441)$$

$$X_{up} = V_D \frac{X\, C_{EM}^{3/2}}{r_{em}} , \qquad (442)$$

where C_{AM} $[g\, C\ m^{-2}]$ and C_{EM} $[g\, C\ m^{-2}]$ are the arbuscular mycorrhizal and ectomycorrhizal biomasses for unit of ground, with the resistance term $r_{am} = \sqrt{2}\, r_{myc}^2\, Z_{biog}^{3/2}\, \rho_{myc}^{3/2}$, and equivalent expression for r_{em}. Note that the above derivation differentiates among fine roots, arbuscular mycorrhizal, and ectomycorrhizal uptake rates based on their biomass amount in the soil (e.g., B_{root}, C_{AM}, and C_{EM}) and on biophysical characteristics such as root or hyphae radius (r_{root} and r_{myc}) and tissue density (ρ_r and ρ_{myc}). Reference values of $r_{root} = 500$, $r_{myc} = 5$ $[\mu m]$ and $\rho_r = 122$, $\rho_{myc} = 200$ $[kg\, C\ m^{-3}]$ are used in T&C following literature (e.g., *Jackson et al.*, 1997; *Smith and Read*, 2008; *Roumet et al.*, 2016), with values for arbuscular mycorrhizal and ectomycorrhizal fungi assumed to be equal for simplicity. Using these values leads to a roughly 4700 times larger resistance in taking up nutrients through fine roots than through hyphae, because of the capability of the latter to explore soil volume in a more efficient way due to their smaller size. A three order of magnitude difference in uptake capacity between roots and mycorrhizae is a value supported by other independent estimates (*Hinsinger et al.*, 2011). The diffusion coefficient could theoretically differ for roots or hyphae and for different solutes but it is assumed here constant for simplicity $V_D = 2.3\ 10^{-7}$ $[m^2\, day^{-1}]$. The selected value is the result of a sensitivity test in the model development phase and is similar to values identified in the literature (*Jungk*, 2002). Note that Eq.(440) has the same dependencies but a different functional form from nutrient uptake formulations based on Michaelis-Menten kinetics, which have been used in other models (e.g., *Zaehle and Friend*, 2010).

Consequently, the root active uptake rates for the different nutrients are given by:

$$NH4_{up,r} = \frac{v_r\, NH4}{r_r} B_{root}^{3/2} , \qquad (443)$$

$$NO3_{up,r} = \frac{v_r\, NO3}{r_r} B_{root}^{3/2} , \qquad (444)$$

$$P_{up,r} = \frac{v_r\, P_{min}}{r_r} B_{root}^{3/2} , \qquad (445)$$

$$K_{up,r} = \frac{v_r\, K_{min}}{r_r} B_{root}^{3/2} , \qquad (446)$$

where B_{root} $[g\, C\ m^{-2}]$ is the total fine root biomass for unit of ground, $v_r = V_D$ $[m^2\, day^{-1}]$ is the diffusion coefficient, and r_r $[g\, C^{3/2}\, m^{-1}]$ is the resistance term defined in Eq. 439. The ectomycorrhizal nutrient uptake rates are:

$$NH4_{up,em} = \frac{v_{em}\, NH4}{r_{em}} C_{EM}^{3/2}, \tag{447}$$

$$NO3_{up,em} = \frac{v_{em}\, NO3}{r_{em}} C_{EM}^{3/2}, \tag{448}$$

$$P_{up,em} = \frac{v_{em}\, P_{min}}{r_{em}} C_{EM}^{3/2}, \tag{449}$$

$$K_{up,em} = \frac{v_{em}\, K_{min}}{r_{em}} C_{EM}^{3/2}, \tag{450}$$

where C_{EM} $[g\,C\ m^{-2}]$ is the ectomycorrhizal biomass for unit of ground, $v_{em} = V_D$ $[m^2\, day^{-1}]$ is the diffusion coefficient, and r_{em} $[g\,C^{3/2}\, m^{-1}]$ is the resistance term defined in analogy to the one for for fine roots. Equivalently, the arbuscular mycorrhizal uptake rates are:

$$NH4_{up,am} = \frac{v_{am}\, NH4}{r_{am}} C_{AM}^{3/2}, \tag{451}$$

$$NO3_{up,am} = \frac{v_{am}\, NO3}{r_{am}} C_{AM}^{3/2}, \tag{452}$$

$$P_{up,am} = \frac{v_{am}\, P_{min}}{r_{am}} C_{AM}^{3/2}, \tag{453}$$

$$K_{up,am} = \frac{v_{am}\, K_{min}}{r_{am}} C_{AM}^{3/2}, \tag{454}$$

where C_{AM} $[g\,C\ m^{-2}]$ is the arbuscular mycorrhizal biomass for unit of ground, $v_{am} = V_D$ $[m^2\, day^{-1}]$ is the diffusion coefficient, and r_{am} $[g\,C^{3/2}\, m^{-1}]$ is the resistance term defined in analogy to the one for for fine roots and ectomycorrhizal fungi.

20 Vegetation phenology

Plant phenology describes the seasonal cycle of the phases vegetation is experiencing and it is essential for simulating the interactions between the biosphere and the hydrosphere since it can control the amount of leaf biomass at a given time of the year. For instance, the timing of leaf onset and abscission determines the annual cycle of LAI and the length of the growing season in a deciduous plant, thus considerably affecting energy and water fluxes.

It has been recognized that phenology is mainly influenced by temperature (warm and cold periods), soil moisture, incoming radiation and length of the photoperiod, and from the ability of the plant to maintain a positive carbon balance (*Botta et al.*, 2000; *Arora and Boer*, 2005; *Ivanov et al.*, 2008b). Notwithstanding, leaf phenology remains one of the most difficult processes to represent in terrestrial ecosystem models (*Richardson et al.*, 2012; *Forkel et al.*, 2014; *Liu et al.*, 2019) because the identification of phenological transitions, e.g., leaf bud formation or leaf senescence from physiological and molecular mechanisms has not been completely unveiled (*Arora and Boer*, 2005; *Chuine and Régnière*, 2017).

Phenological rules vary according to characteristics of the plant species. For example, temperate evergreen, winter deciduous, and drought deciduous plants exhibit different relative sensitivities with respect to soil moisture and temperature. Often, the dates of leaf onset and abscission were prescribed in models (*Ruimy et al.*, 1996) or parameterized with simple methods, such as the number of chilly days or growing degree-days (*Haxeltine and Prentice*, 1996; *Kaduk and Heimann*, 1996; *Friend et al.*, 1997; *Botta et al.*, 2000; *Kucharik et al.*, 2000; *Knorr*, 2000; *Sitch et al.*, 2003; *Arora and Boer*, 2005). The shortcoming of such methods is a certain lack of generality and the fact that they may be implicit functions of current climate, unsuitable for changing climate scenarios. Climate warming is indeed expected to alter phenological phases such as leaf onset and flowering (*nuelas and Filella*, 2001; *Schwartz et al.*, 2006; *Cleland et al.*, 2007; *Liu et al.*, 2019). "Pseudo-mechanistic" models of phenology have been also proposed and are based on a carbon gain approach (*Arora and Boer*, 2005; *Ivanov et al.*, 2008b). The essential assumption in the carbon gain approach is that leaf onset starts when it is beneficial for a plant to produce leaves, in carbon terms; and leaf shedding starts when the production becomes persistently unfavorable. However, pseudo-mechanistic parameterizations are considerably challenging, they require to simulate a virtual leaf at any-time to evaluate the carbon balance and modeling experience suggests that they did not provide satisfactory results. Therefore, a multi-criteria phenological scheme is used in T&C based only on environmental conditions. The phenology phase determines plant physiological activities and allocation patterns as described earlier.

Phenological phases are differentiated among the main vegetation categories (Figure 39). Deciduous ($\Xi = 1$) and herbaceous species ($\Xi = 2$) experience, in the most general case, four phenological states: dormant ($\Phi = 1$), maximum growth ($\Phi = 2$), normal growth ($\Phi = 3$), and senescence ($\Phi = 4$) (*Arora and Boer*, 2005). In warm environments with high radiation loads (e.g., tropical deciduous forest, savannahs), the occurrence of a distinct dry season can lead to shedding leaves without a proper senescence phase. Evergreen ($\Xi = 0$) and tropical seasonal evergreens ($\Xi = 3$) experience three phenological states: preparation to the new season (Φ=1), initial growth (Φ=2, corresponding to the beginning of a new season), and normal growth (Φ=3).

20.1 Deciduous and grass phenology

20.1.1 From dormancy to maximum growth

The transition toward maximum growth ($\Phi = 1 \rightarrow 2$), characterized by leaf onset for seasonal plants ($\Xi = 1$ and $\Xi = 2$) takes place with the arrival of favorable weather. An important criterion for transitioning from dormant to maximum growth is related to temperature (*Baldocchi et al.*, 2005). In T&C a comparison between the average root zone temperature in the preceding 30 days $\overline{T_{R,30}}$ $[^{\circ}C]$ and a prescribed threshold temperature $T_{s,LO}$ $[^{\circ}C]$ is necessary for $\Phi = 1 \rightarrow 2$. The phenological transition takes place when $\overline{T_{R,30}} \geq T_{s,LO}$. The threshold $T_{s,LO}$ is essentially a model phenological parameter and has been found to change considerably with climate.

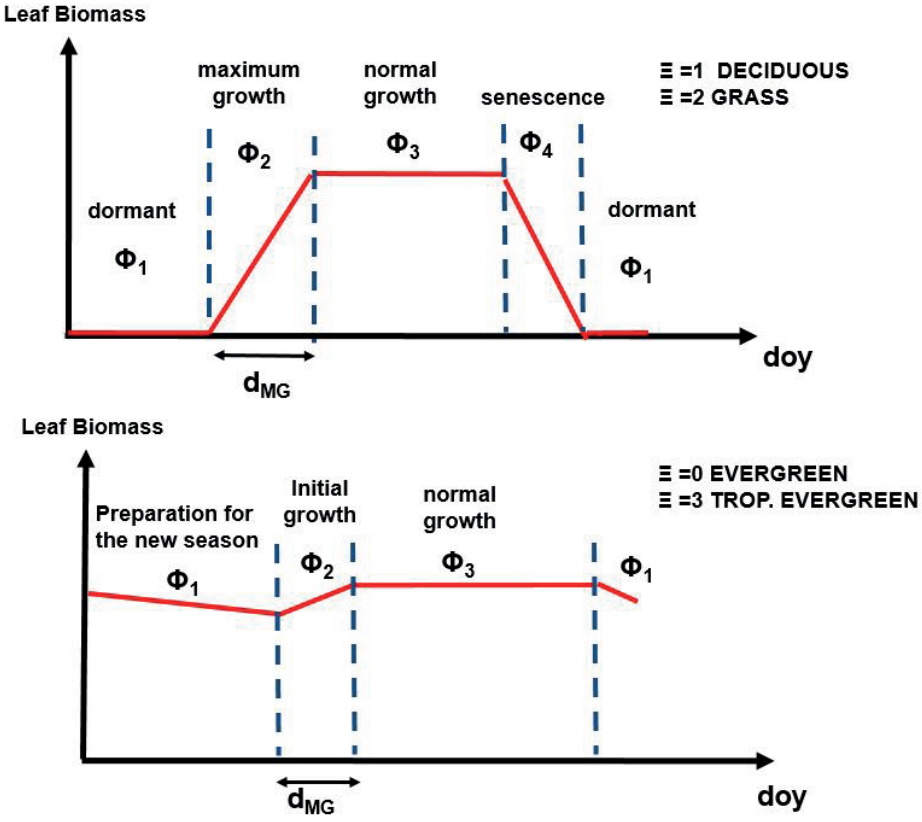

Figure 39: A conceptual illustration of typical phenology phases for deciduous and seasonal grass species ($\Xi = 1$ and $\Xi = 2$), upper plot and evergreen species ($\Xi = 0$ and $\Xi = 3$), lower plot. Vegetation transitions from the dormant phase ($\Phi = 1$) to the maximum growth state ($\Phi = 2$) at the onset of the favorable season, corresponding to leaf onset. After a prescribed period, d_{MG} $[day]$, plant transitions to the normal growth phase ($\Phi = 3$), until photoperiod conditions triggers the senescence phase ($\Phi = 4$). During senescence, leaf are shed and carbon is allocated exclusively to carbohydrate reserves ($\Xi = 1,\ 2$). When all leaves have been shed, the plant is in a dormant state ($\Phi = 1$) until the arrival of a new favorable season. For evergreen species ($\Xi = 0$), the states of senescence and dormancy do not exist, the state ($\Phi = 1$) corresponds to a preparation to the new season and it is identical to normal growth phase where carbon is allocated to all of the plant compartments (except reproductive tissues for temperate evergreen (with $f_f = 0$)). However, the phase $\Phi = 1$ differently from $\Phi = 3$ allows to initiate a new season. The subsequent phase ($\Phi = 2$), indeed, corresponds to a the initial growth phase, when the new season starts and carbon is predominately allocated to leaves, followed by a normal growth phase ($\Phi = 3$).

The second criterion for maximum growth to begin is that the photoperiod length, computed as the daytime length L_{day} [h] is larger than a prescribed threshold $L_{day,LO}$ [h]. The criterion $L_{day} \geq L_{day,LO}$ helps to constrain the leaf onset after a specific day of the year, since for a given geographical position the photoperiod of each day is constant. This criterion avoids unrealistic early season leaf flushing with an exceptionally warm end of the winter or early spring. The photoperiod length has been shown to be an important phenological control also in gardening experiments (*Körner and Basler*, 2010; *Polgar and Primack*, 2011). The threshold $L_{day,LO}$ is a model phenological parameter and has been found to change considerably with latitude and species.

The third criterion for maximum growth is related to soil moisture conditions. A certain amount of water must be available for considering environmental conditions favorable and starting a new growing season. The soil moisture stress factor β_R computed in Eq. 396 (Section 17.4.1) is integrated over a given number of preceding days pdd [day], $\overline{\beta_{R,pdd}}$ [$-$], as a proxy for soil moisture availability for phenology. The criterium is $\overline{\beta_{R,pdd}} \geq \beta_{LO}$, where β_{LO} [$-$] is a prescribed threshold of moisture availability typically assumed to be close to 1.0, i.e., lack of water stress is required for $\Phi = 1 \rightarrow 2$. The integration of $\overline{\beta_{R,pdd}}$ is typically carried out in the seven previous days, however, for certain biomes, which have phenology very responsive to sporadic rainfall events, it has been found that integrating only over one or two previous days provides better results. The soil moisture criterion is easily satisfied in temperate and wet climates but becomes important in climates where light and temperature are typically favorable but soil is too dry for plants to grow, e.g., arid and semiarid ecosystems or seasonally dry tropical climates as savannahs. In these ecosystems the growing season begins only after the return of wet conditions.

A final criterion is imposed on the day of the year, $J_{Day} < J_{Day,LO}$ in the boreal hemisphere and the reverse in the austral hemisphere. This criterion is mostly used for temperate plants and assures that leaf onset cannot start after (or before) a certain calendar date. This is a model control, which prevents the beginning of a new growing season during late fall when exceptionally favorable conditions may occur but persist over a short period only. From a mechanistic point of view, it mimics genetic memory that has been observed in plants (*Thomas and Stoddart*, 1980).

20.1.2 From maximum growth to normal growth

The transition from the maximum to the normal growth phase ($\Phi = 2 \rightarrow 3$) typically occurs after a certain number of days, which for deciduous forest and grasslands is typically sufficient to attain a certain leaf biomass. In T&C the transition $\Phi = 2 \rightarrow 3$ takes place after a prescribed number of days: $d_{LO} > d_{MG}$ [day], where d_{LO} [$days$] are the days from the beginning of $\Phi = 2$ and d_{MG} is a model parameter, which typical value ranges between 10 and 40 [$days$].

20.1.3 From normal growth to senescence

The normal growth phase ($\Phi = 3$) is the classic period of full vegetative growth during summer for seasonal plants when the plant allocates products of photosynthesis to all of the carbon compartments (leaves, fine roots, living sapwood, fruit-flowers, and carbohydrate reserves). The transition from the normal growth to the senescence state ($\Phi = 3 \rightarrow 4$) occurs only for deciduous plants ($\Xi = 1$), and is preceding the onset of unfavorable weather conditions. This transition is less clear than the one for leaf onset and fewer parameterizations have been proposed in literature. A simple criterion based on the day length is implemented. When the length of the day goes below a certain threshold $L_{day} < L_{day,SE}$ $[h]$, the normal growth state is completed and senescence starts. During senescence there is no more use of carbon for reproductive purposes (i.e., $f_f = 0$), and photosynthetic compounds are entirely allocated to the reserve pool.

For grass and herbaceous species ($\Xi = 2$) there is a direct transition from the normal growth to the dormant phase ($\Phi = 3 \rightarrow 1$) and the senescence state is not experienced.

20.1.4 Transition to dormancy

For deciduous species ($\Xi = 1$), the end of the senescence state is reached through a complete defoliation, i.e., when $LAI < LAI_{min}$ the plant is considered in a dormant state ($\Phi = 4 \rightarrow 1$) and it is simply waiting favorable conditions to begin a new growing season.

Herbaceous and grass species ($\Xi = 2$) transition from the normal growth phase to the dormant phase directly ($\Phi = 3 \rightarrow 1$) when the length of the day goes below a certain threshold $L_{day} < L_{day,SE}$ $[h]$. Given that many grasses are resilient to unfavorable conditions and ageing, LAI might also remain above LAI_{min} during winter or the dry season, differently from deciduous species. The dormancy phase is then treated similarly to senescence in deciduous trees, where no more use of carbon for reproductive purposes is allowed (i.e., $f_f = 0$), and carbon is entirely allocated to the reserve pool.

The vegetation category $\Xi = 2$, especially in Mediterranean and semi-arid climates can have several phenological cycles during a single year, due to moisture pulses triggering leaf onset in different seasons. For instance, in Mediterranean climates, grass grows during spring and fall, recovering from the drought induced summer die-out (*Montaldo et al.*, 2008). Hence, the condition $LAI < LAI_{min}$ can lead to a transition to the dormant state, $\Phi = 3 \rightarrow 1$. Herbaceous plants in dormant state are then ready to onset new leaves at the arrival of the next favorable season.

20.2 Evergreen phenology

Temperate evergreen phenological transition follows closely the one for deciduous forest, even though the phenological phases are slightly different. However, the phenology module is modified to consider the peculiarities of tropical biomes, i.e.

observed synchronization of new leaf growth and litterfall with sunlight during the dry season (*Huete et al.*, 2006; *Wu et al.*, 2016).

20.2.1 Transition to a new growing season

In temperate evergreen ($\Xi = 0$), the transition toward the initial growth ($\Phi = 1 \rightarrow 2$) is characterized by leaf flushing and takes place with the arrival of favorable weather following photoperiod length, temperatures and soil moisture availability thresholds as indicated in Section 20.1.1.

For tropical evergreen species ($\Xi = 3$), all the environmental controls (photoperiod length, warm temperatures, soil moisture availability) are always satisfied, which would imply a continuous normal growth phase without phenological transitions. However, this is contradicted by observations of a phenological cycle in tropical forests with most of the leaf flushing and shedding occurring at the beginning of the dry season with higher solar radiation loads (*Wu et al.*, 2016). Based on the consideration that dry season greening closely tracks sunlight seasonality (*Huete et al.*, 2006; *Wu et al.*, 2016), changes in photosynthetic active radiation (PAR) are used as the driver of leaf development. A new season ($\Phi = 1 \rightarrow 2$) is set to begin when $\overline{\Delta PAR} > \Delta PAR_{th}$, where $\overline{\Delta PAR} = \left\langle \langle PAR(t) \rangle_{30} - \langle PAR(t) \rangle_{45} \right\rangle_{10}$ is a smoothed time derivative of PAR and ΔPAR_{th} is a specific threshold. The smoothing proceedure is employed to remove the daily and sub-daily oscillations. This is achieved by computing the 10 days average of the difference between $\langle PAR(t) \rangle_{30}$ and $\langle PAR(t) \rangle_{45}$, i.e. PAR averages over 30 and 45 preceding days, respectively. $\overline{\Delta PAR}$ is negative when PAR (on average) decreases with time (e.g., with the arrival of the wet season), positive otherwise (e.g., with the arrival of the dry season). This choice is guided by the hypothesis that vegetation "senses" the arrival of a new light-rich dry season by detecting an increase in sunlight availability (*Wright and Van Schaik*, 1994) and is in accordance with observations of maximum leaf production one to two months before the peak in PAR (*Wu et al.*, 2016). Note that a similar mechanism based on light controls was used to explain observed synchronous flowering in the tropics (*Borchert et al.*, 2005). The signal ($\overline{\Delta PAR}$) is a non-istantaneous sunlight control on rainforest greening as the new season starts when the threshold ΔPAR_{th} is reached. The threshold ΔPAR_{th} is theoretically zero (i.e. the new season starts when $\overline{\Delta PAR}$ switches from negative to positive) but values of 0.75-1 [W m^{-2} d^{-1}] are used here to account for the remaining noise in $\overline{\Delta PAR}$ (*Manoli et al.*, 2018). At the end of stage Φ=1 and during Φ=2 a large fraction of the assimilated carbon is allocated to new leaf biomass NB_L to support the observed light-controlled green-up.

20.2.2 From initial growth to normal growth

For both temperate ($\Xi = 0$) and tropical evergreen species ($\Xi = 3$), the transition from the initial to the normal growth phase ($\Phi = 2 \rightarrow 3$) occurs after a prescribed number of days: $d_{LO} > d_{MG}$ $[day]$, where d_{LO} $[days]$ are the days from the beginning of $\Phi = 2$ and d_{MG} is a model parameter as for the other vegetation types that for tropical forests is typically around 45 $[days]$.

20.2.3 Evergreens: preparation for the next growing season

Temperate evergreen species ($\Xi = 0$) transition directly from the normal growth phase to the subsequent state ($\Phi = 3 \rightarrow 1$), preparation for the new season ($\Phi = 1$), that coincides almost perfectly with the normal growth because evergreen species can actively assimilate carbon during winter if allowed by meteorological conditions. The only exception is that allocation to reproductive tissues is inhibited (i.e., $f_f = 0$). The transition occurs when the length of the day goes below a certain threshold $L_{day} < L_{day,SE}$ $[h]$. Passing through $\Phi = 1$ is fundamental because it signals the plant to be ready for a new initial growth phase, which cannot occur from normal growth $\Phi = 3$ directly.

For tropical evergreen species ($\Xi = 3$), changes in L_{day} are typically quite constrained and they would not allow for any phenological transition. Therefore, the transition $\Phi = 3 \rightarrow 1$ occurs when $d_{LO} > A_{cr}$. The critical leaf age parameters A_{cr} for tropical forests is estimated to be 270 $[days]$ (*Manoli et al.*, 2018). Even though allocation dynamics are variable throughout the year (Section 17.3), from a modeling perspective phase Φ=1 is identical to normal growth (Φ=3) with the only difference that it allows for the preparation to a new season. The criterion used for the transition to Φ=1 (i.e. $d_{flo} > A_{L,cr}$) ensures that the new season cannot start before the leaves produced in the previous year have reached maturity. During phase Φ=1, d_{flo} is scaled back as $d_{flo}(t+dt) = d_{flo}(t) - \frac{365}{365-A_{L,cr}}dt$ to progressively increase allocation to new leaves and prepare for phase Φ=2 (*Manoli et al.*, 2018).

20.3 Disturbances and phenology

The normal phenological cycle can be modified by severe disturbances and management practices. When an external disturbance defoliates the plant reducing the LAI below the critical threshold LAI_{min} (e.g., a wind-storm, grass cuts or grazing activity) vegetation can start a new growing season provided that the cause of the disturbance is not in place anymore and all conditions listed in Section 20.1.1 are satisfied, e.g., soil moisture, photoperiod length, and temperature conditions are still favorable.

20.4 Leaf age and new biomass

The new biomass of leaves produced at each time step NB_{Leaf} $[g\, C\; m^{-2}\, VEG\; day^{-1}]$ can be computed as:

$$NB_{Leaf}(t) \quad = \quad \frac{\Big[C_{leaf}(t) - C_{leaf}(t-1) + S_{leaf}dt\Big]}{dt}, \qquad (455)$$

where dt is the daily time step. The value of NB_{Leaf} is inferiorly limited to zero, since there cannot be a negative production of new biomass. These cases would correspond to a lack of new biomass production. The quantity NB_{Leaf} is used in the computation of tissue turnover for tropical evergreen species (Section 17.4).

Another quantity needed to parameterize leaf shedding is the leaf age, which represents the average age of the leaf biomass. Younger leaves are expected to be shed at a much slower rate then older ones (Section 17.4). While, leaves of the same tree may have different ages, especially in evergreens (Figure 40 and *Wu et al.* (2016)) this is not accounted for in T&C, which tracks a single average age Ag_L $[day]$, for alive leaves, and one $Ag_{L,dead}$ $[day]$ for dead standing leaves:

$$Ag_L(t) \quad = \quad \frac{\Big[LAI(t) - N_{LAI}\Big]\Big[Ag_L(t-dt) + dt\Big] + N_{LAI}\ dt}{LAI(t)}\,, \tag{456}$$

where N_{LAI} $[m^2\ leaf\ area\ m^{-2}\ VEG\,area]$ is the new leaf area onset between the time $t - dt$ $[day]$ and t $[day]$, where dt is the daily time step:

$$N_{LAI} \quad = \quad LAI(t) - LAI(t-dt) - LAI_{turn}\,, \tag{457}$$

where N_{LAI} is only computed when it is positive and LAI_{turn} $[m^2\ leaf\ area\,m^{-2}\ VEG\,area]$ represent the LAI of leaves turned over during the time step dt. Equivalently, the age of dead leaves can be also estimated as:

$$Ag_{L,dead}(t) \quad = \quad \frac{\Big[LAI_{dead}(t) - N_{LAI,dead}\Big]\Big[Ag_{L,dead}(t-dt) + dt\Big] + N_{LAI,dead}\ dt}{LAI_{dead}(t)}\,, \tag{458}$$

where $N_{LAI,dead}$ $[m^2\ leaf\ area\ m^{-2}\ VEG\,area]$ is the new leaf amount of dead leaves between the time $t - dt$ and t $[day]$, computed similarly to Eq. (457) but for dead leaves.

Finally, the number of days from the beginning of the maximum growth phase $\Phi = 2$, d_{LO} $[days]$, which is used to modify allocation fractions for tropical seasonal evergreen species ($\Xi = 3$) (Section 17.3.1) is computed incrementally $d_{LO}(t + dt) = d_{LO}(t) + 1$ during phenological phases $\Phi = 2$ and $\Phi = 3$ but is scaled back $d_{LO}(t + dt) = d_{LO}(t) - 365/(365 - A_{cr})$, during $\Phi = 1$. This model formulation serves to bring d_{LO} back to zero, and therefore to progressively increase the allocation to new leaves, in preparation of the next growing season.

Figure 40: An example of leaves with different ages, picture taken in late October in a chestnut (Castanea sativa) deciduous wood in Tuscany.

20.5 Relative photosynthetic efficiency

There is evidence that leaf age or photoperiod can affect photosynthetic capacity (*Wilson et al.*, 2001; *Bauerle et al.*, 2012) and parameterizations of relative photosynthetic efficiency, e_{rel} $[-]$, depending on these quantities have been proposed (*Krinner et al.*, 2005; *Medvigy et al.*, 2009; *Bauerle et al.*, 2012). In T&C, e_{rel} is modified only for deciduous species ($\Xi = 1$) and tropical evergreen species ($\Xi = 3$) using two different parameterizations supported by recent literature results.

For deciduous species, which are experiencing a variability in the seasonal day length, photosynthetic efficiency e_{rel} is parameterized as function of the day length L_{day} and maximum day length for a given location $L_{day,max}$ (*Bauerle et al.*, 2012):

$$e_{rel} = \left(\frac{L_{day}}{L_{day,max}}\right)^2 . \tag{459}$$

For tropical evergreen species photosynthetic efficiency e_{rel} is parameterized as a function of leaf age Ag_L $[day]$, and the fraction between the new biomass created in the previous 30 days $\overline{NB_{Leaf,30}}$ $[g\,C\,m^{-2}\,VEG\,day^{-1}]$ and the current leaf biomass C_{leaf}, following *Wu et al.* (2016):

$$e_{rel} = 1.6104 - 0.0601\frac{Ag_L}{30} - 1.2007\frac{30\overline{NB_{Leaf,30}}}{C_{leaf}} , \tag{460}$$

with e_{rel} superiorly limited to 1. This parametrization accounts for the fact that photosynthetic efficiency is lower for young and old leaves while it is maximal for mature leaves (*Wu et al.*, 2016). The coefficient are derived using data observed in *Wu et al.* (2016) for a seasonal tropical forest in the Amazon (*Manoli et al.*, 2018).

Given the even larger uncertainties in the parametrization of e_{rel} for grass ($\Xi = 2$) and normal evergreens ($\Xi = 3$), T&C always considers a constant maximum photosynthetic efficiency for these plant life forms, e.g., $e_{rel} = 1$.

21 Soil biogeochemistry

21.1 Litter generation

Litter is produced by the plant as a consequence of tissue turnover due to ageing and environmental stresses or because of disturbances and management actions (Section 22). The total carbon export, C_{export} $[g\,C\ m^{-2}\,VEG\ day^{-1}]$, from the plant to the litter pools and mycorrhizae in absence of major disturbances and management is:

$$C_{export} = S_{flfr} + S_{wood} + S_{ldea} + S_{root} + R_{exmy}\,, \tag{461}$$

where the terms in the right-hand-side of the equation represent the carbon turnover fluxes (turnover of reproductive tissues S_{flfr}, woody tissues S_{wood}, standing dead leaves S_{ldea} and fine roots S_{root}), and R_{exmy} is the rate of root exudation and export to mycorrhizae (Section 17.3.2). The total export from the plant of nitrogen N_{export} $[g\,N\ m^{-2}\,VEG\ day^{-1}]$, phosphorus P_{export} $[g\,P\ m^{-2}\,VEG\ day^{-1}]$, and potassium K_{export} $[g\,K\ m^{-2}\,VEG\ day^{-1}]$ are:

$$N_{export} = \frac{S_{ldea}}{CN_{ld}} + r_{N_c}\frac{S_{flfr}}{CN_f} + r_{N_c}(1 - f_{transf,r})\frac{S_{root}}{CN_r} + \frac{S_{wood}}{CN_h}\,, \tag{462}$$

$$P_{export} = \frac{S_{ldea}}{CP_{ld}} + r_{P_c}\frac{S_{flfr}}{CP_f} + r_{P_c}(1 - f_{transf,r})\frac{S_{root}}{CP_r} + \frac{S_{wood}}{CP_h}\,, \tag{463}$$

$$K_{export} = \frac{S_{ldea}}{CK_{ld}} + r_{K_c}\frac{S_{flfr}}{CK_f} + r_{K_c}(1 - f_{transf,r})\frac{S_{root}}{CK_r} + \frac{S_{wood}}{CK_h}\,, \tag{464}$$

where the plant relative nutrient concentrations for nitrogen r_{N_c} $[-]$, phosphorus r_{P_c} $[-]$, and potassium r_{K_c} $[-]$ are described in Section 17.3.5 and the other terms are previously defined. The total nutrient export in the form of litter (e.g., N_{export} for nitrogen) differs from the nutrient export from the plant (e.g., $N_{export,l}$) computed in Eq. (414) because of the buffering effect of standing dead leaves (Section 19.1). The term S_{ldea} is indeed the flux of leaf abscised from the plant and CN_{ld} $[g\,C\ g\ N^{-1}]$ is the carbon to nitrogen ratio of standing dead leaves, while S_{leaf} is the turnover rate of live leaves. The variable CN_{ld}, and equivalently CP_{ld} $[g\,C\ g\ P^{-1}]$ and CK_{ld} $[g\,C\ g\ K^{-1}]$, are computed as the ratio of the carbon C_{ldea} and nutrient contents (N_{ldea}, P_{ldea}, K_{ldea}) in the standing dead leaves. The nutrient content of standing dead leaves is a prognostic variable that is computed as:

$$\frac{dN_{ldea}}{dt} = r_{N_c}(1 - f_{transf,l})\frac{S_{leaf}}{CN_l} - \frac{S_{ldea}}{CN_{ld}}\,, \tag{465}$$

$$\frac{dP_{ldea}}{dt} = r_{P_c}(1 - f_{transf,l})\frac{S_{leaf}}{CP_l} - \frac{S_{ldea}}{CP_{ld}}\,, \tag{466}$$

$$\frac{dK_{ldea}}{dt} = r_{K_c}(1 - f_{transf,l})\frac{S_{leaf}}{CK_l} - \frac{S_{ldea}}{CK_{ld}}\,. \tag{467}$$

The nutrient content in the dead leaves is therefore a function of the relative nutrient concentration, resorption coefficients ($f_{transf,l}$ and $f_{transf,r}$), and the rates of leaf turnover and abscission.

The total carbon exported by the plant in litter form is subdivided in eight chemically different fluxes $I_{C,litter,i}$ $[g\,C\ m^{-2}\,VEG\ day^{-1}]$, which serve as inputs to the litter pools that are described in the following. One additional flux corresponding to the carbon export to mycorrhizal I_{myc} $[g\,C\ m^{-2}\,VEG\ day^{-1}]$ is computed in Section 17.3.2 ($I_{myc} = R_{ex,2}$). Eight distinct carbon fluxes are necessary because litter is subdivided between belowground and aboveground compartments and among woody, metabolic, and structural components, with the structural and woody litter in turn subdivided into non-lignin and lignin components (Fig. 42, see further explanations in Section 21.2). The woody litter is separated from structural litter only in the aboveground, while in the belowground compartment woody debris is assumed to contribute directly to metabolic and structural litter.

$$
\begin{aligned}
I_{C,litter,1} &= f_{met,l} S_{ldea} + f_{met,fr} S_{flfr}\,, && (468)\\
I_{C,litter,2} &= (1 - f_{met,l}) S_{ldea}\,(1 - Lig_{fr,l}) + \\
&\quad (1 - f_{met,fr}) S_{flfr}\,(1 - Lig_{fr,fr})\,, && (469)\\
I_{C,litter,3} &= (1 - f_{met,l}) S_{ldea}\,Lig_{fr,l} + (1 - f_{met,fr}) S_{flfr}\,Lig_{fr,fr}\,, && (470)\\
I_{C,litter,4} &= f_{ab} S_{wood}\,(1 - Lig_{fr,w})\,, && (471)\\
\\
I_{C,litter,5} &= f_{ab} S_{wood}\,Lig_{fr,w}\,, && (472)\\
I_{C,litter,6} &= R_{ex,1} + f_{met,r} S_{root} + f_{met,w}(1 - f_{ab}) S_{wood}\,, && (473)\\
I_{C,litter,7} &= R_{ex,3} + (1 - f_{met,r}) S_{root}(1 - Lig_{fr,r}) + \\
&\quad (1 - f_{met,w})(1 - f_{ab}) S_{wood}(1 - Lig_{fr,w})\,, && (474)\\
I_{C,litter,8} &= (1 - f_{met,r}) S_{root} Lig_{fr,r} + \\
&\quad (1 - f_{met,w})(1 - f_{ab}) S_{wood} Lig_{fr,w}\,, && (475)\\
I_{myc} &= R_{ex,2}\,, && (476)
\end{aligned}
$$

where the name and meaning of the different litter pools C_{litter} is specified in Table 3. The term f_{ab} $[-]$ is the aboveground fraction of the C_{heaw} pool. The terms $Lig_{fr,p}$ $[g\,Lignin\ g\ DM^{-1}]$ are the lignin to dry mass ratios (e.g., concentrations) in the different pools p (with p corresponding to leaves l, fruits fr, root r, and heartwood/dead sapwood w). The turnover fluxes and R_{ex} components are defined earlier. Note that root exudation $R_{ex,1}$ is considered to flow entirely to the metabolic belowground carbon pool, while carbon investment in root nodules for biological fixation $R_{ex,3}$ are added directly to the structural non-lignin litter pool.

The fraction of metabolic $f_{met,p}$ $[-]$ versus structural $f_{str,p}$ $[-]$ litter is computed for each pool p (leaves l, fruits fr, root r, and heartwood/dead sapwood w) based on the lignin to nitrogen ratio (*Parton et al.*, 1988; *Krinner et al.*, 2005; *Orwin et al.*, 2011):

$$f_{met,p} = 0.85 - 0.018 \left(\frac{CN_p}{r_{N_c}} 2\, Lig_{fr,p} \right) , \quad (477)$$

$$f_{str,p} = 1 - f_{met,p} , \quad (478)$$

where CN_p $[g\,C\ g\,N^{-1}]$ is the carbon to nitrogen ratio of a given pool p and $Lig_{fr,p}$ needs to be multiplied by 2 to obtain the $[g\,Lignin\ g\ C^{-1}]$, since the carbon content of dry mass is roughly 0.5 $[g\,C\ g\ DM^{-1}]$ (*Thomas and Martin*, 2012). The lignin content of a given tissue is a model parameter prescribed in the list of stoichiometric parameters (Table 2). The expression in Eq. (477) allocates progressively more carbon to structural litter when the lignin content of the tissue increases or the nitrogen content decreases as illustrated in Figure 41.

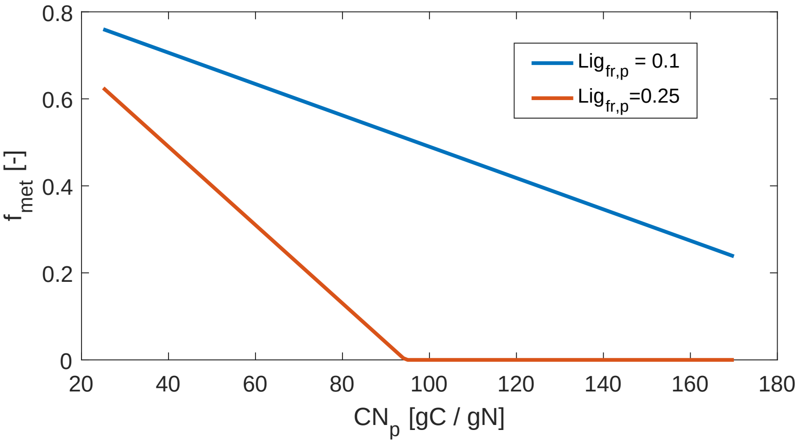

Figure 41: Fraction of metabolic f_{met} $[-]$ litter as a function of carbon to nitrogen ratio CN_p $[g\,C\ g\,N^{-1}]$ for various levels of lignin to dry mass ratio $Lig_{fr,p}$ $[g\,Lignin\ g\ DM^{-1}]$.

Each nutrient has only three litter pools (aboveground, belowground and aboveground woody). For nutrients T&C do not distinguish between lignin versus hemicellulose/cellulose compartments and the distinction between structural and metabolic litter nutrient pools is pre-imposed using a ratio between the structural and metabolic C:N equal to 5 as suggested in the original CENTURY model and used in subsequent developments (*Parton et al.*, 1988; *Kirschbaum and Paul*, 2002). Therefore, the nitrogen input to the three litter pools is computed as:

$$I_{N,litter,sur} = \frac{S_{ldea}}{CN_{ld}} + r_{N_c} \frac{S_{flfr}}{CN_f} \quad (479)$$

$$I_{N,litter,wod} = f_{ab} \frac{S_{wood}}{CN_h} \quad (480)$$

$$I_{N,litter,ssr} = r_{N_c} (1 - f_{transf,r}) \frac{S_{root}}{CN_r} + (1 - f_{ab}) \frac{S_{wood}}{CN_h} , \quad (481)$$

where $I_{N,litter,sur}$ $[g\,N\ m^{-2}\,VEG\ day^{-1}]$ is the nitrogen input to above-ground non-woody litter, $I_{N,litter,wod}$ $[g\,N\ m^{-2}\,VEG\ day^{-1}]$ is the nitrogen input to aboveground woody litter, and $I_{N,litter,ssr}$ $[g\,N\ m^{-2}\,VEG\ day^{-1}]$ is the nitrogen input to belowground litter. Equivalent expressions can be written for phosphorus and potassium.

The fluxes entering the various pools are computed for unit of vegetation and thus they must be integrated over the entire computational element to calculate the total input to any given litter pool at the element scale (Table 3). The total input for unit of ground area I_{litter} $[g\,C\ m^{-2}\ day^{-1}]$ is computed as a weighted sum of the crown areas C_{crown} (Section 2.2) and summing litter inputs from upper and lower vegetation:

$$I_{litter} = \sum_{j} C_{crown,j}\,(I^{j}_{litter,H} + I^{j}_{litter,L})\,, \tag{482}$$

where $I_{litter,H}$ and $I_{litter,L}$ are the flux of litter from high and low-vegetation respectively.

21.2 Litter Carbon budget

The carbon decomposition rates of the eight litter pools (Table 3 and Fig. 42) are assumed to follow linear kinetics as in the original version of the CENTURY model and subsequent modifications (*Parton et al.*, 1988, 1993; *Kirschbaum and Paul*, 2002). This formulation relies on the assumption that microbial communities are typically not representing a limiting factor for aboveground (air-exposed) litter decomposition, and therefore decomposition rates can be assumed to scale linearly with the litter mass. Interactions with macrofauna are also neglected, even though they might be important in specific conditions (*Fahey et al.*, 2013). In the soil, such a hypothesis is more critical but it is maintained for simplicity, considering that belowground C-litter represents a rather small portion of the total belowground soil organic carbon. Eight distinct C-litter pools are simulated explicitly, as turn-over times and nutrient composition of belowground and aboveground compartments, and metabolic, structural, and woody litter can differ greatly (*Kirschbaum and Paul*, 2002). Furthermore, chemical composition in terms of litter lignin concentration affects decomposition rates (e.g *Freschet et al.*, 2012) and is explicitly accounted for in the model. Note that even though eight distinct C-litter pools are simulated, only five pools are physically separated in reality since the separation within the structural and woody components is just based on the chemical composition. The mass balance of each litter carbon pool is computed as:

$$\frac{dC_{litter,i}}{dt} = I_{C,litter,i} - D_i\,C_{litter,i}\,, \tag{483}$$

where $C_{litter,i}$ $[g\,C\ m^{-2}]$ is the amount of carbon in pool i, $I_{C,litter,i}$ $[g\,C\ m^{-2}\ day^{-1}]$ is the carbon input and D_i $[day^{-1}]$ is the decomposition rate of the litter pool i, which is function of intrinsic chemical properties (via decay coefficients k_i) and environmental conditions (Fig. 42).

An additional variable that can be computed is the total aboveground litter mass

B_{litter} $[kg\, DM\, m^{-2}]$, which is used to compute litter resistance for each crown area in Section 6.5. This term is computed summing the aboveground $C_{litter,i}$ terms as: $B_{litter} = 0.002 \sum_{i=1}^{5} C_{litter,i}\, C_{crown}$.

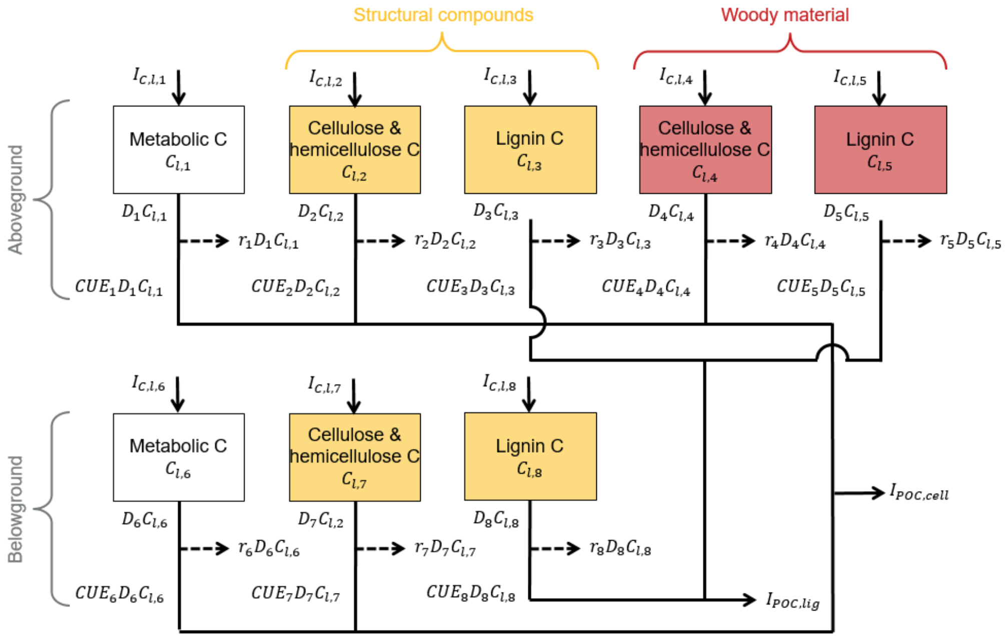

Figure 42: A scheme of the 8 litter carbon pools simulated by the model. Aboveground litter pools are subdivided in metabolic, structural and woody and belowground pools are subdivided in metabolic and structural only. Decomposition rates D_i, respiration coefficients r_i and carbon use efficiencies CUE_i $(r_i = 1 - CUE_i)$ are also illustrated.

The distinction between metabolic and structural pools is mostly used in the soil-biogeochemistry modeling literature (*Parton et al.*, 1988; *Kirschbaum and Paul*, 2002; *Yang et al.*, 2009; *Zaehle and Friend*, 2010), however the link between these pools, measurable quantities, and the litter generated by different plant tissues require additional explanations. This subdivision maps onto observable litter fractions, because the metabolic component can be regarded as the hot-water extractable litter, while the structural non-lignin and lignin components can be regarded as the acid-soluble (hydrolyzable) and acid-insoluble (unhydrolyzable) fractions as defined in more recent models (*Campbell et al.*, 2016; *Robertson et al.*, 2019). A link with plant tissue components can be also made (*Poorter*, 1994; *Poorter and Villar*, 1997; *Kögel-Knabner*, 2002), if we consider that metabolic pools mostly encompasses proteins, starch, fructans, NSC and chlorophyll that are typically characterized by fast decay times. Conversely, the litter structural pools are characterized by slower decay when compared to metabolic pools and include mostly cellulose and non-cellulose (hemicellulose-pectin) and also tannin, poliphenols, lipids and cutine. Lignin is considered as a separate pool to track the lignin content in the structural and woody pools. The metabolic litter is assumed to be lignin free. Each pool is characterized by a decay coefficient k_i, which determines how fast or slow a given pool is turning over under standard environmental conditions and by a carbon use efficiency CUE_i, which controls the fraction of carbon respired $r_i = 1 - CUE_i$ in the process of litter decomposition (Table 3).

Litter Pool	**Description**	**CUE$_i$ base**	**Decay coefficient k_i**
$C_{litter,i}$		$[-]$	$[day^{-1}]$
1	Aboveground Metabolic	$CUE_{met,sur} = 0.45$	$k_{met,sur} = 1/12.5$
2	Aboveground Structural (Cell./Hemicell.)	$CUE_{str,sur} = 0.55$	$k_{str,sur} = 1/46$
3	Aboveground Structural (Lignin)	$CUE_{str,sur} = 0.55$	$k_{str,sur} = 1/46$
4	Aboveground Woody (Cell./Hemicell.)	$CUE_{wod,sur} = 0.55$	$k_{wod,sur} = 1/150$
5	Aboveground Woody (Lignin)	$CUE_{wod,sur} = 0.55$	$k_{wod,sur} = 1/150$
6	Belowground Metabolic	$CUE_{met,ssr} = 0.45$	$k_{met,ssr} = 1/10$
7	Belowground Structural (Cell./Hemicell.)	$CUE_{str,ssr} = 0.45$	$k_{str,ssr} = 1/37$
8	Belowground Structural (Lignin)	$CUE_{str,ssr} = 0.45$	$k_{str,ssr} = 1/37$

Table 3: Description of the eight pools used to represent different characteristics and composition of litter in T&C, standard carbon use efficiencies (when temperature and stoichiometric dependencies are not considered) and decay coefficients at a reference temperature of 40 $°C$, as given by *Kirschbaum and Paul* (2002). Cell. stands for cellulose and Hemicell. for hemicellulose. Different colors in the numeration and description are lumping the five physically separated litter pools (see also Fig. 42). A link with observable quantities can be made because the metabolic component can be regarded as the hot-water extractable litter, while the structural non-lignin and lignin components can be regarded as the acid-soluble (hydrolyzable) and acid-insoluble (unhydrolyzable) fractions.

The non-lignin and lignin pools in the structural (belowground and aboveground) and woody compartments are physically connected and therefore the decay coefficients and CUEs are identical. However, the lignin content affects the litter decomposition rates D $[day^{-1}]$, since the rates are dependent on the amount of lignin (the exponential argument in the equations below), which is considered an inhibitory factor for decomposition (*Parton et al.*, 1988; *Kirschbaum and Paul*, 2002). Additional factors controlling the litter decomposition rates D $[day^{-1}]$ are air or soil temperature and soil moisture:

$$D_1 = k_{met,sur}\, f_{T1}\,, \tag{484}$$

$$D_2 = k_{str,sur}\, f_{T1} \exp\left(\frac{-5\, C_{litter,3}}{C_{litter,2} + C_{litter,3}}\right)\,, \tag{485}$$

$$D_3 = k_{str,sur}\, f_{T1} \exp\left(\frac{-5\, C_{litter,3}}{C_{litter,2} + C_{litter,3}}\right)\,, \tag{486}$$

$$D_4 = k_{wod,sur}\, f_{T1} \exp\left(\frac{-5\, C_{litter,5}}{C_{litter,4} + C_{litter,5}}\right)\,, \tag{487}$$

$$D_5 = k_{wod,sur}\, f_{T1} \exp\left(\frac{-5\, C_{litter,5}}{C_{litter,4} + C_{litter,5}}\right)\,, \tag{488}$$

$$D_6 = k_{met,ssr}\, f_{T2}\, f_{SM.Litter}\,, \tag{489}$$

$$D_7 = k_{str,ssr}\, f_{T2}\, f_{SM.Litter} \exp\left(\frac{-5\, C_{litter,8}}{C_{litter,7} + C_{litter,8}}\right)\,, \tag{490}$$

$$D_8 = k_{str,ssr}\, f_{T2}\, f_{SM.Litter} \exp\left(\frac{-5\, C_{litter,8}}{C_{litter,7} + C_{litter,8}}\right)\,, \tag{491}$$

where the k_i $[day^{-1}]$ are the litter decay coefficients defined in Table (3), f_{T1}, f_{T2} are temperature dependent functions for decomposition at a reference temperature of 40 $^{\circ}C$ and $f_{SM.Litter}$ is a soil moisture dependent function applied only to the belowground litter pools, since aboveground litter moisture content is neglected (see Section 21.5 for the definition of these environmental dependencies).

The total litter respiration R_{litter} and subsurface litter respiration $R_{litter,ssr}$ $[g\,C\ m^{-2}\ day^{-1}]$ can be computed directly from the litter decomposition:

$$R_{litter} = \sum_{i=1}^{8} D_i\, C_{litter,i}\, r_i\,, \tag{492}$$

$$R_{litter,ssr} = \sum_{i=6}^{8} D_i\, C_{litter,i}\, r_i\,, \tag{493}$$

where r_i are the respiration coefficients for the eight different carbon litter pools, derived from the carbon use efficiency CUE_i:

$$r_i = 1 - CUE_i\,. \tag{494}$$

An option to introduce a temperature dependence of the carbon use efficiency can be added in T&C (*Wang et al.*, 2013):

$$r_i = 1 - \min\left[CUE_{max}, CUE_i + m_T\left(T_{bg} - T_{ref}\right)\right]\,, \tag{495}$$

where $CUE_{max} = 0.6$ is the maximum physiological limit to carbon use efficiency of microbial biomass (*Sinsabaugh et al.*, 2013), CUE_i $[-]$ is the carbon use efficiency corresponding to a given C-litter pool (Table 3), m_T $[^{\circ}C^{-1}]$ is a temperature sensitivity coefficient of CUE (*Devevre and Horwath*, 2000; *Wang et al.*, 2013; *Li et al.*, 2014), T_{bg} $[^{\circ}C]$ is the soil temperature in the biogeochemically active zone, and $T_{ref} = 20^{\circ}C$ is a reference temperature.

Rather than using prescribed values of CUE_i from Table 3, CUE_i can be also computed using the carbon to nitrogen ratio of the litter pool and therefore accounting for stoichiometric dependencies of CUE_i. Litter bag decomposition studies showed that carbon use efficiency is not a constant or a simple function of the amount of recalcitrant carbon compounds (e.g., lignin), but it also depends on the nutrient stoichiometry (*Manzoni et al.*, 2008; *Sinsabaugh et al.*, 2013). Specifically, CUE tends to increase for nutrient rich substrates and decreases when the carbon to nitrogen ratio is large. The expression derived by *Sinsabaugh et al.* (2013) from a meta-analysis of published studies can be used to compute litter CUE_i:

$$CUE_i = \frac{CUE_{max}}{1 + 0.015\, CN_i}\,, \tag{496}$$

where CN_i is the carbon to nitrogen ratio of a given litter pool (e.g., Eq. 503-507).

The default option in T&C is to use constant values of CUE as specified in Table 3. However, temperature (Eq. 495) and stoichiometric (Eq. 496) dependencies can be enabled if there is an interest in simulating CUE variability.

The fraction of decomposed litter that is not respired represents the carbon input to the particulate organic carbon (POC) (Section 21.4). Specifically, the inputs to the POC carbon pools are computed separately for lignin $I_{POC,lig}$ and cellulose/hemicellulose $I_{POC,cel}$ compounds:

$$\begin{aligned}
I_{POC,lig} &= (1-r_3)D_3\,C_{litter,3} + (1-r_5)D_5\,C_{litter,5} \\
&\quad +(1-r_8)D_8\,C_{litter,8}\,, && (497)\\
I_{POC,cel} &= (1-r_1)D_1\,C_{litter,1} + (1-r_2)D_2\,C_{litter,2} + (1-r_6)D_6\,C_{litter,6} \\
&\quad +(1-r_7)D_7\,C_{litter,7} + (1-r_4)D_4\,C_{litter,4}\,. && (498)
\end{aligned}$$

During the litter decomposition process a fraction of carbon $\lambda_c\, I_{POC,cel}$ is assumed to directly contribute to the dissolved organic carbon (DOC) pool, with λ_c $[-]$ representing the C-leaching coefficient.

Note that litter inputs are computed for unit of ground area, while all the subsequent soil biogeochemistry dynamics are computed for unit of soil mass (Section 21.4) therefore a unit conversion operation is needed. Given the lumped treatment of soil-biogeochemistry processes in T&C the conversion from $[g\,C\,m^{-2}\,day^{-1}]$ to $[g\,C\;g\,soil^{-1}\,day^{-1}]$ is computed as:

$$I_{POC}\;\left[g\,C\;g\,soil^{-1}\,day^{-1}\right] = \frac{I_{POC}\left[g\,C\,m^{-2}\,day^{-1}\right]}{Z_{biog}\,\rho_d}\,, \tag{499}$$

where Z_{biog} $[m]$ is the depth of the biogeochemically active zone and ρ_d $[g\,m^{-3}]$ is the bulk density of dry soil.

21.3 Litter Nutrient budget

While there are eight carbon litter pools, nutrient (N, P, and K) dynamics are only tracked in three litter pools. In the following, the notation refers only to nitrogen but equivalent expressions can be written for phosphorus and potassium. The three pools are aboveground litter ($N_{litter,sur}$), belowground litter ($N_{litter,ssr}$), and aboveground woody litter ($N_{litter,wod}$). Only three pools are necessary because lignin does not contain N and the distinction between structural and metabolic nutrient pools is pre-imposed assigning a fixed ratio $r_{CN} = 5$ between the structural and metabolic C:N ratios (*Parton et al.*, 1988; *Kirschbaum and Paul*, 2002). When the r_{CN} value is prescribed, tracking a single litter pool is sufficient to know at any time the amounts of nitrogen in the metabolic and structural pools. The mass balances of the litter nitrogen pools are:

$$\begin{aligned}
\frac{dN_{litter,sur}}{dt} &= I_{N,litter,sur} - \frac{D_1 C_{litter,1}}{CN_{met,sur}} - \frac{D_2 C_{litter,2} + D_3 C_{litter,3}}{CN_{str,sur}}\,, && (500)\\
\frac{dN_{litter,wod}}{dt} &= I_{N,litter,wod} - \frac{D_4 C_{litter,4} + D_5 C_{litter,5}}{CN_{wod,sur}}\,, && (501)\\
\frac{dN_{litter,ssr}}{dt} &= I_{N,litter,ssr} - \frac{D_6 C_{litter,6}}{CN_{met,ssr}} - \frac{D_7 C_{litter,7} + D_8 C_{litter,8}}{CN_{str,ssr}}\,, && (502)
\end{aligned}$$

where the carbon to nitrogen ratio can be computed for each litter type as:

$$
\begin{aligned}
CN_{met,sur} &= \frac{C_{litter,1}}{(1-f_{str,sur})N_{litter,sur}}\,, &(503)\\
CN_{str,sur} &= \frac{C_{litter,2}+C_{litter,3}}{f_{str,sur}N_{litter,sur}}\,, &(504)\\
CN_{wod,sur} &= \frac{C_{litter,4}+C_{litter,5}}{N_{litter,wod}}\,, &(505)\\
CN_{met,ssr} &= \frac{C_{litter,6}}{(1-f_{str,ssr})N_{litter,ssr}}\,, &(506)\\
CN_{str,ssr} &= \frac{C_{litter,7}+C_{litter,8}}{f_{str,ssr}N_{litter,ssr}}\,. &(507)
\end{aligned}
$$

The fraction of nutrients belonging to the structural litter in the aboveground and belowground compartments $f_{str,sur}$ and $f_{str,ssr}$ are:

$$
\begin{aligned}
f_{str,sur} &= 1-\frac{1}{1+\frac{C_{litter,2}+C_{litter,3}}{r_{CN}C_{litter,1}}}\,, &(508)\\
f_{str,ssr} &= 1-\frac{1}{1+\frac{C_{litter,7}+C_{litter,8}}{r_{CN}C_{litter,6}}}\,. &(509)
\end{aligned}
$$

The expressions above are analytically derived to preserve a ratio of structural to metabolic C:N equal to r_{CN}. Even though Eq. (508) and (509) are computed using the carbon to nitrogen ratio, the fractions $f_{str,sur}$ and $f_{str,ssr}$ are subsequently applied to all the other nutrients, expecting the same relative (not absolute) proportion between structural and metabolic nutrient content as for nitrogen.

The input of nitrogen to the SOM nitrogen pool $I_{som,nit}$ $[g\,N\ g\,soil^{-1}\,day^{-1}]$ is computed using the carbon decomposition rates $D_i\,C_{litter,i}$ $[g\,C\ g\,soil^{-1}\ day^{-1}]$ and the carbon to nitrogen ratio of each pool:

$$
\begin{aligned}
I_{som,nit} &= \frac{D_1C_{litter,1}}{CN_{met,sur}}+\frac{D_2C_{litter,2}+D_3C_{litter,3}}{CN_{str,sur}}+\frac{D_4C_{litter,4}+D_5C_{litter,5}}{CN_{wod,sur}}\\
&\quad+\frac{D_6C_{litter,6}}{CN_{met,ssr}}+\frac{D_7C_{litter,7}+D_8C_{litter,8}}{CN_{str,ssr}}\,. &(510)
\end{aligned}
$$

During the litter decomposition process a fraction of nitrogen $\lambda_n\,I_{som,nit}$ is assumed to directly contribute to the dissolved organic nitrogen (DON) pool (Section 21.6), with λ_n $[-]$ representing the N-leaching coefficient.

In a similar manner of Eq. 510 inputs of phosphorus $I_{som,pho}$ $[g\,P\ g\,soil^{-1}\,day^{-1}]$ and potassium $I_{som,pot}$ $[g\,K\ g\,soil^{-1}\,day^{-1}]$ to the soil organic matter can be computed, with the respective fractions $\lambda_p\ I_{som,pho}$ and $\lambda_k\ I_{som,pot}$ contributed to the dissolved organic phosphorus (DOP) and to the mineral available potassium pool K_{min}. We assumed that C, N and P are leached completely in organic form, while K is leached in inorganic form. Potassium is not a constituent of biomolecules and due to its high solubility can be easily and quickly leached during the decomposition process (*Sardans and nuelas*, 2015). Therefore, organic matter in soils contains a relatively small amount of K. Phosphorus is assumed to be leached in a small proportion. This is reflected in a much higher leaching coefficient for K and smaller for P in comparison to C and N (Table 4). However, recent results from litter decomposition studies also suggest $\lambda_p > \lambda_n$, since P is predominantly contained in soluble organic forms (*Manzoni*, 2017). Thus, these values may be modified for future applications when nutrient leaching is of primary importance.

Leaching coefficient	**Description**	**Reference Value**
λ_c	C-leaching fraction	0.0015
λ_n	N-leaching fraction	0.0015
λ_p	P-leaching fraction	0.0001
λ_k	K-leaching fraction	0.90

Table 4: Description of the values used for the leaching coefficients, their order of magnitude was estimated in the model development phase to obtain realistic amounts of dissolved organic matter in leaching water.

21.4 Soil Organic Carbon (SOC) budget

Traditionally, models have represented soil organic carbon (SOC) subdivided in three pools- fast, slow, and passive (*Parton et al.*, 1988; *Foley*, 1995; *Sitch et al.*, 2003; *Krinner et al.*, 2005; *Sato et al.*, 2007). These pools were characterized by linear kinetics and different decay rates in an attempt to preserve variability in decomposition for different degrees of soil organic protection or recalcitrance of the substrate (*Talbot and Treseder*, 2012; *Freschet et al.*, 2012). Traditional models do not distinguish between substrate and microbial biomass and therefore implicitly assume that microbial biomass is not a limiting factor in SOC decomposition. Models with an explicit separation of substrate and biomass and higher order kinetics have been also introduced (*Manzoni and Porporato*, 2009), even though applications in ecosystem models are still limited (*Orwin et al.*, 2011; *Wieder et al.*, 2014, 2015; *Abramoff et al.*, 2018; *Robertson et al.*, 2019). Lumping together different fractions of soil organic carbon in these three pools creates a discrepancy between modeled quantities and the measurable SOC fractions in the soil and it does not allow to properly represent physical and chemical processes (*Six et al.*, 2001; *Schmidt et al.*, 2011; *Abramoff et al.*, 2018). For instance, *Six et al.* (2002) identified different SOC protection mechanisms defining at least four functional pools of SOC: biochemically protected (due to presence of recalcitrant C-compounds), physically protected (related to microaggregate and soil structure, e.g., microaggreagrate embedded in macroaggregrate), chemically protected (association of carbon with silt and clay particles), and unprotected SOC.

In T&C, we follow the separation of SOC fractions proposed by *Wang et al.* (2013) for the MEND model introducing a few changes. The C-substrate in the soil is separated into particulate organic carbon (POC), mineral-associated organic carbon (MOC, C_{moc}), and dissolved organic carbon (DOC) (Figure S3 and 43, 44). Physically, POC corresponds to the soil organic carbon associated with particle size $\geq$ 53 μm, while MOC refers to the fraction with particle size $<$ 53 μm (e.g., *Aoyama* *et al.*, 1999; *Wang et al.*, 2013). MOC typically corresponds to the physiochemically protected SOC and its turnover rate can be orders of magnitude slower than for POC (*Conant et al.*, 2011); DOC is instead immediately available to microbes provided the appropriate environmental conditions are met. The POC fraction is, in turn, subdivided according to its chemical composition into POC-lignin, $C_{poc,lig}$ and POC-cellulose/hemicellulose, $C_{poc,cel}$. This separation follows the rationale of the MEND model that accounts for the fact that POC-lignin is decomposed by oxidative enzymes (ligninases) produced only by fungi, while POC-cellulose/hemicellulose is decomposed with hydrolytic enzymes (cellulases) produced by both bacteria and fungi (*Wang et al.*, 2012, 2013), leading to different decomposition rates. Note that in this representation, the role of soil aggregates that provide physical protection to organic matter (*Abramoff et al.*, 2018), is not explicitly modeled and only the chemical composition of POC is considered.

Representing and modeling SOC pools that correspond to measurable fractions, does not automatically imply a mechanistic description of SOC dynamics. SOC depolymerization and ultimately decomposition is mediated by extracellular enzymes that are produced by different microorganisms (*Conant et al.*, 2011; *Sinsabaugh et al.*, 2014; *Manzoni et al.*, 2016). Extracellular enzymes and the different organisms composing the soil microbial community should be represented if a mechanistic description of SOC decomposition is sought. For this reason, an explicit representation of microbial mechanisms of soil C cycling and the role of extracellular enzymes has been recently introduced in a few models (*Allison et al.*, 2010; *Orwin et al.*, 2011; *Wieder et al.*, 2013, 2014, 2015) following the pioneering work of *Schimel and Weintraub* (2003). When compared to the assumptions of conventional first-order decomposition models (*Parton et al.*, 1988), SOC decomposition rates do not depend only on the size of the soil carbon pools but also on the size of the extracellular enzymes, which in turn depend on the size and activity of the microbial pools (*Schimel and Weintraub*, 2003). Modeling enzyme kinetics and microbial pools require assumptions on the kinetics and parameters used to simulate SOC decomposition, microbial life cycles, and enzyme production (*Wang and Post*, 2012; *Wang et al.*, 2012, 2013; *Manzoni et al.*, 2016; *Schimel et al.*, 2017). In general, it is more difficult to parameterize microbial and enzyme explicit models than first-order kinetics, because few estimates of the maximum specific reaction rates, half-saturation constants, and turnover rates have been presented outside of the literature on aquatic systems (*Moorhead and Sinsabaugh*, 2006; *Lawrence et al.*, 2009). The uncertainty around parameter values (not to mention structural uncertainties) hampered the development of a mechanistic representation of SOC dynamics. However, recently, studies as the one of *Wang et al.* (2013) have provided estimates and plausible ranges for many parameters needed in mechanistic SOC models, and metanalyses are becoming progressively available to constrain the relative magnitude of some model parameters (*Sinsabaugh et al.*, 2014, 2015; *Allison*, 2017; *Xu et al.*, 2017).

When compared to other models including extracellular enzymes and microbial pools, T&C further separates the microbial organisms into four categories (Fig. 43

and 44): (i) bacteria C_{bac}, (ii) saprotrophic fungi C_{fun}, (iii) arbuscular mycorrhizae C_{AM}, and (iv) ectomycorrhizae C_{EM}. Arbuscular mycorrhizae (AM), and ectomycorrhizae (EM) can co-occur in an ecosystem, but commonly one of the two types is dominant (*Finlay*, 2008; *Brundrett*, 2009; *Shi et al.*, 2016), which partially reduces the number of SOC pools.

In any given computational element (e.g., grid cell), the term EM $[-]$ indicates the areal fraction of plants associated with ectomycorrhizal, with $1 - EM$ corresponding to the areal fraction associated with arbuscular mycorrhizal. Mycorrhizal fungi, conversely to bacteria and saprotrophic fungi, are unable to feed on DOC and receive their carbon only from the host plant (*Koide et al.*, 2008; *Finlay*, 2008; *Johnson et al.*, 2013) (Section 17.3.2). However, ectomycorrhizal fungi can produce extracellular enzymes, which degrade SOC and produce DOC subsequently used by other microbes (*Read et al.*, 2004; *Talbot et al.*, 2013; *Lindahl and Tunlid*, 2015). Extracellular enzymes used for the degradation of POC and MOC produced by bacteria and fungi are separated, for a total of four extracellular enzyme pools $C_{ep,b}$, $C_{ep,f}$, $C_{em,b}$, $C_{em,f}$, which correspond to the enzymes for decomposition of POC (subscript ep) and MOC (subscript em) produced by bacteria and fungi (subscripts b and f), respectively. The DOC derived from the depolymerization of SOC due to extracellular enzyme produced by bacteria and fungi is also accounted for separately in the $C_{DOC,b}$ and $C_{DOC,f}$ pools. This separation reflects the fact that enzyme production, SOC depolymerization, and DOC acquisition are typically occurring in very localized areas or niches of microbial activity (*Allison*, 2005; *Tecon and Or*, 2017). Such an assumption is also necessary in the model, since the alternative of a unique DOC pool, where bacteria and fungi feed on the same DOC, did not provide realistic results. With a single DOC pool, a dominant microbial organism (fungi or bacteria) always emerged as a function of the specific model parametrization. This is not observed in nature, where multiple organisms and communities with different characteristics co-exist (*Fierer and Jackson*, 2006; *Fierer et al.*, 2009).

A carbon pool corresponding to soil macrofauna C_{ew} is also explicitly modeled in T&C because macrofauna activity can consume a non-negligible portion of soil carbon for its metabolism, with impacts on soil carbon cycling (*Lubbers et al.*, 2013; *Ruiz et al.*, 2015). Soil macrofauna can include different groups, e.g., acari, collembola, enchytraeids, nematoda, and earthworms (*Fierer et al.*, 2009), but the overall parameterization of macrofauna in T&C is tailored to earthworms, which often represent the largest mass fraction of soil macrofauna. Soil macrofauna is modeled to feed exclusively on POC, because of its higher carbon density when compared to DOC and easier accessibility when compared to MOC. Furthermore, soil macrofuana is assumed to interact only with belowground soil carbon and thus does not affect litter decomposition (Section 21.2). In other words, modeled macrofauna should be mostly regarded as having the characteristics of endogeic earthworms. The activity of anecic and epigeic species of earthworms that feed on surface litter can be quite significant (*Fahey et al.*, 2013) but it is not modeled and can be only implicitly included in the first order litter decay parameterizations.

21.4.1 SOC pools

The temporal dynamics of $C_{poc,lig}$, $C_{poc,cel}$, C_{moc}, $C_{DOC,b}$, and $C_{DOC,f}$, with all the pools in $[g\,C\ g\,soil^{-1}]$, obeys the following set of coupled first order ordinary differential equations (see also Figure 43):

$$\begin{aligned}
\frac{dC_{poc,lig}}{dt} &= I_{POC,lig} - F_{2l}\,, && (511)\\
\frac{dC_{poc,cel}}{dt} &= (1-\lambda_c)I_{POC,cel} - F_{2cb} - F_{2cf} + (1-g_d)(F_{8b} + F_{8f} + F_{8am} + F_{8em} + M_{ew}) \\
&\quad -F_{ew}\,, && (512)\\
\frac{dC_{moc}}{dt} &= (1-f_d)(F_{2l} + F_{2cb} + F_{2cf}) - F_{3b} - F_{3f}\,, && (513)\\
\frac{dC_{DOC,b}}{dt} &= r_{bf}\,\lambda_c I_{POC,cel} + f_d(F_{2cb}) + r_{bf}\,g_d(F_{8b} + F_{8f} + F_{8am} + F_{8em} + M_{ew}) \\
&\quad +F_{3b} + F_{10ep,b} + F_{10em,b} - F_{1b} - r_{bf}L_{k,DOC}\,, && (514)\\
\frac{dC_{DOC,f}}{dt} &= (1-r_{bf})\lambda_c I_{POC,cel} + f_d(F_{2cf} + F_{2l}) + (1-r_{bf})g_d(F_{8b} + F_{8f} + F_{8am} + F_{8em} + M_{ew}) + \\
&\quad F_{3f} + F_{10ep,f} + F_{10em,f} - F_{1f} - (1-r_{bf})L_{k,DOC}\,, && (515)
\end{aligned}$$

where λ_c $[-]$ is the C-leaching coefficient and $I_{POC,lig}$ $I_{POC,cel}$ are the inputs to the POC carbon pools from litter decomposition, separated for lignin and cellulose/hemicellulose compounds as defined in Section 21.2. The term $r_{bf} = C_{DOC,b}/(C_{DOC,b} + C_{DOC,f})$ is the ratio between the DOC available to the bacteria and the total DOC, $L_{k,DOC}$ $[g\,C\ g\,soil^{-1}\ day^{-1}]$ is the DOC leaching at the bottom of the soil column (Section 21.9). The term g_d $[-]$ is the fraction of dead microbes allocated to DOC, f_d $[-]$ is the fraction of decomposed POC allocated to DOC, and $1-f_d$ is allocated to MOC. The terms F_{ew} and M_{ew} $[g\,C\ g\,soil^{-1}\ day^{-1}]$ are the macrofauna carbon assimilation and mortality rates, respectively. The soil carbon fluxes F_x $[g\,C\ g\,soil^{-1}\ day^{-1}]$ are defined below. Briefly, F_{1x} corresponds to microbial carbon assimilation rates, F_{2x} corresponds to POC decomposition rates, F_{3x} corresponds to MOC decomposition rates, F_{8x} corresponds to microbial mortality rates, and F_{10x} to the turnover rates of extracellular enzymes, where x indicates a general subscript referring to a specific microbial or enzyme type.

The temporal dynamics of the four extracellular enzyme pools $C_{ep,b}$, $C_{ep,f}$, $C_{em,b}$, $C_{em,f}$ is:

$$\begin{aligned}
\frac{dC_{ep,b}}{dt} &= F_{9ep,b} + r_{bf}F_{9ep,em} - F_{10ep,b}\,, && (516)\\
\frac{dC_{ep,f}}{dt} &= F_{9ep,f} + (1-r_{bf})F_{9ep,em} - F_{10ep,f}\,, && (517)\\
\frac{dC_{em,b}}{dt} &= F_{9em,b} + r_{bf}F_{9em,em} - F_{10em,b}\,, && (518)\\
\frac{dC_{em,f}}{dt} &= F_{9em,f} + (1-r_{bf})F_{9em,em} - F_{10em,f}\,, && (519)
\end{aligned}$$

where the fluxes F_{9x} $[g\,C\ g\,soil^{-1}\ day^{-1}]$ are the productions of the extracellular enzymes used for the decomposition of POC and MOC, which are defined in the

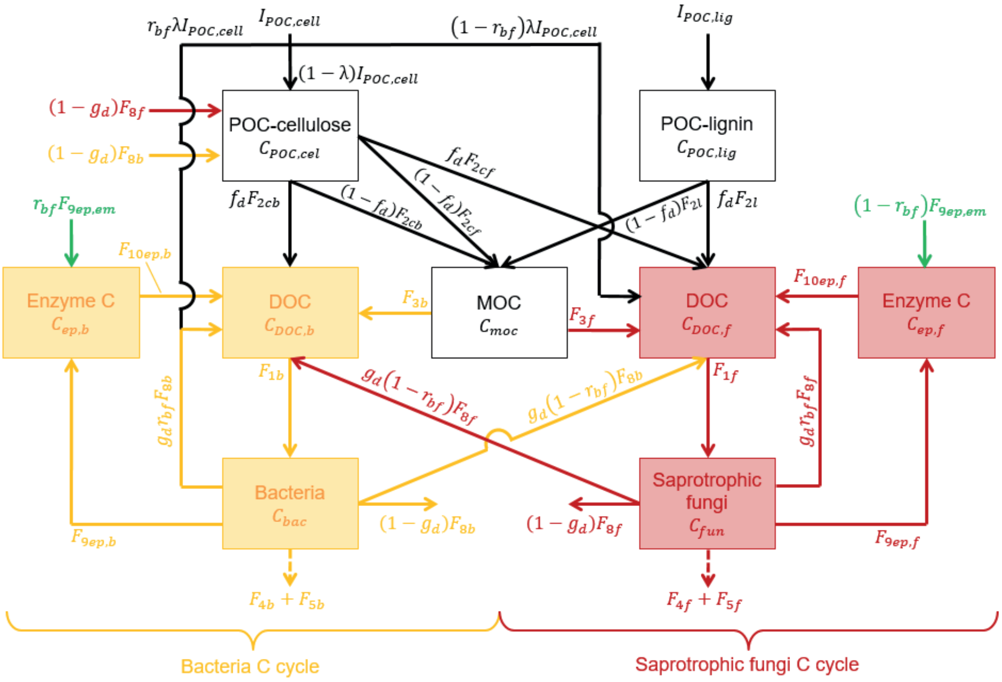

Figure 43: Scheme illustrating carbon fluxes among pools composing soil organic carbon (e.g., $C_{poc,lig}$, $C_{poc,cel}$, C_{moc}, $C_{DOC,b}$, $C_{DOC,f}$, $C_{ep,b}$, and $C_{ep,f}$) mediated by bacteria C_{bac} and saprotrophic fungi C_{fun} .

following section 21.4.2.

The dynamics of bacteria C_{bac}, saprotrophic fungi C_{fun}, arbuscular mycorrhizal C_{AM} and ectomycorrhizal C_{EM} fungi are computed as follows (Figure 44):

$$\frac{dC_{bac}}{dt} = F_{1b} - (F_{4b} + F_{5b}) - F_{8b} - (F_{9ep,b} + F_{9em,b})\,, \tag{520}$$

$$\frac{dC_{fun}}{dt} = F_{1f} - (F_{4f} + F_{5f}) - F_{8f} - (F_{9ep,f} + F_{9em,f})\,, \tag{521}$$

$$\frac{dC_{AM}}{dt} = (1 - EM)I_{myc} - F_{8am} - R_{m,AM}\,, \tag{522}$$

$$\frac{dC_{EM}}{dt} = (EM)I_{myc} - F_{8em} - R_{m,EM} - (F_{9ep,em} + F_{9em,em})\,, \tag{523}$$

where the carbon export to arbuscular mycorrhizal and ectomycorrhizal $I_{myc} = R_{ex,2}$ is computed in Section 17.3.2. The fluxes $R_{m,AM}$ and $R_{m,EM}$ $[g\,C\;g\,soil^{-1}\;day^{-1}]$ are the maintenance respiration costs of arbuscular mycorrhizal and ectomycorrhizal fungi respectively, F_{4x} are the growth respiration costs and F_{5x} are the maintenance respiration costs of the other microbial pools.

Changes in macrofaunal mass C_{ew} are computed as:

$$\frac{dC_{ew}}{dt} = F_{ew} - R_{ew} - M_{ew}\,, \tag{524}$$

where F_{ew} and M_{ew} are the macrofauna carbon assimilation and mortality rates and

R_{ew} $[g\,C\; g\,soil^{-1}\; day^{-1}]$ is the total respiration cost of the macrofauna (Figure 44).

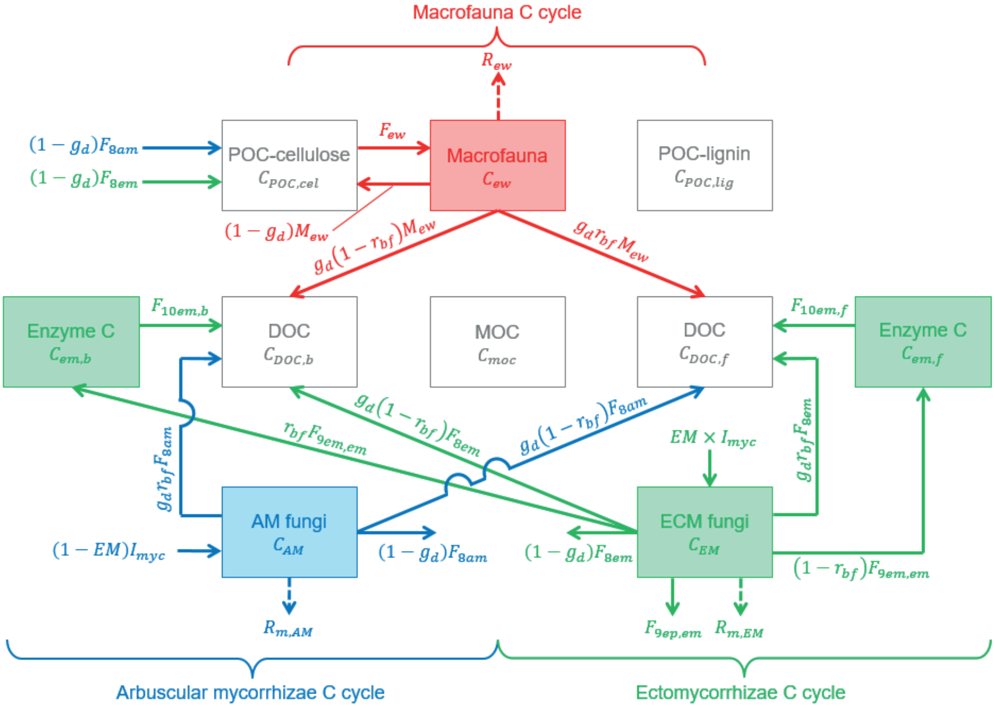

Figure 44: Scheme illustrating carbon fluxes among pools composing soil organic carbon (e.g., $C_{poc,lig}$, $C_{poc,cel}$, C_{moc}, $C_{DOC,b}$, $C_{DOC,f}$, $C_{em,b}$, $C_{em,f}$) mediated by macrofaunal mass C_{ew}, arbuscular mycorrhizal C_{AM}, and ectomycorrhizal C_{EM} fungi .

21.4.2 SOC fluxes

The carbon fluxes F_x among the SOC fraction are computed using the same kinetics of the MEND model (*Wang et al.*, 2013), which employs Michaelis-Menten kinetics considering that SOC decomposition is the product of extracellular enzymes produced by microorganisms and substrate mass (POC or MOC), while carbon assimilation is proportional to microbial biomass and DOC.

$$F_{1b} = \left(\frac{1}{E_{cb}}\right) \frac{(V_{db} + m_{rb})\,(f_{ad}\, C_{DOC,b}\, C_{bac})}{K_{db} + f_{ad}\, C_{DOC,b}}\,, \tag{525}$$

$$F_{1f} = \left(\frac{1}{E_{cf}}\right) \frac{(V_{df} + m_{rf})\,(f_{ad}\, C_{DOC,f}\, C_{fun})}{K_{df} + f_{ad}\, C_{DOC,f}}\,, \tag{526}$$

$$F_{2cb} = \frac{V_{pc}\,(C_{ep,b}\, C_{poc,cel})}{K_{pc} + C_{poc,cel}}\,, \tag{527}$$

$$F_{2cf} = \frac{V_{pc}\,(C_{ep,f}\, C_{poc,cel})}{K_{pc} + C_{poc,cel}}\,, \tag{528}$$

$$F_{2l} = \frac{V_{pl}\,(C_{ep,f}\, C_{poc,lig})}{K_{pl} + C_{poc,lig}}\,, \tag{529}$$

$$F_{3b} = \frac{V_{m}\,(C_{em,b}\, C_{moc})}{K_{m} + C_{moc}}\,, \tag{530}$$

$$F_{3f} = \frac{V_{m}\,(C_{em,f}\, C_{moc})}{K_{m} + C_{moc}}\,. \tag{531}$$

The fluxes F_{1b} and F_{1f} are the assimilation rates of DOC of the microorganisms: bacteria and saprotrophic fungi, respectively. The fluxes F_{2cb}, F_{2cf} are the decomposition rates of the cellulose/hemicellulose in POC mediated by enzymes produced by bacteria and saprotrophic fungi. The decomposition of lignin in POC, F_{2l}, is assumed to be exclusively due to enzymes associated with saprotrophic fungi, which have been observed to be able to decompose the most recalcitrant substrates (*Hanson et al.*, 2008). A fraction f_d $[-]$ of decomposed POC is then assumed to become DOC, while the remaining fraction $1 - f_d$ becomes MOC. The terms F_{3b} and F_{3f} are the decomposition rates of the MOC pool into DOC carried out by enzymes associated to bacteria and saprotrophic fungi. The terms E_{cb} and E_{cf} $[-]$ are the carbon use efficiencies of bacteria and saprotrophic fungi (Table 5), f_{ad} $[-]$ is the fraction of DOC that is accessible to microbes (Section 21.5) and the meaning and units of the other parameters V_{db}, V_{df}, V_{pc}, V_{pl}, V_m, m_{rb}, m_{rf}, K_{db}, K_{df}, K_{pc}, K_{pl}, and K_m are presented in Table 5.

Both microbial growth and maintenance respiration are modeled (*Schimel and Weintraub*, 2003; *Lawrence et al.*, 2009; *Wang et al.*, 2013). The scheme to quantify growth respiration rates, maintenance respiration rates, enzyme production rates, and microbial mortality rates assumes that maintenance respiration depends on both DOC and microbial biomass (*Wang and Post*, 2012) and that mortality coefficients are equal to the respiration maintenance coefficients. Respiration and mortality fluxes are defined as:

$$\begin{aligned}
F_{4b} &= \left(\frac{1}{E_{cb}} - 1\right) \frac{V_{db}\,(f_{ad}\,C_{DOC,b}\,C_{bac})}{K_{db} + f_{ad}\,C_{DOC,b}}\,, && (532)\\
F_{4f} &= \left(\frac{1}{E_{cf}} - 1\right) \frac{V_{df}\,(f_{ad}\,C_{DOC,f}\,C_{fun})}{K_{df} + f_{ad}\,C_{DOC,f}}\,, && (533)\\
F_{5b} &= \left(\frac{1}{E_{cb}} - 1\right) \frac{m_{rb}\,(f_{ad}\,C_{DOC,b}\,C_{bac})}{K_{db} + f_{ad}\,C_{DOC,b}}\,, && (534)\\
F_{5f} &= \left(\frac{1}{E_{cf}} - 1\right) \frac{m_{rf}\,(f_{ad}\,C_{DOC,f}\,C_{fun})}{K_{df} + f_{ad}\,C_{DOC,f}}\,, && (535)\\
Rm_{AM} &= m_{rm}\,C_{AM}\,, && (536)\\
Rm_{EM} &= m_{rm}\,C_{EM}\,, && (537)\\
F_{8b} &= [1 - K_{pb}(p_{epb} + p_{emb})]m_{rb}\,C_{bac}\,, && (538)\\
F_{8f} &= [1 - K_{pf}(p_{epf} + p_{emf})]m_{rf}\,C_{fun}\,, && (539)\\
F_{8am} &= m_{rm}\,C_{AM}\,, && (540)\\
F_{8em} &= [1 - K_{pf}(p_{epf} + p_{emf})]m_{rm}\,C_{EM}\,. && (541)
\end{aligned}$$

The terms F_{4m} and F_{4f} are the growth respiration fluxes, and F_{5m} and F_{5f} are the maintenance respiration fluxes for bacteria and saprotrophic fungi, respectively. The fluxes F_{8b}, F_{8f}, F_{8am}, and F_{8em} are the microbial mortality rates for bacteria, saprotrophic, arbuscular mycorrhizal and ectomycorrhizal fungi. The terms K_{pb} and K_{pf} $[-]$ are scaling factors for the enzyme production defined below. The meaning and units of the other parameters E_{cb}, E_{cf}, V_{db}, V_{df}, m_{rb}, m_{rf}, m_{rm}, p_{epb}, p_{emb}, p_{epf}, and p_{emf} are presented in Table 5.

The total microbial respiration of bacteria, saprotrophic fungi and mychorrizal fungi is:

$$R_{microbial} = F_{4b} + F_{4f} + F_{5b} + F_{5f} + Rm_{AM} + Rm_{EM}\,. \tag{542}$$

The production of the four extracellular enzymes is assumed to be proportional to the maintenance respiration and therefore to the microbial pools, while the extracellular enzyme turnover rates are proportional to the enzyme pools. The arbuscular mycorrhiza do not contribute to enzyme production. The fractions of maintenance respiration for the production of enzymes (p_{epf} and p_{emf}) are assumed to be the same for ectomycorrhizal and saprotrophic fungi. Differently from *Wang et al.* (2013), we use scaling factors $K_{pb} = 0.0078C_{bac}^{-0.5}$ and $K_{pf} = 0.0134C_{fun}^{-0.5}$ for the enzyme production rate to introduce a non-linear dependence between the microbial biomass and decomposition rates (productivity and respiration of microbes), which has been observed empirically (*Zak et al.*, 1994; *Sinsabaugh et al.*, 2014). Microbial productivity and respiration scale less than linearly with microbial biomass, which suggest the occurrence of larger specific decomposition rates (microbial metabolic quotients) with low biomass or equivalently a saturating effect of biomass activity for large biomass values. The exponent -0.5 is derived from *Sinsabaugh et al.* (2014) and the coefficients are fitted to obtain $K_{pf} = 1$ and $K_{pb} = 1$ at typical values of microbial biomass (*Xu et al.*, 2013). The use of these scaling factors is fundamental to reproduce changes in SOC as the litter input to the soil is modified, e.g., during bare fallow experiments. Following these assumptions, extracellular enzyme production rates are defined as:

$$F_{9ep,b} = (K_{pb}\, p_{epb})\, m_{rb}\, C_{bac}\,, \tag{543}$$

$$F_{9em,b} = (K_{pb}\, p_{emb})\, m_{rb}\, C_{bac}\,, \tag{544}$$

$$F_{9ep,f} = (K_{pf}\, p_{epf})\, m_{rf}\, C_{fun}\,, \tag{545}$$

$$F_{9em,f} = (K_{pf}\, p_{emf})\, m_{rf}\, C_{fun}\,, \tag{546}$$

$$F_{9ep,em} = (K_{pf}\, p_{epf})\, m_{rm}\, C_{EM}\,, \tag{547}$$

$$F_{9em,em} = (K_{pf}\, p_{emf})\, m_{rm}\, C_{EM}\,, \tag{548}$$

$$F_{10ep,b} = r_{ep}\, C_{ep,b}\,, \tag{549}$$

$$F_{10ep,f} = r_{ep}\, C_{ep,f}\,, \tag{550}$$

$$F_{10em,b} = r_{em}\, C_{em,b}\,, \tag{551}$$

$$F_{10em,f} = r_{em}\, C_{em,f}\,. \tag{552}$$

The fluxes $F_{9ep,b}$, $F_{9em,b}$, $F_{9ep,f}$ $F_{9em,f}$, $F_{9ep,em}$, $F_{9em,em}$ are the production rates of extracellular enzymes for the degradation of POC (first subscript *ep*) and MOC (first subscript *em*) produced by bacteria (second subscript *b*), saprotrophic fungi (second subscript *f*), and ectomycorrhizal fungi (second subscript *em*). The terms $F_{10ep,b}$, $F_{10ep,f}$, $F_{10em,b}$, and $F_{10em,f}$ are the turnover rates of the four extracellular enzyme pools. The meaning and units of the parameters p_{epb}, p_{emb}, p_{epf}, p_{emf}, p_{epf}, p_{emf}, r_{ep}, and r_{em} are presented in Table 5.

Parameter	**Description**	**Reference Value**
E'_{cb}	bacteria carbon use efficiency	0.27 $[-]$
E'_{cf}	saprotrophic fungi carbon use efficiency	0.27 $[-]$
V'_{pc}	maximum specific decomposition rate of POC - cell./hemicell.	200 $[g\,C\;g\,C^{-1}\;day^{-1}]$
V'_{pl}	maximum specific decomposition rate of POC - lignin	23 $[g\,C\;g\,C^{-1}\;day^{-1}]$
V'_{m}	maximum specific decomposition rate for MOC	100 $[g\,C\;g\,C^{-1}\;day^{-1}]$
V'_{db}	maximum specific uptake rate of DOC for growth of bacteria	0.04 $[g\,C\;g\,C^{-1}\;day^{-1}]$
V'_{df}	maximum specific uptake rate of DOC for growth of saprotrophic fungi	0.02 $[g\,C\;g\,C^{-1}\;day^{-1}]$
K'_{pc}	half-saturation constant for decomposition of POC - cell./hemicell.	0.05 $[g\,C\;g\,soil^{-1}]$
K'_{pl}	half-saturation constant for decomposition of POC - litter	0.05 $[g\,C\;g\,soil^{-1}]$
K'_{m}	half-saturation constant for decomposition of MOC	0.25 $[g\,C\;g\,soil^{-1}]$
K'_{db}	half-saturation constant of uptake of DOC for growth of bacteria	0.00026 $[g\,C\;g\,soil^{-1}]$
K'_{df}	half-saturation constant of uptake of DOC for growth of saprotrophic fungi	0.00026 $[g\,C\;g\,soil^{-1}]$
m'_{rb}	specific maintenance factor or rate of bacteria	0.005 $[g\,C\;g\,C^{-1}\;day^{-1}]$
m'_{rf}	specific maintenance factor or rate of saprotrophic fungi	0.002 $[g\,C\;g\,C^{-1}\;day^{-1}]$
m'_{rm}	specific maintenance factor or rate of mycorrhizal	0.0012 $[g\,C\;g\,C^{-1}\;day^{-1}]$
r'_{em}	turnover rate of EM	0.018 $[g\,C\;g\,C^{-1}\;day^{-1}]$
r'_{ep}	turnover rate of EP	0.018 $[g\,C\;g\,C^{-1}\;day^{-1}]$
p'_{epb}	fraction of maintenance respiration for production of enzymes for POC from bacteria	0.012 $[-]$
p'_{emb}	fraction of maintenance respiration for production of enzymes for MOC from bacteria	0.005 $[-]$
p'_{epf}	fraction of maintenance respiration for production of enzymes for POC from fungi	0.006 $[-]$
p'_{emf}	fraction of maintenance respiration for production of enzymes for MOC from fungi	0.010 $[-]$
g'_{d}	fraction of dead microbe allocated to DOC	0.2 $[-]$
f'_{d}	fraction of decomposed POC allocated to DOC	0.4 $[-]$

Table 5: Description of the parameters used in the biogeochemistry module; the prime superscript indicates the reference parameter before any environmental rate modifier is applied (Section 21.4.3). Carbon use efficiency values are derived from *Sinsabaugh et al.* (2016), other values are in the realistic ranges published by *Wang et al.* (2013); *Allison* (2017). Relative differences between bacteria and fungi for V'_d and m'_r are inferred from the meta-analysis of *Sinsabaugh et al.* (2014).

21.4.3 Environmental effects on biogeochemical kinetics

The parameters used to describe SOM biogeochemical reactions (Table 5) are also a function of environmental conditions via rate modifier functions for temperature (f_{Tmic}), soil water potential ($f_{SM.Microbe}$), pH (f_{PH}), clay content (f_{clay} and $f_{clay,2}$), mineral associated organic carbon C_{moc}, and the silt plus clay content (described in Section 21.5). The temperature function f_{Tmic} has a similar shape for the different parameters but different values of activation energy E_a $[kJ\ mol^{-1}]$ (*Wang et al.*, 2013).

$$
\begin{aligned}
V_{pc} &= V'_{pc} f_{Tmic}(E_a = 37) f_{SM.Microbe} f_{PH} , && (553)\\
V_{pl} &= V'_{pl} f_{Tmic}(E_a = 53) f_{SM.Microbe} f_{PH} , && (554)\\
V_{m} &= V'_{m} f_{Tmic}(E_a = 47) f_{SM.Microbe} f_{PH} , && (555)\\
V_{db} &= V'_{db} f_{Tmic}(E_a = 47) f_{SM.Microbe} f_{PH} , && (556)\\
V_{df} &= V'_{df} f_{Tmic}(E_a = 47) f_{SM.Microbe} f_{PH} , && (557)\\
K_{pc} &= K'_{pc} f_{Tmic}(E_a = 30) f_{clay} , && (558)\\
K_{pl} &= K'_{pl} f_{Tmic}(E_a = 30) f_{clay} , && (559)\\
K_{m} &= K'_{m} f_{Tmic}(E_a = 30) f_{clay} , && (560)\\
K_{db} &= K'_{db} f_{Tmic}(E_a = 30) , && (561)\\
K_{df} &= K'_{df} f_{Tmic}(E_a = 30) , && (562)\\
m_{rb} &= m'_{rb} f_{Tmic}(E_a = 20) , && (563)\\
m_{rf} &= m'_{rf} f_{Tmic}(E_a = 20) , && (564)\\
m_{rm} &= m'_{rm} f_{Tmic}(E_a = 20) , && (565)\\
f_{d} &= F(f'_{d}) , && (566)\\
g_{d} &= g'_{d} f_{clay,2} . && (567)
\end{aligned}
$$

Carbon use efficiency of microbial biomass, E_{cm} for bacteria and E_{cf} for saprotrophic fungi, can be assumed constant (E'_{cm} and E'_{cf} as in Table 5) or computed as a function of temperature:

$$
\begin{aligned}
E_{cm} &= \min\left[CUE_{max}, E'_{cm} + m_T(T_{bg} - T_{ref})\right] && (568)\\
E_{cf} &= \min\left[CUE_{max}, E'_{cf} + m_T(T_{bg} - T_{ref})\right] , && (569)
\end{aligned}
$$

where T_{bg} $^{\circ}C$ is the soil temperature in the biogeochemically active zone, $CUE_{max} = 0.6$ is the maximum carbon use efficiency, which represents a physiological limit to carbon assimilation (*Manzoni et al.*, 2008; *Sinsabaugh et al.*, 2013), $T_{ref} = 20^{\circ}C$ is a reference temperature, and m_T is the temperature sensitivity of carbon use efficiency (*Allison et al.*, 2010; *Li et al.*, 2014), set to be $m_T = -0.008\ ^{\circ}C^{-1}$.

21.4.4 Soil macrofauna

Soil macrofauna C_{ew} feeds exclusively on the carbon pool $C_{POC,cel}$, because of its higher carbon density and easier accessibility. The macrofauna assimilation rate

F_{ew} $[g\,C \;\; g\,soil^{-1} \;\; day^{-1}]$ is modeled with a linear kinetic, which was found more stable than a Michaelis-Menten kinetic, modulated by various environmental controls such as soil temperature, f_{T3}, effective saturation f_{aew}, clay content $f_{clay,3}$, pH f_{PH}, and substrate palatability f_{pal} (*Curry*, 1998; *Whalen et al.*, 1999; *Ruiz et al.*, 2015). The parameterizations of environmental controls are described in Section 21.5 and shown in Fig. 47. In particular, the factor f_{aew} defines a relative degree of activity of macrofauna from 1 corresponding to completely active to 0 corresponding to completely passive macrofauna waiting for favourable conditions. The term $V_{max,ew}$ is the maximum carbon ingestion rate of macrofauna for unit of POC (Table 6) (*Curry and Schmidt*, 2007). However, only a fraction $f_{abs,e}$ of the total ingested carbon is assimilated and processed. The total respiration cost R_{ew} $[g\,C \;\; g\,soil^{-1} \;\; day^{-1}]$ is the sum of maintenance respiration $R_{ew,m}$ and growth respiration $R_{ew,g}$. Maintenance respiration is computed according to the degree of activity of the macrofauna (*Ruiz et al.*, 2015) using a linear kinetic with a temperature dependence f_{T4} (*Whalen et al.*, 1999). Two coefficients are introduced, one for passive $r_{m,Pew}$ and one for active $r_{m,Aew}$ maintenance respiration costs, with active maintenance cost roughly doubling the passive cost (Table 6). Growth respiration is proportional to assimilated carbon and is computed using a carbon use efficiency, corresponding to the maximum $CUE_{max} = 0.6$. Finally, the macrofauna mortality rate M_{ew} $[g\,C \;\; g\,soil^{-1} \;\; day^{-1}]$ is modeled as a linear kinetic (*Whalen et al.*, 1999):

$$
\begin{aligned}
F_{ew} &= f_{abs,e} V_{max,ew} \, C_{POC,cel} \, f_{pal} \, f_{T3} \, f_{clay,3} \, f_{PH} \, f_{aew} && (570)\\
R_{ew,m} &= f_{aew}(r_{m,Aew}) C_{ew} f_{T4} + (1 - f_{aew})(r_{m,Pew}) C_{ew} f_{T4} \;, && (571)\\
R_{ew,g} &= (1 - CUE_{max}) F_{ew} \;, && (572)\\
R_{ew} &= R_{ew,m} + R_{ew,g} \;, && (573)\\
M_{ew} &= d_{ew} C_{ew} f_{T4} \;. && (574)
\end{aligned}
$$

Parameter	**Description**	**Reference Value**
$V_{max,ew}$	Maximum C-ingestion rate	0.005 $[g\,C \; g\,C^{-1} \; day^{-1}]$
$f_{abs,e}$	Fraction of absorbed food	0.15 $[-]$
$r_{m,Pew}$	Passive specific maintenance factor	0.0146 $[g\,C \; g\,C^{-1} \; day^{-1}]$
$r_{m,Aew}$	Active specific maintenance factor	0.03 $[g\,C \; g\,C^{-1} \; day^{-1}]$
d_{ew}	Turnover rate	0.01 $[g\,C \; g\,C^{-1} \; day^{-1}]$

Table 6: Description of the parameters used to describe macrofaunal activity.

21.5 Environmental rate modifiers

In this section we list all the functions used to introduce environmental dependencies in the biogeochemical kinetics (see Section 21.4.3 for a general description). The amount of water in the soil, expressed as soil water potential, exerts a control on decomposition and microbial activity. Two functions are used to account for soil water potential, one regulates the microbial activity and the other one the belowground litter decomposition (*Moyano et al.*, 2013; *Manzoni et al.*, 2012) as follows:

$$f_{SM.Litter} = 1 - \left(\frac{\log(\Psi_s) - \log(\Psi_{opt,1})}{\log(\Psi_{th,1}) - \log(\Psi_{opt})} \right)^{\alpha_1} , \quad (575)$$

$$f_{SM.Microbe} = 1 - \left(\frac{\log(\Psi_s) - \log(\Psi_{opt,2})}{\log(\Psi_{th,2}) - \log(\Psi_{opt})} \right)^{\alpha_2} , \quad (576)$$

where Ψ_s $[kPa]$ is the averaged soil water potential over the biogeochemically active zone, and $\Psi_{opt,1} = -3$ kPa, $\Psi_{th,1} = -15800$ kPa, $\alpha_1 = 1.47$, $\Psi_{opt,2} = -10$ kPa $\Psi_{th,1} = -28800$ kPa, $\alpha_2 = 1.0$ are parameters derived from observations (*Moyano et al.*, 2013; *Manzoni et al.*, 2012), see also Fig. 45. Oxygen limitation in soils close to saturation is neglected.

Macrofauna is inhibited mechanically and not only physiologically by very low and very high water contents, therefore it is simulated to respond to effective saturation S_e rather than to water potential (*Curry*, 1998; *Ruiz et al.*, 2015). The activity of macrofauna with water content is parameterized as f_{aew}:

$$f_{aew} = 0.000008575 \exp \left[11.67 \frac{S_e}{S_{e,fc}} \right] , \qquad \text{if } S_e > 0.2 \quad (577)$$

$$f_{aew} = 0.002729\, S_e^{-56.03} , \qquad \text{if } S_e > 0.9 , \quad (578)$$

where $S_{e,fc}$ is the effective saturation at field capacity and f_{aew} cannot be larger than 1 or smaller than 0. Such a function ensures that macrofauna activity is maximal for water contents around field capacity and decreases to 0 for very dry and very wet conditions (Fig. 47).

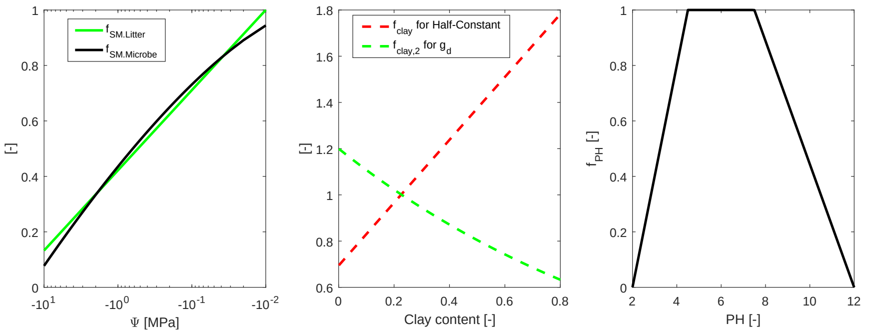

Figure 45: Dependencies of microbial activity $f_{SM.Microbe}$ and litter decomposition $f_{SM.Litter}$ on soil water potential (a); changes in the half-saturation constant for soil organic matter decay, f_{clay} (red-line), and changes in the fraction of dead microbe allocated to DOC, $f_{clay,2}$ (green-line), in dependence of the clay content in the soil (b). Soil pH controls on microbial and macrofaunal activity, f_{PH} (c).

The pH of soil also affects certain parameters and macrofauna activity (Section 21.4) (*Wang et al.*, 2012). Here, we parameterize pH controls, f_{PH}, as in *Orwin et al.* (2011), where $f_{PH} = 1$ for pH values between 4.5 and 7.5 and decrease linearly to $f_{PH} = 0$ for pH values of 2 and 12 respectively, at which biogeochemical acitivy is considered impaired (Figure 45c). Since T&C-BG is not simulating pH evolution through time, the pH value is prescribed at the beginning of the simulation for each location and remains constant thereafter.

The fraction $1 - f_d$ $[-]$ of decomposed POC that becomes MOC is also assumed to be affected by external conditions. Specifically, the mineral associated organic carbon fraction has been observed to reach a maximum with increasing carbon inputs once the physical surfaces in the soil are progressively saturated with MOC (*Six et al.*, 2002; *Stewart et al.*, 2007a,b). Adsorption to silt- and clay-sized particles, indeed, protects organic carbon from decomposition and is mostly controlled by the availability of reactive surface area (*Stewart et al.*, 2007b). For these reasons, the reference value of f_d, i.e., f'_d (Table 5) is corrected accounting for the soil clay and silt fractions, F_{cla} and F_{sil} $[-]$ and the amount of MOC already present in the soil, C_{moc} in $[g\,C\;kg\,soil^{-1}]$ (Eq. 579). This implies that C accumulation does not only depend on the protective capacity (i.e., texture) of the soil alone, but also on the degree to which this protective capacity is already occupied by organic matter (*Hassink and Whitmore*, 1997; *Stewart et al.*, 2007b) (Fig. 46):

$$f_d = f'_d + (1 - f'_d)\left(\frac{C_{moc}}{4.825(F_{sil} + F_{cla})^{0.6287}}\right)^{3.322} . \tag{579}$$

Equation (579) accounts for the fact that f_d increases (i.e., less decomposed POC becomes MOC) with increasing C_{moc} because reactive surfaces are progressively saturated. When $f_d = 1$, there is no space to store additional MOC, and the soil becomes carbon saturated with regards to the MOC fraction (*Stewart et al.*, 2007a,b). However, less protected fractions as POC or DOC can continue to increase if input of organic carbon allows. This effect is mediated by the presence of fine particles (e.g., silt and clay), so that a larger fine fraction increases the capacity to store MOC. In other words, for a given C_{moc}, f_d is higher for lower values of silt plus clay (Fig. 46). The parametrization of Eq. (579) is derived assuming a minimum value of f_d equal to the reference value f'_d and using the upper envelope of MOC values reported by *Six et al.* (2002) as a function of clay plus silt content.

Other environmental dependencies are related to the clay content (*Six et al.*, 2002; *Wieder et al.*, 2015), which is assumed to affect the half-saturation constants for soil organic matter decay, through the coefficient f_{clay}, and the fraction of dead microbe allocated to DOC g_d through the coefficient $f_{clay,2}$ (Fig. 45):

$$f_{clay} = 0.694 + 1.36F_{cla} , \tag{580}$$

$$f_{clay,2} = 1.2\exp\left[-0.8F_{cla}\right] , \tag{581}$$

where F_{cla} $[-]$ is the fraction of clay in the soil, and the expressions are adapted from *Wieder et al.* (2015) and they contribute to inhibit soil organic matter decomposition in the presence of high-clay content values. Macrofauna activity is also inhibited by elevated clay contents through $f_{clay,3}$ (Fig. 47):

$$f_{clay,3} = 2.938\exp\left[-4.82F_{cla}\right] - 2.509\exp\left[-11.82F_{cla}\right] , \tag{582}$$

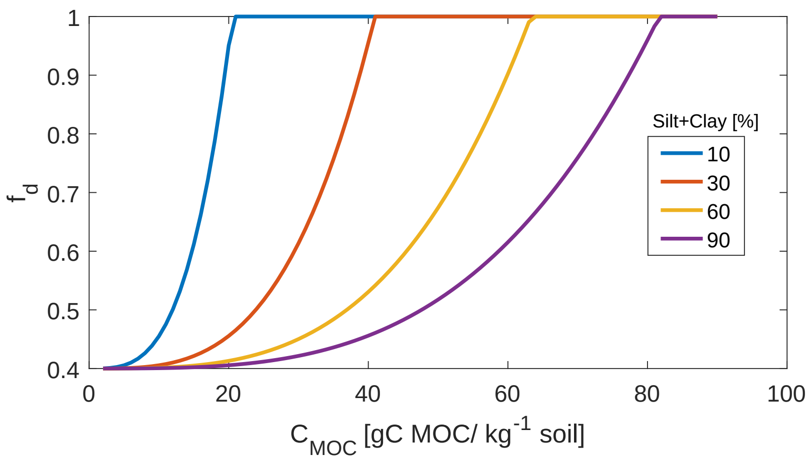

Figure 46: The fraction of decomposed POC allocated to DOC f_d $[-]$, where $1 - f_d$ is the decomposed POC that becomes MOC, as function of the mineral associated organic carbon C_{moc} $[g\,C\;kg\,soil^{-1}]$ already in the soil, for different percentages of clay plus silt in the soil. A reference value of f_d, equal to $f'_d = 0.4$ is used for low values of C_{moc}.

and $f_{clay,3} = 1$ for $F_{cla} < 0.15$.

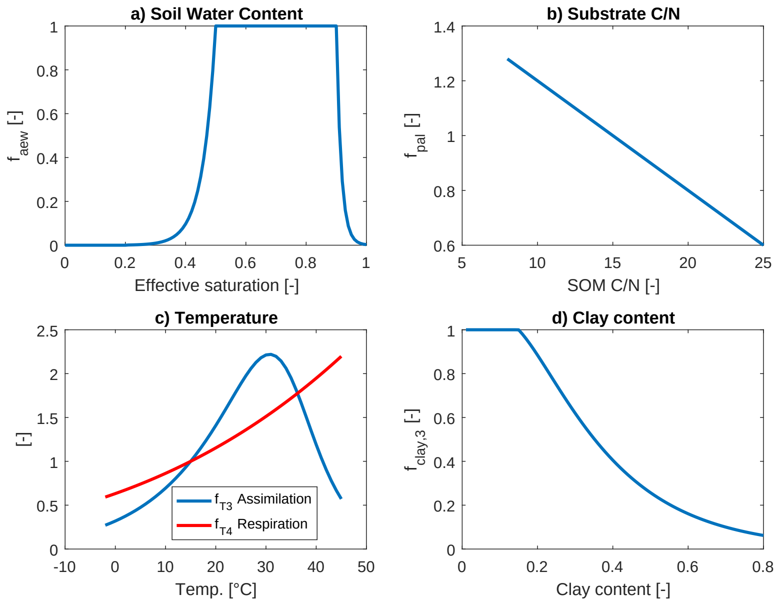

Figure 47: Environmental dependencies of the macrofauna activity. Change in the activity with (a) effective saturation (f_{aew}), (b) substrate palatability expressed as C:N ratio of SOM (f_{pal}), (c) soil temperature (f_{T3} in blue and f_{T4} in red), and (d) clay content ($f_{clay,3}$).

Soil temperature is controlling (i) the parameters of the soil biogeochemistry reactions through $f_{Tmic}(E_a)$ (*Wang et al.*, 2012), (ii) the litter decomposition rates through f_{T1} and f_{T2} (*Kirschbaum and Paul*, 2002), and (iii) macrofaunal activity through f_{T3} and f_{T4} (*Whalen et al.*, 1999). These temperature functions reflect the fact that chemical and enzymatic reactions are faster at higher temperatures.

$$f_{Tmic} = \exp\left[\frac{-E_a}{R}\left(\frac{1}{T_{bg}+273.15}-\frac{1}{T_{ref}+273.15}\right)\right], \quad (583)$$

$$f_{T1} = \exp\left[3.36\frac{T_a-40}{T_a+31.79}\right], \quad (584)$$

$$f_{T2} = \exp\left[3.36\frac{T_{bg}-40}{T_{bg}+31.79}\right], \quad (585)$$

$$f_{T3} = \exp\left[\frac{50}{R}\frac{(T_{bg}-T_{ref,2})}{(T_{bg}+273.15)(T_{ref,2}+273.15)}\right)\frac{1+\exp(\frac{(T_{ref,2}+273.15)0.649-200}{R(T_{ref,2}+273.15)})}{1+\exp(\frac{(T_{bg}+273.15)0.649-200}{R(T_{bg}+273.15)})}, \quad (586)$$

$$f_{T4} = \exp\left[\frac{-20}{R}\left(\frac{1}{T_{bg}+273.15}-\frac{1}{T_{ref,2}+273.15}\right)\right], \quad (587)$$

where T_a [$°C$] is the air temperature and T_{bg} [$°C$] is the soil temperature averaged over the biogeochemically active zone, E_a [$kJ\,mol^{-1}$] is the activation energy, $R = 8.314$ [$J\,mol^{-1}\,K^{-1}$] is the universal gas constant, and $T_{ref} = 12$, $T_{ref,2} = 15$ [$°C$] are reference temperatures.

The fraction of DOC that is accessible to microbes, f_{ad}, is currently assumed to be always equal to 1, implying that DOC is available to microbes even in dry conditions. Potentially, a dependence on effective saturation S_e can be introduced to account for the fact that in dry conditions microbes can have limitations in accessing the whole pool of dissolved carbon, as they have a constrained mobility (*Ebrahimi and Or*, 2014) and solute diffusivity is slower (*Manzoni et al.*, 2016). However, since this relation is very uncertain, $f_{ad} = 1$ is currently assumed for simplicity.

Finally, the food palatability for macrofauna is parameterized as a function of the carbon to nitrogen ratio of soil organic matter following *Whalen et al.* (1999):

$$f_{pal} = 1.6 - 0.04\,CN_{som}\,. \quad (588)$$

Changes in f_{pal} are illustrated in Figure 47. Note that this is an important simplification since animals may also feed on low palatability food at high rates but with large C losses via excretion and respiration and therefore a lower carbon use efficiency.

21.6 Nitrogen budget

Soil organic nitrogen dynamics are assumed to follow the carbon fluxes described in Section 21.4 according to the specific carbon to nitrogen ratio C:N of a given pool (*Kirschbaum and Paul*, 2002). The C:N of microbial biomass has been observed to be a quite constrained value (*McGroddy et al.*, 2004; *Cleveland and Liptzin*, 2007; *Manzoni et al.*, 2010; *Mouginot et al.*, 2014; *Mooshammer et al.*, 2014); for this reason, target values (Table 7) are prescribed in T&C and nitrogen mineralization or immobilization is modeled to occur whenever the C:N of microbial biomass departs from these target values as described below. The model does not track the nitrogen content of extracellular enzyme pools, which is a very small amount, when compared to the total organic nitrogen.

The temporal dynamics of the soil organic matter nitrogen pool N_{som} $[g\,N\ g\,soil^{-1}]$, dissolved organic nitrogen DON $[g\,N\ g\,soil^{-1}]$, nitrogen of the macrofuana N_{ew}, and the nitrogen composing the microbial biomass pools N_{bac}, N_{fun}, N_{AM}, and N_{EM} $[g\,N\ g\,soil^{-1}]$, e.g., bacteria, saprotrophic fungi, arbuscular mycorrhizae and ectomycorrhizae, respectively, are computed as:

$$\begin{aligned}
\frac{dN_{som}}{dt} &= (1-\lambda_n)I_{som,nit} - \frac{f_d(F_{2l}+F_{2cb}+F_{2cf})+(F_{3b}+F_{3f})}{CN_{som}} + \frac{F_{8b}}{CN_{bac}} + \frac{F_{8f}}{CN_{fun}} \\
&\quad + \frac{F_{8am}}{CN_{AM}} + \frac{F_{8em}}{CN_{EM}} - F_{ew,N} + S_{DON}\,, && (589)\\
\frac{dDON}{dt} &= f_{org,lea}\lambda_n I_{som,nit} + \lambda_n \frac{f_d(F_{2l}+F_{2cb}+F_{2cf})+(F_{3b}+F_{3f})}{CN_{som}} \\
&\quad - L_{k,DON} - S_{DON}\,, && (590)\\
\frac{dN_{bac}}{dt} &= (1-\lambda_n)\frac{f_d F_{2cb}+F_{3b}}{CN_{som}} - \frac{F_{8b}}{CN_{bac}} + N_{b,imm/min}\,, && (591)\\
\frac{dN_{fun}}{dt} &= (1-\lambda_n)\frac{f_d(F_{2cf}+F_{2l})+F_{3f}}{CN_{som}} - \frac{F_{8f}}{CN_{fun}} + N_{f,imm/min}\,, && (592)\\
\frac{dN_{AM}}{dt} &= -\frac{F_{8am}}{CN_{AM}} + N_{AM,imm/min}\,, && (593)\\
\frac{dN_{EM}}{dt} &= -\frac{F_{8em}}{CN_{EM}} + N_{EM,imm/min}\,, && (594)\\
\frac{dN_{ew}}{dt} &= \frac{F_{ew}-R_{ew}-M_{ew}}{CN_{ew}}\,, && (595)
\end{aligned}$$

where the $I_{som,nit}$ is the input to the soil organic nitrogen pool from litter decomposition defined in Section 21.3. The term CN_{som} is the mass carbon to nitrogen ratio of soil organic matter, computed from the sum of $C_{poc,lig} + C_{poc,cel} + C_{moc}$ divided by N_{som} and CN_{bac}, CN_{fun}, CN_{AM}, and CN_{EM} are the carbon to nitrogen ratios of bacteria, saprotrophic fungi, arbuscular mycorrhizae, and ectomycorrhizae, respectively. The carbon fluxes are defined above, where F_{2x} corresponds to POC decomposition rates, F_{3x} corresponds to MOC decomposition rates, F_{8x} corresponds to microbial mortality rates, and f_d $[-]$ is the fraction of decomposed POC allocated to DOC. The carbon fluxes associated with macrofauna are the macrofauna carbon assimilation and mortality rates, F_{ew} and M_{ew}, and the macrofauna total respiration cost R_{ew}, where CN_{ew} is the mass carbon to nitrogen ratio of macrofauna (Table 7). The nitrogen flux to macrofauna is simply computed to preserve a prescribed carbon to nitrogen content in macrofauna CN_{ew} (Table 7). The coefficient λ_n is the N-leaching fraction (Table 4) and $f_{org,lea}$ is the fraction of leaching that is transferred in organic form. The term $L_{k,DON}$ is the DON leaching from the soil biogeochemically active zone, which is described in Section 21.9. The flux $S_{DON} = 0.01DON$ is a dissolved organic nitrogen stabilization term and prevents DON to increase infinitely in case leaching from the soil biogeochemistry active zone is not able to remove

DON. Finally, the terms $N_{b,imm/min}$, $N_{f,imm/min}$, $N_{AM,imm/min}$, $N_{EM,imm/min}$ are the net immobilization/mineralization fluxes for bacteria, saprotrophic fungi, and arbuscular mycorrhizal and ectomycorrhizal fungi described below. Note that in the formulation above the nitrogen associated with the carbon decomposed from MOC and POC and transformed in DOC is assimilated by bacteria and saprotrophic fungi, except for a fraction λ_n, which is leached as DON.

Microbial	**C:N (mass basis)**	**C:P (mass basis)**
Bacteria	5.2	16
Saprotrophic fungi	6.5	40
Arbuscular mycorrhizal	18	120
Ectomycorrhizal	18	120
Macrofauna	10	NA

Table 7: Target stoichiometric relations (C:N and C:P on a mass basis) for microbial biomass and macrofauna. Reference values are adapted from *McGroddy et al.* (2004); *Cleveland and Liptzin* (2007); *Manzoni et al.* (2010); *Orwin et al.* (2011); *Mouginot et al.* (2014); *Mooshammer et al.* (2014) for microbes and *Whalen et al.* (1999) for macrofauna.

The temporal dynamics of the inorganic nitrogen pools corresponding to ammonium NH_4^+ and nitrate NO_3^- $[g\,N\;g\,soil^{-1}]$ are:

$$\begin{aligned}\frac{dNH4}{dt} &= (1 - f_{org,lea})\lambda_n I_{som,nit} - NH4_{imm/min} - NO3_{flx} - NH4_{up} \\ &\quad - L_{k,NH4} - N_{VOL} + Ex_N\,, \qquad (596)\\ \frac{dNO3}{dt} &= -NO3_{imm/min} + NO3_{flx} - NO3_{up} - L_{k,NO3} - N_2\,, \qquad (597)\end{aligned}$$

where $I_{som,nit}$, λ_n and $f_{org,lea}$ are defined above. The nutrient leaching fluxes for NH_4^+ and NO_3^-, $L_{k,NH4}$, $L_{k,NO3}$ $[gN\;g\,soil^{-1}\;day^{-1}]$ are described in Section 21.9. The actual plant nutrient uptake rates per unit of ground $NH4_{up}$, $NO3_{up}$ are defined in Section 19.2. The net immobilization/mineralization fluxes $NH4_{imm/min}$ and $NO3_{imm/min}$ $[gN\;g\,soil^{-1}\;day^{-1}]$ for NH_4^+ and NO_3^- are defined below. The $NO3_{flx}$ $[gN\;g\,soil^{-1}\;day^{-1}]$ is the nitrification flux converting the ammonium to nitrate, while N_2 $[gN\;g\,soil^{-1}\;day^{-1}]$ is the denitrification flux and N_{VOL} $[gN\;g\,soil^{-1}\;day^{-1}]$ is the ammonia volatilization flux. Finally, Ex_N is the input of nitrogen from other sources due to deposition, biological fixation, and fertilization, which is assumed to completely occur in the form of ammonium for simplicity.

The net fluxes of immobilization minus mineralization in the bacteria, saprotrophic fungi, arbuscular mycorrhizae, and ectomycorrhizae, are computed as in *Kirschbaum* *and Paul* (2002):

$$N_{b,imm/min} = \left[\frac{C_{bac}}{R_{CN,bac}} - N_{bac}\right]/\tau\,, \tag{598}$$

$$N_{f,imm/min} = \left[\frac{C_{fun}}{R_{CN,fun}} - N_{fun}\right]/\tau\,, \tag{599}$$

$$N_{AM,imm/min} = \left[\frac{C_{AM}}{R_{CN,AM}} - N_{AM}\right]/\tau\ , \tag{600}$$

$$N_{EM,imm/min} = \left[\frac{C_{EM}}{R_{CN,EM}} - N_{EM}\right]/\tau\ , \tag{601}$$

where the terms are the immobilization (if $C_x : N_x \geq R_{CN,x}$) or mineralization (if $C_x : N_x < R_{CN,x}$) occurring to reach the target carbon to nitrogen ratio of bacteria, saprotrophic fungi, or mychorriza: $R_{CN,mic}$, $R_{CN,fun}$, $R_{CN,AM}$, $R_{CN,EM}$ $[g\,C\ g\,N^{-1}]$, which are defined in Table 7. Note that the above parameterization implies that mineralization and immobilization fluxes are occurring rapidly within a time span τ, which is assumed to be equal to one daily time step and therefore that the prescribed carbon to nitrogen contents in the microbial biomasses are almost exactly preserved whenever enough nutrients are available, otherwise C:N ratios of microbial biomass increase. The total net immobilization/mineralization fluxes is then partitioned among the ammonium NH_4^+ and nitrate NO_3^- pool:

$$NH4_{imm/min} = 0.9(N_{m,imm/min} + N_{f,imm/min} + N_{AM,imm/min} + N_{EM,imm/min}) + 0.001NH4\ , \tag{602}$$

$$NO3_{imm/min} = 0.1(N_{m,imm/min} + N_{f,imm/min} + N_{AM,imm/min} + N_{EM,imm/min}) + 0.001NO3\ , \tag{603}$$

where the last terms in the above equations represent continue immobilization due to chemical stabilization (*Kirschbaum and Paul*, 2002) and the relative partition of N immobilization/mineralization between ammonium NH_4^+ and nitrate NO_3^- pool follows the reference value in *Porporato et al.* (2003). To conserve properly the N mass budget the terms $0.001\,NH4$ and $0.001\,NO3$ are subtracted from the bacteria and fungi mineralization, respectively.

The nitrification $NO3_{flx}$, denitrification N_2 and ammonia volatilization N_{VOL} fluxes are computed with simplified first order kinetics as proposed by *Dickinson et al.* (2002):

$$NO3_{flx} = K_{N,max,n}\, f_{T5}\, f_{moist,1}\, NH4\ , \tag{604}$$

$$N_2 = K_{N,max,d}\, f_{T6}\, f_{moist,2}\, NO3\,, \tag{605}$$

$$N_{VOL} = k_V NO3\ , \tag{606}$$

where $K_{N,max,n} = 0.086$, $K_{N,max,d} = 0.217$ and $k_V = 8.5\,10^{-5}$ $[day^{-1}]$ are reaction rate parameters provided by *Dickinson et al.* (2002), f_{T5} and f_{T5} are computed exactly as in *Xu-Ri and Prentice* (2008) and the soil moisture controls on nitrification and denitrification are computed as a function of effective saturation S_e:

$$f_{moist,1} = \frac{S_e(1-S_e)}{0.25}\,, \tag{607}$$

$$f_{moist,2} = S_e^2\,, \tag{608}$$

$$f_{T5} = \left(\frac{70-T_{bg}}{70-38}\right)^{12} \exp\left[12\left(\frac{T_{bg}-38}{70-38}\right)\right]\,, \tag{609}$$

$$f_{T6} = \exp\left[308.56\left(\frac{1}{68.02}-\frac{1}{T_{bg}+46.02}\right)\right]\,, \tag{610}$$

where T_{bg} $[^\circ C]$ is the soil temperature in the biogeochemically active zone.

21.7 Phosphorus budget

Soil organic phosphorus dynamics are modeled similarly to nitrogen dynamics and organic phosphorus follows the carbon fluxes described in Section 21.4 using specific carbon to phosphorus ratio C:P for each pool. The C:P of microbial biomass has been observed to be a quite constrained value, even though less than C:N (*McGroddy et al.*, 2004; *Cleveland and Liptzin*, 2007; *Mouginot et al.*, 2014; *Mooshammer et al.*, 2014), and target values (Table 7) are prescribed in T&C. Phosphorus mineralization or immobilization is simulated to occur whenever the C:P of microbial biomass departs from the target values. The model does not track the phosphorus content of macrofuana or phosphorus in the extracellular enzyme pools.

The temporal dynamics of the soil organic matter phosphorus pool P_{som} $[g\,P\ g\,soil^{-1}]$, dissolved organic phosphorus DOP $[g\,P\ g\,soil^{-1}]$, and the phosphorus composing microbial biomass pools P_{bac}, P_{fun}, P_{AM}, and P_{EM} $[g\,P\ g\,soil^{-1}]$, e.g., bacteria, saprotrophic fungi, arbuscular mycorrhizae, and ectomycorrhizae, respectively, are computed as:

$$\frac{dP_{som}}{dt} = (1-\lambda_p)I_{som,pho} - \frac{f_d(F_{2l}+F_{2cb}+F_{2cf})+(F_{3b}+F_{3f})}{CP_{som}} + \frac{F_{8b}}{CP_{bac}} + \frac{F_{8f}}{CP_{fun}} + \frac{F_{8am}}{CP_{AM}} + \frac{F_{8em}}{CP_{EM}} + S_{DOP}\,, \tag{611}$$

$$\frac{dDOP}{dt} = f_{org,lea}\lambda_p I_{som,pho} + \lambda_p \frac{f_d(F_{2l}+F_{2cb}+F_{2cf})+(F_{3b}+F_{3f})}{CP_{som}} - L_{k,DOP} - S_{DOP}\,, \tag{612}$$

$$\frac{dP_{bac}}{dt} = (1-\lambda_p)\frac{f_dF_{2cb}+F_{3b}}{CP_{som}} - \frac{F_{8b}}{CP_{bac}} + P_{b,imm/min}\,, \tag{613}$$

$$\frac{dP_{fun}}{dt} = (1-\lambda_p)\frac{f_d(F_{2cf}+F_{2l})+F_{3f}}{CP_{som}} - \frac{F_{8f}}{CP_{fun}} + P_{f,imm/min}\,, \tag{614}$$

$$\frac{dP_{AM}}{dt} = -\frac{F_{8am}}{CP_{AM}} + P_{AM,imm/min} \tag{615}$$

$$\frac{dP_{EM}}{dt} = -\frac{F_{8em}}{CP_{EM}} + P_{EM,imm/min} \tag{616}$$

where the $I_{som,pho}$ $[g\,P\ g\,soil^{-1}\,day^{-1}]$ is the input to the soil organic phosphorus pool from litter decomposition defined in Section 21.3. The term CP_{som} is the mass carbon to phosphorus ratio of soil organic matter computed from the sum of $C_{poc,lig} + C_{poc,cel} + C_{moc}$ divided by P_{som}. The ratios CP_{bac}, CP_{fun}, CP_{AM} and CP_{EM} are the carbon to phosphorus ratios of bacteria, saprotrophic fungi, arbuscular mycorrhizae, and ectomycorrhizae, respectively. The carbon fluxes are all defined previously.

The coefficient λ_p is the P-leaching fraction (Table 4) and $f_{org,lea}$ is the fraction of leaching that is transferred in organic form. The DOP leaching $L_{k,DOP}$ is described in Section 21.9. The term $S_{DOP} = 0.01 DOP$ is a dissolved organic phosphorus stabilization function and prevents DOP to increase infinitely in case leaching is not able to remove DOP. Finally, the terms $P_{b,imm/min}$, $P_{f,imm/min}$, $P_{AM,imm/min}$, $P_{EM,imm/min}$ are the net phosphorus immobilization/mineralization fluxes for bacteria, saprotrophic fungi, and arbuscular mycorrhizal and ectomycorrhizal fungi described below. Note that as for nitrogen, the phosphorus associated with the carbon decomposed from MOC and POC and transformed in DOC is assimilated by bacteria and saprotrophic fungi, except for a fraction λ_p, which is leached as DOP.

The temporal dynamics of the inorganic phosphorus pools are simulated following the approach of the CENTURY model (*Parton et al.*, 1988), where P_{min} $[g\,P\ g\,soil^{-1}]$ is the mineral phosphorus and represents an undifferentiated sum of PO_4^{3-}, HPO_4^{2-} and $H_2PO_4^{-}$ (*Zhu et al.*, 2016). The pools P_{pri}, P_{sec}, P_{occ}, $[g\,P\ g\,soil^{-1}]$ represent the amount of phosphorus in the primary minerals, secondary minerals, and occluded phosphorus (*Parton et al.*, 1988; *Buendia et al.*, 2010; *Yang et al.*, 2014; *Zhu et al.*, 2016). Primary mineral sources of phosphorus are fed by the tectonic uplift $T_{P,up}$ $[g\,P\ g\,soil^{-1}\,day^{-1}]$ that adds new parent material, while secondary and occluded P minerals are formed through physical and chemical weathering, which lead to formation of soils (e.g. *Buendia et al.*, 2010). All these exchanges are regulated through simple linear kinetics:

$$\begin{aligned}
\frac{dP_{min}}{dt} &= (1 - f_{org,lea})\lambda_p I_{som,pho} - P_{b,imm/min} - P_{f,imm/min} - P_{AM,imm/min} \\
&\quad - P_{EM,imm/min} - P_{up} - L_{k,P} - P_{sec,ex} + P_{pri,ex} + Ex_P\,, \qquad (617)\\
\frac{dP_{pri}}{dt} &= T_{P,up} - P_{pri,ex}\,, \qquad (618)\\
\frac{dP_{sec}}{dt} &= P_{sec,ex} - P_{occ,ex}\,, \qquad (619)\\
\frac{dP_{occ}}{dt} &= P_{occ,ex}\,, \qquad (620)
\end{aligned}$$

where $I_{som,pho}$, λ_p and $f_{org,lea}$ are defined above. The mineral phosphorus leaching $L_{k,P}$ $[gP\ g\,soil^{-1}\ day^{-1}]$ is described in Section 21.9. The actual phosphorus uptake for units of ground P_{up} is defined in Section 19.2. The net immobilization/mineralization fluxes for P_{min} are defined below. The term Ex_P is the input of phosphorus from other sources due to deposition and fertilization. The flux $P_{pri,ex}$ $[gP\ g\,soil^{-1}\ day^{-1}]$ is the phosphorus converted from primary phosphorus into mineral phosphorus, $P_{sec,ex}$ $[gP\ g\,soil^{-1}\ day^{-1}]$ is the flux converting mineral phosphorus into secondary P, and $P_{occ,ex}$ $[gP\ g\,soil^{-1}\ day^{-1}]$ is the flux of P that becomes occluded and therefore unavailable. Note that $P_{occ,ex}$ is excluded by further exchanges and in absence of erosion will accumulate indefinitely in an infinite time. These exchanges between inorganic phosphorus pools are regulated by first order kinetics (*Parton et al.*, 1988):

$$\begin{aligned} P_{sec,ex} &= K_{1P}\, P_{min} - K_{2P}\, P_{sec}\,, && (621) \\ P_{pri,ex} &= K_{4P}\, P_{pri}\,, && (622) \\ P_{occ,ex} &= K_{3P}\, P_{sec}\,, && (623) \end{aligned}$$

and $K_{1P} = 1/600$, $K_{2P} = 1/13500$, $K_{3P} = 1/(30 \cdot 10^6)$, and $K_{4P} = 1/(4.38 \cdot 10^6)$ $[day^{-1}]$ are kinetic reaction coefficients (*Parton et al.*, 1988).

The net fluxes of phosphorus immobilization minus mineralization in the bacteria, saprotrophic fungi, arbuscular mycorrhizae, and ectomycorrhizae are computed similarly to nitrogen:

$$\begin{aligned} P_{b,imm/min} &= \left[\frac{C_{bac}}{R_{CP,bac}} - P_{bac}\right] / \tau\,, && (624) \\ P_{f,imm/min} &= \left[\frac{C_{fun}}{R_{CP,fun}} - P_{fun}\right] / \tau\,, && (625) \\ P_{AM,imm/min} &= \left[\frac{C_{AM}}{R_{CP,AM}} - P_{AM}\right] / \tau\,, && (626) \\ P_{EM,imm/min} &= \left[\frac{C_{EM}}{R_{CP,EM}} - P_{EM}\right] / \tau\,, && (627) \end{aligned}$$

where the terms are the immobilization (if $C_x : P_x \geq R_{CP,x}$) or mineralization (if $C_x : P_x < R_{CP,x}$) occurring to reach the target carbon to phosphorus ratio in the bacteria, saprotrophic fungi or mychorrizae: $R_{CP,mic}$ $R_{CP,fun}$ $R_{CP,AM}$ $R_{CP,EM}$ $[g\,C\ g\,P^{-1}]$, which are defined in Table 7. Note that, as for nitrogen, the above parametrization implies that mineralization and immobilization fluxes are occurring rapidly within the time τ (assumed equal to 1 day) and therefore that the prescribed carbon to phosphorus content of microbial biomass is almost exactly preserved.

21.8 Potassium budget

Due to its high solubility (high λ_k) a large fraction of potassium is leached during the litter decomposition process and the amount of potassium remaining in the organic material is relatively small when compared to the other analyzed nutrients (*Sardans and nuelas*, 2015). For this reason and because microbial stoichiometry of potassium is substantially unknown, we do not model potassium content in microbial biomass or macrofuana and only one generic pool of potassium, corresponding to potassium still trapped in the organic matter is simulated:

$$\frac{dK_{som}}{dt} = (1-\lambda_k) I_{som,pot} - \frac{f_d(F_{2l} + F_{2cb} + F_{2cf}) + (F_{3b} + F_{3f})}{CK_{som}} \qquad (628)$$

where the $I_{som,pot}$ $[g\,K\ \ g\,soil^{-1}\,day^{-1}]$ is the input to the potassium in the soil organic pool from litter decomposition defined in Section 21.3. The term CK_{som} is the mass carbon to potassium ratio of soil organic matter, computed from the sum of $C_{poc,lig} + C_{poc,cel} + C_{moc}$ divided by K_{som} and all other carbon fluxes are defined previously. In Eq. (628) the potassium associated with the decomposed soil organic carbon is fully transferred to the mineral solution.

Four phases of inorganic potassium in the soil are considered: (i) potassium in the mineral solution K_{min}, (ii) exchangeable potassium K_{ex}, (iii) non-exchangeable potassium K_{nex}, and (iv) potassium in the primary minerals K_{pri} (*Sparks and Huang*, 1985; *Sparks*, 1987). Plant uptake and leaching occur only from the K_{min} pool. Potassium in the solution is in direct contact with the exchangeable phase through adsorption/desorption kinetics $K_{ex,sol}$ (*Selim et al.*, 1976). Furthermore, the flux between exchangeable K and non-exchangeable (complex secondary minerals), $K_{fix,sol}$, is also governed by linear reactions. Potassium in primary minerals K_{pri} is converted to K_{min} through physical and chemical weathering $K_{min,rel}$. Concurrently, the primary mineral potassium is fed by the tectonic uplift $T_{K,up}$ $[g\,K\ \ g\,soil^{-1}\,day^{-1}]$ that contributes new parent material and thus primary soil potassium to the biogeochemically active zone.

$$\begin{aligned}
\frac{dK_{min}}{dt} &= (\lambda_k) I_{som,pot} + \frac{f_d(F_{2l} + F_{2cb} + F_{2cf}) + (F_{3b} + F_{3f})}{CK_{som}} + K_{min,rel} \\
&\quad - K_{fix,sol} - K_{ex,sol} - K_{up} - L_{k,K} + Ex_K \,, && (629) \\
\frac{dK_{pri}}{dt} &= T_{K,up} - K_{min,rel} \,, && (630) \\
\frac{dK_{ex}}{dt} &= K_{ex,sol} \,, && (631) \\
\frac{dK_{nex}}{dt} &= K_{fix,sol} \,, && (632)
\end{aligned}$$

where $I_{som,pot}$ and λ_k are defined above. The leaching of mineral potassium $L_{k,K}$ $[gK\ \ g\,soil^{-1}\ \ day^{-1}]$ is described in Section 21.9. The actual potassium uptake for unit of ground K_{up} is defined in Section 19.2. Since microbial potassium is neglected, the decomposition rates of organic matter F_{2x} and F_{3x} are assumed to generate only soluble potassium K_{min}. The term Ex_K is the input of potassium from other sources due to deposition and fertilization. The fluxes $K_{ex,sol}$, $K_{fix,sol}$, $K_{min,rel}$ $[g\,K\ \ g\,soil^{-1}\,day^{-1}]$ are assumed to be regulated by first order kinetics (*Selim et al.*, 1976):

$$\begin{aligned}
K_{min,rel} &= K_{3K} K_{pri} \,, && (633) \\
K_{fix,sol} &= K_{1K} K_{min} - K_{2K} K_{nex} \,, && (634) \\
K_{ex,sol} &= K_{aK} K_{min} - K_{dK} K_{ex} \,, && (635)
\end{aligned}$$

where $K_{1K} = 1/600$, $K_{2K} = 1/13500$, $K_{3K} = 1/350000$, and $K_{aK} = 1/2$ and $K_{dK} = 1/2$ $[day^{-1}]$ are kinetic reaction coefficients for soil potassium dynamics, which are assumed of the same magnitude than phosphorus for K_{1K} and K_{2K} or for obtaining plausible size of K_{pri} for typical tectonic uplift rates: K_{3K}. The adsorption K_{aK} and desorption K_{dK} are typically fast enough to occur within a day (*Selim et al.*, 1976; *Sparks and Carski*, 1985). However, since the minimum time step is one day, they are assumed to be 0.5 $[day^{-1}]$. Note that contrary to phosphorus, the K_{nex} that becomes non-exchangeable may be converted back to K_{min} and be available at a later stage.

21.9 Nutrient leaching

Leaching of nutrients from the soil is assumed to be proportional to the amount of dissolved nutrients and water leakage L_k $[mm\ h^{-1}]$ at the soil bottom divided by the water volume V $[mm]$ in the entire soil column (*Porporato et al.*, 2003). This is an approximation, since most of the dissolved nutrients is physically located in the upper part of the soil column in the biogeochemically active zone. However, such an approximation is likely to mostly affect short-temporal dynamics of nutrient leaching (in the order of days) rather than the integrated leaching in the long-term, where an equilibrium between leaching from the biogeochemically active zone and leaching at the soil bottom is expected. In total, seven leaching fluxes for the different solutes are computed: $L_{k,NH4}$, $L_{k,NO3}$, $L_{k,DON}$, $L_{k,P}$, $L_{k,DOP}$, $L_{k,K}$ and $L_{k,DOC}$ (with units $[g\,X\ m^{-2}\,day^{-1}]$). The conversion from the units used earlier (e.g., $[g\,X\ g\,soil^{-1}\,day^{-1}]$) to $[g\,X\,m^{-2}\,day^{-1}]$ is computed as explained in Eq. (499).

$$L_{k,NH4} = a_{NH4}\,NH4\,\frac{L_k}{V}\,, \qquad (636)$$

$$L_{k,NO3} = a_{NO3}\,NO3\,\frac{L_k}{V}\,, \qquad (637)$$

$$L_{k,DON} = a_{DON}\,DON\,\frac{L_k}{V}\,, \qquad (638)$$

$$L_{k,P} = a_{P}\,P_{min}\,\frac{L_k}{V}\,, \qquad (639)$$

$$L_{k,DOP} = a_{DOP}\,DOP\,\frac{L_k}{V}\,, \qquad (640)$$

$$L_{k,K} = a_{K}\,K_{min}\,\frac{L_k}{V}\,, \qquad (641)$$

$$L_{k,DOC} = a_{DOC}\,DOC\,\frac{L_k}{V}\,, \qquad (642)$$

where a_X $[-]$ are the solubility coefficients for the different solutes (Table 8).

21.10 Nutrient deposition

Nutrients in gaseous form and as aeolian particles may be deposited with rainfall as wet deposition. Concurrently, dust and organic matter particles or aerosols can also contain and deposit nutrients through dry deposition. Different databases are combined in T&C to provide geographical maps of total deposition for nitrogen and phosphorus and wet deposition for potassium. Specifically, present-day nitrogen deposition is obtained from *Vet et al.* (2014), who provide a one-degree latitude

Solubility coefficients	**Description**	**Value**
a_{DOC}	DOC - solubility coefficient	0.05
a_{NH4}	NH4 - solubility coefficient	0.05
a_{NO3}	NO3 - solubility coefficient	1
a_{DON}	DON - solubility coefficient	1
a_{P}	P - solubility coefficient	0.005
a_{DOP}	DOP - solubility coefficient	1
a_{K}	K - solubility coefficient	1

Table 8: Description of the values of the solubility coefficients for the different solutes, their order of magnitude was estimated to obtain realistic amounts of leached DOC and considering the relative solubility among the various substances, e.g., mineral potassium and nitrate are easily leached, while for phosphorus adsorption is very important.

longitude map of wet plus dry deposition of nitrogen reduced and nitrogen oxidized forms (Figure 48). The pre-industrial nitrogen is obtained from a global gridded estimates of atmospheric deposition of total inorganic nitrogen for the year 1860 (*Galloway et al.*, 2004; *Dentener*, 2006). Total atmospheric phosphorus deposition maps for current and preindustrial time are obtained from *Mahowald et al.* (2008), as shown in Figure 48. Finally, wet potassium deposition is available for about 480 stations around the world for the period 2005-2007 (*Vet et al.*, 2014), a nearest neighbor interpolation among these values is carried out to obtain an estimate of local potassium deposition as input for T&C.

21.11 Biological nitrogen fixation

Symbioses between certain plant species and nitrogen-fixing bacteria have an important role in several terrestrial ecosystems because they may represent the major natural source of nitrogen (*Cleveland et al.*, 1999; *Menge et al.*, 2009). For instance, many tropical forests possess tree species capable of developing symbiosis with nitrogen fixing bacteria and obtain atmospheric N_2 (*Batterman et al.*, 2013). The amount of nitrogen N_{bnf} $[gN\ m^{-2}\ day^{-1}]$ that is biologically fixed through bacteria in root-nodules is computed using the carbon cost of biological nitrogen fixation, $C_{fix,N}$ $[g\,C\ g\,N^{-1}]$, described in Section 17.3.2 (*Brzostek et al.*, 2014). Specifically, following Eq. 363, we have:

$$N_{bnf} \quad = \quad \frac{R_{exmy}}{C_{fix,N}}\,, \tag{643}$$

where R_{exmy} is the total carbon exported through roots and the term N_{bnf} is computed only if there are plant species in a given vegetated patch that allocate carbon to form root nodules for biological N fixation (e.g., $R_{ex,3} > 0$). Provided a realistic assumption about the carbon cost of biological nitrogen fixation, this formulation preserves coherence between the carbon allocation (Section 17.3.2) and the actual amount of biologically fixed nitrogen. The nitrogen flux N_{bnf} is considered to be in the form of ammonium NH_4^+ (Eq. 596) as in *Fisher et al.* (2010).

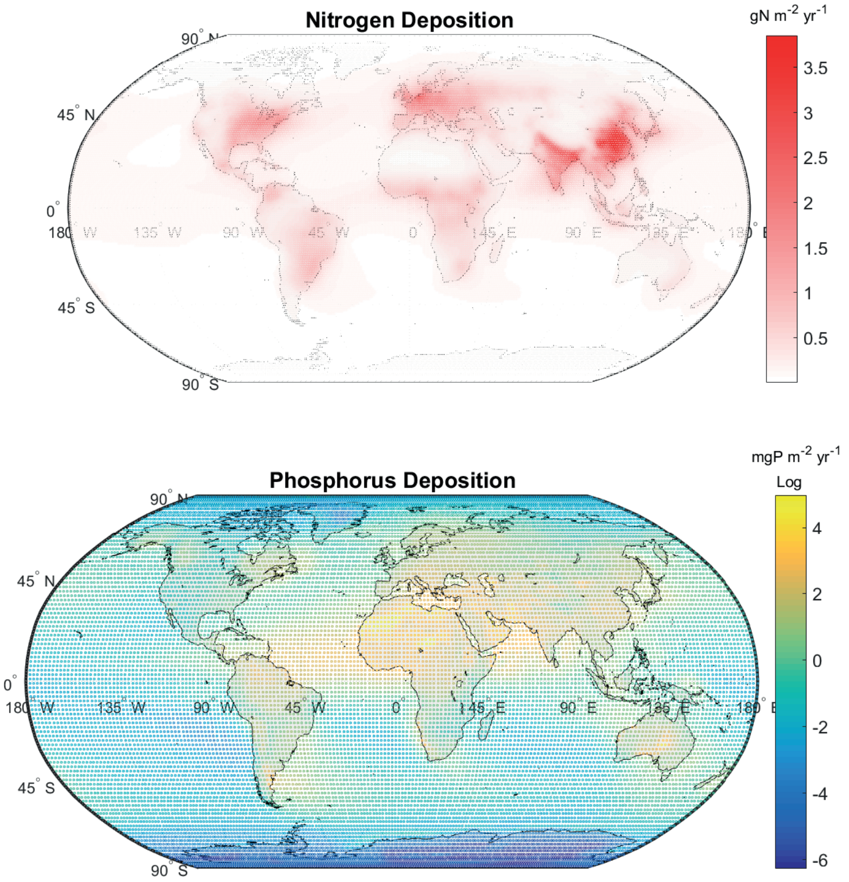

Figure 48: (a) Present-day nitrogen deposition including wet plus dry deposition of nitrogen in reduced and nitrogen oxidized forms (*Vet et al.*, 2014). (b) Present-day total phosphorus deposition (*Mahowald et al.*, 2008).

21.12 Supply of primary minerals

Primary minerals in terms of phosphorus and potassium are supplied by tectonic uplift T_{up} $[mm\, year^{-1}]$ that contributes new parent material that can be subsequently weathered, where T_{up} is a model input, which may vary by order of magnitudes. For decadal scale simulations, T_{up} can also be assumed equal to zero since contribution of minerals from new parent material is negligible. The supply of new phosphorus $T_{P,up}$ $[g\, P\ m^{-2}\, day^{-1}]$ and potassium $T_{K,up}$ $[g\, K\ m^{-2}\, day^{-1}]$ through tectonic uplift is computed as:

$$T_{P,up} = \frac{T_{up}\rho_{rock}C_{el,P}}{365}, \tag{644}$$

$$T_{K,up} = \frac{T_{up}\rho_{rock}C_{el,K}}{365}, \tag{645}$$

where $\rho_{rock} = 2500$ $[kg\, m^{-3}]$ is the rock density, assumed constant for simplicity and $C_{el,P}$, $C_{el,K}$ $[-]$ are the element concentration of phosphorus and potassium in the parent material. Their value is a function of the specific rock type and may vary considerably (see *Yang et al.* (2013) for phosphorus), however, for simplicity reference values of $C_{el,P} = 0.0005$, $C_{el,K} = 0.021$ are assumed as representative of average concentrations of these elements in the Earth surface crust.

Recently, also nitrogen has been shown to be released from near-surface rocks, especially in mountain and high-latitude ecosystems (*Houlton et al.*, 2018). This nitrogen source is not considered yet in T&C.

22 Vegetation Management

To be completed

References

Abbott, M. B., J. C. Bathurst, J. A. Cunge, P. E. O'Connell, and J. Rasmussen (1986), An introduction to the european hydrologic system-systeme hydrologique europeen, SHE, 2: Structure of a physically-based, distributed modeling system, *Journal of Hydrology*, *87*, 61–77.

Abdella, K., and N. A. McFarlane (1996), Parameterization of the surface-layer exchange coefficients for atmospheric models, *Boundary-Layer Meteorology*, *80*, 223–248.

Abramoff, R., X. Xu, M. Hartman, S. O'Brien, W. Feng, E. Davidson, A. Finzi, D. Moorhead, J. Schimel, M. Torn, and M. A. Mayes (2018), The Millennial model: in search of measurable pools and transformations for modeling soil carbon in the new century, *Biogeochemistry*, *137*, 51–71, doi.org/10.1007/s10533-017-0409-7.

Ainsworth, E. A., and S. P. Long (2005), What have we learned from 15 years of Free-Air CO_2 Enrichment (FACE)? A meta-analytic review of the responses of photosynthesis, canopy properties and plant production to rising CO_2, *New Phytologist*, *165*(2), 351–371.

Allen, R. G., M. E. Jensen, J. L. Wright, and R. D. Burman (1989), Operational estimates of reference evapotranspiration, *Agronomy Journal*, *81*(4), 650–662.

Allen, R. G., L. S. Pereira, D. Raes, and M. Smith (1998), *Crop evapotranspiration-Guidelines for computing crop water requirements*, *FAO Irrigation and drainage paper*, vol. 300, FAO - Food and Agriculture Organization of the United Nations.

Allison, S. D. (2005), Cheaters, diffusion, and nutrients constrain decomposition by microbial enzymes in spatially structured environments, *Ecol. Lett.*, *8*, 626–635.

Allison, S. D. (2017), *Microbial Biomass: A Paradigm Shift in Terrestrial Biogeochemistry*, chap. Building Predictive Models for Diverse Microbial Communities in Soil, UC Irvine, [UCPMS ID.

Allison, S. D., M. D.Wallenstein, and M. A. Bradford (2010), Soil-carbon response to warming dependent on microbial physiology, *Nature Geosciences*, *3*, 336–340.

Amthor, J. S. (1984), The role of maintenance respiration in plant growth, *Plant, Cell and Environment*, *7*, 561–569.

Amthor, J. S. (2000), The McCree-de Wit-Penning de Vries-Thornley respiration paradigms: 30 years later, *Annals of Botany*, *86*, 1–20.

Anderson, E. A. (1968), Development and testing of snowpack energy balance equations, *Water Resources Research*, *4*(1), 19–37.

Anderson, E. A., and N. H. Crawford (1964), The synthesis of continuous snowmelt runoff hydrographs on a digital computer, *Tech. Rep. 36*, Stanford, California Stanford University Dep. of Civil Engineering.

Anderson, M. C., J. M. Norman, T. P. Meyers, and G. R. Diak (2000), An analytical model for estimating canopy transpiration and carbon assimilation fluxes based on canopy light-use efficiency, *Agricultural and Forest Meteorology*, *101*, 265–289.

Aoki, T., A. Hachikubo, and M. Hori (2003), Effects of snow physical parameters on shortwave broadband albedos, *Journal of Geophysical Research*, *108*(D19,4616), doi:10.1029/2003JD003506.

Aoyama, M., D. A. Angers, and A. N'Dayegamiye (1999), Particulate and mineral-associated organic matter in waterstable aggregates as affected by mineral fertilizer and manure applications, *Canadian Journal of Soil Science*, *79*, 295–302.

Arora, V. K. (2002), Modelling vegetation as a dynamic component in soil-vegetation-atmosphere- transfer schemes and hydrological models, *Reviews of Geophysics*, *40*(2), doi:10.1029/2001RG000103.

Arora, V. K., and G. J. Boer (2003), A representation of variable root distribution in dynamic vegetation models, *Earth Interactions*, *7*(6), 1–19.

Arora, V. K., and G. J. Boer (2005), A parameterization of leaf phenology for the terrestrial ecosystem component of climate models, *Global Change Biology*, *11*(1), 39–59.

Arya, S. P. (2001), *Introduction to Micrometeorology*, 2nd ed., Academic Press.

Asner, G. P., C. A. Wessman, D. S. Schimel, and S. Archer (1998), Variability in leaf and litter optical properties: Implications for BRDF model inversions using AVHRR, MODIS, and MISR, *Remote Sensing of Environment*, *63*, 243–257.

Assmann, S. M. (1999), The cellular basis of guard cell sensing to rising CO_2, *Plant, Cell and Environment*, *22*, 629–637.

Assouline, S. (2004), Rainfall-induced soil surface sealing: A critical review of observations, conceptual models, and solutions, *Vadose Zone Journal*, *3*, 570–591.

Assouline, S., and Y. Mualem (1997), Modeling the dynamics of seal formation and its effect on infiltration as related to soil and rainfall characteristics, *Water Resources Research*, *33*, 1527–1536.

Assouline, S., and Y. Mualem (2001), Soil seal formation and its effect on infiltration: Uniform versus nonuniform seal approximation, *Water Resources Research*, *37*, 297–305.

Assouline, S., and Y. Mualem (2006), Runoff from heterogeneous small bare catchments during soil surface sealing, *Water Resources Research*, *42*(W12405), doi:10.1029/2005WR004592.

Assouline, S., and D. Or (2006), Anisotropy factor of saturated and unsaturated soils, *Water Resour. Res.*, *42*, W12,403, doi:10.1029/2006WR005001.

Assouline, S., and D. Or (2013), Conceptual and parametric representation of soil hydraulic properties: A review, *Vadose Zone Journal*, *12*(4), –, doi:10.2136/vzj2013.07.0121.

Atkin, O. K., M. H. M. Westbeek, M. L. Cambridge, H. Lambers, and T. L. Pons (1997), Leaf respiration in light and darkness. a comparison of slow- and fast-growing Poa species, *Plant Physiology*, *113*, 961–965.

Baker, D. G., D. L. Ruschy, and D. B. Wall (1990), The albedo decay of prairie snows, *Journal of Applied Meteorology*, *29*, 179–187.

Baldocchi, D., E. Falge, L. Gu, R. Olson, D. Hollinger, S. Running, P. Anthoni, C. Bernhofer, K. Davis, R. Evans, J. Fuentes, A. Goldstein, G. Katul, B. Law, X. Lee, Y. Malhi, T. Meyers, W. Munger, W. Oechel, U. K. T. Paw, K. Pilegaard, H. P. Schmid, R. Valentini, S. Verma, T. Vesala, K. Wilson, and S. Wofsy (2001), FLUXNET: A new tool to study the temporal and spatial variability of ecosystem-scale carbon dioxide, water vapor, and energy flux densities, *Bulletin of the American Meteorological Society*, *82*(11), 2415–2434.

Baldocchi, D. D., and P. C. Harley (1995), Scaling carbon dioxide and water vapour exchange from leaf to canopy in a deciduous forest. II: Model testing and application, *Plant, Cell and Environment*, *18*, 1157–1173.

Baldocchi, D. D., and K. B. Wilson (2001), Modeling CO_2 and water vapor exchange of a temperate broadleaved forest across hourly to decadal time scales, *Ecological Modelling*, *142*, 155–184.

Baldocchi, D. D., T. A. Black, P. S. Curtis, E. Falge, J. D. Fuentes, A. Granier, L. Gu, A. Knohl, K. Pilegaard, H. P. Schmid, R. Valentini, K. Wilson, S. Wofsy, L. Xu, and S. Yamamoto (2005), Predicting the onset of net carbon uptake by deciduous forests with soil temperature and climate data: a synthesis of FLUXNET data, *International Journal of Biometeorology*, *49*, 377–387, doi: 10.1007/s00484-005-0256-4.

Ball, J. T., I. E. Woodrow, and J. A. Berry (1987), A model predicting stomatal conductance and its contribution to the control of photosynthesis under different environmental conditions, in *Progress in photosynthesis research*, edited by Biggins, pp. 221–224, Martinus Nijhoff, Netherlands.

Baskaran, P., R. Hyvönen, S. L. Berglund, K. E. Clemmensen, G. I. Ågren, B. D. Lindahl, and S. Manzoni (2017), Modelling the influence of ectomycorrhizal decomposition on plant nutrition and soil carbon sequestration in boreal forest ecosystems, *New Phytologist*, *213*(3), 1452–1465.

Batterman, S. A., L. O. Hedin, M. van Breugel, J. Ransijn, D. J. Craven, and J. S. Hall (2013), Key role of symbiotic dinitrogen fixation in tropical forest secondary succession, *Nature*, *502*, 224–227.

Bauerle, W. L., R. Oren, D. A. Way, S. S. Qian, P. C. Stoy, P. E. Thornton, J. D. Bowden, F. M. Hoffman, and R. F. Reynolds (2012), Photoperiodic regulation of the seasonal pattern of photosynthetic capacity and the implications for carbon cycling, *Proc. Natl. Acad. Sci. USA*, *109*(22), 8612–8617.

Bedford, D. R., and E. E. Small (2008), Spatial patterns of ecohydrologic properties on a hillslope-alluvial fan transect, central New Mexico, *Catena*, *73*, 34–48, doi:10.1016/j.catena.2007.08.005.

Belair, S., R. Brown, J. Mailhot, B. Bilodeau, and L.-P. Crevier (2003), Operational implementation of the ISBA land surface scheme in the Canadian regional weather forecast model. Part II: Cold season results, *Journal of Hydrometeorology*, *4*, 371–386.

Beljaars, A. C. M. (1994), The parametrization of surface fluxes in large-scale models under free convection, *Q. J . R. Meteorol. Soc.*, *121*, 255–270.

Beljaars, A. C. M., and A. A. M. Holtslag (1991), Flux parameterization over land surfaces for atmospheric models, *Journal of Applied Meteorology*, *30*, 327–341.

Bernacchi, C. J., E. L. Singsaas, C. Pimentel, J. A. R. Portis, and S. P. Long (2001), Improved temperature response functions for models of rubisco-limited photosynthesis, *Plant Cell Environ.*, *24*, 253–259, doi:10.1111/j.1365-3040.2001.00668.x.

Bernacchi, C. J., C. Pimentel, and S. P. Long (2003), In vivo temperature response functions of parameters required to model RuBP-limited photosynthesis, *Plant Cell Environ.*, *26*, 1419–1430, doi:10.1046/j.0016-8025.2003.01050.x.

Bernhardt, M., and K. Schulz (2010), SnowSlide: A simple routine for calculating gravitational snow transport, *Geophysical Research Letters*, *37*(11), 1–6.

Bertoldi, G., R. Rigon, and T. M. Over (2006a), Impact of watershed geomorphic characteristics on the energy and water budgets, *Journal of Hydrometeorology*, *7*, 389–403.

Bertoldi, G., R. Rigon, D. Tamanini, and F. Zanotti (2006b), GEOtop version 0.875: Technical description and programs guide, *Tech. Rep. dica-06-001*, University of Trento E-Prints.

Beven, K. J. (1982), On subsurface stormflow: An analysis of response times, *Hydrological Sciences Journal*, *4*, 505–521.

Beven, K. J., and J. Freer (2001), A dynamic TOPMODEL, *Hydrological Processes*, *15*, 1993–2011, doi: 10.1002/hyp.252.

Beven, K. J., and M. J. Kirkby (1979), A physically based, variable contributing area model of basin hydrology, *Hydrological Sciences Bulletin*, *24*, 43–69.

Bhark, E. W., and E. E. Small (2003), Association between plant canopies and the spatial patterns of infiltration in shrubland and grassland of the Chihuahuan desert, New Mexico, *Ecosystems*, *6*, 185–196, doi:10.1007/s10021-002-0210-9.

Bohrer, G., H. Mourad, T. A. Laursen, D. Drewry, R. Avissar, D. Poggi, R. Oren, and G. G. Katul (2005), Finite element tree crown hydrodynamics model (FETCH) using porous media flow within branching elements: A new representation of tree hydrodynamics, *Water Resources Research*, *41*(W11404), doi:10.1029/2005WR004181.

Bonan, G. (2002), *Ecological Climatology: Concept and Applications*, Cambridge Univ. Press, New York.

Bonan, G. B. (1991), A biophysical surface energy budget analysis of soil temperature in the boreal forests of interior Alaska, *Water Resour. Res.*, *27*(5), 767–781.

Bonan, G. B. (1996), A land surface model (LSM version 1.0) for ecological, hydrological, and atmospheric studies: Technical description and user's guide, *Tech. Rep. NCAR Tech. Note NCAR/TN-417*, Natl. Cent. for Atmos. Res., Boulder, Colorado.

Bonan, G. B., S. Levis, L. Kergoat, and K. W. Oleson (2002), Landscapes as patches of plant functional types: An integrating concept for climate and ecosystem models, *Global Biogeochemical Cycles*, *16*(2,1021), doi:10.1029/2000GB001360.

Bonan, G. B., S. Levis, S. Sitch, M. Vertenstein, and K. W. Oleson (2003), A dynamic global vegetation model for use with climate models: concepts and description of simulated vegetation dynamics, *Global Change Biology*, *9*, 1543–1566, doi: 10.1046/j.1529-8817.2003.00681.x.

Bonan, G. B., P. J. Lawrence, K. W. Oleson, S. Levis, M. Jung, M. Reichstein, D. M. Lawrence, and S. C. Swenson (2011), Improving canopy processes in the Community Land Model version 4 (CLM4) using global flux fields empirically inferred from FLUXNET data, *Journal of Geophysical Research*, *116*(G02014), doi:10.1029/2010JG001593.

Bonan, G. B., M. Williams, R. A. Fisher, and K. W. Oleson (2014), Modeling stomatal conductance in the earth system: linking leaf water-use efficiency and water transport along the soil-plant-atmosphere continuum, *Geosci. Model Dev.*, *7*, 2193–2222.

Boone, A., V. Masson, T. Meyers, and J. Noilhan (2000), The influence of the inclusion of soil freezing on simulations by a soil-vegetation-atmosphere transfer scheme, *Journal of Applied Meteorology*, *39*, 1544–1569.

Borchert, R., S. S. Renner, Z. Calle, D. Navarrete, A. Tye, L. Gautier, R. Spichiger, and P. von Hildebrand (2005), Photoperiodic induction of synchronous flowering near the equator, *Nature*, *433*(7026), 627.

Botta, A., N. Viovy, P. Ciais, and P. Friedlingstein (2000), A global prognostic scheme of leaf onset using satellite data, *Global Change Biology*, *6*, 709–726.

Brandt, C. J. (1989), The size distribution of throughfall drops under vegetation canopies, *Catena*, *16*, 507–524.

Brandt, C. J. (1990), Simulation of the size distribution and erosivity of raindrops and throughfall drops, *Earth Surface Processes and Landforms*, *15*, 687–698.

Bras, R. L. (1990), *Hydrology, An introduction to hydrologic science*, Addison-Wesley, Reading, MA.

Braud, I., A. C. Dantas-Antonino, M. Vauclin, J. L. Thony, and P. Ruelle (1995), A simple soil-plant-atmosphere transfer model (SiSPAT) development and field verification, *Journal of Hydrology*, *166*, 213–250.

Bristow, K. L., G. S. Campbell, R. I. Papendick, and L. F. Elliott (1986), Simulation of heat and moisture transfer through a surface residue-soil system, *Agric. For. Meteorol*, *36*, 193–214.

Brooks, R. H., and A. T. Corey (1964), Hydraulic properties of porous media, *Hydrology Paper 3*, Colorado State University, Ft. Collins, CO.

Brundrett, M. C. (2009), Mycorrhizal associations and other means of nutrition of vascular plants: understanding the global diversity of host plants by resolving conflicting information and developing reliable means of diagnosis, *Plant and Soil*, *320*, 37–77, doi:10.1007/s11104-008-9877-9.

Brutsaert, W. (1975), On a derivable formula for long-wave radiation from clear skies, *Water Resources Research*, *11*(5), 742–744.

Brutsaert, W. (1982), *Evaporation into the atmosphere*, D. Reidel.

Brutsaert, W. (2005), *Hydrology. An Introduction*, Cambridge University Press, Cambridge, UK.

Brzostek, E. R., J. B. Fisher, and R. P. Phillips (2014), Modeling the carbon cost of plant nitrogen acquisition: Mycorrhizal trade-offs and multipath resistance uptake improve predictions of retranslocation, *J. Geophys. Res. Biogeosci*, *119*, 1684–1697, doi:10.1002/2014JG002660.

Buckley, T. N. (2005), The control of stomata by water balance, *New Phytologist*, *169*, 275–292, doi: 10.1111/j.1469-8137.2005.01543.x.

Buckley, T. N., K. A. Mott, and G. D. Farquhar (2003), A hydromechanical and biochemical model of stomatal conductance, *Plant, Cell and Environment*, *26*, 1767–1785.

Buendia, C., A. Kleidon, and A. Porporato (2010), The role of tectonic uplift, climate, and vegetation in the long-term terrestrial phosphorous cycle, *Biogeosciences*, *7*, 2025–2038.

Bugmann, H., and C. Bigler (2011), Will the co2 fertilization effect in forests be offset by reduced tree longevity?, *Oecologia*, *165*(2), 534–544.

Businger, J. A., J. C. Wyngaard, Y. Izumi, and E. F. Bradley (1971), Flux profile relationships in the atmospheric surface layer, *Journal of the Atmospheric Sciences*, *28*, 181–189.

Camillo, P. J., and R. J. Gurney (1986), A resistance parameter for bare soil evaporation models, *Soil Sci.*, *141*, 95–105.

Campbell, E. E., W. J. Parton, J. L. Soong, K. Paustian, N. T. Hobbs, and M. F. Cotrufo (2016), Using litter chemistry controls on microbial processes to partition litter carbon fluxes with the litter decomposition and leaching (LIDEL) model, *Soil Biology and Biochemistry*, *100*, 160–174.

Campbell, G. S. (1974), A simple method for determining unsaturated conductivity from moisture retention data, *Soil Science*, *117*, 311–314.

Camporese, M., C. Paniconi, M. Putti, and S. Orlandini (2010), Surface-subsurface flow modeling with path-based runoff routing, boundary condition-based coupling, and assimilation of multisource observation data, *Water Resources Research*, *46*(W02512), doi:10.1029/2008WR007536.

Cannell, M. G. R., and J. H. M. Thornley (2000), Modelling plant respiration :some guiding principles, *Annals of Botany*, *85*, 45–54.

Celia, M. A., E. T. Bouloutas, and R. L. Zarba (1990), A general mass-conservative numerical solution for the unsaturated flow equation, *Water Resources Research*, *26*(7), 1483–1496.

Chanson, H. (2004), *The Hydraulics of Open Channel Flow: An Introduction*, Elsevier Butterworth Heinemann.

Chapin III, F. S., E.-D. Schulze, and H. A. Mooney (1990), The ecology and economics of storage in plants, *Annual Review of Ecology and Systematics*, *21*, 423–447.

Chen, Y., A. Hall, and K. N. Liou (2006), Application of three-dimensional solar radiative transfer to mountains, *Journal of Geophysical Research*, *111*(D21111), doi:10.1029/2006JD007163.

Cheng, D.-L., and K. J. Niklas (2007), Above- and below-ground biomass relationships across 1534 forested communities, *Annals of Botany*, *99*, 95–102, doi:10.1093/aob/mcl206.

Choudhury, B. J., and J. L. Monteith (1988), A four-layer model for the heat budget of homogeneous land surfaces, *Quarterly Journal of the Royal Meteorological Society*, *114*, 378–398.

Chow, V. T. (1988), *Applied Hydrology*, McGraw-Hill Science Engineering.

Chu, C., M. Bartlett, Y. Wang, F. He, J. Weiner, J. Chave, and L. Sack (2016), Does climate directly influence npp globally?, *Global Change Biology*, *22*, 12–24, doi: 10.1111/gcb.13079.

Chuine, I., and J. Régnière (2017), Process-based models of phenology for plants and animals, *Annual Review of Ecology, Evolution, and Systematics*, *48*(1), 159–182.

Ciarapica, L., and E. Todini (2002), TOPKAPI: a model for the representation of the rainfall-runoff process at different scales, *Hydrological Processes*, *16*, 207–229.

Cichota, R., E. A. Elias, and Q. de Jong van Lier (2004), Testing a finite-difference model for soil heat transfer by comparing numerical and analytical solutions, *Environmental Modelling & Software*, *19*, 495–506.

Clapp, R. B., and G. M. Hornberger (1978), Empirical equations for some soil hydraulic properties, *Water Resources Research*, *14*(4), 601–604.

Clark, D. B., L. M. Mercado, S. Sitch, C. D. Jones, N. Gedney, M. J. Best, M. Pryor, G. G. Rooney, R. L. H. Essery, E. Blyth, O. Boucher, R. J. Harding, C. Huntingford, and P. M. Cox (2011), The Joint UK Land Environment Simulator (jules), model description - Part 2: Carbon fluxes and vegetation dynamics, *Geosci. Model Dev.*, *4*(3), 701–722.

Cleland, E. E., I. Chuine, A. Menzel, H. A. Mooney, and M. D. Schwartz (2007), Shifting plant phenology in response to global change, *Trends in Ecology and Evolution*, *22*(7), 357–365, doi:10.1016/j.tree.2007.04.003.

Cleveland, C. C., and D. Liptzin (2007), C:N:P stoichiometry in soil: is there a redfield ratio for the microbial biomass?, *Biogeochemistry*, *85*, 235–252.

Cleveland, C. C., A. R. Townsend, D. S. Schimel, H. Fisher, R. W. Howarth, L. O. Hedin, S. S. Perakis, E. F. Latty, J. C. VonFischer, A. Elseroad, and M. F. Wasson (1999), Global patterns of terrestrial biological nitrogen (N_2) fixation in natural ecosystems, *Glob. Biogeochem. Cycles*, *13*, 623–645.

Cleveland, C. C., B. Z. Houlton, W. K. Smith, A. R. Marklein, S. C. Reed, W. Parton, S. J. D. Grosso, and S. W. Running (2013), Patterns of new versus recycled primary production in the terrestrial biosphere, *Proc. Natl Acad. Sci. USA*, *110*, 12,733–12,737.

Collatz, G. J., J. T. Ball, C. Grivet, and J. A. Berry (1991), Physiological and environmental regulation of stomatal conductance, photosynthesis and transpiration-a model that includes a laminar boundary-layer, *Agricultural and Forest Meteorology*, *54*, 107–136.

Collatz, G. J., M. Ribas-Carbo, and J. A. Berry (1992), Coupled photosynthesis-stomatal conductance model for leaves of C4 plants, *Australian Journal of Plant Physiology*, *19*, 519–538.

Collins, D. B. G., and R. L. Bras (2007), Plant rooting strategies in water-limited ecosystems, *Water Resources Research*, *43*(W06407), doi:10.1029/2006WR005541.

Conant, R. T., M. G. Ryan, G. I. Ågren, H. E. Birge, E. A. Davidson, P. E. Eliasson, S. E. Evans, S. D. Frey, C. P. Giardina, F. M. Hopkins, R. Hyvönen, M. U. F. Kirschbaum, J. M. Lavallee, J. Leifeld, W. J. Parton, J. Megan Steinweg, M. D. Wallenstein, J. Å. Martin Wetterstedt, and M. A. Bradford (2011), Temperature and soil organic matter decomposition rates-synthesis of current knowledge and a way forward, *Global Change Biology*, *17*, 3392–3404.

Costa-Cabral, M., and S. J. Burges (1994), Digital elevation model networks (DEMON): A model of flow over hillslopes for computation of contributing and dispersal areas, *Water Resources Research*, *30*, 1681–1692.

Cox, P. M. (2001), Description of the TRIFFID Dynamic Global Vegetation Model, *Technical Note 24*, Hadley Centre.

Cox, P. M., R. A. Betts, C. B. Bunton, R. L. H. Essery, P. R. Rowntree, and J. Smith (1999), The impact of new land surface physics on the GCM simulation of climate and climate sensitivity, *Climate Dynamics*, *15*, 183–203.

Cuffey, K., and W. Paterson (2010), *The Physics of Glaciers*, Elsevier, Burlington, MA, USA.

Curry, J. P. (1998), *Earthworm ecology*, chap. Factors affecting earthworm abundance in soils, pp. 37–64, St. Lucie Press, Boca Raton FL.

Curry, J. P., and O. Schmidt (2007), The feeding ecology of earthworms - a review, *Pedobiologia*, *50*, 463–477.

Dai, Q., and S. Sun (2006), A generalized layered radiative transfer model in the vegetation canopy, *Advances in Atmospheric Sciences*, *23*(2), 243–257.

Dai, Q., and S. Sun (2007), A comparison of two canopy radiative models in land surface processes, *Advances in Atmospheric Sciences*, *24*(3), 421–434.

Dai, Y., R. E. Dickinson, and Y.-P. Wang (2004), A two-big-leaf model for canopy temperature, photosynthesis, and stomatal conductance, *Journal of Climate*, *17*, 2281–2299.

Daly, E., A. Porporato, and I. Rodriguez-Iturbe (2004), Coupled dynamics of photosynthesis, transpiration, and soil water balance. part I: Upscaling from hourly to daily level, *Journal of Hydrometeorology*, *5*, 546–558.

de Pury, D. G. G., and G. D. Farquhar (1997), Simple scaling of photosynthesis from leaves to canopies without the errors of big-leaf models, *Plant, Cell and Environment*, *20*(5), 537–557.

de Vries, D. A. (1963), Thermal properties of soils, in *Physics of the Plant Environment*, edited by W. van Wijk, North-Holland, Amsterdam.

Deardorff, J. W. (1978), Efficient prediction of ground surface temperature and moisture with inclusion of a layer of vegetation, *Journal of Geophysical Research*, *83*, 1889–1903.

Deckmym, G., H. Verbeeck, M. O. de Beeck, D. Vansteenkiste, K. Steppe, and R. Ceulemans (2008), ANAFORE: A stand-scale process-based forest model that includes wood tissue development and labile carbon storage in trees, *Ecological Modelling*, *215*, 345–368, doi:10.1016/j.ecolmodel.2008.04.007.

Deckmyn, G., S. P. Evans, and T. J. Randle (2006), Refined pipe theory for mechanistic modeling of wood development, *Tree Physiology*, *26*, 703–717.

Dentener, F. J. (2006), Global maps of atmospheric nitrogen deposition, 1860, 1993, and 2050, Available on-line [http://daac.ornl.gov/] from Oak Ridge National Laboratory Distributed Active Archive Center, Oak Ridge, Tennessee, U.S.A. doi:10.3334/ORNLDAAC/830, data set.

DeRoo, A. P. J., C. G. Wesseling, and C. J. Ritsema (1996), LISEM: a single-event physically based hydrological and soil erosion model for drainage basins: I: Theory, input and output, *Hydrological Processes*, *10*, 1107–1117.

Devevre, O. C., and W. R. Horwath (2000), Decomposition of rice straw and microbial carbon use efficiency under different soil temperatures and moistures, *Soil Biology & Biochemistry*, *32*, 1773–1785.

Dewar, R. C. (2002), The Ball-Berry-Leuning and Tardieu-Davies stomatal models: synthesis and extension within a spatially aggregated picture of guard cell function, *Plant, Cell and Environment*, *25*, 1383–1398.

Dewar, R. C., L. Tarvainen, K. Parker, G. Wallin, and R. E. McMurtrie (2012), Why does leaf nitrogen decline within tree canopies less rapidly than light? an explanation from optimization subject to a lower bound on leaf mass per area, *Tree Physiology*, *32*, 520–534, doi:10.1093/treephys/tps044.

Dickinson, R. E. (1983), Land surface processes and climate-surface albedos and energy balance, *Advances in Geophysics*, *25*, 305–353.

Dickinson, R. E. (1988), The force-restore method for surface temperature and its generalization, *Journal of Climate*, *1*, 1086–1097.

Dickinson, R. E. (2008), Determination of the multi-scattered solar radiation from a leaf canopy for use in climate models, *Journal of Computational Physics*, *227*, 3667–3677.

Dickinson, R. E., A. Henderson-Sellers, and P. J. Kennedy (1993), Biosphere-atmosphere transfer scheme (BATS) version 1E as coupled to the NCAR Community Climate Model, *Tech. Rep. NCAR/TN-387+STR*, Natl. Cent. for Atmos. Res., Boulder, Colorado.

Dickinson, R. E., M. Shaikh, R. Bryant, and L. Graumlich (1998), Interactive canopies for a climate model, *Journal of Climate*, *11*, 2823–2836.

Dickinson, R. E., J. A. Berry, G. B. Bonan, G. J. Collatz, C. B. Field, I. Y. Fung, M. Goulden, W. A. Hoffmann, R. B. Jackson, R. Myneni, P. J. Sellers, and M. Shaikh (2002), Nitrogen controls on climate model evapotranspiration, *Journal of Climate*, *15*, 278–294.

Dilley, A. C., and D. M. O'Brien (1998), Estimating downward clear sky long-wave irradiance at the surface from screen temperature and precipitable water, *Quat. J. R. Meteorol. Soc.*, *124*, 1391–1401.

Dingman, S. L. (1994), *Physical Hydrology*, Prentice-Hall, New Jersey.

Dolman, A. J. (1993), A multiple-source land surface energy balance model use in general circulation models, *Agric. For. Meteorol.*, *65*(1-2), 21–45.

Dorman, J. L., and P. J. Sellers (1989), A global climatology of albedo, roughness length and stomatal resistance for atmospheric general circulation models as represented by the simple biosphere model (SiB), *Journal of Applied Meteorology*, *28*, 833–855.

Dormand, J. R., and P. J. Prince (1980), A family of embedded Runge-Kutta formulae, *Journal of Computational and Applied Mathematics*, *6*, 19–26.

Doussan, C., G. Vercambre, and L. Pages (1998), Modelling of the hydraulic architecture of root systems: An integrated approach to water absorption - distribution of axial and radial conductances in maize, *Annals of Botany*, *81*, 225–232.

Douville, H., J.-F. Royer, and J.-F. Mahfouf (1995), A new snow parameterization for the Meteo-France climate model. Part I: Validation in stand-alone experiments, *Climate Dynamic*, *12*, 21–35.

Dozier, J., and J. Frew (1990), Rapid calculation of terrain parameters for radiation modeling from digital elevation data, *IEEE Transactions on Geoscience and Remote Sensing*, *28*, 963–969.

Drewry, D. T., P. Kumar, S. Long, C. Bernacchi, X. Z. Liang, and M. Sivapalan (2010), Ecohydrological responses of dense canopies to environmental variability: 1. Interplay between vertical structure and photosynthetic pathway, *Journal of Geophysical Research*, *115*(G04022), doi:10.1029/2010JG001340.

Dubayah, R., and S. Loechel (1997), Modeling topographic solar radiation using GOES data, *Journal of Applied Meteorology*, *36*, 141–154.

Ducoudré, N. I., K. Laval, and A. Perrier (1993), SECHIBA, a new set of parameterizations of the hydrologic exchanges at the land atmosphere interface within the lmd atmospheric general circulation model, *Journal of Climate*, *6*, 248–272.

Dye, D. G. (2004), Spectral composition and quanta-to-energy ratio of diffuse photosynthetically active radiation under diverse cloud conditions, *Journal of Geophysical Research*, *109*(D10203), doi:10.1029/2003JD004251.

Dyer, A. J. (1974), A review of flux-profile relationships, *Boundary-Layer Meteorology*, *7*, 368–372.

Ebrahimi, A. N., and D. Or (2014), Microbial dispersal in unsaturated porous media: Characteristics of motile bacterial cell motions in unsaturated angular pore networks, *Water Resour. Res.*, *50*, 7406–7429, doi:10.1002/2014WR015897.

Eltahir, E. A. B., and R. L. Bras (1993), A description of rainfall interception over large-areas, *Journal of Climate*, *6*, 1002–1008.

Enquist, B. J. (2002), Universal scaling in tree and vascular plant allometry: toward a general quantitative theory linking plant form and function from cells to ecosystems, *Tree Physiology*, *22*, 1045–1064.

Enquist, B. J., A. J. Kerkhoff, S. C. Stark, N. G. Swenson, M. C. McCarthy, and C. A. Price (2007), A general integrative model for scaling plant growth, carbon flux, and functional trait spectra, *Nature*, *449*(218-222), doi:10.1038/nature06061.

Enquist, B. J., G. B. West, and J. H. Brown (2009), Extensions and evaluations of a general quantitative theory of forest structure and dynamics, *Proc. Natl Acad. Sci. USA*, *106*(17), 7046–7051, doi:10.1073/pnas.0812303106.

Essery, R., E. Martin, H. Douville, A. Fernandez, and E. Brun (1999), A comparison of four snow models using observations from an alpine site, *Climate Dynamic*, *15*, 583–593.

Fahey, T. J., J. B. Yavitt, R. E. Sherman, J. C. Maerz, P. M. Groffman, M. C. Fisk, and P. J. Bohlen (2013), Earthworms, litter and soil carbon in a northern hardwood forest, *Biogeochemistry*, *114*, 269–280, doi:10.1007/s10533-012-9808-y.

Falster, D. S., R. A. Duursma, M. I. Ishihara, D. R. Barneche, R. G. FitzJohn, A. Vårhammar, M. Aiba, M. Ando, N. Anten, M. J. Aspinwall, J. L. Baltzer, C. Baraloto, M. Battaglia, J. J. Battles, B. Bond-Lamberty, M. van Breugel, J. Camac, Y. Claveau, L. Coll, M. Dannoura, S. Delagrange, J.-C. Domec, F. Fatemi, W. Feng, V. Gargaglione, Y. Goto, A. Hagihara, J. S. Hall, S. Hamilton, D. Harja, T. Hiura, R. Holdaway, L. S. Hutley, T. Ichie, E. J. Jokela, A. Kantola, J. W. G. Kelly, T. Kenzo, D. King, B. D. Kloeppel, T. Kohyama, A. Komiyama, J.-P. Laclau, C. H. Lusk, D. A. Maguire, G. le Maire, A. Mäkelä, L. Markesteijn, J. Marshall, K. McCulloh, I. Miyata, K. Mokany, S. Mori, R. W. Myster, M. Nagano, S. L. Naidu, Y. Nouvellon, A. P. O'Grady, K. L. O'Hara, T. Ohtsuka, N. Osada, O. O. Osunkoya, P. L. Peri, A. M. Petritan, L. Poorter, A. Portsmuth, C. Potvin, J. Ransijn, D. Reid, S. C. Ribeiro, S. D. Roberts, R. Rodríguez, A. Saldaña Acosta, I. Santa-Regina, K. Sasa, N. G. Selaya, S. C. Sillett, F. Sterck, K. Takagi, T. Tange, H. Tanouchi, D. Tissue, T. Umehara, H. Utsugi, M. A. Vadeboncoeur, F. Valladares, P. Vanninen, J. R. Wang, E. Wenk, R. Williams, F. de Aquino Ximenes, A. Yamaba, T. Yamada, T. Yamakura, R. D. Yanai, and R. A. York (2015), Baad: a biomass and allometry database for woody plants., *Ecology*, *96*, 1445, doi: 10.1890/14-1889.1.

Farouki, O. T. (1981), The thermal properties of soils in cold regions, *Cold Regions Science and Technology*, *5*, 67–75.

Farquhar, G. D. (1989), Models of integrated photosynthesis of cells and leaves, *Philosophical Transactions of the Royal Society of London. Series B. Biological Sciences*, *323*, 357–367.

Farquhar, G. D., and S. C. Wong (1984), An empirical model of stomatal conductance, *Australian Journal of Plant Physiology*, *11*, 191–210.

Farquhar, G. D., S. V. Caemmerer, and J. A. Berry (1980), A biochemical model of photosynthetic CO_2 assimilation in leaves of C3 species, *Planta*, *149*, 78–90.

Farquhar, G. D., S. vonCaemmerer, and J. A. Berry (2001), Models of photosynthesis, *Plant Physiology*, *125*, 42–45.

Farrar, J., M. Hawes, D. Jones, and S. Lindow (2003), How roots control the flux of carbon to the rhizosphere, *Ecology*, *84*(4), 827–837.

Fatichi, S. (2010), The modeling of hydrological cycle and its interaction with vegetation in the framework of climate change, Ph.D. thesis, University of Firenze, Italy, and T.U. Braunschweig, Germany.

Fatichi, S., and S. Leuzinger (2013), Reconciling observations with modeling: the fate of water and carbon allocation in a mature deciduous forest exposed to elevated CO_2, *Agricultural and Forest Meteorology*, *174-175*, 144–157, doi:10.1016/j.agrformet.2013.02.005.

Fatichi, S., V. Y. Ivanov, and E. Caporali (2011), Simulation of future climate scenarios with a weather generator, *Advances in Water Resources*, *34*, 448–467, doi:10.1016/j.advwatres.2010.12.013.

Fatichi, S., V. Y. Ivanov, and E. Caporali (2012a), A mechanistic ecohydrological model to investigate complex interactions in cold and warm water-controlled environments. 1 Theoretical framework and plot-scale analysis, *Journal of Advances in Modeling Earth Systems*, *4*(M05002).

Fatichi, S., V. Y. Ivanov, and E. Caporali (2012b), A mechanistic ecohydrological model to investigate complex interactions in cold and warm water-controlled environments. 2. Spatiotemporal analyses, *Journal of Advances in Modeling Earth Systems*, *4*(M05003).

Fatichi, S., S. Leuzinger, and C. Körner (2014a), Moving beyond photosynthesis: from carbon source to sink-driven vegetation modeling, *New Phytologist*, *201*, 1086–1095, doi: 10.1111/nph.12614.

Fatichi, S., M. J. Zeeman, J. Fuhrer, and P. Burlando (2014b), Ecohydrological effects of management on subalpine grasslands: from local to catchment scale, *Water Resources Research*, *50*, doi:10.1002/2013WR014535.

Fatichi, S., S. Manzoni, D. Or, and A. Paschalis (2019), A mechanistic model of microbially mediated soil biogeochemical processes - a reality check., *Global Biogeochemical Cycles*, *33*(6), 620–648, doi.org/10.1029/2018GB006077.

Feddes, R. A., H. Hoff, M. Bruen, T. Dawson, P. de Rosnay, P. Dirmeyer, R. B. Jackson, P. Kabat, A. Kleidon, A. Lilly, and A. J. Pitmank (2001), Modeling root water uptake in hydrological and climate models, *Bulletin of the American Meteorological Society*, *82*(12), 2797–2809.

Fierer, N., and R. B. Jackson (2006), The diversity and biogeography of soil bacterial communities, *Proceedings of the National Academy of Sciences of the United States of America*, *103*(3), 626–631.

Fierer, N., M. S. Strickland, D. Liptzin, M. A. Bradford, and C. C. Cleveland (2009), Global patterns in belowground communities, *Ecology Letters*, *12*, 1238–1249, doi: 10.1111/j.1461-0248.2009.01360.x.

Finlay, R. D. (2008), Ecological aspects of mycorrhizal symbiosis: with special emphasis on the functional diversity of interactions involving the extraradical mycelium, *Journal of Experimental Botany*, *59*(5), 1115–1126.

Fisher, J. B., S. Sitch, Y. Malhi, R. A. Fisher, C. Huntingford, and S.-Y. Tan (2010), Carbon cost of plant nitrogen acquisition: a mechanistic, globally applicable model of plant nitrogen uptake, retranslocation, and fixation, *Global Biogeochemical Cycles*, *24*, GB1014.

Flerchinger, G. N., W. Xaio, D. Marks, T. J. Sauer, and Q. Yu (2009), Comparison of algorithms for incoming atmospheric long-wave radiation, *Water Resources Research*, *45*(W03423), doi:10.1029/2008WR007394.

Flexas, J., M. Ribas-Carbó, A. Dáaz-Espejo, J. Galmés, and H. Medrano (2008), Mesophyll conductance to co_2: Current knowledge and future prospects, *Plant, Cell and Environment*, *31*, 602–621.

Flexas, J., M. M. Barbour, O. Brendel, H. M. Cabrera, M. Carriqui, A. Dáaz-Espejo, C. Douthe, E. Dreyer, J. P. Ferrio, J. Gago, A. Gallé, J. Galmés, N. Kodama, H. Medrano, U. Niinemets, J. J. Peguero-Pina, A. Pou, M. T. Miquel Ribas-Carbó, T. Tosens, and C. R. Warren (2012), Mesophyll diffusion conductance to co_2: An unappreciated central player in photosynthesis, *Plant Science*, *193-194*, 70–84.

Foley, J. (1995), An equilibrium model of the terrestrial carbon budget, *Tellus B*, *47*, 310–319.

Foley, J., I. Prentice, N. Ramankutty, S. Levis, D. Pollard, S. Sitch, and A. Haxeltine (1996), An integrated biosphere model of land surface processes, terrestrial carbon balance, and vegetation dynamics, *Global Biogeochemical Cycles*, *10*, 603–628.

Foot, K., and R. P. C. Morgan (2005), The role of leaf inclination, leaf orientation and plant canopy architecture in soil particle detachment by raindrops, *Earth Surface Processes and Landforms*, *30*, 1509–1520, doi: 10.1002/esp.1207.

Forkel, M., N. Carvalhais, S. Schaphoff, W. v. Bloh, M. Migliavacca, M. Thurner, and K. Thonicke (2014), Identifying environmental controls on vegetation greenness phenology through model-data integration, *Biogeosciences*, *11*, 7025–7050.

Forsythe, G. E., M. A. Malcolm, and C. B. Moler (1976), *Computer Methods for Mathematical Computations*, Prentice-Hall.

Francipane, A., V. Y. Ivanov, L. V. Noto, E. Istanbulluoglu, E. Arnone, and R. L. Bras (2012), tRIBS-Erosion: A parsimonious physically-based model for studying catchment hydro-geomorphic response, *Catena*, *92*, 216–231, doi:10.1016/j.catena.2011.10.005.

Franklin, O., J. Johansson, R. C. Dewar, U. Dieckmann, R. E. McMurtrie, Å. Brännström, and R. Dybzinski (2012), Modeling carbon allocation in trees: a search for principles, *Tree Physiology*, *32*, 648–666, doi:10.1093/treephys/tpr138.

Freschet, G. T., R. Aerts, and J. H. C. Cornelissen (2012), A plant economics spectrum of litter decomposability, *Functional Ecology*, *26*, 56–65.

Friedlingstein, P., G. Joel, C. B. Field, and I. Fung (1998), Toward an allocation scheme for global terrestrial carbon models, *Global Change Biology*, *5*, 755–770.

Friend, A. D., and N. Y. Kiang (2005), Land-surface model development for the GISS GCM: Effects of improved canopy physiology on simulated climate, *Journal of Climate*, *18*, 2833–2902.

Friend, A. D., A. K. Stevens, R. G. Knox, and M. G. R. Cannell (1997), A process-based, terrestrial biosphere model of ecosystem dynamics (Hybrid v3.0), *Ecological Modelling*, *95*, 249–287.

Galloway, J. N., F. J. Dentener, D. G. Capone, E. W. Boyer, R. W. Howarth, S. P. Seitzinger, G. P. Asner, C. Cleveland, P. Green, E. Holland, D. M. Karl, A. F. Michaels, J. H. Porter, A. Townsend, and C. Vörösmarty. (2004), Nitrogen cycles:ast, present and future, *Biogeochemistry*, *70*, 153–226.

Gao, Q., P. Xhao, X. Zeng, X. Cai, and W. Shen (2002), A model of stomatal conductance to quantify the relationship between leaf transpiration, microclimate, and soil water stress, *Plant, Cell and Environment*, *25*, 1373–1381.

Gardner, A. S., and M. J. Sharp (2010), A review of snow and ice albedo and the development of a new physically based broadband albedo parameterization, *Journal of Geophysical Research*, *115*(F01009), doi:10.1029/2009JF001444.

Garratt, J. R. (1992), *The Atmospheric Boundary Layer*, Cambridge University Press.

Garrote, L., and R. L. Bras (1995), A distributed model for real-time flood casting using digital elevation models, *Journal of Hydrology*, *167*, 279–306.

Gelfan, A. N., J. W. Pomeroy, and L. S. Kuchment (2004), Modeling forest cover influences on snow accumulation, sublimation, and melt, *Journal of Hydrometeorology*, *5*, 785–803.

Gerrits, A. M. J., H. H. G. Savenije, L. Hoffmann, and L. Pfister (2007), New technique to measure forest floor interception - an application in a beech forest in Luxembourg, *Hydrology and Earth System Science*, *11*, 695–701.

Gill, R. A., and R. B. Jackson (2000), Global patterns of root turnover for terrestrial ecosystems, *New Phytologist*, *147*, 13–31.

Goudriaan, J. (1977), Crop micrometeorology: A simulation study, *Tech. rep.*, Wageningen Center for Agricultural Publishing and Documentation.

Gough, C. M., C. E. Flower, C. S. Vogel, D. Dragoni, and P. S. Curtis (2009), Whole-ecosystem labile carbon production in a north temperate deciduous forest, *Agricultural and Forest Meteorology*, *149*, 1531–1540, doi:10.1016/j.agrformet.2009.04.006.

Gough, C. M., C. E. Flower, C. S. Vogel, and P. S. Curtis (2010), Phenological and temperature controls on the temporal non-structural carbohydrate dynamics of Populus grandidentata and Quercus rubra, *Forests*, *1*, 65–81, doi:10.3390/f1010065.

Grachev, A. A., E. L. Andreas, C. W. Fairall, P. S. Guest, and P. O. G. Persson (2007), On the turbulent Prandtl number in the stable atmospheric boundary layer, *Boundary-Layer Meteorology*, *125*, 329–341, doi: 10.1007/s10546-007-9192-7.

Grimaldi, S., F. Nardi, B. F. Di, E. Istanbulluoglu, and R. L. Bras (2007), A physically-based method for removing pits in digital elevation models, *Advances in Water Resources*, *30*, 2151–2158, doi:10.1016/j.advwatres.2006.11.016.

Gruber, S. (2007), A mass-conserving fast algorithm to parameterize gravitational transport and deposition using digital elevation models, *Water Resour. Res.*, *43*(W06412), doi:10.1029/2006WR004868.

Gueymard, C. A. (2008), REST2: High-performance solar radiation model for cloudless-sky irradiance illuminance and photosynthetically active radiation - validation with a bechmark dataset, *Solar Energy*, *82*, 272–285.

Gumiere, S. J., Y. Le Bissonnais, and D. Raclot (2009), Soil resistance to interrill erosion: Model parameterization and sensitivity, *Catena*, *77*, 274–284, doi:10.1016/j.catena.2009.02.007.

Guswa, A. J., M. A. Celia, and I. Rodriguez-Iturbe (2002), Models of soil moisture dynamics in ecohydrology: A comparative study, *Water Resources Research*, *38*(9), doi:10.1029/2001WR000826.

Haghighi, E., E. Shahraeeni, P. Lehmann, and D. Or (2013), Evaporation rates across a convective air boundary layer are dominated by diffusion, *Water Resour. Res.*, *49*, 1602–1610, doi:10.1002/wrcr.20166.

Hanan, N. P. (2001), Enhanced two-layer radiative transfer scheme for a land surface model with a discontinuous upper canopy, *Agricultural and Forest Meteorology*, *109*, 265–281.

Hansen, J., and E. Beck (1990), The fate and path of assimilation products in stem of 8-year-old Scots pine (Pinus sylvestris L.) trees, *Trees*, *4*, 16–21.

Hanson, C. A., S. D. Allison, M. A. Bradford, M. D. Wallenstein, and K. K. Treseder (2008), Fungal taxa target different carbon sources in forest soil, *Ecosystems*, *11*(7), 1157–1167.

Hassink, J., and A. P. Whitmore (1997), A model of the physical protection of organic matter in soils, *Soil Sci. Soc. Am. J.*, *61*, 131–139.

Hawkes, C. (2000), Woody plant mortality algorithms: description, problems and progress, *Ecological Modelling*, *126*, 225–248.

Haxeltine, A., and I. C. Prentice (1996), BIOME3: An equilibrium terrestrial biosphere model based on ecophysiological constraints, resource availability, and competition among plant functional types, *Global Biogeochemical Cycles*, *10*(4), 693–709.

Haynes, R. J. (1990), Active ion uptake and maintenance of cation-anion balance: A critical examination of their role in regulating rhizosphere pH, *Plant and Soil*, *126*(2), 247–264.

He, W., and T. Kobayashi (1998), A rational parameterization of evaporation from dry, bare soil, *Journal of the Meteorological Society of Japan*, *76*(6), 955–963.

Hedstrom, N. R., and J. W. Pomeroy (1998), Measurements and modelling of snow interception in the boreal forest, *Hydrological Processes*, *12*, 1611–1625.

Hillel, D. (1998), *Environmental Soil Physics: Fundamentals, Applications, and Environmental Considerations*, Academic Press, London, UK.

Hinsinger, P., A. Brauman, N. Devau, F. Gérard, C. Jourdan, J.-P. Laclau, E. L. Cadre, B. Jaillard, and C. Plassard (2011), Acquisition of phosphorus and other poorly mobile nutrients by roots. Where do plant nutrition models fail?, *Plant Soil*, *348*, 29–61, doi:10.1007/s11104-011-0903-y.

Hoch, G., A. Richter, and C. Körner (2003), Non-structural carbon compounds in temperate forest trees, *Plant, Cell and Environment*, *26*, 1067–1081.

Hölttä, T., H. Cochard, E. Nikinmaa, and M. Mencuccini (2009), Capacitive effect of cavitation in xylem conduits: results from a dynamic model, *Plant, Cell & Environment*, *32*, 10–21.

Horton, R. E. (1919), Rainfall interception, *Monthly Weather Review*, *47*(9), 603–623.

Houlton, B. Z., S. L. Morford, and R. A. Dahlgren (2018), Convergent evidence for widespread rock nitrogen sources in Earth's surface environment, *Science*, *360*(6384), 58–62.

Hsiao, T. C. (1973), Plant responses to water stress, *Annu. Rev. Plant Physiol.*, *24*, 519–570.

Hu, Z., and S. Islam (1995), Prediction of ground surface temperature and soil moisture content by the force restore-method, *Water Resources Research*, *31*(10), 2531–2539.

Huete, A. R., K. Didan, Y. E. Shimabukuro, P. Ratana, S. R. Saleska, L. R. Hutyra, W. Yang, R. R. Nemani, and R. Myneni (2006), Amazon rainforests green-up with sunlight in dry season, *Geophysical research letters*, *33*(6).

Idso, S. B. (1981), A set of equations for full spectrum and 8- to 14-μm and 10.5- to 12.5 μm thermal radiation from cloudless skies, *Water Resources Research*, *17*(2), 295–304.

Ivanov, V. Y. (2006), Effects of dynamic vegetation and topography on hydrological processes in semi-arid areas, Ph.D. thesis, Department of Civil and Environmental Engineering, Massachusetts Institute of Technology.

Ivanov, V. Y., E. R. Vivoni, R. L. Bras, and D. Entekhabi (2004), Catchment hydrologic response with a fully-distributed triangulated irregular network model, *Water Resources Research*, *40*(11), W11,102, doi:10.1029/2004WR003218.

Ivanov, V. Y., R. L. Bras, and E. R. Vivoni (2008a), Vegetation-hydrology dynamics in complex terrain of semiarid areas: 1. A mechanistic approach to modeling dynamic feedbacks, *Water Resources Research*, *44*(W03429), doi:10.1029/2006WR005588.

Ivanov, V. Y., R. L. Bras, and E. R. Vivoni (2008b), Vegetation-hydrology dynamics in complex terrain of semiarid areas: 1. A mechanistic approach to modeling dynamic feedbacks, *Water Resources Research*, *44*(W03429), doi:10.1029/2006WR005588.

Ivanov, V. Y., R. L. Bras, and E. R. Vivoni (2008c), Vegetation-hydrology dynamics in complex terrain of semiarid areas: 2. Energy-water controls of vegetation spatiotemporal dynamics and topographic niches of favorability, *Water Resources Research*, *44*(W03430), doi:10.1029/2006WR005595.

Iziomon, M. G., H. Mayer, and A. Matzarakis (2003), Downward atmospheric longwave irradiance under clear and cloudy skies: Measurement and parameterization, *Journal of Atmospheric and Solar-Terrestrial Physics*, *65*, 1107–1116, doi:10.1016/j.jastp.2003.07.007.

Jackson, R. B., J. Canadell, J. R. Ehleringer, H. A. Mooney, O. E. Sala, and E. D. Schulze (1996), A global analysis of root distributions for terrestrial biomes, *Oecologia*, *108*(3), 389–411.

Jackson, R. B., H. A. Mooney, and E. D. Schulze (1997), A global budget for fine root biomass, surface area, and nutrient contents, *Proc. Natl. Acad. Sci. USA*, *94*, 7362–7366.

Jarvis, A. J., and W. J. Davies (1998), The coupled response of stomatal conductance to photosynthesis and transpiration, *Journal of Experimental Botany*, *49*, 399–406.

Javaux, M., T. Schröder, J. Vanderborght, and H. Vereecken (2008), Use of a three-dimensional detailed modeling approach for predicting root water uptake, *Vadose Zone Journal*, *7*(3), 1079–1088, doi:10.2136/vzj2007.0115.

Johnson, N. C., C. Angelard, I. R. Sanders, and E. T. Kiers (2013), Predicting community and ecosystem outcomes of mycorrhizal responses to global change, *Ecology Letters*, *16*, 140–153, doi: 10.1111/ele.12085.

Jones, H. G. (1983), *Plants and Microclimate*, Cambridge University Press, New York.

Jones, H. G. (1998), Stomatal control of photosynthesis and transpiration, *Journal of Experimental Botany*, *49*, 387–398.

Jungk, A. O. (2002), *Plant roots: the hidden half*, chap. Dynamics of nutrient movement at the soil-root interface, pp. 587–616, Marcel Dekker Inc., New York.

Juszak, I., and F. Pellicciotti (2013), A comparison of parameterizations of incoming longwave radiation over melting glaciers: Model robustness and seasonal variability, *Journal of Geophysical Research*, *118*, 3066–3084, doi:10.1002/jgrd.50277.

Kaduk, J., and M. Heimann (1996), A prognostic phenology scheme for global terrestrial carbon cycle models, *Climate Research*, *5*, 1–19.

Kampf, S. K., and S. J. Burges (2007), A framework for classifying and comparing distributed hillslope and catchment hydrologic models, *Water Resources Research*, *43*(W05423), doi:10.1029/2006WR005370.

Kamphorst, E., V. G. Jetten, J. Guerif, J. Pitkanen, B. Iversen, J. Douglas, and A. Paz (2000), Predicting depressional storage from soil surface roughness, *Soil Science Society of America Journal*, *64*, 1749–1758.

Kattge, J., and W. Knorr (2007), Temperature acclimation in a biochemical model of photosynthesis: a reanalysis of data from 36 species, *Plant, Cell and Environment*, *30*, 1176–1190, doi: 10.1111/j.1365-3040.2007.01690.x.

Kattge, J., W. Knorr, T. Raddatz, and C. Wirth (2009), Quantifying photosynthetic capacity and its relationship to leaf nitrogen content for global-scale terrestrial biosphere models, *Global Change Biology*, *15*, 976–991, doi: 10.1111/j.1365-2486.2008.01744.x.

Katul, G. G., R. Leuning, and R. Oren (2003), Relationship between plant hydraulic and biochemical properties derived from a steady-state coupled water and carbon transport model, *Plant, Cell and Environment*, *26*, 339–350.

Keeling, H. C., and O. L. Phillips (2007), The global relationship between forest productivity and biomass, *Global Ecology and Biogeography*, *16*, 618–631.

Keith, H., B. G. Mackey, and D. B. Lindenmayer (2009), Re-evaluation of forest biomass carbon stocks and lessons from the world's most carbon-dense forests, *Proceedings of the National Academy of Sciences of the United States of America*, *106*(28), 11,635–11,640.

Khanna, J., and D. Medvigy (2014), Strong control of surface roughness variations on the simulated dry season regional atmospheric response to contemporary deforestation in Rondônia, Brazil, *Journal of Geophysical Research, Atmos.*, *119*, 13,067–13,078, doi:10.1002/2014JD022278.

Kirkham, M. B. (2005), *Principles of soil and plant water relations*, Elsevier Academic Press.

Kirschbaum, M. F. (199), CenW, a forest growth model with linked carbon, energy, nutrient and water cycles, *Ecological Modelling*, *118*, 17–59.

Kirschbaum, M. U. F., and K. I. Paul (2002), Modelling C and N dynamics in forest soils with a modified version of the CENTURY model, *Soil Biology & Biochemistry*, *34*, 341–354.

Knorr, W. (2000), Annual and interannual CO_2 exchanges of the terrestrial biosphere: Process based simulations and uncertainties, *Global Ecology and Biogeography*, *9*, 225–252.

Kobe, R. K. (1997), Carbohydrate allocation to storage as a basis of interspecific variation in sapling survivorship and growth, *Oikos*, *80*(2), 226–233.

Koch, G. W., S. C. Sillett, G. M. Jennings, and S. D. Davis (2004), The limits to tree height, *Nature*, *428*, 851–854.

Kögel-Knabner, I. (2002), The macromolecular organic composition of plant and microbial residues as inputs to soil organic matter, *Soil Biology and Biochemistry*, *34*, 139–162.

Koide, R. T., J. N. Sharda, J. R. Herr, and G. M. Malcolm (2008), Ectomycorrhizal fungi and the biotrophy-saprotrophy continuum., *New Phytologist*, *178*, 230–233.

Kollet, S. J., and R. M. Maxwell (2006), Integrated surface-groundwater flow modeling: A free-surface overland flow boundary condition in a parallel groundwater flow model, *Advances in Water Resources*, *29*, 945–958.

Kollet, S. J., and R. M. Maxwell (2008), Capturing the influence of groundwater dynamics on land surface processes using an integrated, distributed watershed model, *Water Resources Research*, *44*, doi:10.1029/2007WR006004.

Kondo, J., and S. Ishida (1997), Sensible heat flux from the Earth's surface under natural convective conditions, *Journal of the Atmospheric Sciences*, *54*, 498–509.

Kondo, J., N. Saigusa, and T. Sato (1990), A parametrization of evaporation from bare soil surfaces, *Journal of Applied Meteorology*, *29*, 385–389.

Kondo, J., A. Yanagihara, and N. Saigusa (1993), An experimental study on evaporation parameters of soil, *Tenki*, *40*, 11–17, in Japanese.

Körner, C. (2003), Carbon limitation in trees, *Journal of Ecology*, *91*, 4–17.

Körner, C. (2008), Winter crop growth at low temperature may hold the answer for alpine treeline formation, *Plant Ecol. Divers.*, *1*, 3–11.

Körner, C. (2015), Paradigm shift in plant growth control, *Current Opinion in Plant Biology*, *25*, 107–114.

Körner, C., and D. Basler (2010), Phenology under global warming, *Science*, *327*, 1461–1462, doi:10.1126/science.1186473.

Kot, S. C., and Y. Song (1998), An improvement of the louis scheme for the surface layer in an atmopsheric modelling system, *Boundary-Layer Meteorology*, *88*, 239–254.

Koven, C. D., W. J. Riley, Z. M. Subin, J. Y. Tang, M. S. Torn, W. D. Collins, G. B. Bonan, D. M. Lawrence, and S. C. Swenson (2013), The effect of vertically resolved soil biogeochemistry and alternate soil C and N models on C dynamics of CLM4, *Biogeosciences*, *10*, 7109–7131.

Kozlowski, T. T., and S. G. Pallardy (1997), *Physiology of Woody Plants*, Academic Press.

Kozlowski, T. T., and S. G. Pallardy (2002), Acclimation and adaptive responses of woody plants to environmental stresses, *The Botanical Review*, *68*(2), 270–334.

Krinner, G., N. Viovy, N. de Noblet-Ducoudre, J. Ogee, J. Polcher, P. Friedlingstein, P. Ciais, S. Sitch, and I. C. Prentice (2005), A dynamic global vegetation model for studies of the coupled atmosphere-biosphere system, *Global Biogeochemical Cycles*, *19*(GB1015), doi:10.1029/2003GB002199.

Kucharik, C., J. Foley, C. Delire, V. Fisher, M. Coe, J. Lenters, C. Young-Molling, N. Ramankutty, J. Norman, and S. Gower (2000), Testing the performance of a dynamic global ecosystem model: Water balance, carbon balance, and vegetation structure, *Global Biogeochemical Cycles*, *14*, 795–825.

Kumar, L., A. K. Skidmore, and E. Knowles (1997), Modeling topographic variation in solar radiation in a GIS environment, *International Journal of Geographic Information Science*, *11*, 475–497.

Laio, F., A. Porporato, L. Ridolfi, and I. Rodriguez-Iturbe. (2001), Plants in water-controlled ecosystems: active role in hydrological processes and response to water stress. II. Probabilistic soil moisture dynamics, *Advances in Water Resources*, *24*, 707–723.

Lambers, H., I. F. S. Chapin, and T. L. Pons (1998), *Plant Physiological Ecology*, Springer, New York.

Larcher, W. (2001), *Physiological Plant Ecology*, 4th ed., Springer, New York.

Launiainen, J. (1995), Derivation of the relationship between the Obukhov stability parameter and the bulk Richardson number for flux-profile studies, *Boundary-Layer Meteorology*, *76*, 165–179.

Lawrence, C. R., J. C. Neff, and J. P. Schimel (2009), Does adding microbial mechanisms of decomposition improve soil organic matter models? A comparison of four models using data from a pulsed rewetting experiment, *Soil Biology and Biochemistry*, *41*, 1923–1934.

Lazzarotto, P., P. Calanca, and J. Fuhrer (2009), Dynamics of grass-clover mixtures-An analysis of the response to management with the PROductive GRASsland simulator (PROGRASS), *Ecological Modelling*, *220*, 703–724.

Lee, H. S., C. J. Matthews, R. D. Braddock, G. C. Sander, and F. Gandola (2004), A MATLAB method of lines template for transport equations, *Environmental Modelling & Software*, *19*, 603–614, doi:10.1016/j.envsoft.2003.08.017.

Lee, J.-E., C. Frankenberg, v. d. T. Christiaan, J. A. Berry, L. Guanter, C. K. Boyce, J. B. Fisher, E. Morrow, J. R. Worden, S. Asefi, G. Badgley, and S. Saatchi (2013), Forest productivity and water stress in Amazonia: observations from GOSAT chlorophyll fluorescence, *roceedings of the Royal Society B: Biological Sciences*, *280*, 1761, doi:10.1098/rspb.2013.0171.

Lee, J.-E., J. A. Berry, C. van der Tol, X. Yang, L. Guanter, A. Damm, I. Baker, and C. Frankenberg (2015), Simulations of chlorophyll fluorescence incorporated into the Community Land Model version 4, *Global Change Biology*, *21*, 3469–3477, doi: 10.1111/gcb.12948.

Lee, T. J., and R. A. Pielke (1992), Estimating the soil surface specific humidity, *J. Appl. Meteorol*, *31*, 480–484.

Lee, Y.-H., and L. Mahrt (2004), An evaluation of snowmelt and sublimation over short vegetation in land surface modelling, *Hydrological Processes*, *18*, 3543–3557, doi: 10.1002/hyp.5799.

LeRoux, X., A. Lacointe, A. Escobar-Gutiérrez, and S. LeDizès (2001), Carbon-based models of individual tree growth: A critical appraisal, *Annals of Forest Science*, *58*, 459–506.

Leuning, R. (1990), Modelling stomatal behaviour and photosynthesis of eucalyptus grandis, *Australian Journal of Plant Physiology*, *17*, 159–175.

Leuning, R. (1995), A critical appraisal of a combined stomatal- photosynthesis model for C3 plants, *Plant, Cell and Environment*, *18*, 357–364.

Leuning, R., F. M. Kelliher, D. G. G. Pury, and E.-D. Schulze (1995), Leaf nitrogen, photosynthesis, conductance and transpiration: Scaling from leaves to canopies, *Plant, Cell and Environment*, (18), 1183–1200.

Levis, S., G. B. Bonan, M. Vertenstein, and K. W. Oleson (2004), The Community Land Model's Dynamic Global Vegetation Model (CLMDGVM): Technical description and user's guide, *Tech. note*, NCAR/TN-459+IA, Natl. Cent. for Atmos. Res., Boulder, Colorado.

Lhomme, J. P. (2001), Stomatal control of transpiration: Examination of the Jarvis-type representation of canopy resistance in relation to humidity, *Water Resources Research*, *37*, 689–699.

Li, J., G. Wang, S. D. Allison, M. A. Mayes, and Y. Luo (2014), Soil carbon sensitivity to temperature and carbon use efficiency compared across microbial-ecosystem models of varying complexity, *Biogeochemistry*, *119*, 67–84, doi:10.1007/s10533-013-9948-8.

Liebethal, C., and T. Foken (2007), Evaluation of six parameterization approaches for the ground heat flux, *Theoretical and Applied Climatology*, *88*(43-56), doi: 10.1007/s00704-005-0234-0.

Lin, J. D. (1980), On the force-restore method for prediction of ground surface temperature, *Journal of Geophysical Research*, *85*, 3251–3254.

Lindahl, B. D., and A. Tunlid (2015), Ectomycorrhizal fungi - potential organic matter decomposers, yet not saprotrophs, *New Phytologist*, *205*(4), 1443–1447, doi: 10.1111/nph.13201.

Link, T. E., M. Unsworth, and D. Marks (2004), The dynamics of rainfall interception by a seasonal temperate rainforest, *Agricultural and Forest Meteorology*, *124*, 171–191, doi:10.1016/j.agrformet.2004.01.010.

Lischke, H., N. E. Zimmermann, J. Bolliger, S. Rickebusch, and T. J. Löffler (2006), Treemig: A forest-landscape model for simulating spatio-temporal patterns from stand to landscape scale, *Ecological Modelling*, *199*, 409–420, doi:10.1016/j.ecolmodel.2005.11.046.

Liston, G. E., and K. Elder (2006), A distributed snow-evolution modeling system (SnowModel), *Journal of Hydrometeorology*, *7*, 1259–1276.

Litton, C. M., J. W. Raich, and M. G. Ryan (2007), Carbon allocation in forest ecosystems, *Global Change Biology*, *13*, 2089–2109, doi: 10.1111/j.1365-2486.2007.01420.x.

Liu, Q., S. Piao, Y. H. Fu, M. Gao, J. Penuelas, and I. A. Janssens (2019), Climatic warming increases spatial synchrony in spring vegetation phenology across the Northern Hemisphere, *Geophysical Research Letters*, *46*, 1641–1650, doi:10.1029/2018GL081370.

Liu, S., L. Lu, D. Mao, and L. Jia (2007), Evaluating parameterizations of aerodynamic resistance to heat transfer using field measurements, *Hydrology and Earth System Science*, *11*, 769–783.

Lockhart, J. A. (1965), An analysis of irreversible plant cell elongation, *Journal of Theoretical Biology*, *8*, 264–275.

LoSeen, D., A. Chehbouni, E. Njoku, S. Saatchi, E. Mougin, and B. Monteny (1997), An approach to couple vegetation functioning and soil-vegetation-atmopshere-transfer models for semiarid grasslands during the HAPEX-Sahel experiment, *Agricultural and Forest Meteorology*, *83*, 49–74.

Louis, J.-F. (1979), A parametric model of the vertical eddy fluxes in the atmosphere, *Boundary-Layer Meteorology*, *17*, 187–202.

Louis, J.-F., M. Tiedtke, and J. F. Geleyn (1982), A short history of the operational PBL parameterization of ECMWF, in *Workshop on Planetary Boundary Layer Parameterization*, pp. 59–79, Shinfield Park, Reading, Berkshire, UK, European Centre for Medium Range Weather Forecasts.

Lubbers, I. M., K. J. van Groenigen, S. J. Fonte, J. Six, L. Brussaard, and J. W. van Groenigen (2013), Greenhouse-gas emissions from soils increased by earthworms, *Nature Climate Change*, *3*, 187–194, doi:10.1038/nclimate1692.

Lüdeke, M. K. B., F.-W. Badeck, R. D. Otto, C. Häger, S. Dönges, J. Kindermann, G. Würth, T. Lang, U. Jäkel, A. Klaudius, P. Ramge, S. Habermehl, and G. H. Kohlmaier (1994), The Frankfurt biosphere model: A global process-oriented model of seasonal and long-term CO_2 exchange between terrestrial ecosystems and the atmosphere. I. Model description and illustrative results for cold deciduous and boreal forests, *Climate Research*, *4*(2), 143–166.

Lundquist, J. D., S. E. Dickerson-Lange, J. A. Lutz, and N. C. Cristea (2013), Lower forest density enhances snow retention in regions with warmer winters: A global framework developed from plot-scale observations and modeling, *Water Resources Research*, *49*(10), 6356–6370, doi:10.1002/wrcr.20504.

Madsen, M. D., D. G. Chandler, and J. Belnap (2008), Spatial gradients in ecohydrologic properties within a pinyon-juniper ecosystem, *Ecohydrology*, *1*, 349–360, doi: 10.1002/eco.29.

Magill, A. H., J. D. Aber, W. S. Currie, K. J. Nadelhoffer, M. E. Martin, W. H. McDowell, J. M. Melillo, and P. Steudler (2004), Ecosystem response to 15 years of chronic nitrogen additions at the Harvard Forest LTER, Massachusetts, USA, *Forest Ecology and Management*, *196*, 7–28.

Mahat, V., D. G. Tarboton, and N. P. Molotch (2013), Testing above- and below-canopy representations of turbulent fluxes in an energy balance snowmelt model, *Water Resources Research*, *49*, 1107–1122, doi:10.1002/wrcr.20073.

Mahfouf, J.-F., and B. Jacquemin (1989), A study of rainfall interception using a land surface parameterization for mesoscale meteorological models, *Journal of Applied Meteorology*, *28*, 1282–1302.

Mahfouf, J.-F., and J. Noilhan (1991), Comparative study of various formulations from bare soil using in situ data, *Journal of Applied Meteorology*, *30*, 1354–1365.

Mahowald, N., T. D. Jickells, A. R. Baker, P. Artaxo, C. R. Benitez-Nelson, G. Bergametti, T. C. Bond, Y. Chen, D. D. Cohen, B. Herut, N. Kubilay, R. Losno, C. Luo, W. Maenhaut, K. A. McGee, G. S. Okin, R. L. Siefert, and S. Tsukud (2008), Global distribution of atmospheric phosphorus sources, concentrations and deposition rates, and anthropogenic impacts, *Global Biogeochem. Cycles*, *22*, GB4026, doi:10.1029/2008GB003240.

Mäkelä, A. (2012), On guiding principles for carbon allocation in eco-physiological growth models, *Tree Physiology*, *32*, 644–647, doi:10.1093/treephys/tps033.

Manoli, G., V. Y. Ivanov, and S. Fatichi (2018), Dry season greening and water stress in amazonia: the role of modeling leaf phenology, *Journal of Geophysical Research-Biogeosciences*, *123*, 1909–1926, doi:10.1029/2017JG004282.

Manusch, C., H. Bugmann, C. Heiri, and A. Wolf (2012), Tree mortality in dynamic vegetation models - a key feature for accurately simulating forest properties, *Ecological Modelling*, *243*, 101–111.

Manzoni, S. (2017), Flexible carbon-use efficiency across litter types and during decomposition partly compensates nutrient imbalances-results from analytical stoichiometric models, *Front Microbiol.*, *8*(661), doi:10.3389/fmicb.2017.00661.

Manzoni, S., and A. Porporato (2009), Soil carbon and nitrogen mineralization: Theory and models across scales, *Soil Biology & Biochemistry*, *41*, 1355–1379, doi:10.1016/j.soilbio.2009.02.031.

Manzoni, S., R. B. Jackson, J. A. Trofymow, and A. Porporato (2008), The global stoichiometry of litter nitrogen mineralization, *Science*, *321*(684-686), 89–106.

Manzoni, S., J. A. Trofymow, R. B. Jackson, and A. Porporato (2010), Stoichiometric controls on carbon, nitrogen, and phosphorus dynamics in decomposing litter, *Ecological Monographs*, *80*(1), 89–106.

Manzoni, S., J. P. Schimel, and A. Porporato (2012), Responses of soil microbial communities to water stress: results from a meta-analysis, *Ecology*, *93*, 930–938.

Manzoni, S., G. Vico, G. Katul, S. Palmroth, and A. Porporato (2014), Optimal plant water-use strategies under stochastic rainfall, *Water Resources Research*, *50*, 5379–5394, doi:10.1002/2014WR015375.

Manzoni, S., F. Moyano, T. Kätterer, and J. Schimel (2016), Modeling coupled enzymatic and solute transport controls on decomposition in drying soils, *Soil Biology & Biochemistry*, *95*, 275–287.

Marks, D., J. Domingo, D. Susong, T. Link, and D. Garen (1999), A spatially distributed energy balance snowmelt model for application in mountain basins, *Hydrological Processes*, *13*, 1935–1959.

Marschner, H., and B. Dell (1994), Nutrient uptake in mycorrhizai symbiosis, *Plant and Soil*, *159*, 89–102.

Marshall, I. S., and W. M. Palmer (1948), Relation of raindrop size to intensity, *Journal of Meteorology*, *5*, 165–166.

Martin, N., and S. M. Gorelick (2005), MOD_FreeSurf2D: A MATLAB surface fluid flow model for rivers and streams, *Computers & Geosciences*, *31*, 929–946, doi:10.1016/j.cageo.2005.03.004.

Mascart, P., J. Noilhan, and H. Giordani (1995), A modified parameterization of flux-profile relationships in the surface layer using different roughness lengthvalues for heat and momentum, *Boundary-Layer Meteorology*, *72*, 331–334.

Massman, W. J. (1997), An analytical one-dimensional model of momentum transfer by vegetation of arbitrary structure, *Boundary-Layer Meteorology*, *83*, 407–421.

Maxwell, R. M., and S. J. Kollet (2008), Quantifying the effects of three-dimensional subsurface heterogeneity on hortonian runoff processes using a coupled numerical, stochastic approach, *Advances in Water Resources*, *31*, 807–817, doi:10.1016/j.advwatres.2008.01.020.

Mayr, T., and N. J. Jarvis (1999), Pedotransfer functions to estimate soil water retention parameters for a modified Brooks-Corey type model, *Geoderma*, *91*, 1–9.

McCree, K. J. (1970), An equation for the rate of respiration of white clover plants grown under controlled conditions, in *Proceedings of the technical meeting IBP, Trebon (CSK), 1969*, edited by C. for Agricultural Publishing and N. Documentation, Wageningen, pp. 221–229.

McDowell, N., W. Pockman, C. Allen, D. D. Breshears, N. Cobb, T. Kolb, J. Sperry, A. West, D. Williams, and E. Yepez (2008), Mechanisms of plant survival and mortality during drought: Why do some plants survive while others succumb to drought?, *New Phytologist*, *178*, 719–739, doi:10D1111/j.1469-8137D2008D02436.x.

McGroddy, M. E., T. Daufresne, and L. O. Hedin (2004), Scaling of C:N:P stoichiometry in forests worldwide: implications of terrestrial redfield-type ratios, *Ecology*, *85*, 2390–2401.

Medvigy, D., S. C. Wofsy, J. W. Munger, D. Y. Hollinger, and P. R. Moorcroft (2009), Mechanistic scaling of ecosystem function and dynamics in space and time: Ecosystem Demography model version 2, *Journal of Geophysical Research*, *114*(G01002), doi:10.1029/2008JG000812.

Melloh, R. A., J. P. Hardy, R. N. Bailey, and T. J. Hall (2002), An efficient snow albedo model for the open and sub-canopy, *Hydrological Processes*, *16*, 3571–3584, doi: 10.1002/hyp.1229.

Menge, D. N. L., S. A. Levin, and L. O. Hedin (2009), Facultative versus obligate nitrogen fixation strategies and their ecosystem consequences, *The American Naturalist*, *174*(4).

Mengelkamp, H.-T., K. Warrach, and E. Raschke (1999), SEWAB - a parameterization of the surface energy and water balance for atmospheric and hydrologic models, *Advances in Water Resources*, *23*, 165–175.

Meyerholt, J., and S. Zaehle (2015), The role of stoichiometric flexibility in modelling forest ecosystem responses to nitrogen fertilization, *New Phytologist*, *208*, 1042–1055, doi: 10.1111/nph.13547.

Michaletz, S. T., D. Cheng, A. J. Kerkhoff, and B. J. Enquist (2014), Convergence of terrestrial plant production across global climate gradients, *Nature*, *512*, 39–43.

Millard, P., and G.-A. Grelet (2010), Nitrogen storage and remobilization by trees: ecophysiological relevance in a changing world, *Tree Physiology*, *30*, 1083–1095, doi:10.1093/treephys/tpq042.

Miller, C. T., C. Abhishek, and M. W. Farthing (2006), A spatially and temporally adaptive solution of Richards' equation, *Advances in Water Resources*, *29*, 525–545, doi:10.1016/j.advwatres.2005.06.008.

Mölders, N., H. Luijting, and K. Sassen (2008), Use of atmospheric radiation measurement program data from Barrow, Alaska, for evaluation and development of snow-albedo parameterizations, *Meteorology and Atmopheric Physics*, *99*, 199–219, doi: 10.1007/s00703-007-0271-6.

Monin, A. S., and A. M. Obukhov (1954), Dimensionless characteristics of turbulence in the surface layer of the atmosphere, *Trudy Geofiz. Inst. Akad. Nauk. SSSR*, *24*, 163–187, (In Russian).

Monsi, M., and T. Saeki (2005), On the factor light in plant communities and its importance for matter production, *Annals of Botany*, *95*, 549–567, originally published in German in Japanese Journal of Botany 14, 22-52, 1953.

Montaldo, N., R. Rondena, J. D. Albertson, and M. Mancini (2005), Parsimonious modeling of vegetation dynamics for ecohydrologic studies of water-limited ecosystems, *Water Resources Research*, *41*(W10416), doi:10.1029/2005WR004094.

Montaldo, N., J. D. Albertson, and M. Mancini (2008), Vegetation dynamics and soil water balance in a water-limited Mediterranean ecosystem on Sardinia, Italy, *Hydrology and Earth System Sciences*, *12*, 1257–1271.

Monteith, J. L. (1973), *Principles of Environmental Physics*, Edward Arnold, London.

Montgomery, D. R., and W. E. Dietrich (1988), Where do channels begin?, *Nature*, *336*, 232–234.

Montgomery, D. R., and W. E. Dietrich (1989), Source areas, drainage density, and channel initiation, *Water Resources Research*, *25*, 1907–1918.

Moorhead, D. L., and R. L. Sinsabaugh (2006), A theoretical model of litter decay and microbial interaction, *Ecological Monographs*, *76*, 151–174.

Mooshammer, M., W. Wanek, S. Zechmeister-Boltenstern, and A. Richter. (2014), Stoichiometric imbalances between terrestrial decomposer communities and their resources: mechanisms and implications of microbial adaptations to their resources, *Frontiers in Microbiology*, *5*(22), 1–10.

Morgan, R. P. C. (2001), A simple approach to soil loss prediction: a revised Morgan-Morgan-Finney model, *Catena*, *44*, 305–322.

Morgan, R. P. C., J. N. Quinton, R. E. Smith, G. Govers, J. W. A. Poesen, K. Auerswald, G. Chisci, D. Torri, and M. E. Styczen (1998), The european soil erosion model (EUROSEM): a dynamic approach for predicting sediment transport from fields and small catchments, *Earth Surface Processes and Landforms*, *23*, 527–544.

Morin, J., R. Karen, Y. Benjamini, M. Ben-Hur, and I. Shainberg (1989), Water infiltration as affected by soil crust and moisture profile, *Soil Science*, *148*, 53–59.

Mott, K. A. (1988), Do stomata respond to CO_2 concentrations other than intercellular?, *Plant Physiology*, *86*, 200–203.

Mouginot, C., R. Kawamura, K. L. Matulich, R. Berlemont, S. D. Allison, A. S. Amend, and A. C. Martiny (2014), Elemental stoichiometry of fungi and bacteria strains from grassland leaf litter, *Soil Biology & Biochemistry*, *76*, 278–285.

Moyano, F. E., S. Manzoni, and C. Chenu (2013), Responses of soil heterotrophic respiration to moisture availability: An exploration of processes and models, *Soil Biology & Biochemistry*, *59*, 72.85.

Mualem, Y. (1976), A new model for predicting the hydraulic conductivity of unsaturated porous media, *Water Resour. Res*, *12*(3), 513–522, doi:10.1029/WR012i003p00513.

Mualem, Y., and S. Assouline (1989), Modeling soil seal as a non-uniform layer, *Water Resources Research*, *25*, 2101–2108.

Mualem, Y., S. Assouline, and H. Rohdenburg (1990), Rainfall-induced soil seal. C. A dynamic model with kinetic energy instead of cumulative rainfall as independent variable, *Catena*, *17*, 289–303.

Muller, B., F. Pantin, M. Génard, O. Turc, S. Freixes, M. Piques, and Y. Gibon (2011), Water deficits uncouple growth from photosynthesis, increase C content, and modify the relationships between C and growth in sink organs, *Journal of Experimental Botany*, *62*(6), 1715–1729, doi:10.1093/jxb/erq438.

Myneni, R. B., S. Hoffman, Y. Knyazikhin, J. L. Privette, J. Glassy, Y. Tian, Y. Wang, X. Song, Y. Zhang, G. R. Smith, A. Lotsch, M. Friedl, J. T. Morisette, P. Votava, R. R. Nemani, and S. W. Running (2002), Global products of vegetation leaf area and fraction absorbed PAR from year one of MODIS data, *Remote Sensing of Environment*, *83*, 214–231.

Nardi, F., S. Grimaldi, M. Santini, A. Petroselli, and L. Ubertini (2008), Hydrogeomorphic properties of simulated drainage patterns using digital elevation models: the flat area issue, *Hydrological Sciences Journal*, *53*(6), 1176–1193.

Newman, E. I. (1969), Resistance to water flow in soil and plant. i. soil resistance in relation to amounts of root: theoretical estimate, *J. Appl. Ecol.*, *6*, 1–12.

Niinemets, U., and O. Kull (1998), Stoichiometry of foliar carbon constituents varies along light gradients in temperate woody canopies: Implications for foliage morphological plasticity, *Tree Physiology*, *18*, 467–479.

Niinemets, U., and J. D. Tenhunen (1997), A model separating leaf structural and physiological effects on carbon gain along light gradients for the shade-tolerant species Acer saccharum, *Plant, Cell & Environment*, *20*, 845–866.

Niinemets, U., T. F. Keenan, and L. Hallik (2015), A worldwide analysis of within-canopy variations in leaf structural, chemical and physiological traits across plant functional types, *New Phytologist*, *205*, 973–993, doi: 10.1111/nph.13096.

Niklas, K. J., and B. J. Enquist (2001), Invariant scaling relationships for interspecific plant biomass production rates and body size, *Proc. Natl Acad. Sci. USA*, *98*, 2922–2927.

Niklas, K. J., and B. J. Enquist (2002), On the vegetative biomass partitioning of seed plant leaves, stems, and roots, *The American Naturalist*, *159*(5), 482–497.

Niyogi, D. S., and S. Raman (1997), Comparison of four different stomatal resistance schemes using FIFE observations, *Journal of Applied Meteorology*, *36*, 903–917.

Nobel, P. S. (2009), *Physicochemical and Environmental Plant Physiology*, Elsevier Academic Press.

Noilhan, J., and J.-F. Mafhouf (1996), The ISBA land surface parameterisation scheme, *Global and Planetary Change*, *13*, 145–159.

Noilhan, J., and S. Planton (1989), A simple parameterization of land surface processes for meteorological models, *Monthly Weather Review*, *117*, 536–549.

Nouvellon, Y., S. Rambal, D. L. Seen, M. S. Moran, J. P. Lhomme, A. Begue, A. G. Chehbouni, and Y. Kerr (2000), Modelling of daily fluxes of water and carbon from shortgrass steppes, *Agricultural and Forest Meteorology*, *100*, 137–153.

nuelas, J. P., and I. Filella (2001), Phenology: Responses to a warming world, *Science*, *294*(5543), 793–795, doi: 10.1126/science.1066860.

Núnez, C. M., E. A. Varas, and F. J. Meza (2010), Modelling soil heat flux, *Theoretical Applied Climatology*, *100*, 251–260, doi:10.1007/s00704-009-0185-y.

O'Callaghan, J. F., and D. M. Mark (1984), The extraction of drainage networks from digital elevation data, *Computer Vision, Graphics and Image Processing*, *28*, 323–344.

Oleson, K. W., Y. Dai, G. Bonan, M. Bosilovich, R. Dickinson, P. Dirmeyer, F. Hoffman, P. Houser, S. Levis, G. Y. Niu, P. Thornton, M. Vertenstein, Z. L. Yang, and X. Zeng (2004), Technical description of the community land model (CLM), *Tech. Rep. NCAR/TN-461+STR*, Natl. Cent. for Atmos. Res., Boulder, Colorado.

Oleson, K. W., G.-Y. Niu, Z.-L. Yang, D. M. Lawrence, P. E. Thornton, P. J. Lawrence, R. Stockli, R. E. Dickinson, G. B. Bonan, S. Levis, A. Dai, and T. Qian (2008), Improvements to the Community Land Model and their impact on the hydrological cycle, *Journal of Geophysical Research*, *113*(G01021), doi:10.1029/2007JG000563.

Oleson, K. W., D. M. Lawrence, G. B. Bonan, B. Drewniak, M. Huang, C. D. Kowen, S. Levis, F. Li, W. J. Riley, Z. M. Subin, S. C. Swenson, and P. E. Thornton (2013), Technical description of version 4.5 of the community land model (CLM), *Tech. Rep. NCAR/TN-503+STR*, Natl. Cent. for Atmos. Res., Boulder, Colorado.

Olseth, J. A., and A. Skartveit (1997), Spatial distribution of photosynthetically active radiation over complex topography, *Agricultural and Forest Meteorology*, *86*, 205–214.

Olseth, J. A., A. Skartveit, and H. Zou (1995), Spatially continuous mapping of solar resources in a complex high latitude topography, *Solar Energy*, *55*(6), 475–485.

Öquist, G., and W. S. Chow (1992), On the relationship between the quantum yield of Photosystem II electron transport, as determined by chlorophyll fluorescence and the quantum yield of CO_2-dependent O_2 evolution, *Photosynthesis Research*, *33*, 51–62.

Or, D., P. Lehmann, E. Shahraeeni, and N. Shokri (2013), Advances in soil evaporation physics-a review, *Vadose Zone J.*, *12*(4), 1–45, doi: 10.2136/vzj2012.0163.

Orlandini, S. (2002), On the spatial variation of resistance to flow in upland channel networks, *Water Resources Research*, *38*(10), 1197, doi:10.1029/2001WR001187.

Orlandini, S., and G. Moretti (2009), Determination of surface flow paths from gridded elevation data, *Water Resources Research*, *45*(W03417), doi:10.1029/2008WR007099.

Orlandini, S., G. Moretti, M. Franchini, B. Aldighieri, and B. Testa (2003), Path-based methods for the determination of nondispersive drainage directions in grid-based digital elevation models, *Water Resources Research*, *39*(6), doi:10.1029/2002WR001639.

Orlandini, S., P. Tarolli, G. Moretti, and G. D. Fontana (2011), On the prediction of channel heads in a complex alpine terrain using gridded elevation data, *Water Resources Research*, *47*(W02538), doi:10.1029/2010WR009648.

Orwin, K. H., M. U. F. Kirschbaum, M. G. StJohn, and I. A. Dickie (2011), Organic nutrient uptake by mycorrhizal fungi enhances ecosystem carbon storage: a model-based assessment, *Ecology Letters*, *14*, 493–502, doi: 10.1111/j.1461-0248.2011.01611.x.

Pan, Y., R. A. Birdsey, O. L. Phillips, and R. B. Jackson (2013), The structure, distribution, and biomass of the world's forests, *Annual Review of Ecology, Evolution, and Systematics*, *44*, 593–622.

Panday, S., and P. S. Huyakorn (2004), A fully coupled physically-based spatially-distributed model for evaluating surface/subsurface flow, *Advances in Water Resources*, *27*, 361–382.

Pantin, F., T. Simonneau, and B. Muller (2012), Coming of leaf age: control of growth by hydraulics and metabolics during leaf ontogeny, *New Phytologist*, *196*, 349–366.

Pappas, C., S. Fatichi, and P. Burlando (2016), Modeling terrestrial carbon and water dynamics across climatic gradients: does plant diversity matter?, *New Phytologist*, *209*, 137–151, doi: 10.1111/nph.13590.

Parent, B., O. Turc, Y. Gibon, M. Stitt, and F. Tardieu (2010), Modelling temperature compensated physiological rates, based on the co-ordination of responses to temperature of developmental processes, *Journal of Experimental Botany*, *61*, 2057–2069.

Park, H. T., S. Hattori, and T. Tanaka (1998), Development of a numerical model for evaluating the effect of litter layer on evaporation, *Journal of Forest Research*, *3*, 25–33.

Parsons, A. J., J. Wainwright, D. M. Powell, J. Kaduk, and R. E. Brazier (2004), A conceptual model for determining soil erosion by water, *Earth Surface Processes and Landforms*, *29*, 1293–1302, doi: 10.1002/esp.1096.

Parton, W. J., J. W. B. Stewart, and C. V. Cole (1988), Dynamics of C, N, P and S in grassland soils - a model, *Biogeochemistry*, *5*, 109–131.

Parton, W. J., J. M. O. Scurlock, D. S. Ojima, T. G. Gilmanov, R. J. Scholes, D. S. Schimel, T. Kirchner, J.-C. Menaut, T. Seastedt, E. Garcia-Moya, A. Kamnalrut, and J. I. Kinyamario (1993), Observations and modelling of biomass and soil organic matter dynamics for the grassland biome worldwide, *Global Biogeochemical Cycles*, *7*, 785–809.

Paschalis, A., G. G. Katul, S. Fatichi, G. Manoli, and P. Molnar (2016), Matching eco-hydrological processes and scales of banded vegetation patterns in semi-arid catchments, *Water Resources Research*, *52*(3), 2259–2278, doi: 10.1002/2015WR017679.

Pederson, C. A., and J.-G. Winther (2005), Intercomparison and validation of snow-albedo parameterization schemes in climate models, *Climate Dynamic*, *25*, 351–362, doi: 10.1007/s00382-005-0037-0.

Peters-Lidard, C. D., E. Blackburn, X. Liang, and E. F. Wood (1998), The effect of soil thermal conductivity parameterization on surface energy fluxes and temperatures, *Journal of the Atmospheric Sciences*, *55*, 1209–1224.

Philip, J. R. (1957), Evaporation, and moisture and heat fields in the soil, *Journal of Meteorology*, *14*, 354–366.

Phillips, R. P., E. R. Brzostek, and M. G. Midgley (2013), The mycorrhizal-associated nutrient economy: a new framework for predicting carbon-nutrient couplings in temperate forests, *New Phytologist*, *199*, 41–51.

Pirazzini, R., M. Nardino, A. Orsini, F. Calzolari, T. Georgiadis, and V. Levizzani (2001), Parameterization of the downward longwave radiation from clear and cloudy skies at Ny Ålesund (Svalbard), in *IRS 2000: Current Problems in Atmospheric Radiation*, edited by W. Smith and Y. M. Timofeyev, pp. 559–562, A. Deepack Publishing, Hampton, Virginia.

Pockman, W. T., and J. S. Sperry (2000), Vulnerability to xylem cavitation and the distribution of sonoran vegetation, *American Journal of Botany*, *87*(9), 1287–1299.

Pocock, M. J., D. M. Evans, and J. Memmott (2010), The impact of farm management on species-specific leaf area index (LAI): Farm-scale data and predictive models, *Agriculture, Ecosystems and Environment*, *135*, 279–287.

Polgar, C. A., and R. B. Primack (2011), Leaf-out phenology of temperate woody plants: from trees to ecosystems, *New Phytologist*, *191*, 926–941, doi:10.1111/j.1469-8137.2011.03803.x.

Pomeroy, J. W., D. M. Gray, K. R. Shook, B. Toth, R. L. H. Essery, A. Pietroniro, and N. Hedstrom (1998a), An evaluation of snow accumulation and ablation processes for land surface modelling, *Hydrological Processes*, *13*, 2339–2367.

Pomeroy, J. W., N. Parviainen, N. Hedstrom, and D. M. Gray (1998b), Coupled modeling of forest snow interception and sublimation, *Hydrological Processes*, *12*, 2317–2337.

Pomeroy, J. W., D. M. Gray, N. Hedstrom, and J. R. Janowicz (2002), Prediction of seasonal snow accumulation in cold climate forests, *Hydrological Processes*, *16*, 3543–3558.

Poorter, H. (1994), *A whole plant perspective on carbon-nitrogen interactions*, chap. Construction costs and payback time of biomass: a whole plant perspective, pp. 111–127, SPB Academic Publishing bv, The Hague, The Netherlands.

Poorter, H., and R. Villar (1997), *Plant Resource Allocation*, chap. The fate of acquired carbon in plants: chemical composition and construction costs, pp. 39–72, Academic Press, New York.

Porporato, A., P. D'Odorico, F. Laio, and I. Rodriguez-Iturbe (2003), Hydrologic controls on soil carbon and nitrogen cycles. I. Modeling scheme, *Advances in Water Resources*, *26*, 45–58.

Prata, A. J. (1996), A new long-wave formula estimating downward clear-sky radiation at the surface, *Quarterly Journal of the Royal Meteorological Society*, *122*, 1127–1151.

Pregitzer, K. S. (2003), Woody plants, carbon allocation and fine roots, *New Phytologist*, *158*(3), 421–424.

Putuhena, W. M., and I. Cordery (1996), Estimation of interception capacity of the forest floor, *Journal of Hydrology*, *180*, 283–299.

Quinn, P., K. Beven, P. Chevallier, and O. Planchon (1991), The prediction of hillslope flow paths for distributed hydrological modeling using digital terrain models, *Hydrological Processes*, *5*, 59–80.

Quinn, P. F., K. J. Beven, and R. Lamb (1995), The ln(a/tanβ) index: how to calculate it and how to use in within the TOPMODEL framework, *Hydrological Processes*, *9*, 161–182.

Ramírez, J. A., and S. U. S. Senarath (2000), A statistical-dynamical parameterization of interception and land surface-atmosphere interactions, *Journal of Climate*, *13*, 4050–4063.

Raupach, M. R. (1989), A practical acute “Lagrangian” method for relating scalar concentrations to source distributions in vegetation canopies, *Quarterly Journal Royal Meteorological Society*, *115*, 609–632.

Raupach, M. R. (1994), Simplified expressions for vegetation roughness length and zero-plane displacement as a function of canopy height and area index, *Boundary-Layer Meteorology*, *71*, 211–216.

Read, D. J., J. R. Leake, and J. Perez-Moreno (2004), Mycorrhizal fungi as drivers of ecosystem processes in heathland and boreal forest biomes, *Canadian Journal of Botany*, *82*, 1243–1263.

Reed, S. C., A. R. Townsend, E. A. Davidson, and C. C. Cleveland (2012), Stoichiometric patterns in foliar nutrient resorption across multiple scales, *New Phytologist*, *196*, 173–180, doi: 10.1111/j.1469-8137.2012.04249.x.

Reich, P. B., M. B. Walters, and D. S. Ellsworth (1997), From tropics to tundra: global convergence in plant functioning, *Proc. Natl. Acad. Sci. USA*, *94*, 13,730–13,734.

Reich, P. B., D. S. Ellsworth, and M. B. Walters (1998a), Leaf strucuture (specific leaf area) modulates photosynthesis-nitrogen realtions: evidence and across species and functional groups, *Functional Ecology*, *12*, 948–958.

Reich, P. B., M. B. Walters, D. S. Ellsworth, J. M. Vose, J. C. Volin, C. Gresham, and W. D. Bowman (1998b), Relationships of leaf dark respiration to leaf nitrogen, specific leaf area and leaf life-span: a test across biomes and functional groups, *Oecologia*, *114*, 471–482.

Reich, P. B., M. G. Tjoelker, J.-L. Machado, and J. Oleksyn (2006), Universal scaling of respiratory metabolism, size and nitrogen in plants, *Nature*, *339*, doi:10.1038/nature04282.

Richards, L. A. (1931), Capillary conduction of liquids through porous mediums, *Physics*, *1*, 318–333.

Richardson, A. D., R. S. Anderson, M. A. Arain, A. G. Barr, G. Bohrer, G. S. Chen, J. M. Chen, P. Ciais, K. J. Davis, A. R. Desai, M. C. Dietze, D. Dragoni, S. R. Garrity, C. M. Gough, R. Grant, D. Y. Hollinger, H. A. Margolis, H. McCaughey, M. Migliavacca, R. K. Monson, J. W. Munger, B. Poulter, B. M. Raczka, D. M. Ricciuto, A. K. Sahoo, K. Schaefer, H. Q. Tian, R. Vargas, H. Verbeeck, J. F. Xiao, and Y. K. Xue (2012), Terrestrial biosphere models need better representation of vegetation phenology: results from the north american carbon program site synthesis, *Global Change Biology*, *18*, 556–584.

Rigon, R., G. Bertoldi, and T. M. Over (2006), GEOtop: A distributed hydrological model with coupled water and energy budgets, *Journal of Hydrometeorology*, *7*(3), 371–388.

Robertson, A. D., K. Paustian, S. Ogle, M. D. Wallenstein, E. Lugato, and M. F. Cotrufo (2019), Unifying soil organic matter formation and persistence frameworks: the MEMS model, *Biogeosciences Discuss.*, *1*, –, doi.org/10.5194/bg-2018-430.

Robinson, D. A., and C. P. Phillips (2001), Crust development in relation to vegetation and agricultural practice on erosion susceptible, dispersive clay soils from central and southern italy, *Soil & Tillage Research*, *60*, 1–9.

Ross, J. (1975), Radiative transfer in plant communities, in *Vegetation and the Atmosphere*, pp. 13–55, Academic Press.

Ross, P. J. (2003), Modeling soil water and solute transport-fast, simplified numerical solutions, *Agronomy Journal*, *95*, 1352–1361.

Roumet, C., M. Birouste, C. Picon-Cochard, M. Ghestem, N. Osman, S. Vrignon-Brenas, K. fang Cao, and A. Stokes (2016), Root structure-function relationships in 74 species: evidence of a root economics spectrum related to carbon economy, *New Phytologist*, *210*(3), 815–826.

Ruimy, A., G. Dedieu, and B. Saugier (1996), TURC: A diagnostic model of continental gross primary productivity and net primary productivity, *Global Biogeochemical Cycles*, *10*, 269–285.

Ruiz, S., D. Or, and S. J. Schymanski (2015), Soil penetration by earthworms and plant roots-mechanical energetics of bioturbation of compacted soils, *PLoS ONE*, *10*(6), e0128,914, doi:10.1371/journal.pone.0128914.

Rutter, A. J., K. A. Kershaw, P. C. Robins, and A. J. Morton (1971), A predictive model of rainfall interception in forests. 1. Derivation of the model from observation in a plantation of Corsican pine, *Agricultural Meteorology*, *9*, 367–384.

Rutter, A. J., A. J. Morton, and P. C. Robins (1975), A predictive model of rainfall interception in forests. 2. Generalization of model and comparison with observations in some coniferous and hardwood stands, *The Journal of Applied Ecology*, *12*(1), 367–380.

Ryan, M. G. (1991), Effects of cllimate change on plant respiration, *Ecological Applications*, *1*(2), 157–167.

Ryder, J., J. Polcher, P. Peylin, C. Ottlé, Y. Chen, E. van Gorsel, V. Haverd, M. J. McGrath, K. Naudts, J. Otto, A. Valade, and S. Luyssaert (2016), A multi-layer land surface energy budget model for implicit coupling with global atmospheric simulations, *Geoscientific Model Development*, *9*, 223–245.

Sack, L., and N. M. Holbrook (2006), Leaf hydraulics, *The Annual Review of Plant Biology*, *57*, 361–381, doi:10.1146/annurev.arplant.56.032604.144141.

Sakaguchi, K., and X. Zeng (2009), Effects of soil wetness, plant litter, and under-canopy atmospheric stability on ground evaporation in the Community Land Model(CLM3.5), *Journal of Geophysical Research*, *114*(D01107), doi:10.1029/2008JD010834.

Sakai, M., N. Toride, and J. Simunek (2009), Water and vapor movement with condensation and evaporation in a sandy column, *Soil Sci. Soc. Am. J.*, *73*, 707–717.

Sala, A. (2009), Lack of direct evidence for the carbon-starvation hypothesis to explain drought-induced mortality in trees, *Proceedings of the National Academy of Sciences, USA*, *106*(26), E68.

Sala, A., and G. Hoch (2009), Height-related growth declines in ponderosa pine are not due to carbon limitation, *Plant, Cell & Environment*, *32*, 22–30.

Sala, A., W. Founts, and G. Hoch (2011), *Size- and Age- Related Changes in Tree Structure and Function*, chap. Carbon storage in trees: does relative carbon supply decrease with tree size?, pp. 287–306, Springer, Dordrecht.

Sala, A., D. R. Woodruff, and F. C. Meinzer (2012), Carbon dynamics in trees: feast or famine?, *Tree Physiology*, *32*, 764–775, doi:10.1093/treephys/tpr143.

Sardans, J., and J. P. nuelas (2015), Potassium: a neglected nutrient in global change, *Global Ecology and Biogeography*, *24*, 261–275.

Sato, H., A. Itoh, and T. Kohyama (2007), SEIB-DGVM: A new Dynamic Global Vegetation Model using a spatially explicit individual-based approach, *Ecological Modelling*, *200*, 279–307.

Sato, Y., T. Kumagai, A. Kume, K. Otsuki, and S. Ogawa (2004), Experimental analysis of moisture dynamics of litter layers-the effects of rainfall conditions and leaf shapes, *Hydrol. Process.*, *18*, 3007–3018.

Savenije, H. H. G. (2004), The importance of interception and why we should delete the term evapotranspiration from our vocabulary, *Hydrological Processes*, *18*, 1507–1511.

Saxton, K. E., and W. J. Rawls (2006), Soil water characteristic estimates by texture and organic matter for hydrologic solutions, *Soil Science Society of America Journal*, *70*, 1569–1578, doi:10.2136/sssaj2005.0117.

Saxton, K. E., W. J. Rawls, J. S. Romberger, and R. I. Papendick (1986), Estimating generalized soil water characteristics from texture, *Transactions of ASAE*, *50*, 1031–1035.

Schaap, M. G., and W. Bouten (1997), Forest floor evaporation in a dense douglas fir stand, *Journal of Hydrology*, *193*, 97–113.

Schaap, M. G., and M. T. van Genuchten (2006), A modified Mualem-van Genuchten formulation for improved description of the hydraulic conductivity near saturation, *Vadose Zone Journal*, *5*, 27–34, doi:10.2136/vzj2005.0005.

Schenk, H. J., and R. B. Jackson (2002), The global biogeography of roots, *Ecological Monography*, *72*(3), 311–328.

Schimel, J. P., and M. N. Weintraub (2003), The implications of exoenzyme activity on microbial carbon and nitrogen limitation in soil: a theoretical model, *Soil Biology and Biochemistry*, *35*, 549–563.

Schimel, J. P., C. A. Becerra, and J. Blankinship (2017), Estimating decay dynamics for enzyme activities in soils from different ecosystems, *Soil Biology and Biochemistry*, *114*, 5–11.

Schmidt, M. W. I., M. S. Torn, S. Abiven, T. Dittmar, G. Guggenberger, I. A. Janssens, M. Kleber, I. Kögel-Knabner, J. Lehmann, D. A. C. Manning, P. Nannipieri, D. P. Rasse, S. Weiner, and S. E. Trumbore (2011), Persistence of soil organic matter as an ecosystem property, *Nature*, *478*, 49–56.

Schmidt, R. A., and D. R. Gluns (1991), Snowfall interception on branches of 3 conifer species, *Canadian Journal of Forest Research-Revue Canadienne De Recherche Forestiere*, *21*, 1262–1269.

Schuepp, P. H. (1993), Leaf boundary layers, *New Phytologist*, *125*, 477–507.

Schulze, E., F. M. Kelliher, C. Korner, J. Lloyd, and R. Leuning (1994), Relationships among maximum stomatal conductance, ecosystem surface conductance, carbon assimilation rate, and plant nitrogen nutrition: A global ecology scaling exercise, *Annual Reviews in Ecology and Systematics*, *25*, 629–662, doi:10.1146/annurev.es.25.110194.00321.

Schwanghart, W., and N. J. Kuhn (2010), Topotoolbox: A set of Matlab functions for topographic analysis, *Environmental Modelling & Software*, *25*, 770–781, doi:10.1016/j.envsoft.2009.12.002.

Schwartz, M. D., R. Ahas, and A. Aasa (2006), Onset of spring starting earlier across the Northern Hemisphere, *Global Change Biology*, *12*, 343–351, doi: 10.1111/j.1365-2486.2005.01097.x.

Sela, S., T. Svoray, and S. Assouline (2015), The effect of soil surface sealing on vegetation water uptake along a dry climatic gradient, *Water Resour. Res.*, *51*, 7452–7466, doi:10.1002/2015WR017109.

Selim, H. M., R. S. Mansell, and L. Zelazny (1976), Modeling reactions and transport of potassium in soils, *Soil Sci.*, *122*, 77–84.

Sellers, P. J. (1985), Canopy reflectance, photosynthesis and transpiration, *International Journal of Remote Sensing*, *6*, 1335–1372.

Sellers, P. J., Y. Mintz, Y. C. Sud, and A. Dalcher (1986), A simple biosphere model (SiB) for use within general circulation models, *Journal of the Atmospheric Sciences*, *43*(6), 505–531.

Sellers, P. J., J. A. Berry, G. J. Collatz, C. B. Field, and F. G. Hall (1992), Canopy reflectance, photosynthesis, and transpiration. III. A reanalysis using improved leaf models and a new canopy integration scheme, *Remote Sensing of Environment*, *42*(3), 187–216.

Sellers, P. J., S. O. Los, C. J. Tucker, C. O. Justice, D. A. Dazlich, G. J. Collatz, and D. A. Randall (1996a), A revised land surface parameterization (SiB2) for atmospheric GCMs. 2. the generation of global fields of terrestrial biophysical parameters from satellite data, *Journal of Climate*, *9*(4), 706–737.

Sellers, P. J., D. A. Randall, G. J. Collatz, J. A. Berry, C. B. Field, D. A. Dazlich, C. Zhang, G. D. Collelo, and L. Bounoua (1996b), A revised land surface parameterization (SiB2) for atmospheric GCMs. 1. Model formulation, *Journal of Climate*, *9*(4), 674–705.

Sellers, P. J., R. E. Dickinson, D. A. Randall, A. K. Betts, F. G. Hall, J. A. Berry, G. J. Collatz, A. S. Denning, H. A. Mooney, C. A. Nobre, N. Sato, C. B. Field, and A. Henderson-Sellers (1997), Modeling the exchanges of energy, water and carbon between continents and the atmosphere, *Science*, *275*, 502–509.

Shahraeeni, E., P. Lehmann, and D. Or (2012), Coupling of evaporative fluxes from drying porous surfaces with air boundary layer-characteristics of evaporation from discrete pores, *Water Resour. Res.*, *48*, W09,525, doi:10.1029/2012WR011857.

Shampine, L. F., and M. W. Reichelt (1997), The MATLAB ODE suite, *SIAM Journal on Scientific Computing*, *18*, 1–22.

Shi, M., J. B. Fisher, E. R. Brzostek, and R. P. Phillips (2016), Carbon cost of plant nitrogen acquisition: global carbon cycle impact from an improved plant nitrogen cycle in the Community Land Model, *Global Change Biology*, *22*, 1299–1314, doi: 10.1111/gcb.13131.

Shuttleworth, W. J., and R. J. Gurney (1990), The theoretical relationship between foliage temperature and canopy resistance in sparse crops, *Quarterly Journal of the Royal Meteorological Society*, *116*, 497–519.

Simard, M., N. Pinto, J. B. Fisher, and A. Baccini (2011), Mapping forest canopy height globally with spaceborne lidar, *J. Geophys. Res.*, *116*, G04,021, doi:10.1029/2011JG001708.

Sinclair, T. R., C. E. Murphy, and K. R. Knoerr (1976), Development and evaluation of simplified models for simulating canopy photosynthesis and transpiration, *Journal of Applied Ecology*, *13*, 813–829.

Singsaas, E. L., D. R. Ort, and E. H. Delucia (2001), Variation in measured values of photosynthetic quantum yield in ecophysiological studies, *Oecologia*, *128*, 15–23.

Sinsabaugh, R. L., S. Manzoni, D. L. Moorhead, and A. Richter (2013), Carbon use efficiency of microbial communities: stoichiometry, methodology and modelling, *Ecology Letters*, *16*, 930–939, doi: 10.1111/ele.12113.

Sinsabaugh, R. L., J. Belnap, S. G. Findlay, J. J. F. Shah, B. H. Hill, K. A. Kuehn, C. R. Kuske, M. E. Litvak, N. G. Martinez, D. L. Moorhead, and D. D. Warnock (2014), Extracellular enzyme kinetics scale with resource availability, *Biogeochemistry*, *121*, 287–304, doi:10.1007/s10533-014-0030-y.

Sinsabaugh, R. L., J. J. F. Shah, S. G. Findlay, K. A. Kuehn, and D. L. Moorhead (2015), Scaling microbial biomass, metabolism and resource supply, *Biogeochemistry*, *122*, 175–190, doi:10.1007/s10533-014-0058-z.

Sinsabaugh, R. L., B. T. Turner, J. M. Talbot, B. G. Waring, J. S. Powers, C. R. Kuske, D. Moorhead, and J. J. F. Shah (2016), Stoichiometry of microbial carbon use efficiency in soils, *Ecological Monographs*, *86*(2), 172–189.

Sistla, S. A., and J. P. Schimel (2012), Stoichiometric flexibility as a regulator of carbon and nutrient cycling in terrestrial ecosystems under change, *New Phytologist*, *196*, 68–78, doi: 10.1111/j.1469-8137.2012.04234.x.

Sitch, S., B. Smith, I. C. Prentice, A. Arneth, A. Bondeau, W. Cramer, J. O. Kaplan, S. Levis, W. Lucht, M. T. Sykes, K. Thonicke, and S. Venevski (2003), Evaluation of ecosystem dynamics, plant geography and terrestrial carbon cycling in the LPJ dynamic global vegetation model, *Global Change Biology*, *9*, 161–185.

Sivapalan, M., K. J. Beven, and E. F. Wood (1987), On hydrologic similarity 2. A scaled model of storm runoff production, *Water Resources Research*, *23*(12), 2266–2278.

Six, J., G. Guggenberger, K. Paustian, L. Haumaier, E. T. Elliott, and W. Zech (2001), Sources and composition of soil organic matter fractions between and within soil aggregates, *European Journal of Soil Science*, *52*, 607–618.

Six, J., R. T. Conant, E. A. Paul, and K. Paustian (2002), Stabilization mechanisms of soil organic matter: Implications for c-saturation of soils, *Plant and Soil*, *241*, 155–176.

Skillman, J. B. (2008), Quantum yield variation across the three pathways of photosynthesis: not yet out of the dark, *Journal of Experimental Botany*, *59*(7), 1647–1661.

Smith, N. G., and J. S. Dukes (2013), Plant respiration and photosynthesis in global-scale models: incorporating acclimation to temperature and co2, *Glob. Change Biol*, *19*, 45–63.

Smith, S. E., and D. J. Read (2008), *Mycorrhizal Symbiosis*, Academic Press, London, UK.

Smith, S. E., and F. A. Smith (2011), Roles of arbuscular mycorrhizas in plant nutrition and growth: New paradigms from cellular to ecosystem scales, *Annu. Rev. Plant Biol.*, *62*, 227–250.

Smits, K. M., A. Cihan, T. Sakaki, and T. H. Illangasekare (2011), Evaporation from soils under thermal boundary conditions: Experimental and modeling investigation to compare equilibriumand nonequilibrium-based approaches, *Water Resources Research*, *47*(W05540), doi:10.1029/2010WR009533.

Sovilla, B., P. Burlando, and P. Bartelt (2006), Field experiments and numerical modeling of mass entrainment in snow avalanches, *J. Geophys. Res.*, *111*(F03007), doi:10.1029/2005JF000391.

Sparks, D. L. (1987), Potassium dynamics in soils, *Adv Soil Sci*, *6*, 1–63.

Sparks, D. L., and T. H. Carski (1985), Kinetics of potassium exchange in heterogeneous systems, *Appl. Clay Sci*, *1*, 89–101.

Sparks, D. L., and P. M. Huang (1985), *Potassium in Agriculture*, chap. Physical chemistry of soil potassium, pp. 201–276, American Society of Agronomy, Crop Science Society of America, and Soil Science Society of America, Madison, WI.

Sperry, J. S., F. R. Adler, G. S. Campbell, and J. P. Comstock (1998), Limitation of plant water use by rhizosphere and xylem conductance: results from a model, *Plant, Cell and Environment*, *21*, 347–359.

Sperry, J. S., U. G. Hacke, R. Oren, and J. P. Comstock (2002), Water deficits and hydraulic limits to water supply, *Plant, Cell and Environment*, *25*, 251–264.

Sperry, J. S., V. Stiller, and U. G. Hacke (2003), Xylem hydraulics and the soil-plant-atmosphere continuum: Opportunities and unresolved issues, *Agronomy Journal*, *95*, 1362–1370.

Spitters, C. J. T., H. A. J. M. Toussaint, and J. Goudriann (1986), Separating the diffuse and direct component of global radiation and its implications for modeling canopy photosynthesis. Part I. Components of incoming radiation, *Agricultural and Forest Meteorology*, *38*, 217–229.

Steudle, E., and C. A. Peterson (1998), How does water get through roots?, *J. Exper. Bot*, *49*, 775–788.

Stewart, C. E., K. Paustian, R. T. Conant, A. F. Plante, and J. Six (2007a), Soil carbon saturation: concept, evidence and evaluation, *Biogeochemistry*, *86*, 19–31, doi:10.1007/s10533-007-9140-0.

Stewart, C. E., A. F. Plante, K. Paustian, R. T. Conant, and J. Six (2007b), Soil carbon saturation: Linking concept and measurable carbon pools, *Soil Sci. Soc. Am. J.*, *72*, 379–392, doi:10.2136/sssaj2007.0104.

Stokes, V. J., M. D. Morecroft, and J. I. L. Morison (2006), Boundary layer conductance for contrasting leaf shapes in a deciduous broadleaved forest canopy, *Agricultural and Forest Meteorology*, *139*, 40–54, doi:10.1016/j.agrformet.2006.05.011.

Storck, P., D. P. Lettenmaier, and S. M. Bolton (2002), Measurement of snow interception and canopy effects on snow accumulation and melt in a mountainous maritime climate, Oregon, United States, *Water Resources Research*, *38*(11), doi:10.1029/2002WR001281.

Strack, J. E., G. E. Liston, and R. P. Sr. (2004), Modeling snow depth for improved simulation of snow-vegetation-atmosphere interactions, *Journal of Hydrometeorology*, *5*, 723–734.

Strigul, N., D. Pristinski, D. Purves, J. Dushoff, and S. Pacala (2008), Scaling from trees to forests: Tractable macroscopic equations for forest dynamics, *Ecol. Monogr.*, *78*, 523–545.

Su, Z. (2002), The surface energy balance system (SEBS) for estimation of turbulent heat fluxes, *Hydrology and Earth System Sciences*, *6*(1), 85–99.

Su, Z., T. Schmugge, W. P. Kustas, and W. J. Massman (2001), An evaluation of two models for estimation of the roughness height for heat transfer between the land surface and the atmosphere, *Journal of Applied Meteorology*, *40*, 1933–1951.

Subin, Z. M., W. J. Riley, and D. Mironov (2012), Improved lake model for climate simulations, *J. Adv. Model. Earth Syst.*, *4*(M02001), doi:10.1029/2011MS000072.

Sulis, M., S. B. Meyerhoff, C. Paniconi, R. M. Maxwell, M. Putti, and S. J. Kollet (2010), A comparison of two physics-based numerical models for simulating surface water-groundwater interactions, *Advances in Water Resources*, *33*, 456–467, doi:10.1016/j.advwatres.2010.01.010.

Sun, Y., L. Gu, R. E. Dickinson, R. J. Norby, S. G. Pallardy, and F. M. Hoffman (2014), Impact of mesophyll diffusion on estimated global land co$_2$ fertilization, *Proceedings of the National Academy of Sciences of the United States of America*, *111*(44), 15,774–15,779.

Talbot, J. M., and K. K. Treseder (2012), Interactions among lignin, cellulose, and nitrogen drive litter chemistry-decay relationships, *Ecology*, *93*(2), 345–354.

Talbot, J. M., T. D. Bruns, D. P. Smith, S. Branco, S. I. Glassman, S. Erlandson, R. Vilgalys, and K. G. Peay (2013), Independent roles of ectomycorrhizal and saprophytic communities in soil organic matter decomposition, *Soil Biology & Biochemistry*, *57*, 282–291.

Tarboton, D. G. (1997), A new method for the determination of flow directions and upslope areas in grid digital elevation models, *Water Resources Research*, *33*, 309–319.

Tarboton, D. G., and C. H. Luce (1996), Utah Energy Balance snow accumulation and melt model (UEB): Computer model technical description and user's guide, *Tech. rep.*, Utah Water Research Laboratory and USDA Forest Service Intermountain Research Station.

Tarboton, R. L. B., D. G., and I. Rodriguez-Iturbe (1991), On the extraction of channel networks from digital elevation data, *Hydrological Processes*, *5*(1), 81–100.

Tardieu, F., and W. J. Davies (1993), Integration of hydraulic and chemical signalling in the control of stomatal conductance and water status of droughted plants, *Plant, Cell and Environment*, *16*, 341–349.

Tardieu, F., C. Granier, and B. Muller (2011), Water deficit and growth. Co-ordinating processes without an orchestrator?, *Current Opinion in Plant Biology*, *14*, 283–289.

Tecon, R., and D. Or (2017), Biophysical processes supporting the diversity of microbial life in soil, *FEMS Microbiology Reviews*, *41*, 599–623.

Teuling, A. J., R. Uijlenhoet, F. Hupet, and P. A. Troch (2006), Impact of plant water uptake strategy on soil moisture and evapotranspiration dynamics during drydown, *Geophysical Research Letters*, *33*(L03401), doi:10.1029/2005GL025019.

Thomas, H., and J. L. Stoddart (1980), Leaf senescence, *Annual Review of Plant Physiology*, *31*, 83–111, doi:10.1146/annurev.pp.31.060180.000503.

Thomas, S. C., and A. R. Martin (2012), Carbon content of tree tissues: A synthesis, *Forests*, *3*, 332–352, doi:10.3390/f3020332.

Thornley, J. H. M. (1970), Respiration, growth and maintenance in plants, *Nature*, *227*, 304–305.

Thornton, P. E., and N. E. Zimmermann (2007), An improved canopy integration scheme for a land surface model with prognostic canopy structure, *Journal of Climate*, *20*, 3902–3923.

Tjoelker, M. G., J. Oleksyn, and P. B. Reich (2001), Modeling respiration of vegetation: evidence for a general temperature-dependent Q_{10}, *Global Change Biology*, *7*, 223–230.

Torri, D., M. Sfalanga, and M. DelSette (1987), Splash detachment: runoff depth and soil cohesion, *Catena*, *14*, 149–155.

Tromp-van Meerveld, I., and M. Weiler (2008), Hillslope dynamics modeled with increasing complexity, *Journal of Hydrology*, *361*, 24–40, doi:10.1016/j.jhydrol.2008.07.019.

Tucker, G. E., S. T. Lancaster, N. M. Gasparini, R. L. Bras, and S. M. Rybarczyk (2001), An object-oriented framework for distributed hydrologic and geomorphologic modeling using triangulated irregular networks, *Computers & Geosciences*, *27*(8), 959–973.

Tuzet, A., A. Perrier, and R. Leuning (2003), A coupled model of stomatal conductance, photosynthesis and transpiration, *Plant, Cell and Environment*, *26*, 1097–1116.

Unsworth, M. H., and J. L. Monteith (1975), Long-wave radiation at the ground 1. angular distribution of incoming radiation, *Quat. J. R. Meteorol. Soc.*, *105*, 13–24.

USACE (1956), Snow hydrology, summary report of the snow investigations, *Tech. rep.*, U.S. Army Corps of Engineers, North Pacific Division, Portland, Oregon.

van den Hurk, B. J. J. M., and A. A. M. Holtslag (1997), On the bulk parameterization of surface fluxes for various conditions and parameter ranges, *Boundary-Layer Meteorology*, *82*, 119–134.

van der Tol, C., J. Berry, P. Campbell, and U. Rascher (2014), Models of fluorescence and photosynthesis for interpreting measurements of solar-induced chlorophyll fluorescence, *Journal of Geophysical Research: Biogeosciences*, *119*, 2312–2327.

van Genuchten, M. T. (1980), A closed-form equation for predicting the hydraulic conductivity of unsaturated soils, *Soil Science Society of America Journal*, *44*, 892–898.

vanDam, J. C., and R. A. Feddes (2000), Numerical simulation of infiltration, evaporation and shallow groundwater levels with the Richards equation, *Journal of Hydrology*, *233*, 72–85.

Varado, N., I. Braud, and P. J. Ross (2006), Development and assessment of an efficient numerical solution of the richards' equation including root extraction by plants, *Journal of Hydrology*, *323*, 258–275.

Verbeeck, H., K. Steppe, N. Nadezhdina, M. O. DeBeeck, , G. Deckmyn, L. Meiresonne, R. Lemeur, J. Èermák, R. Ceulemans, and I. A. Janssens (2007), Stored water use and transpiration in scots pine: a modeling analysis with ANAFORE, *Tree Physiology*, *27*, 1671–1685.

Vergutz, L., S. Manzoni, A. Porporato, R. F. Novais, and R. B. Jackson (2012), Global resorption efficiencies and concentrations of carbon and nutrients in leaves of terrestrial plants, *Ecological Monographs*, *82*, 205–220.

Verseghy, D. L. (1991), CLASS-A Canadian land surface scheme for GCMs. I. Soil model, *International Journal of Climatology*, *11*, 111–133.

Vesala, T. (1998), On the concept of leaf boundary layer resistance for forced convection, *Journal of Theoretical Biology*, *194*, 91–100.

Vet, R., R. S. Artz, S. Carou, M. Shawa, C.-U. Ro, W. Aas, A. Baker, V. C. Bowersox, F. Dentener, C. Galy-Lacaux, A. Hou, J. J. Pienaar, R. Gillett, M. C. Forti, S. Gromov, H. Hara, T. Khodzherm, N. M. Mahowald, S. Nickovic, P. Rao, and N. W. Reid (2014), A global assessment of precipitation chemistry and deposition of sulfur, nitrogen, sea salt, base cations, organic acids, acidity and ph, and phosphorus, *Atmospheric Environment*, *93*, 3–100.

Vico, G., and A. Porporato (2008), Modelling C3 and C4 photosynthesis under water-stressed conditions, *Plant Soil*, *313*, 187–203, doi:10.1007/s11104-008-9691-4.

Villar, R., A. A. Held, and J. Merino (1995), Dark leaf respiration in light and darkness of an evergreen and a deciduous plant species, *Plant Physiology*, *107*, 421–427.

Viterbo, P., and A. C. M. Beljaars (1995), An improved land surface parameterization scheme in the ECMWF model and its validation, *Journal of Climate*, *8*, 2716–2748.

Vivoni, E. R., V. Y. Ivanov, R. L. Bras, and D. Entekhabi (2005), On the effects of triangulated terrain resolution on distributed hydrologic model response, *Hydrological Processes*, *19*(11), 2101–2122.

vonCaemmerer, S., and G. D. Farquhar (1981), Some relationships between the biochemistry of photosynthesis and the gas exchange of leaves, *Planta*, *153*, 376–387.

Wang, G., and W. M. Post (2012), A theoretical reassessment of microbial maintenance and implications for microbial ecology modeling, *FEMS Microbiology Ecology*, *81*, 610–617.

Wang, G., W. M. Post, M. A. Mayes, J. T. Frerichs, and S. Jagadamma (2012), Parameter estimation for models of ligninolytic and cellulolytic enzyme kinetics, *Soil Biology and Biochemistry*, *48*, 28–38.

Wang, G., W. M. Post, and M. A. Mayes (2013), Development of microbial-enzyme-mediated decomposition model parameters through steady-state and dynamic analyses, *Ecological Applications*, *23*(1), 255–272.

Wang, J., and R. L. Bras (1999), Ground heat flux estimated from surface soil temperature, *Journal of Hydrology*, *216*, 214–226.

Wang, W.-M., Z.-L. Li, and H.-B. Su (2007), Comparison of leaf angle distribution functions: Effects on extinction coefficient and fraction of sunlit foliage, *Agricultural and Forest Meteorology*, *143*, 106–122.

Wang, Y. P. (2003), A comparison of three different canopy radiation models commonly used in plant modeling, *Functional Plant Biology*, *30*, 143–152.

Wang, Y.-P., and R. Leuning (1998), A two-leaf model for canopy conductance, photosynthesis and portioning of available energy I: Model description and comparison with a multi-layered model, *Agricultural and Forest Meteorology*, *91*, 89–111.

Warren, C. R. (2006), Why does photosynthesis decrease with needle age in pinus pinaster?, *Trees*, *20*, 157–164, doi: 10.1007/s00468-005-0021-7.

Warren, C. R. (2008), Stand aside stomata, another actor deserves centre stage: the forgotten role of the internal conductance to co_2 transfer, *Journal of Experimental Botany*, *59*(7), 1475–1487.

Weiler, M., and J. J. McDonnell (2004), Virtual experiments: a new approach for improving process conceptualization in hillslope hydrology, *Journal of Hydrology*, *285*, 3–18, doi:10.1016/S0022-1694(03)00271-3.

Weng, E. S., S. Malyshev, J. W. Lichstein, C. E. Farrior, R. Dybzinski, T. Zhang, E. Shevliakova, and S. W. Pacala (2015), Scaling from individual trees to forests in an Earth system modeling framework using a mathematically tractable model of height-structured competition, *Biogeosciences*, *12*, 2655–2694, doi:10.5194/bg-12-2655-2015.

West, G. B., B. J. Enquist, and J. H. Brown (2009), A general quantitative theory of forest structure and dynamics, *Proc. Natl Acad. Sci. USA*, *106*(17), 7040–7045, doi:10.1073/pnas.0812294106.

Whalen, J. K., K. H. Paustian, and R. W. Parmelee (1999), Simulation of growth and flux of carbon and nitrogen through earthworms, *Pedobiologia*, *43*, 537–546.

White, M. A., P. E. Thornton, S. W. Running, and R. R. Nemani (2000), Parameterization and sensitivity analysis of the BIOME-BGC terrestrial ecosystem model: Net primary production controls, *Earth Interactions*, *4*(3), 1–85.

Wicks, J. M., and J. C. Bathurst (1996), SHESED: a physically based, distributed erosion and sediment yield component for the SHE hydrological modeling system, *Journal of Hydrology*, *175*, 213–238.

Widlowski, J.-L., B. Pinty, M. Clerici, Y. Dai, M. D. Kauwe, K. de Ridder, A. Kallel, H. Kobayashi, T. Lavergne, W. Ni-Meister, A. Olchev, T. Quaife, S. Wang, W. Yang, Y. Yang, and H. Yuan (2011), RAMI4PILPS: An intercomparison of formulations for the partitioning of solar radiation in land surface models, *Journal of Geophysical Research*, *116*(G02019), doi:10.1029/2010JG001511.

Wieder, W. R., G. B. Bonan, and S. D. Allison (2013), Global soil carbon projections are improved by modelling microbial processes, *Nature Climate Change*, *3*, 909–912.

Wieder, W. R., A. S. Grandy, C. M. Kallenbach, G. B., and Bonan (2014), Integrating microbial physiology and physio-chemical principles in soils with the MIcrobial-MIneral Carbon Stabilization (MIMICS) model, *Biogeosciences*, *11*, 3899–3917, doi:10.5194/bg-11-3899-2014.

Wieder, W. R., A. S. Grandy, C. M. Kallenbach, P. G. Taylor, and G. B. Bonan (2015), Representing life in the earth system with soil microbial functional traits in the MIMICS model, *Geosci. Model Dev.*, *8*, 1789–1808, doi:10.5194/gmd-8-1789-2015.

Wieringa, J. (1993), Representative roughness parameters for homogeneous terrain, *Boundary-Layer Meteorology*, *63*, 323–363.

Wigmosta, M. S., and D. P. Lettenmaier (1999), A comparison of simplified methods for routing topographically driven subsurface flow, *Water Resources Research*, *35*(1), 255–264.

Wigmosta, M. S., L. W. Vail, and D. P. Lettenmaier (1994), A distributed hydrology-vegetation model for complex terrain, *Water Resources Research*, *30*(6), 1665–1679.

Williams, K. S., and D. G. Tarboton (1999), The ABC's of snowmelt: a topographically factorized energy component snowmelt model, *Hydrological Processes*, *13*, 1905–1920.

Wilson, K. B., D. D. Baldocchi, and P. J. Hanson (2001), Leaf age affects the seasonal pattern of photosynthetic capacity and net ecosystem exchange of carbon in a deciduous forest, *Plant, Cell and Environment*, *24*, 571–583.

Wiscombe, W. J., and S. G. Warren (1980), A model for the spectral albedo of snow. I. Pure snow, *Journal of Atmospheric Science*, *37*, 2712–2733.

Wolf, A., P. Ciais, V. Bellassen, N. Delbart, C. B. Field, and J. A. Berry (2011a), Forest biomass allometry in global land surface models, *Global Biogeochem. Cycles*, *25*, GB3015, doi:10.1029/2010GB003917.

Wolf, A., C. B. Field, and J. A. Berry (2011b), Allometric growth and allocation in forests: a perspective from FLUXNET, *Ecological Applications*, *21*(5), 1546–1556.

Woodruff, D. R., and F. C. Meinzer (2011), *Size- and Age-Related Changes in Tree Structure and Function*, chap. Size-Dependent Changes in Biophysical Control of Tree Growth: The Role of Turgor, pp. 363–384, Springer, Dordrecht, Netherlands.

Woodruff, D. R., B. J. Bond, and F. C. Meinzer (2004), Does turgor limit growth in tall trees?, *Plant, Cell and Environment*, *27*, 229–236.

Wramneby, A., B. Smith, S. Zaehle, and M. T. Sykes (2008), Parameter uncertainties in the modelling of vegetation dynamics-effects on tree community structure and ecosystem functioning in European forest biomes, *Ecological Modelling*, *216*, 277–290.

Wright, I. J., P. B. Reich, M. Westoby, D. D. Ackerly, Z. Baruch, F. Bongers, J. Cavender-Bares, T. Chapin, J. H. C. Cornelissen, M. Diemer, J. Flexas, E. Garnier, P. K. Groom, J. Gulias, K. Hikosaka, B. B. Lamont, T. Lee, W. Lee, C. Lusk, J. J. Midgley, M. Navas, U. Niinemets, J. Oleksyn, N. Osada, H. Poorter, P. Poot, L. Prior, V. I. Pyankov, C. Roumet, S. C. Thomas, M. G. Tjoelker, E. J. Veneklaas, and R. Villar (2004), The worldwide leaf economics spectrum, *Nature*, *428*, 821–827.

Wright, S. J., and C. P. Van Schaik (1994), Light and the phenology of tropical trees, *The American Naturalist*, *143*(1), 192–199.

Wu, A., T. A. Black, D. L. Verseghy, M. D. Novak, and W. G. Bailey (2000), Testing the α and β methods of estimating evaporation from bare and vegetated surfaces in CLASS, *Atmosphere-Ocean*, *38*, 15–35.

Wu, J., L. P. Albert, A. P. Lopes, N. Restrepo-Coupe, M. Hayek, K. T. Wiedemann, K. Guan, S. C. Stark, B. Christoffersen, N. Prohaska, J. V. Tavares, S. Marostica, H. Kobayashi, M. L. Ferreira, K. S. Campos, R. da Silva, P. M. Brando, D. G. Dye, T. E. Huxman, A. R. Huete, B. W. Nelson, and S. R. Saleska (2016), Leaf development and demography explain photosynthetic seasonality in Amazon evergreen forests, *Science*, *351*, 972–976.

Wythers, K. R., P. B. Reich, M. G. Tjoelker, and P. B. Bolstad (2005), Foliar respiration acclimation to temperature and temperature variable Q_{10} alter ecosystem carbon balance, *Global Change Biology*, *11*, 435–449, doi: 10.1111/j.1365-2486.2005.00922.x.

Xu, X., P. E. Thornton, and W. M. Post (2013), A global analysis of soil microbial biomass carbon, nitrogen and phosphorus in terrestrial ecosystems, *Global Ecology and Biogeography*, *22*, 737–749.

Xu, X., J. P. Schimel, I. A. Janssens, X. Song, C. Song, G. Yu, R. L. Sinsabaugh, D. Tang, X. Zhang, and P. E. Thornton (2017), Global pattern and controls of soil microbial metabolic quotient, *Ecological Monographs*, *87*, 429–441.

Xu-Ri, and I. C. Prentice (2008), Terrestrial nitrogen cycle simulation with a dynamic global vegetation model, *Global Change Biol.*, *14*, 1745–1764, doi:10.1111/j.1365- 2486.2008.01625.x.

Yang, X., V. Wittig, A. K. Jain, and W. Post (2009), Integration of nitrogen cycle dynamics into the integrated science assessment model for the study of terrestrialecosystem responses to global change, *Global Biogeochemical Cycles*, *23*(GB4029), doi:10.1029/2009GB003474.

Yang, X., W. M. Post, P. E. Thornton, and A. Jain (2013), The distribution of soil phosphorus for global biogeochemical modeling, *Biogeosciences*, *10*, 2525–2537, doi:10.5194/bg-10-2525-2013.

Yang, X., P. E. Thornton, D. M. Ricciuto, and W. M. Post (2014), The role of phosphorus dynamics in tropical forests - a modeling study using CLM-CNP, *Biogeosciences*, *11*, 1667–1681, doi:10.5194/bg-11-1667-2014.

Yang, Y., M. Leppäranta, B. Cheng, and Z. Li (2012), Numerical modelling of snow and ice thicknesses in lake Vanajavesi, Finland, *Tellus A*, *64*, 17,202, doi:10.3402/tellusa.v64i0.17202.

Yi, C. (2008), Momentum transfer within canopies, *J. Appl. Meteorol. Clim.*, *47*, 262–275, doi:10.1175/2007JAMC1667.1.

Yoda, K., T. Kira, H. Ogawa, and K. Hozumi (1963), Self thinning in over crowded pure stands under cultivated and natural conditions, *J Inst. Polytech. Osaka City Univ. Ser. D*, *14*, 107–129.

Zaehle, S., and D. Dalmonech (2011), Carbon-nitrogen interactions on land at global scales: current understanding in modelling climate biosphere feedbacks, *Current Opinion in Environmental Sustainability*, *3*, 311–320, doi:10.1016/j.cosust.2011.08.008.

Zaehle, S., and A. Friend (2010), Carbon and nitrogen cycle dynamics in the O-CN land surface model: 1. model description, site-scale evaluation, and sensitivity to parameter estimates, *Global Biogeochemical Cycles*, *24*(GB1005), doi:10.1029/2009GB003521.

Zaehle, S., B. E. Medlyn, M. G. De Kauwe, A. P. Walker, M. C. Dietze, T. Hickler, Y. Luo, Y.-P. Wang, B. El-Masri, P. Thornton, A. Jain, S. Wang, D. Warlind, E. Weng, W. Parton, C. M. Iversen, A. Gallet-Budynek, H. McCarthy, A. Finzi, P. J. Hanson, I. C. Prentice, R. Oren, and R. J. Norby (2014), Evaluation of 11 terrestrial carbon-nitrogen cycle models against observations from two temperate Free-Air CO_2 enrichment studies, *New Phytologist*, *202*, 803–822, doi: 10.1111/nph.12697.

Zak, D. R., D. Tilman, R. R. Parmenter, C. W. Rice, F. M. Fisher, J. Vose, D. Milchunas, and C. W. Martin (1994), Plant production and soil microorganisms in late-successional ecosystems: A continental-scale study, *Ecology*, *75*(8), 2333–2347.

Zanotti, F., S. Endrizzi, G. Bertoldi, and R. Rigon (2004), The GEOTOP snow module, *Hydrological Processes*, *18*, 3667–3679, doi: 10.1002/hyp.5794.

Zeng, X., and A. Wang (2007), Consistent parameterization of roughness length and displacement height for sparse and dense canopies in land models, *Journal of Hydrometeorology*, *8*, 730–737, doi: 10.1175/JHM607.1.

Zeng, X., R. Dickinson, M. Barlage, Y. Dai, G. Wang, and K. Oleson (2005), Treatment of undercanopy turbulence in land models, *Journal of Climate*, *18*, 5086–5094.

Zhang, H.-Y., X.-T. Lu, H. Hartmann, A. Keller, X.-G. Han, S. Trumbore, and R. P. Phillips (2018), Foliar nutrient resorption differs between arbuscular mycorrhizal and ectomycorrhizal trees at local and global scales, *Global Ecol Biogeogr.*, *27*(7), 875–885.

Zhao, W., and R. J. Qualls (2005), A multiple-layer canopy scattering model to simulate shortwave radiation distribution within a homogeneous plant canopy, *Water Resources Research*, *41*(W08409), doi:10.1029/2005WR004016.

Zhao, W., R. J. Qualls, and P. R. Berliner (2008), A two-concentric-loop iterative method in estimation of displacement height and roughness length for momentum and sensible heat, *International Journal of Biometeorology*, *52*, 849–858, doi:10.1007/s00484-008-0181-4.

Zhu, Q., W. J. Riley, J. Tang, and C. D. Koven (2016), Multiple soil nutrient competition between plants, microbes, and mineral surfaces: model development, parameterization, and example applications in several tropical forests, *Biogeosciences*, *13*, 341–363.

Zweifel, R., K. Steppe, and F. J. Sterck (2007), Stomatal regulation by microclimate and tree water relations: interpreting ecophysiological field data with a hydraulic plant model, *Journal of Experimental Botany*, *58*(8), 2113–2131, doi:10.1093/jxb/erm050.